D. Pérez Grande

uc3m | 2018

Fluid modeling and simulation of the electron population in Hall Effect Thrusters with complex magnetic topologies

uc3m | Universidad Carlos III de Madrid

Fluid modeling and simulation of the electron population in Hall Effect Thrusters with complex magnetic topologies

Tesis Doctoral

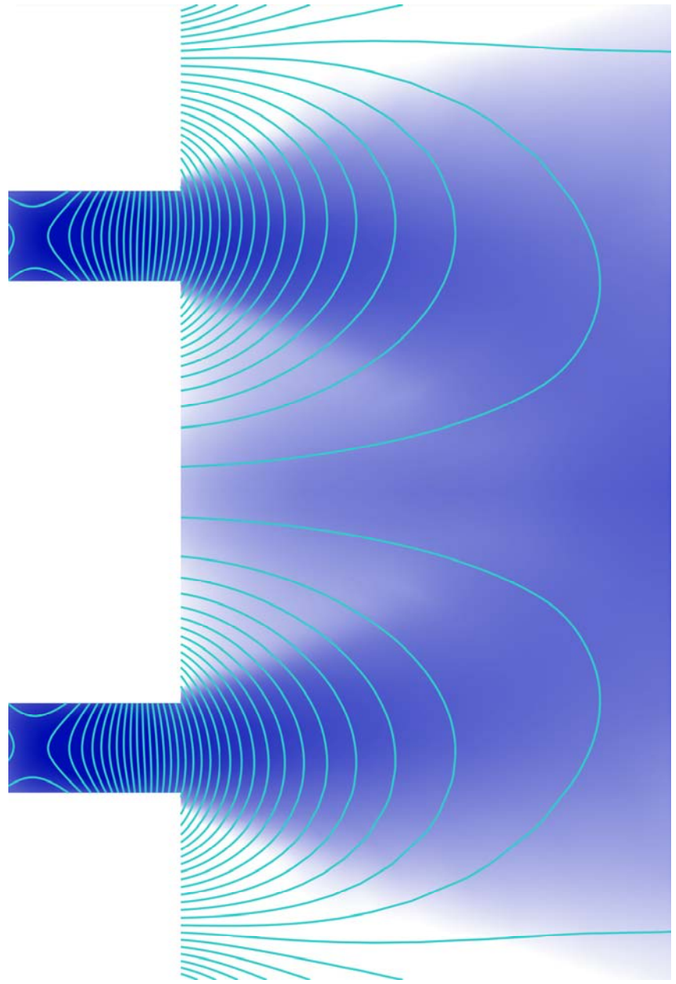

Daniel Pérez Grande

Dpto. de Bioingenería e Ingeniería Aeroespacial
Escuela Politécnica Superior

Dpto. de Bioingenería e Ingeniería Aeroespacial
Escuela Politécnica Superior

Fluid modeling and simulation of the electron population in Hall Effect Thrusters with complex magnetic topologies

Tesis Doctoral

Autor
Daniel Pérez Grande

Directores de Tesis:
Eduardo Ahedo Galilea
Pablo Fajardo Peña

Leganés,

Tesis doctoral

Fluid modeling and simulation of the electron population in Hall Effect Thrusters with complex magnetic topologies

Autor: Daniel Pérez Grande

Directores de Tesis: Eduardo Ahedo Galilea, Pablo Fajardo Peña

Firma del Tribunal Calificador:

Firma

Presidente:

Secretario:

Vocal:

Calificación:

Leganés, de de

Acknowledgements

It's difficult for me to write these last lines without looking back, trying to connect all of the little experiences, events, conversations and hard work that have brought me to this moment. It's a strange feeling to finish something that has taken up most of the last four years of my life and I believe my brain is trying to assign it some sort of *transcendence*. At the same time, I'm conscious that it is a relatively fleeting moment, which, like every other moment in life, will serve as the starting point for all that comes next.

If I must take something with me from this period, it will be two things that, I would assume, are pretty universal to the human experience: *stories* and *people*.

To the first, the stories woven through all of the books, music, movies, and every other piece of media I may have gone through, and to the people that authored and played them (who I am likely to never meet), thank you for being a source of inspiration. I have learned over the years that one must never dismiss the power of a good story; after all, if us humans are one thing above everything else, it's story-tellers. I hope that this small piece of work may, somehow and somewhere, become ingrained in one of the best stories we have ever told: the exploration of Space.

To the many people in my life, and, of course, to the human stories that come with them, I have tried to thank everyone in the next few paragraphs; apologies for some *spanglish* cropping up.

First and foremost, to my family: to my father, who showed me the value of curiosity, to my mother, who showed me the meaning of perseverance, and to my brother for... everything, really, this whole *life* thing would be a lot less fun without you in it. Thank you for putting up with my difficult moments and for always supporting me, even when my decisions seemed questionable (at best); I am very lucky for having you all in my life.

To my uncle Javi and to my aunt, Cova, and their beautiful children; in particular, to Diego: please, never stop being amazed by Rocket science and Space, and if you ever do, I'll be there to remind you why it's awesome.

To my thesis advisor, Eduardo, thank you for the opportunity you presented me with. It allowed me to be closer, professionally speaking, to Space, and opened the door to fulfill one of my life-long dreams: visiting NASA; also, thank you for your patience and support in some of the more complicated junctures. To my tutor, Pablo, thank you for your guidance and for the long conversations discussing all sorts of topics related to this work, I truly believe it is better because of them. To Mario, for all of the things that have brought us together over these last few years, its been a pleasure exploring them with you; let's hope that the future holds bigger and better adventures. To the EP2 pre-doctoral group (some post-doc now), thanks for all of the enlightening moments, for all that we have learned together, for reviewing quite a few chapters of the thesis and for the occasional, much needed, beer. In particular, thanks to Adri, without whom this work would be missing almost one half, and to Jiewei, for some of the last minute support with HYPHEN.

To my other colleagues, both PhD candidates and professors, thank you for making it a little bit easier to go to work every day. Specially, to Manu, Sara, Dani, Carlos, David and Mick; not only have you been able to put a smile in my face during the hardest moments, but you have undoubtedly proven that scientists can party as hard as anybody else, or possibly *harder*. To many more great moments together. In particular, thanks to Manu for being an anchor in those first moments of the PhD, *esperemos que "no cambie nada"*. A big shout-out to Manuel Sanjurjo as well, for your general good vibes and for pushing us to embrace the "outreach" part of science (and sorry for complaining about the MOOC so much). To the Young Visionaries crew: it was a pretty awesome feeling to win that competition and to be able to inject some creativity into this line of work. It was a great final touch for my time as a PhD candidate and I have you to thank for it.

To both of my temporary homes throughout the thesis: JPL and Ad Astra, and to the people I met there. In particular, to the crew at JPL: my time working there has been one of the most fulfilling both professionally and personally, even if it was only for a short while; thanks to Yiangos and Ben (who were also kind enough to review this document and provide me with insightful comments), to Chris, Dan, Jay, Ryan and the rest of the team. To Sam, Chris, Dim and Nina, who made my stay in Pasadena a truly unforgettable one, here's hoping for more encounters all over the globe. Also, to all the *Ticos* in Ad Astra, who welcomed me more than warmly into their little family, thank you.

To my students, Borja and Oscar, thank you for reminding me that teamwork feels great, and thank you for your contributions, which are now part of a larger project. I hope I was able to pass down a passion for the topic at hand!

To the inhabitants of Abtao 16, 3A, I love living with you guys and I love that house, you feel like family. Forgive my inability to deliver Sake, I'll make it up to you; possibly, with ice-cream.

To the everyone at CELERA: it's a tremendous feeling being around so many talented and inspiring individuals. I believe we have something truly great in our hands and we must do our best to make it shine; here's hoping to many more generations! To the "survivors" of the G2, thank you for your friendship and for making the whole journey worth it.

To Fran Rodriguez (whom I have, indeed, never met in person), for allowing me to showcase his amazing art in this thesis; it's a reminder that Space can feel both familiar (we're all stardust, after all) and awe inspiring.

To Grace, for being my wine and PhD struggles buddy. Now that our PhDs are ending, we can just focus on the former.

To my surf and climbing crews, which are wide and populous, and also to the sports themselves, which I haven't had a chance to practice as much as I would have wanted to lately, but have become great stress relievers and cornerstones in my life. In particular, thanks to Scofield, Guille and Maria for all of the fun times together, thinking of them always makes me smile. Also to the Urban Monkey crew, especially to Angel, Olga and Lucía, best team ever.

To my new friends from Arenal Sound: Jaime, Jules, Manu and Rojo, to their partners and the crew that you made me a part of, what a great gift that was; *a ver si encontramos a Antonio un día de estos*! To my not-as-new friends: Javi, Juan, Jesús, José, Nacho, and Aaron, thank you for still being there after my very prolonged absences, and the for general geekiness that we all

enjoy so much; here's to life-long friendships.

To the ex-Derbians, Eduardo, Jesús and Pep, those were some fun and crazy times up in the shire and I'm glad that even though we all live in different countries we can always share a good rant about what Elon Musk is doing next.

To all of my friends from the University years which I still am close to (there's quite a few, you know who you are): engineering brought us together but we stayed for everything else, thanks for all of the great times together, and for making the survival of *la Escuela* bearable. In particular, to Dani (and his growing family) who has become a true brother, thank you for everything.

To the Marcushof family: it's almost impossible to believe we still keep in touch, meet almost yearly and that many of us see each other often; we are the embodiment of what the Erasmus program promised and I am so glad to have met you all. Don't forget, we're all retiring back there! Specially, to Ting, you've been a constant in my life over the last few years and it's been amazing to watch each other grow and, more often than not, think alike about life. I'm lucky to have you.

To the people whom I have performed some of the truly crazy endeavors of my life with: to Joe, Mason and Thom, of the Mikel Hera, I think about our trip often and when I do, it takes most of my worries away. It taught me to trust the goodness of people and life, even if that was not the original intention; thank you for that. To the people that made up *Partido X*, what a great experiment that was and, even though I might not be writing these words if we had succeeded, it showed us what being an empowered citizen looks like; maybe it was simply too soon. Specially, to Raul, for all the adventures that came after, and the ones that are still to come. Lastly, to the SIE crew, thanks for demonstrating that Art and Science can intersect and not destroy each other in the process; here's to the endless possibilities that stem from that idea.

Finally, to Sara: although I have already mentioned you a few times (the perks of having more than a few things in common, I guess), this last one is for you and you only: let's hope to always be *home* for one another.

This work has been partially supported by the CHEOPS project, that received funding from the European Union's Horizon 2020 research and innovation program, under grant agreement No. 730135. Additional support came from Project ESP2016-75887, funded by the National research and development program of Spain.

Abstract

Electric propulsion is an established technology used for non-atmospheric spacecraft maneuvering. This type of rockets have been present in numerous applications in the last decades, and their uses range from station keeping of commercial satellites to interplanetary transfers in deep space exploration missions. While electric propulsion thrusters are multi-faceted, presenting numerous and distinct types, their best selling point is the capability to deliver a given impulse at much lower propellant cost, in comparison to other types of propulsion.

The maturation of plasma thrusters, the most common type of electric propulsion devices, has faced more limitations than chemical rockets, for example, due to the complexity of the physical interactions at play, and the difficulties associated with experimental campaigns. Over the past two decades, numerical simulations were introduced as a novel tool in the characterization of these devices. While true computer-aided-design is not yet a reality, the increment of computational resources and the heightened fidelity of the physical models have allowed to describe numerous physical mechanisms, explore the design space of these devices and complement experimental testing.

This thesis focuses on the numerical study of the electron population in weakly collisional plasma discharges, under the influence of applied magnetic and electric fields. The work has been a primary contribution in the development of a new, quasi-neutral, two-dimensional, axisymmetric, hybrid simulation tool, called HYPHEN. Its hybrid nature responds to the different treatment of the heavy species populations, described through a well known discrete-particle approach, and the electron population, described as a fluid. One of our main contributions has been the introduction of a two-temperature anisotropic approach, which allows capturing of the magnetic non-uniformity effects over electron transport; this feature paves the way for the characterization of some novel electromagnetic propulsion technologies. Presently, the code is oriented to the simulation of the channel and near-plume regions in Hall effect thrusters, which have been the main focal point of the thesis. Dedicated efforts have been directed to providing the capabilities for the simulation of the plasma under complex magnetic field topologies.

The manuscript details the motivation and design methodology behind HYPHEN, as well as the influence of previous work. Special attention has been given to the particularities of the proposed fluid model; this includes the use of a magnetic field aligned mesh for the numerical treatment of the electron population under magnetic confinement, for which ad-hoc spatial and temporal discretization methods have been proposed. Additional ancillary physical models have also been developed, characterizing the response of plasma boundary layers and the various collisional processes in the plasma. The numerical aspects of the model have been investigated, including the sensitivity to initial conditions, time-step values, mesh refinement, etc. Finally, HYPHEN has been tested in the context of a representative Hall-thruster configuration. The results were found to be in line with experimentally reported thruster performances and plasma discharge quantities. Additionally, a parametric investigation has been carried out in order to investigate the dependency of the thruster response with the most relevant model parameters, such as the anomalous electron transport or the boundary layer thermalization fraction, and the different collisional models.

Resumen

La propulsión eléctrica es una tecnología consolidada, utilizada por vehículos espaciales para llevar a cabo maniobras no atmosféricas. Este tipo de motores cohete ha estado presente en numerosas aplicaciones en las últimas décadas y sus usos van desde el mantenimiento de la posición orbital de satélites comerciales a transferencias interplanetarias en misiones de exploración. La mayor ventaja de los numerosos tipos de propulsores eléctricos es su capacidad de proporcionar un determinado impulso a un coste de propelente reducido, en comparación con otros tipos de propulsión.

El desarrollo de los motores de plasma, la clase más común de propulsor eléctrico, se ha visto impedido en mayor medida que los cohetes químicos, por ejemplo, debido a la complejidad de la interacción de los fenómenos físicos y a dificultades asociadas con las campañas experimentales. En las últimas dos décadas se ha introducido el uso de simulaciones numéricas para ayudar a la caracterización de estos aparatos. A pesar de que el diseño asistido por ordenador juega aún un papel muy reducido, el incremento de recursos computacionales y la creciente exactitud de los modelos físicos han permitido a estas simulaciones describir numerosos mecanismos físicos, explorar el espacio de diseño de estos aparatos y complementar los ensayos experimentales.

Esta tesis está centrada en el estudio numérico de la población de electrones en descargas de plasma poco colisionales, bajo la influencia de campos eléctricos y magnéticos. El trabajo realizado ha contribuido al desarrollo de una nueva herramienta de simulación híbrida, cuasi-neutra, bidimensional y axisimétrica, denominada HYPHEN; su naturaleza híbrida se debe al tratamiento por separado de las especies pesadas, descritas a través de un conocido método de partículas, y de la población de electrones, descrita como un fluido. Una de nuestras mayores contribuciones es la introducciÃşn de un modelo anisotrÃşpico de dos temperaturas, que permite capturar los efectos de la falta de uniformidad del campo magnético sobre el transporte de electornes. Esta función abre el camino para la caracterización de nuevos propulsores electromagnéticos. Actualemente, el código está orientado hacia la simulación de las regiones del canal y de la pluma cercana en motores de efecto Hall, en los que se enfoca esta tesis. Parte del trabajo se ha dedicado a dotar al código de las capacidades necesarias para la simulación de topologías magnéticas complejas.

El presente documento detalla la motivación detrás de HYPHEN, su metodología de diseño y la influencia de trabajos previos. Se ha prestado una especial atención al modelo fluido propuesto, detallando el uso de una malla alineada con el campo magnético para el tratamiento numérico de la población confinada de electrones, para la cual se han utilizado diversos métodos ad-hoc de discretización temporal y espacial. Varios modelos auxiliares también se han descrito, con el objetivo de caracterizar la respuesta de la capa límite del plasma y de los distintos procesos colisionales en el seno del mismo. Se presenta también el estudio de los aspectos numéricos del modelo fluido, incluyendo la sensibilidad a condiciones iniciales, a los valores del paso temporal, el refinamiento de la malla, etc. Finalmente, HYPHEN se ha testeado para la configuración de un conocido motor Hall. Los resultados demuestran que las propiedades físicas y las actuaciones obtenidas son comparables con resultados provenientes de estudios experimentales. Bajo este contexto, se ha llevado a cabo un estudio paramétrico para determinar la dependencia de la respuesta del motor con algunos de los parámetros más relevantes del modelo, tales como el transporte anómalo de electrones o la fracción de termalización de la capa límite, y con los diferentes modelos colisionales.

Contents

List of Tables

List of Figures

Glossary

ΔV Delta-V

v_{ex} Exhaust velocity

T Thrust

I_{sp} Specific Impulse

$\vec{v}$ Velocity vector

$\vec{r}$ Position space vector

t Time

$F_{S\delta}$ Dirac delta Distribution Function for species S

N_S Total number of particles of species S

M_S Total number of macro-particles of species S

F_S Velocity Distribution Function for species S

n_S Particle density of species S

$\vec{g}_S$ Particle flux of species S

$\vec{u}_S$ Drift velocity of species S

e_S Energy density of species S

f_S Probability Distribution Function for species S

e Electron charge

q_S Electrical charge of species S

c Speed of light

k_B Boltzmann constant

ϵ_0 Vacuum electric permittivity

μ_0 Vacuum magnetic permeability

ρ_q Electric charge density

r_L Larmor radius

λ_D Debye length

MFP Mean Free Path

Z Ion Charge Number

ϕ Electric or Plasma potential

$\vec{E}$ Electric field

$\vec{B}$ Magnetic field

$\vec{j}$ Current density

$\omega_{pe} = \sqrt{\frac{n_e e^2}{m_e \epsilon_0}}$ Plasma frequency

$\Omega_e = \frac{e|\vec{B}|}{m_e}$ Electron cyclotron frequency

ν_{e^*} Electron effective total collision frequency

ν_{eM} Electron maxwellian collision frequency

β_e Total Hall parameter

β_{e^*} Effective total Hall parameter

η_{e^*} Electron effective total resistivity

ν_{ano} Electron anomalous or turbulent collision frequency

α_{ano} Anomalous collision frequency factor

F_θ Anomalous momentum forcing term

ν_{wall} Electron near-wall collision frequency

m_i Ion mass

m_n Neutral mass

n_{iZ} Particle density of ions with charge number Z

n_n Particle density of neutrals

m_e Electron mass

n_e Particle density of electrons

$\vec{v}_e$ Particle velocity of electrons

$\vec{u}_e = \langle \vec{v}_e \rangle$ Drift velocity of electrons

$\vec{c}_e = \vec{v}_e - \vec{u}_e$ Thermal velocity of electrons

$c_{e\perp} = \sqrt{\left(v_{e\perp} - u_{e\perp}\right)^2 + \left(v_{e\theta} - u_{e\theta}\right)^2}$ Perpendicular Thermal velocity of electrons

$c_{e\parallel} = \sqrt{\left(v_{e\parallel} - u_{e\parallel}\right)^2}$ Parallel Thermal velocity of electrons

$T_{e\perp} = \frac{m_e}{2k_B}\left\langle c_{e\perp}^2 \right\rangle$ Electron perpendicular temperature

$T_{e\parallel} = \frac{m_e}{k_B}\left\langle c_{e\parallel}^2 \right\rangle$ Electron parallel temperature

$T_e = \frac{m_e}{k_B}\left\langle c_e^2 \right\rangle$ Electron temperature

$p_{e\perp} = \frac{n_e m_e}{2}\left\langle c_{e\perp}^2 \right\rangle$ Electron perpendicular pressure

$p_{e\parallel} = n_e m_e \left\langle c_{e\parallel}^2 \right\rangle$ Electron parallel pressure

$\vec{q}_{e\parallel} = n_e m_e \left\langle c_{e\parallel}^2 \vec{c}_e \right\rangle = \left\{ q_{e\parallel\top}, q_{e\parallel\theta}, q_{e\parallel\parallel} \right\}$ Electron parallel heat-flow vector

$\vec{q}_{e\perp} = \frac{1}{2} n_e m_e \left\langle c_{e\perp}^2 \vec{c}_e \right\rangle = \left\{ q_{e\perp\top}, q_{e\perp\theta}, q_{e\perp\parallel} \right\}$ Electron perpendicular heat-flow vector

$\vec{q}_e = \frac{1}{2} n_e m_e \left\langle c_e^2 \vec{c}_e \right\rangle = \left\{ q_{e\top}, q_{e\theta}, q_{e\parallel} \right\}$ Electron heat-flow vector

$\bar{\bar{P}}_e = n_e m_e \left\langle \vec{c}_e \vec{c}_e \right\rangle$ Electron pressure tensor

$\bar{\bar{\tau}}_e = \bar{\bar{P}}_e - p_{e\perp}\bar{\bar{I}} - (p_{e\parallel} - p_{e\perp})\vec{1}_\parallel \vec{1}_\parallel$ Electron viscous stress tensor

$\bar{\bar{\mu}}_{e\parallel} = n_e m_e \left\langle c_{e\parallel}^2 \vec{c}_e \vec{c}_e \right\rangle$ Higher order pressure tensor for electron parallel energy

$\bar{\bar{\mu}}_{e\perp} = n_e m_e \left\langle c_{e\perp}^2 \vec{c}_e \vec{c}_e \right\rangle$ Higher order pressure tensor for electron perpendicular energy

$\bar{\bar{\bar{Q}}}_e = n_e m_e \left\langle \vec{c}_e \vec{c}_e \vec{c}_e \right\rangle$ Electron heat-flow tensor

$\bar{\bar{\bar{\bar{R}}}}_e = n_e m_e \left\langle \vec{c}_e \vec{c}_e \vec{c}_e \vec{c}_e \right\rangle$ Electron 4^{th} order pressure tensor

S_e Electron particle density source term

$\frac{\delta \vec{M}_e}{\delta t}$ Rate of change of electron momentum due to collisional processes

$\frac{\delta E_{e\parallel}}{\delta t}$ Rate of change of electron parallel energy due to collisional processes

$\frac{\delta E_{e\perp}}{\delta t}$ Rate of change of electron perpendicular energy due to collisional processes

$\frac{\delta \vec{H}_{e\parallel}}{\delta t}$ Rate of change of electron parallel heat-flow due to collisional processes

$\frac{\delta \vec{H}_{e\perp}}{\delta t}$ Rate of change of electron perpendicular heat-flow due to collisional processes

$\frac{\delta \vec{H}_{e}}{\delta t}$ Rate of change of electron heat-flow due to collisional processes

$\hat{T}_{e\perp} = \frac{T_{e\perp}}{T_{e\parallel}}$ Perpendicular-to-parallel electron temperature ratio

$\hat{T}_{e} = \frac{T_{e}}{T_{e\parallel}}$ Total-to-parallel electron temperature ratio

$\Delta\phi_{sh}$ Plasma Sheath potential drop

v_{sh} Velocity lost or gained due to plasma sheath potential drop

σ_{th} Thermalization fraction parameter

δ_{r} Reflected electron yield

δ_{b} Secondary Electron Emission or Beam electron yield

E_{r} Reflected electron crossover energy

E_{b} Secondary Electron Emission or Beam electron crossover energy

α_{m} Magnetic angle at the boundary

I_{d} Discharge current

I_{i} Ion beam current

η_{a} Anode efficiency

η_{utiliz} Utilization efficiency

η_{curr} Current efficiency

η_{prod} Production efficiency

η_{div} Divergence efficiency

P_{d} Discharge power

P_{elec} Electric power

P_{jet} Power of the jet

P_{sh} Power lost to a plasma sheath

P_{adv} Power lost to advection

P_{exp} Power lost to the expansion of a gas

P_{inj} Power of the injected propellant

P_{heat} Heating power

P_{inel} Power lost to inelastic collisions

Acronyms

EP Electric Propulsion

EP^2 Electric Propulsion & Plasmas

UC3M Universidad Carlos III de Madrid

TRL Technology Readiness Level

HET Hall Effect Thruster

SPT Stationary Plasma Thruster

TAL Thruster with Anode Layer

HEMPT High Efficiency Multi-stage Plasma Thruster

GIT Gridded Ion Thruster

MPDT Magneto-Plasma-Dynamic Thruster

VASIMR VAriable Specific Impulse Magneto Rocket

ARRM Asteroid Redirect Robotic Mission

HPT Helicon Plasma Thruster

PPT Pulsed Plasma Thruster

ECR Electron Cyclotron Resonance

PPU Power Processing Unit

PIC Particle-In-Cell

MCC Monte-Carlo Collisions

DSMC Direct-Simulation-Monte-Carlo

HPHall Hybrid PIC Hall

HPHall-2 Hybrid PIC Hall-2

HallMa Hall Madrid

JPL Jet Propulsion Laboratory

HDF5 Hierarquical Data Format version 5

FEMM Finite Element Method Magnetic

HYPHEN HYbrid Plasma-thruster Holistic-simulation ENvironment

NOMADS NOn-structured Magnetically Aligned electron-Discharge Simulation

CFL Courant Fredrich Levy number

LED Local Extremum Diminishing

BC Bondary Condition

TCL Thruster Center Line

NAR Near-Anode-Region

MFAM Magnetic Field Aligned Mesh

FVM Finite Volume Method

FEM Finite Element Method

FFT Fast Fourier Transform

MHD Magneto Hydro Dynamic

CFD Computational Fluid Dynamics

CC Cell Centered

GR Gradient Reconstruction

GG Green-Gauss

LSQR Least Squares

ULSQR Unweighted Least Squares

WLSQR Weighted Least Squares

OOA Order Of Accuracy

FI Face Interpolation

GUI Graphical User Interface

TDD Test Driven Design

SSM Self Similar Method

DF Distribution Function

VDF Velocity Distribution Function

PDF Probability Distribution Function

EVDF Electron Velocity Distribution Function

EPDF Electron Probability Distribution Function

IVDF Ion Velocity Distribution Function

IEDF Ion Energy Distribution Function

SEE Secondary Electron Emission

CSL Charge Saturation Limit

CSR Charge Saturation Regime

CEX Charge Exchange Collision

1D One Dimensional

2D Two Dimensional

3D Three Dimensional

"The surface of the Earth is the shore of the cosmic ocean. On this shore, we've learned most of what we know. Recently, we've waded a little way out, maybe ankle-deep, and the water seems inviting. Some part of our being knows this is where we came from. We long to return, and we can, because the cosmos is also within us. We're made of star stuff. We are a way for the cosmos to know itself."

- Carl Sagan, Cosmos

Preface

At the time of writing these words, the Voyager 1 spacecraft was at a distance from Earth almost 141.46 times larger than the average distance between the Earth and the Sun[1]. Alongside its sister probe, Voyager 2, the 10^{th} and 11^{th} Pioneer missions, and the New Horizons[2] spacecraft, they form the *very* select club of man-made objects to have attained escape velocity from the Solar System's gravitational pull. Incidentally, on July 14^{th} of 2015, New Horizons also made history by becoming the last spacecraft to visit a new planet in the Solar System: Pluto. Technically, Pluto stopped being considered a fully fledged planet in 2006, but, since the probe was launched almost a year earlier, it doesn't need to know that.

When Carl Sagan delivered his famous introduction to *Cosmos* in September of 1980, Voyager 1 was about to perform the second ever flyby of Saturn. If, by his standards, we were "ankle-deep" back then, where are we now, forty years later and reaching into interstellar space? Is it knee-deep? Or are we still warming up to the idea of taking a dip...

Figure 1: Are we ready to jump into the cosmic ocean?[3]

If not exactly us, then we have definitively thrown out our toys into the ocean: little submarines and sail-ships full of hope and clever ingenuity, some closer to shore and others so far already that they are almost out of sight. With decades of effort behind, these marvels of the modern world have helped us *reach the stars* (or, more correctly, those celestial objects that would have passed as "stars" over 300 years ago) and, along the way, made the achievements of a handful of countries, space agencies and companies belong to us all: it was *Humanity*, after all, who had reached for those stars.

As has occurred many times throughout history, Space was first and foremost a frontier, one to explore and push against, which spurred the fierce competition of the Space Race during the decade of the 1960s and the Lunar landings. However, in the time that passed between the first image of Earth-rise from the Moon, and the first image of Pluto, rising from the depths of the Solar System, "Space" became something more: a major sector in the Global Economy (one worth more that $330,000m\$$[4]), and an unrelenting contributor to the pursuit of knowledge through scientific and technological achievements (which, of course, are priceless).

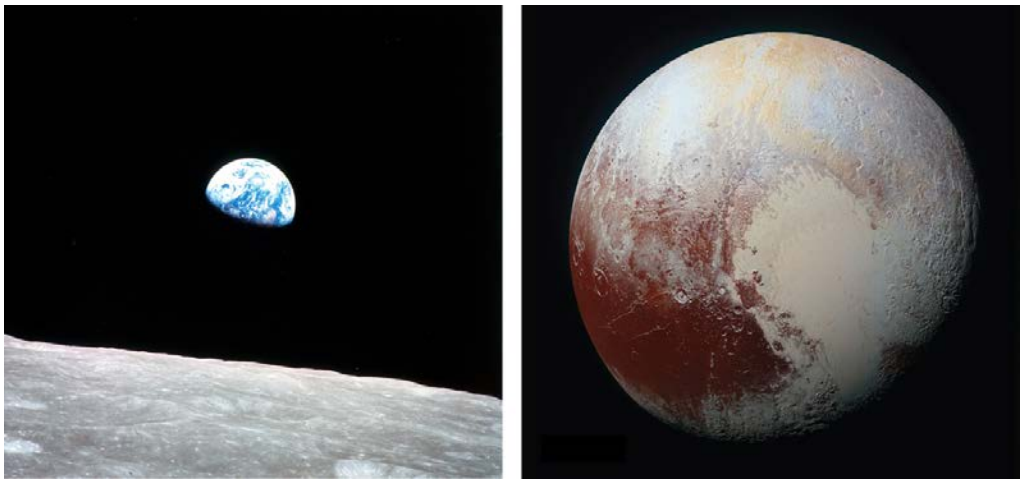

Figure 2: Earth-rise from the Moon (1958)[5] and Pluto, as viewed from the New-Horizons spacecraft (2016)[6]

The Space sector today underpins many of the technologies we use in our daily lives and encompasses a breadth of uses, from Commercial and Civil to Defense, and a far greater number of applications: communication, navigation, Earth observation, scientific exploration, and others. New trends in the industry, such as miniaturization and satellite swarms, are enabling exciting new applications and cost-reduction[7]. The future of this sector is intimately tied to the development of new technologies, which will allow us to expand our reach and capabilities in the Space environment, paving the way for bold missions such as NASA's Deep Space Gateway[8, 9] or ESA's Bepi-Colombo[10], which hold the promise of continued study of the solar system under international cooperation. Space enthusiasts will notice that these last two missions boast yet another, relatively recent, trend in Space exploration, one which was cemented by the SMART1[11, 12] and

Dawn[13, 14] missions: the first probes to visit other celestial bodies using Electric Propulsion.

This thesis represents a "small dip" into the topic of Electric Propulsion, a versatile and possibly game-changing rocket technology, advanced by a dedicated and inspiring community. This technology adds to an ever growing number of tools at our disposal in the task of navigating the cosmic oceans which Dr. Sagan spoke about. Let them boldly take us where no one has gone before.

CHAPTER
ONE

Introduction

1.1 Space Propulsion and Plasma Thrusters

Space propulsion is inherently tied to conservation of momentum: rockets propel a payload, typically within a vehicle of some sort, by ejecting propellant mass at high velocities; the higher these velocities, the less mass that needs to be ejected for the same momentum gain. Newton's second law describes the relation between the forces exerted over a system and the change in linear momentum, p, of its N parts as:

$$\sum F = \sum_{i=1,N} \frac{dp_i}{dt} \tag{1.1}$$

Konstantin Tsiolkovsky, quoted as being one of the "fathers" of rocketry, derived the momentum conservation equation for the motion of a body of variable mass, which he applied to demonstrate the possibility of space-flight (Fig. 1.1).

Tsiolkovsky's equation, obtained by integrating Eq. 1.1, provides the change in velocity, ΔV, achievable between two instants of time by ejecting mass at a constant velocity, v_{ex}, when no external forces are present:

$$\Delta V = v_{ex} ln\left(\frac{m_0}{m_1}\right) \; ; \; \frac{m_1}{m_0} = exp\left(\frac{-\Delta V}{v_{ex}}\right) \tag{1.2}$$

where m_0 and m_1 are the mass of the rocket at the initial and final times, respectively. Tsiolkovsky's equation implies that the total mass required as propellant changes *exponentially* with its exhaust velocity, which is the effect of having to accelerate the propellant mass alongside the rocket before it is ejected. While the equation was derived for no external forces acting on the rocket, these can be equated, simply, to an additional ΔV. For example, in launches from Earth, atmospheric drag accounts for about $1.5 - 2^{Km}/_{s}$ of ΔV, together with gravity "drag", which represents the penalty for accelerating within a gravity field.

The ΔV, thus, becomes a "universal" figure of merit to determine the requirements to perform a certain mission. Figure 1.2 shows some typical values for missions around the solar system. As an interesting fact, the aforementioned Dawn mission[13, 14] to Vesta and Ceres holds the record for highest ΔV achieved through the on-board propulsion system.


К. Ціолковскій.

Изслѣдованіе

міровыхъ пространствъ реактивными приборами

(дополненіе къ I и II части труда того-же названія).

Схема „ракеты".

цѣна 15 коп.

Калуга, Коровинская, д. № 61, К. Э. Ціолковскому.

ИЗДАНІЕ И СОБСТВЕННОСТЬ АВТОРА.

КАЛУГА.
Типографія С. А. Семенова, Никитскій пер., соб. д.
1914.

Figure 1.1: "Exploration of Outer Space by Means of Rocket Devices", K. Tsiolkovsky, 1903

Equation 1.1 can expressed in terms of the force being generated by the rocket, known as Thrust, T, the mass-flow of propellant, $\dot{m}$, and the exhaust velocity as:

$$T = v_{ex}\dot{m} \tag{1.3}$$

The exhaust velocity is commonly replaced by the Specific Impulse, I_{sp}, which is measured in seconds:

$$I_{sp} = \frac{v_{ex}}{g_0} \tag{1.4}$$

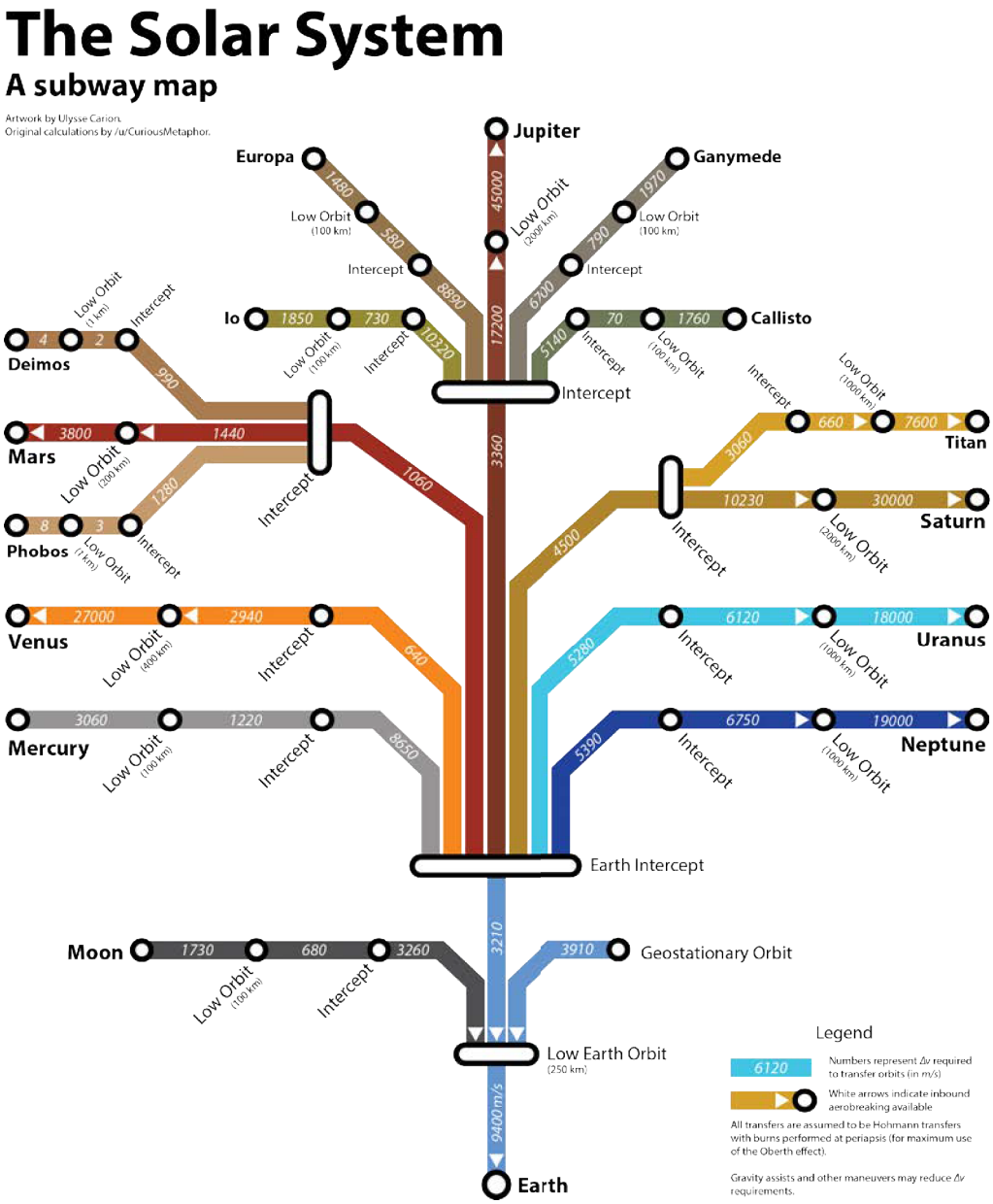

Figure 1.2: ΔV budgets for missions to the Solar System, values in $(^{m}/_{s})$[15]

where g_0 is the standard gravity. Using the I_{sp}, the Thrust and Tsiolkovsky equations become:

$$T = g_0 I_{sp} \dot{m}$$
$$\Delta V = g_0 I_{sp} ln\left(\frac{m_0}{m_1}\right) \tag{1.5}$$

These last two equations correlate the two most important figures of merit describing the performance of a rocket and the mission requirements. Different rocket technologies are capable

of providing different values of these figures, making them more, or less, appropriate, depending on the particular mission.

Rockets can be classified according to the origin of the energy which is converted into momentum in the propellant: if the energy is stored within the chemical bonds of one or more propellants, the propulsion type is *chemical*; alternatively, if the energy is stored within the vehicle and transferred to the propellant via heaters, radio-antenna or electro-magnetic fields, the propulsion type is *electric*. A third type of propulsion is *nuclear*, where the energy is provided by a nuclear reaction. Chemical and nuclear rockets, as well as some types of electric rockets, can also be classified as *thermal* rockets, due to the fact that they convert thermal energy of some sort into kinetic energy of the propellant.

Table 1.1 shows typical values for the figures of merit of a short comparative list of various types of propulsion systems, which have either been flown or developed to high Technology Readiness Level (TRL); additional information on EP thrusters may be found in Table 1.2.

Type	**Sub-type**	$\mathbf{I_{sp}}$ **(s)**	**Thrust-to-weight**	**Propulsion duration**	**Example propellant**
Chemical	Solid, Liquid - bipropellant	$200 - 500$	$10^{-2} - 10^{2}$	seconds-minutes	LOx/LH_2
	Liquid - monopropellant	~ 200	$10^{-2} - 10^{-1}$	seconds-minutes	N_2H_4
Nuclear	Solid core	$500 - 900$	$10^{-2} - 30$	seconds-minutes	H_2
Electric	Resisto-jet	$150 - 300$	$10^{-4} - 10^{-2}$	days-weeks	N_2H_4, H_2
	Arc-jet	$300 - 1200$	$10^{-4} - 10^{-2}$	days-weeks	N_2H_4, H_2
	Hall-effect	$1300 - 3000$	10^{-4}	months-years	Xe, Kr, Ar
	Ion Thruster	$1500 - 8000$	$10^{-6} - 10^{-4}$	months-years	Xe, Kr, Ar

Table 1.1: Performance values for various propulsion systems; source Ref. [16]

Chemical (and nuclear) propulsion systems have low I_{sp}, but thrust-to-weight ratios that can be much larger than 1. This makes them suitable for orbital launchers[1], where high thrust is needed to overcome Earth's gravitational well. Furthermore, since the penalty for ΔV due to accelerating in a gravity field during a time Δt can be demonstrated to be $\sim g\Delta t$, it is also important that acceleration to orbital velocity be achieved in as little time as possible, favoring higher thrust-to-weight ratios. For in-space propulsion, since the propulsion duration is short, impulsive type maneuvers, such as Hohmann or direct transfers (Fig, 1.3), are favored.

EP technology, on the other hand, is clearly very different to chemical and nuclear rockets. Conceptually, the latter are high power devices, releasing a large amount of energy over a very short period of time (on the order of millions of kilo-Watts), while the former are low power devices (on the order of kilo-Watts), releasing small amounts of energy over very long periods of time.

[1] In the case of nuclear rockets, they can be considered suitable for the upper stages of orbital rockets due to their lower cap in thrust-to-weight ratio; historically, this would have been the case of the Saturn C-5N rocket variant, which was designed with a nuclear third stage[17].

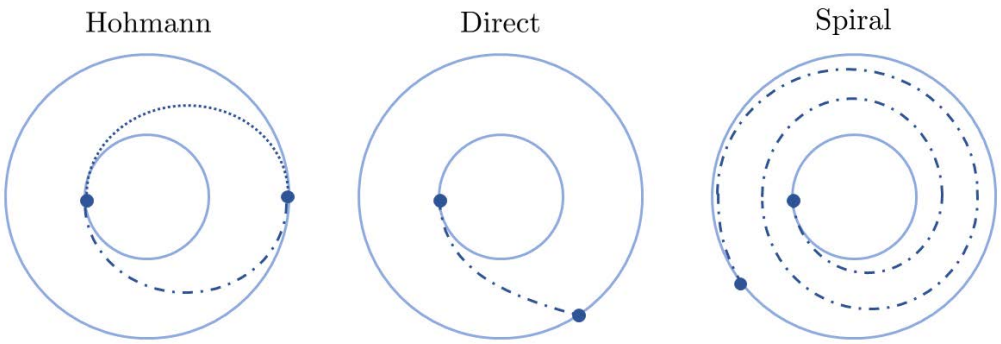

Figure 1.3: Various orbital transfers: Hohmann, Direct and Spiral maneuvers

The total specific energy (energy per unit of mass) released during operation, however, can be comparable.

A first distinction amongst EP exists between *thermal-electric* rockets and electrostatic and electromagnetic *plasma thrusters*[2]. The former type, exemplified by Resisto-jets or Arc-jets, convert electrical energy into thermal energy in the propellant, and then into kinetic energy; they do not necessarily present the same advantages and challenges of other types of EP and, for the present work, should be disregarded when referencing this type of propulsion (unless explicitly mentioned). Plasma thrusters, on the other hand, use a different mechanism to generate thrust: some energy is spent in converting the propellant into an electrically charged or electrically conducting state, typically in the form of an ionized gas, or plasma, which can be accelerated through electric or magnetic fields. It is through this last mechanism that Plasma thrusters are capable of achieving the highest I_{sp} of *all* existing operational rockets. It is precisely this characteristic which makes EP so attractive, since propellant mass for a given mission (i.e., for a particular ΔV) will be exponentially smaller than in the case of thermal rockets, as per Eq. 1.5.

Plasma thrusters typically operate for extended periods of time (thousands of hours) at very low thrust; they are unsuitable for orbital launches and cannot typically operate within a planet's atmosphere, due to their large densities, in comparison to the nominal operating density of the propellant. Because of this, EP is reserved solely for in-space propulsion, where transfer trajectories typically adopt spiral shapes (which carry some penalty over the ΔV, due to the Oberth effect[19]). Large operational times imply that the reliability of the system and its robustness must be kept in mind when designing the propulsion system. Furthermore, they are limited by the state of the art of the electrical power sources aboard the spacecraft (solar-electric, nuclear, etc.).

Despite its limitations, EP has gone a long way from the technology demonstrators in the SERT missions[20] to being present in almost all applications in space: as station keeping in large satellite platforms[21], propelling some of the smallest spacecrafts ever built to interplanetary missions[22], and, as new control schemes and larger on-board power become available, used in

[2]Technically, other types of EP devices also exist, such as Space Tethers[18], although these are "propellant-less" and thus don't fall into the category of rockets.

scientific exploration missions[10] and, potentially, future manned missions[9, 23, 24][3].

While it is not the purpose of this introduction to delve into the specifics of the numerous types of EP thrusters existing today and their application in various spacecrafts, the reader may be pointed to a review on EP technologies by Jahn & Choueri[25] and Martinez-Sanchez[26] or to the more extensive classical work by Goebel & Katz[27]. A brief summary on the different capabilities of a number of Plasma thruster types is given in Table 1.2, for both flight-proven and in-development technologies. Note that, for the sake of brevity, this table enumerates only a limited number of EP types; the reader may find that many other types and sub-types exist in various stages of development.

The physical mechanisms associated to EP are always the same, independently of the particular technology:

- An *electrical-charge inducing mechanism* on the propellant, which may range from changing the electric charge at the atomic level (by ionizing to create cations or anions, in which case the propellant is exhausted in a plasma state) to simply separating the elementary components of an ionic fluid, also known as a liquid salt.

- An *acceleration mechanism* on the propellant, which can be either electromagnetic, if the magnetic field is the main driver (through the Lorentz force over an electrical current) or electrostatic, if an electric field is the the primary acceleration mechanism.

- A main *thrust coupling mechanism*, which, in principle, could differ from the acceleration mechanism: in the same way that in a chemical rocket thrust is coupled due to the pressure exerted by the expanding propellant over the rocket's Laval nozzle[16], thrust in EP can be coupled through various mechanisms. For example, in Electron Cyclotron Resonance (ECR) thrusters and Helicon Plasma Thrusters (HPT), which both employ magnetic nozzles to expand the plasma, the thrust in the engine mainly appears due to the magnetic pressure of the plasma over the magnetic field lines in the nozzle. The acceleration mechanism, on the other hand, is electrostatic, due to the ambipolar electric field in the plasma.

- A *neutralization mechanism* which ensures that a charge imbalance between the thruster (and, therefore, the spacecraft) and the propellant leaving the thruster cannot happen. This might come in the form of an external neutralizer (typically, a hollow cathode[4]), a plasma plume's own current-free condition and others.

Of the technologies presented in Table 1.2, the most advanced and widely proven are Pulsed Plasma Thrusters (PPT), Gridded Ion Thrusters (GIT) and Hall-Effect Thrusters (HET). The last two (shown in Fig. 1.4) are continuous-flow devices, while the PPT is not.

[3] It is generally considered that the break-even point between chemical and electric propulsion for manned missions or support missions for manned spaceflight requires on-board power on the order of the mega-watt range.

[4] A hollow cathode employs an active electron emitter material which is heated to expel electrons; the device uses a fraction of the thruster propellant, which is ionized within the device and neutralizes the space-charge of the electrons produced by the emitter material. hollow cathodes can provide high currents at low voltages. More information on these devices can be found in Ref. [27].

Type	**Accel. mechanism / T coupling**	$\mathbf{I_{sp}}$ **(s)**	**T (mN)**	**Eff.**	**Thrust-to-power** (mN/kW)
Pulsed Plasma Thruster (PPT)	EM / EM	$1500 - 5000$	$1 - 1000$	~ 20	~ 20
Ion Engine / GIT	ES / ES	$1500 - 8000$	$10^{-2} - 200$	$60 - 80$	$10 - 90$
Magnetoplasma-dynamic (MPDT)	EM / EM	$2000 - 5000$	$10^{-2} - 10000$	~ 40	$10 - 60$
Hall-Effect (HET)	ES / EM	$1300 - 3000$	$10^{-2} - 3000$	$40 - 60$	$10 - 50$
Helicon (HPT)	ES / EM	$500 - 1500$	$3 - 20$	< 20	< 30
Electron-cyclotron (ECR)	ES / EM	~ 1000	~ 1	~ 15	~ 30
Electrospray	ES / ES	~ 1500	~ 1	~ 50	~ 60
VASIMR	ES / EM	$2000 - 5000$	$3000 - 6000$	$40 - 70$	~ 30

Table 1.2: Performance values and operation mechanism for various EP systems (ES stands for electrostatic, EM stands for electromagnetic); various sources[28, 16, 25, 29, 30, 31, 32]

Focusing on GITs and HETs, we may describe how these technologies operate under widely different mechanisms: GITs produce thrust accelerating ions by imposing a differential electric potential among a number of grids, the repelled electrons are then collected and expelled externally to the thruster in order to neutralize the ejected ion plume[5]; ionization is achieved either by electron bombardment within the thruster chamber or through electromagnetic waves (typically in the radio-frequency range). The thrust coupling mechanism is electrostatic: the acceleration grids experience an equal and opposite force to the one exerted over the ions. However, this acceleration mechanism is space-charge limited, i.e., there is a maximum ion current that can be extracted through the grids before effects due to the plasma's own electrical charge become dominant.

While HETs are discussed in-depth in the following section, they present some basic competitive advantages in comparison to GITs. First, they operate at lower voltages; this is is advantageous from the perspective of the Power Processing Unit (PPU), which does not become the limiting factor in the subsystem design, as sometimes happens with GITs. Second, they produce larger thrusts and, although they do so at lower I_{sp} and nominal efficiency, they retain larger efficiency values over different *throttle* conditions, which is useful from the perspective of mission optimization. These advantages mean that HETs are currently the main technological solution for near-earth EP (with the exception of micro-EP). In terms of disadvantages, however, this technology suffers from thruster erosion issues, due to sputtering of the thruster's wall materials

[5]Typically this is done through a hollow cathode, but some Ion thrusters switch the polarity of the electric potential in the acceleration grids to eject electrons and ions in alternating cycles, obtaining a neutral plume on average.

under ion bombardment; erosion also extends to other components of the sub-system, such as the hollow cathode.

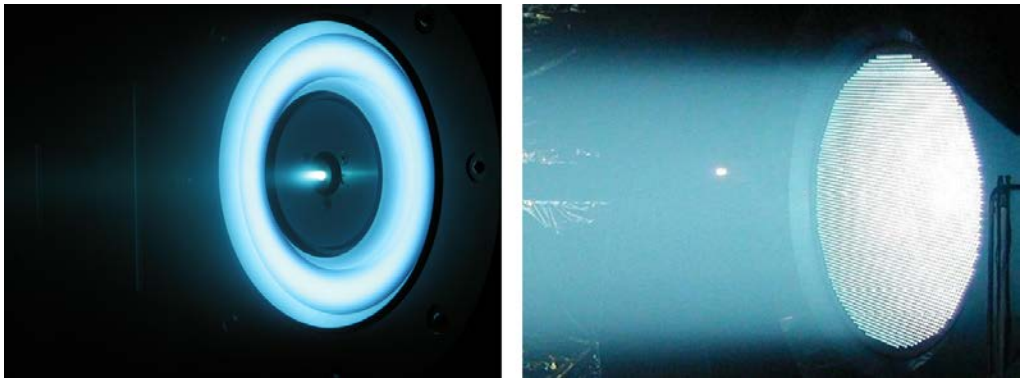

Figure 1.4: Hall-Effect Thruster[33] (left) and Gridded Ion Thruster[34] (right)

The operating life limitations are currently slightly more stringent than in the case of GITs, falling in the order of thousands of hours. Traditionally this limitation has been in the order of $10,000h$; however recent developments in HETs, which are commented next, have purportedly doubled this value[35].

From a purely "theoretical" perspective, HETs also present some very interesting interactions among a variety of physical mechanisms, which make them prime targets for academic and industry research. The work presented in this thesis focuses primarily in the study of HETs.

1.1.1 Hall Effect Thrusters

Historical perspective and main physical mechanisms

Hall-Effect thrusters were first developed in the U.R.S.S. in the 1960s, based on the work by Morozov[36]. They were successfully deployed in space in 1971 by the Soviet Union, which remained the only country with access to this technology until its dissolution in 1990. Early attempts by the U.S. had been waived in favor of Ion thrusters, due to the initially low efficiency and lower I_{sp} capability of HETs[37, 25]. After 1991, and due to the considerable development of the technology in the previous decades, renewed interest appeared in the U.S.[38], Japan, Italy and France.

These devices receive their name from the *Hall current*, which appears in ionized gases permeated by an electric field, $\vec{E}$, perpendicular to an applied magnetic field, $\vec{B}$, due to the known $\vec{E} \times \vec{B}$ drift of the *guiding center*. In HETs, the electron population exhibits a Larmor radius, r_{L_e}, that is small in comparison to the characteristic length of the device:

$$r_{L_e} = \frac{m_e v_{e\perp}}{eB} \tag{1.6}$$

where e, m_e and $v_{e\perp}$ are, respectively, the electron charge, the electron mass and the velocity of gyration of the electron, i.e., the velocity in the plane perpendicular to the magnetic field.

The intensity of the magnetic field is such that magnetic confinement plays an important role in the physics of the electron population, and allows for correct functioning of the device. Ions, on the other hand, are considered un-magnetized (from the perspective of magnetic confinement), since the typical magnetic fields found in the majority of EP devices, including HETs, impose an ion Larmor radius which is, at least, one order of magnitude larger than the typical device size.

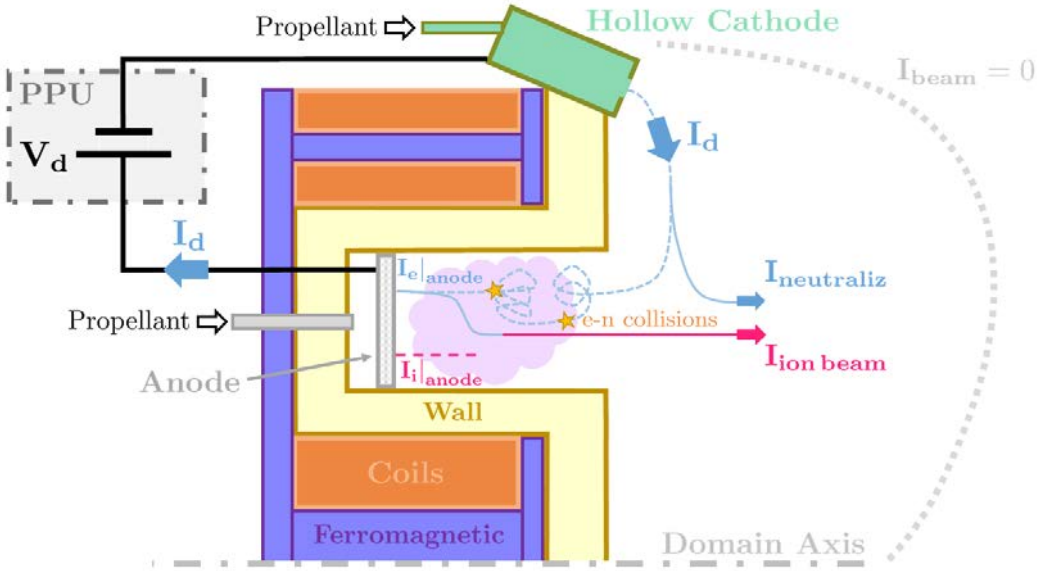

Figure 1.5: HET cross-section, PPU schematic and current distribution; the device pictured is a typical Stationary Plasma Thruster, with electro-magnets, a hollow cathode emitter and dielectric walls

Figures 1.6 and 1.5 provide some insight into the operation of HETs: these devices are traditionally configured with an annular shape, where the magnetic field is established either by permanent magnets or by electro-magnets, and is mainly *radial*. An *axial* electric field is imposed by an electric potential differential between an external electron emitter (generally, a hollow cathode), and an internal anode; the potential difference, as well as the electron current expelled by the emitter are provided by a PPU. The magnetically confined electron population will drift azimuthally in the annular thuster channel leading to a "closed" path, which is why these devices are also known as *closed-drift* plasma thrusters.

The azimuthal drift of electrons is only hindered by collisions with other particles: the dominant collisions within (and in the vicinity of) the thruster channel occur with the neutral atoms of the propellant, which is typically injected near the anode. Sufficiently energetic collisions will ionize the propellant, creating the plasma discharge. Other, more frequent collisions, allow the electrons to traverse in the direction opposite to the electric field (toward the anode) by interrupting the azimuthal drift and permitting the electron to accelerate with the electric field. This happens until the electron velocity, and thus the Lorentz force, Eq. (1.9), becomes large enough for electrons to be magnetically confined once again. The axial electron current (together with a small back-flow ion current) is responsible for closing the PPU electrical circuit.

Lastly, the electric field in HETs creates counter-streaming electron and ion currents. While the first are generated mostly within the channel (due to ionization), the later need to be neutralized after exiting the thruster. The neutralization current, $I_{neutraliz}$, is provided by a large fraction of the *discharge* current, I_d, expelled by the external emitter, making the plasma beam current free.

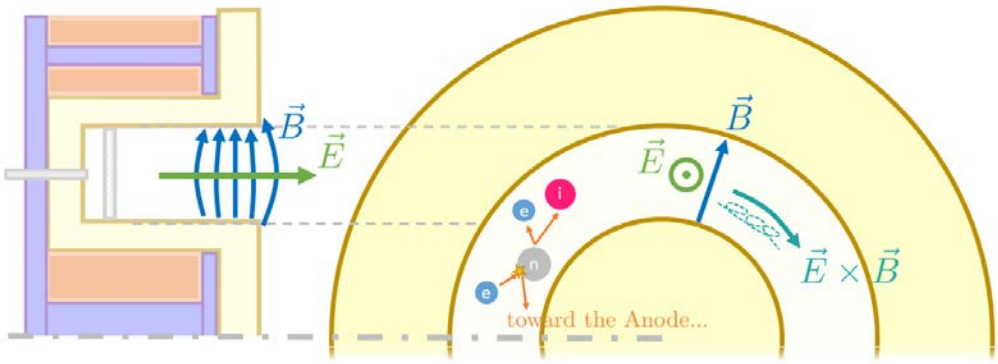

Figure 1.6: HET main physical mechanisms: Hall current and electron-neutral collisions

The main drivers of any EP device happen sequentially in HETs; thus, the Near-Anode-Region (NAR) is typically considered the ionization region, the thruster channel exit is the acceleration region and the area downstream from the thruster exit becomes the neutralization region. Out of the variety of physical mechanisms that may occur, *magnetic confinement* in the form of the Hall current (which impedes the PPU becoming short-circuited), and *electron-neutral collisions* (those which are ionizing and those responsible for cross-field transport) are the basis for any HET type device, independently of its geometry and magnetic topology.

Regarding classification, as shown in Table 1.2, the acceleration mechanism in HETs is clearly electrostatic, due to the electric potential difference imposed by the PPU. The electric field in the plasma self-adjusts based mainly on the relative importance of those physical mechanisms that either magnetically confine, or transport electrons across the magnetic field. Traditionally, this is measured through the plasma *Hall parameter*. However, non-classical effects (which, presumably, include turbulence, oscillations and wall-interaction effects) are responsible for larger-than-expected electron cross-field mobility in these devices, which has an effect over both the distribution of the plasma potential and the total electron current in the device.

The thrust coupling mechanism, on the other hand, is electromagnetic, due to the $\vec{j} \times \vec{B}$ Lorentz force that appears over the magnetic circuit because of the large azimuthal electron Hall current. It can be demonstrated that the Lorentz force is equal to the momentum change experienced by the ions due to electrostatic acceleration.

Hall thruster variants and optimization opportunities

Since their inception, a number of different HET designs have appeared; the most common distinction is between the Stationary Plasma Thruster (SPT) and the Thruster with Anode Layer (TAL). The former was depicted in Figs. 1.6 and 1.5 and is the most common type of HET; it is

characterized by separate anode and wall materials: the anode is a metallic conducting wall, while the channel walls are made of insulating dielectric materials; most recently, Boron-Nitride. The TAL also has an annular configuration, but replaces the dielectric walls by conducting metallic walls; these may act as an extension of the anode, or be biased at more negative potentials in order to limit electron losses. TAL thrusters also present a much shorter channel than those of SPT types. A first principles approach to the effects over the plasma discharge of either configuration was presented by Choueiri[39], although the references given there show that the matter has been taken into serious consideration by many other authors. The main difference between both types seems to reside in the peak temperature reached by the electron population (which is larger in TAL, due to, reportedly, lower wall losses) and the "length" of the acceleration region (and whether is operates in a space-charge limited regime or not).

Alternatively to the wall configuration, the relevance of the magnetic topology has also been widely studied for HETs, leading, mainly, to various sub-versions of the SPT. For example, Hofer[40, 41, 42] and others[43, 44] have studied the phenomenon of *magnetic lensing* (Fig. 1.7), which modifies the plasma potential profile in the acceleration region to reduce plume divergence. A more recent, but impacting, trend is what has been dubbed *magnetic shielding*. In 2010, a commercial thruster called the BPT-4000 (now XR-5), designed and developed by Aerojet Rocketdyne, eroded typically in the beginning of a $\sim 10,000$ hour life test but after $\sim 5,600$ hours the thruster exhibited a "zero-erosion" state, as reported by deGrys[45]. It was unclear if this was an anomaly related to facility or other elusive effects, since the detailed physics behind this observation were not identified upon the conclusion of the life test. Ensuing numerical simulations by Mikellides[46, 47] explained the physics that led to the zero-erosion state. Thus, the BPT-4000 test results, theoretical modeling and simulations enabled the development of the first principles of *magnetic shielding*, leading to a new paradigm in the design of HETs which promises to significantly extend their operational life and lower plasma wall losses (Fig. 1.7).

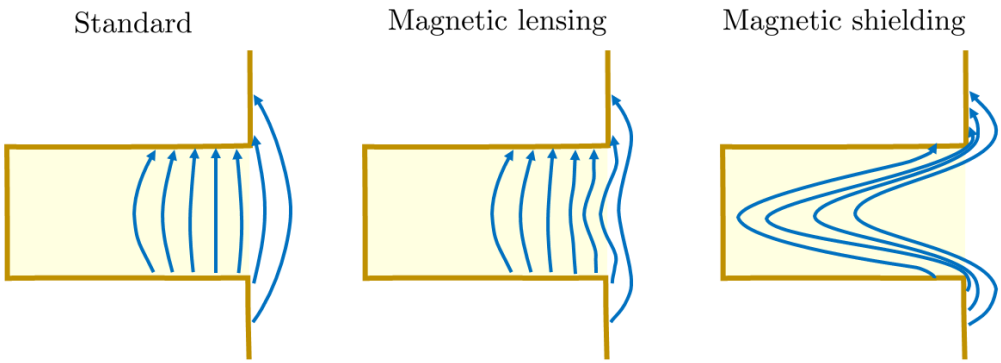

Figure 1.7: Various magnetic topologies in Stationary Plasma Thrusters

Other types of Hall-type thrusters have been developed exploring more "exotic" configurations, such as the High Efficiency Multi-stage Plasma Thruster (HEMPT)[48], or cylindrical[49], linear[50] or nested[51] HETs, all of which share commonalities with the physics of the SPT and the TAL variants.

In general, the relative straightforwardness and simplicity in the construction of all of these devices betrays the complexity of the physical interactions within them, many of which are not yet understood. Although it is clear that the magnetic topology, physical geometry and wall configuration all affect the characteristics of the plasma discharge, the problem is, at best, an inverse one. This means that the design of HET is limited to being informed by extensive know-how, trial and error and sometimes, such as the in case of the BPT-4000, by chance. For this reason, in order to fully characterize the response and design space of HETs, it is important to broaden the various fronts of study in these devices, which, over the last few decades, have included the field of computer simulation. This last topic is discussed in-depth in the following section, being the main focus of this thesis.

1.2 Characterization of Electric Propulsion Thrusters: Plasma discharge modeling and simulation

Considering the current state of the art in EP technologies and their potential impact in the future of both Space exploration and commercial Space endeavors, dedicated and continued development efforts have been established across industry players, research groups, the academic community and the different Space agencies. One of the main areas of development, pertaining to the advancement and maturation of EP devices, relates to the physical modeling and simulation of the plasma discharge produced by a thruster.

From the perspective of concurrent engineering, the design cycle of any plasma thruster would be informed by the interaction between three key aspects: Thruster Design, Plasma Discharge Physics and Thruster Performance, which, as the reader will suspect at this point, are heavily coupled. A simplistic view of the problem at hand, using a HET as an example, is presented in Fig. 1.8. Note that the physics involved in the discharge are typically classified between "near-plume" and "far-plume", since they present different dominating physical effects.

A first principles approach toward understanding their interdependencies is typically referred to as a "scaling law" or $0th$-order model.These have been developed for the various EP platforms, from GITs[52, 53, 54, 55], passing through HETs[56, 57, 58, 59, 60, 61], to more recent devices, such as ECR thrusters[62, 63]. Scaling laws are limited to providing orders of magnitude for different figures of merit, such as I_{sp}, Thrust, efficiencies, etc., as well as deriving certain higher-level physical relations and informing the base design of the device. They may not, however, provide an accurate description of the competing physical effects in the plasma discharge and how these can be linked to the resulting performances of the thruster. Furthermore, they are incapable of predicting unexpected emergent behaviors, such as the one exemplified by the case of BPT-4000 (see Section1.1.1), and, similarly, of exploring optimization opportunities in the thruster's design space.

As an example, one could "naively" assume that the design space for low-power HETs ($\sim 50W - 400W$) may be charted solely through a first principle's approach, and that thrusters in a similar power range would be inclined to show similar behaviors; however, as Fig. 1.9[64] contrarily shows, this is not the case and, thus, a more comprehensive approach to understanding the nature

of plasma discharges is required.

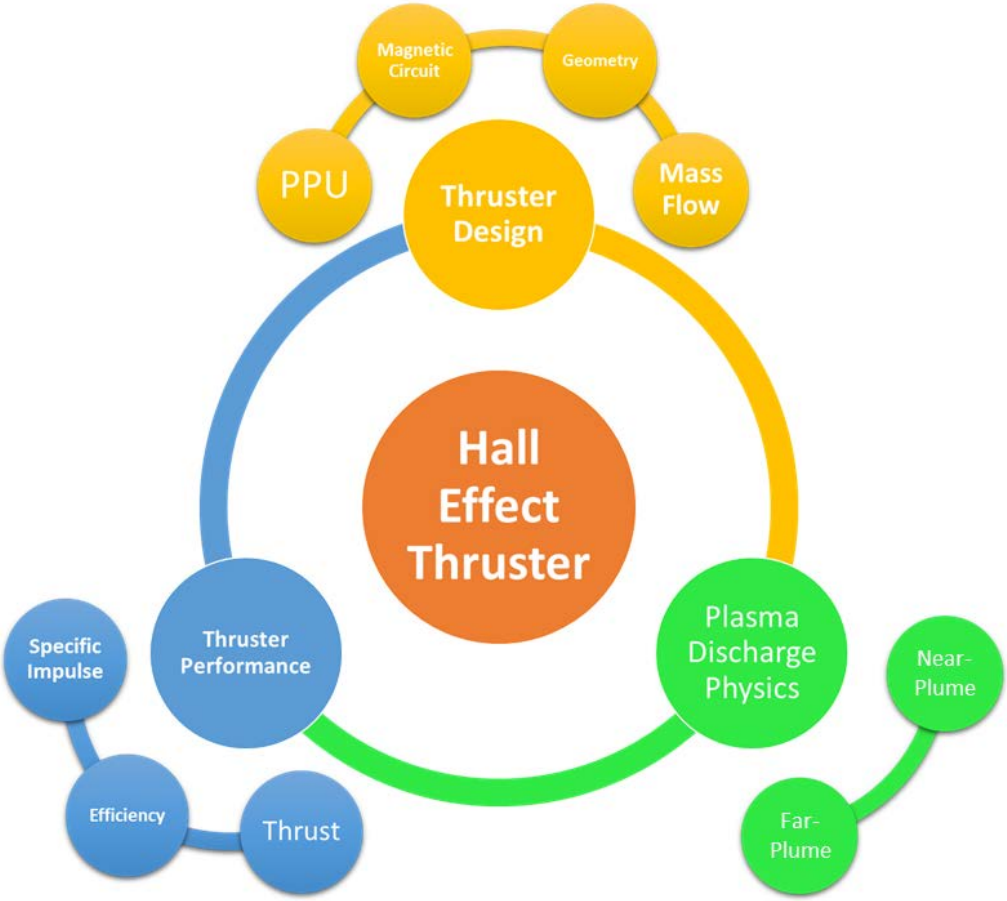

Figure 1.8: Operation and design aspects of a Hall Effect plasma thruster

In-depth knowledge typically requires either experimental or numerical studies. Until the last two decades, experimental campaigns, which require the construction of the device and its testing, either in vacuum chambers or on-board dedicated satellite platforms, were the only reliable approach toward characterizing the response of the thruster. Unsurprisingly, plasma diagnostics, in its multitude of forms, remains today an essential field in the study of the physical phenomena in plasma discharges[65, 66, 67], as well as thruster performances[27, 68, 69] and life-time effects[70, 71, 72], which play an essential role in the qualification campaign of any new thruster.

The experimental approach, nonetheless, is constrained by the available budget and the limitations associated to the experimental platforms. In the case of vacuum chambers, these are related to the cost of the platform (typically on the order of hundreds of thousands of Dollars) and its cost of operation (which may easily exceed the cost of the machine), as well as constraints related to the capacity for pumping out a certain mass-flow from the device, the vacuum pressure which may be reached and the interaction of the plasma with the chamber walls. In the case of technological demonstrators, the cost may be various orders of magnitude higher than that of vacuum

chambers, and logistical constraints can become a major hurdle, as, for example, in the case of the Asteroid Redirect Robotic Mission (ARRM)[73]; furthermore, performance measurements which are gathered once in-orbit, are, typically, of an indirect nature.

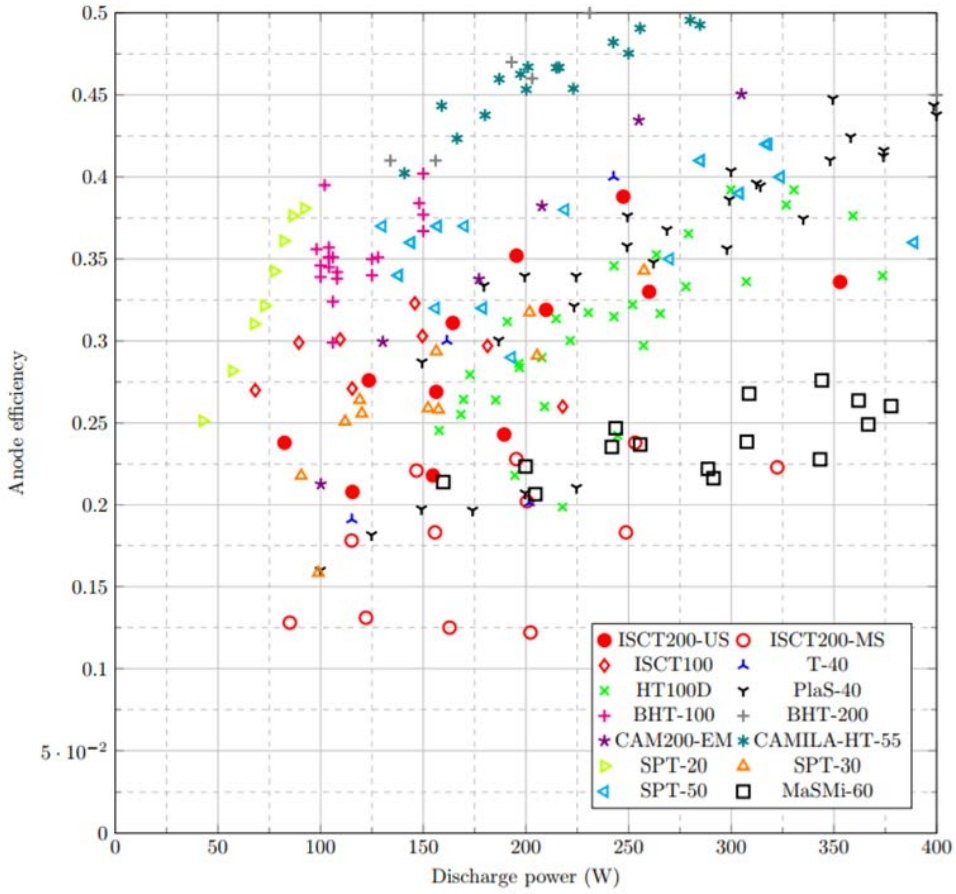

Figure 1.9: Low power HET comparison by Grimaud[64]

Finally, the subject of "time" is non-trivial since experimental campaigns can be lengthy and their cost is generally tied to said length. This is particularly true in qualification testing, which exposes EP devices to operation times in the order of the expected operational lifetime ($\mathcal{O}(1,000h)$).

An alternative, and more recent, approach is that of the numerical simulations of the plasma; the seminal work of Fife[74, 75, 76], which is the base for much of this thesis, approached the simulation of the "full" response of the plasma in HETs devices in the late 1990s. The origin of the field, however, may be traced back to the 1940s and many of the concepts employed today were first developed in the 1960s[77]. The advent of affordable and scalable computational resources and power transformed a nascent field into one capable of providing us with a virtual laboratory, where different models and interactions may be tested in an attempt to both understand the physical response of a thruster and to predict its capabilities.

The advantages of numerical simulation are apparent in terms of savings in cost and time:

cycling through and reviewing different designs and configurations, in order to characterize the response of a thruster, has little material cost (aside to the one associated to computing resources) and can potentially be done in the order of days (in comparison to much larger periods for testing campaigns). In this sense, numerical simulations have the potential to explore the aforementioned design space which we previously mentioned in a way that is simply not possible from the perspective of experimental studies. Finally, from the point of view of qualification, certain predictive results, such as, for example, the erosion rate of the walls of the thruster[78, 79, 80], are of importance in order to understand the performance of the device throughout its lifetime, without necessarily carrying out expensive and time-consuming "wear" tests[81, 82, 83], which are generally sought out for due to their impact on performance degradation.

As a detriment to numerical simulations, we can say that the fidelity of the results and the nature of the physical response of the simulated plasma tend to be questioned. Indeed, the breadth of physical effects which are present in the plasma have a direct impact on the response of the plasma discharge and the performances that may be recovered from the simulation of a thruster. More importantly, these physical effects may be modeled through a variety of approaches, which determine the scales (both temporal and spatial) that need to be resolved in the simulation and on the computational resources needed to do so. This leads to a classification on the different simulation approaches. A first division was foreshown in Fig. 1.8: simulations typically address either the *near* or *far* regions of the plasma plume, since the regimes in which they operate are quite different from the point of view of the "main" physical effects in the plasma. Typical simulation codes for the near-plume may be categorized according to:

- Kinetic Models { Particle models / Boltzmann-Vlasov models
- Fluid models
- Hybrid models

With the exception of hybrid codes, the previous classification follows, from top to bottom, an increasing level of assumptions over the behavior of the ensemble of particles that makes up the plasma.

The state of the art for numerical simulation platforms of the plasma in EP devices is reviewed next. The review is mainly centered on simulation approaches to the near-plume, where ionization, acceleration and/or neutralization mechanisms take place in the plasma; special attention is given to simulation codes for HETs, in line with the main theme of this thesis. It is worth noting that some of the codes presented are versatile enough to tackle both the near and far regimes of plasma discharges[6], with far-plume simulations focused on physical effects such as plasma expansion and detachment or spacecraft-plume interaction[85, 86, 55]. Additionally, some topics such as Secondary Electron Emission (SEE), anomalous electron transport, etc., are not explicitly treated for each of the codes reviewed, but will be tackled throughout this document.

To close this section, some comments will be made on the simulation of plasma-wall and plasma-wave interactions.

[6]For a comprehensive review of far-plume simulation codes, the reader may refer to Ref. [84]

1.2.1 Kinetic models

Kinetic models are oriented towards describing a collection of particles in both the physical and velocity spaces. This is known as a *Distribution Function* (DF), which provides a statistical depiction of the number of particles of a given species in a certain position with a certain velocity. This statistical representation of a particle ensemble permits macroscopic quantities to be derived. The Distribution Function may be quantitatively described in a discrete or continuous way, which provides two distinct kinetic approaches:

Particle models

A thorough introduction toward particle models is provided in this section, since the numerical code developed as part of this thesis is related to such models, even if the particularities fall outside of the scope of this work.

For a given collection of particles for a species S, N_S , if the positions, $\vec{r}$, and velocities, $\vec{v}$, are known for each particle at any given time, t, then the DF may be defined using the Dirac delta function[87], δ:

$$F_{S\delta}\left(\vec{r},\vec{v},t\right)=\sum_{i=1}^{N_S}\delta\left(\vec{r}-\vec{r}_i\left(t\right)\right)\delta\left(\vec{v}-\vec{v}_i\left(t\right)\right) \tag{1.7}$$

Integrating $F_{S\delta}$ in the 6-dimensional *phase-space* (defined by positions both in space and in velocity) provides the total number of particles, N_S:

$$N_S=\int F_{S\delta}d\vec{r}d\vec{v}$$

The Dirac-delta DF gives rise to a well consolidated approach towards the modeling of space propulsion plasmas known as direct kinetic simulations. These codes fall within the classification of Eulerian and Lagrangian[88] in their description of the plasma flow, modeling it, not through a full ensemble of particles, but through aggregates of those, typically called "macro-particles". The Dirac-delta DF is then replaced by:

$$F_{S\delta}\left(\vec{r},\vec{v},t\right)\approx\sum_{j=1}^{M_S}W_j\delta\left(\vec{r}-\vec{r}_j\left(t\right)\right)\delta\left(\vec{v}-\vec{v}_j\left(t\right)\right) \tag{1.8}$$

where W_j represents "weight" of the macro-particle, i.e., the number of particles contained in a specific aggregate, and M_S represents the number of macro-particles of a certain species; the following relationship holds true:

$$\sum_{j=1}^{M_S}W_j=N_S$$

The populations simulated in particle models belong to the electron species and ions and neutrals from one or more atomic elements. The macro-particle approach allows to inversely scale the number of computational resources required with increasing W_j and decreasing M_S, generally at the expense of larger statistical variation or "numerical noise", as the issue is typically referred to in the Particle-In-Cell (PIC) community. Macroscopic quantities are thus derived from the ensemble of macro-particles, instead of elementary particles. These are typically extensive quantities, such as the partial densities of each species, particle fluxes, etc. and also intensive quantities such as the species temperature and pressure or a species' drift velocities.

The macro-particles respond through basic Newtonian movement to volumetric forces; particularly, since a plasma consists of electrically charged particles, to the electromagnetic Lorentz force:

$$F_L = q_S \left(\vec{E} + \vec{v}_S \times \vec{B} \right) \tag{1.9}$$

where $\vec{E}$ and $\vec{B}$ are the electric and magnetic fields, and q_S and $\vec{v}_S$ the charge and velocity of a particle belonging to species S. Maxwell's equations allow to self-consistently determine the relation between the electric and magnetic fields and the charged particles in the plasma:

$$\begin{aligned} &\nabla \cdot \vec{B} = 0 \\ &\text{Poisson Equation: } \nabla \cdot \vec{E} = \frac{\rho_q}{\epsilon_0} \\ &\nabla \times \vec{E} = -\frac{\partial \vec{B}}{\partial t} \\ &\nabla \times \vec{B} = \mu_0 \vec{j} + \frac{1}{c^2} \frac{\partial \vec{E}}{\partial t} \end{aligned} \tag{1.10}$$

where ρ_q and $\vec{j}$ are the total electric charge density and current density, and ϵ_0 and μ_0 are, respectively, the vacuum electric permittivity and magnetic permeability, and c is the speed of light in vacuum. Finally, collisional events between particles of the same or different species (which may lead to a variety of chemical reactions) and to physical boundaries in the simulation (such as the thruster's walls, for example) must also be taken into account.

The smallest spatial and temporal scales that are solved for in particle codes, which directly affect the computational resources required, are determined by the physics that are implemented, i.e., the subset of Maxwell's equations resolved[7], the dimensionality of the problem, the chosen particle model approach, and the dynamics of the fastest species simulated, which is typically the electron population.

Any type of particle interaction may be modeled in a direct or indirect manner, which leads to an initial classification in particle codes: particle-mesh, more commonly known as PIC, codes[89,

[7]By necessity, particle models must at least consider a purely electrostatic closure, solving for the Poisson equation. This aspect serves as a distinctive property in the classification of different simulation codes, since fluid and hybrid codes typically do not solve Poisson. Note that none of the codes reviewed in this section solve for the wave interaction aspect of Maxwell's equations, which introduce an additional level of complexity.

87, 90, 91] and particle-particle codes. In PIC codes, macro-particles are first sorted and "weighted" to a spatial mesh, which is utilized to calculate the electric and magnetic fields (as given by Maxwell's equations) and to limit the amount of collision type interactions to the particles located within the same mesh cell, typically done through the Monte-Carlo Collisions (MCC) or Direct-Simulation-Monte-Carlo (DSMC) approaches[8]. Particle-particle codes, on the other hand, rely on a "sphere of influence" centered around any individual particle, which determines the extent of particles that are allowed to interact with it. One major difference between the two approaches relates to the scaling of computational resources with the number of macro-particles: PIC codes require a number of operations on the order of $\mathcal{O}(M)+\mathcal{O}(N_{nodes})$, where N_{nodes} is the number of nodes of the spatial mesh and and represents the computational cost associated to the weighting step. On the other hand, particle-particle codes require $\mathcal{O}\left(M^2\right)$, and since, typically, $N_{nodes} \ll M$, the cost savings are apparent. This last argument explains the preference of the community toward the PIC approach, as shown next.

Particle codes were perhaps the first employed towards the modeling of the plasma behavior in varying environments; a comprehensive survey of early attempts and the evolution of the method was presented by Hockney[87] and, more sucintly, by Birdsal[77]. A recent review of the PIC method, within the scope of EP, is presented by Tskhakaya[90].

PIC codes are sometimes seen as a "parameter free" approach toward the simulation of plasma discharges, implying that no extraneous models are necessary to recover the plasma behavior. In practice, this is not necessarily true, specially in those cases in which some aspect of the physics, such as the boundary conditions, are not fully understood.

On the other hand, the PIC approach may also be viewed as a "brute force" approach, generally due to the sheer scale of computational power they require. PIC codes must resolve spatial scales down to the Debye length, λ_D, and temporal scales down to the plasma frequency, ω_{pe}. These requirements imply *very* large numerical resources and computation times (on the order of months, for some of the simulation codes reviewed). Thus, PIC codes utilize a number of strategies to reduce the computational load: considering neutrals particles as a fluid or a static background, considering different "mover" time-steps for different particles (based on their weight), solving a reduced simulation domain (using sometimes periodic boundary conditions), reducing the number of spatial dimensions to 2D or 1D[9], imposing physical scaling through artificial electron-ion mass ratios[10] or electrical permitivitty[11], etc. Additionally, no PIC code is truly exempt of ancillary models such as collisional or plasma-wall interaction, which typically do require a set of parameters as input.

[8] See Section 2.2.1 for further reference.

[9] Typically, only the spatial dimensions of the DF are limited, with the velocity space left to be fully resolved; the term 3V in Table 1.3 makes reference to the latter.

[10] Changing the ion-mass ratio allows ions to be more reactive to changes in the electron population, reducing the amount of time required for simulations to achieve a "converged" solution.

[11] Increasing the electrical permitivitty constant, ϵ_0, increases λ_D and reduces $\omega_{pe} = \sqrt{\frac{n_e e^2}{m_e \epsilon_0}}$, allowing for coarser spatial meshes and larger time-steps

`Code Name`/Author	Publication date	Model	Characteristics	References
Adam, J.C. & Héron A.	2003	2D(z-θ)-3V PIC	fluid neutrals, semi-cylindrical domain & periodic boundaries, artificial sheath	[92, 93, 94]
Taccogna, F. et al.	2004-present(multiple codes)	PIC-MCC: • 2D(z-r)-3V • 2D(r-θ)-3V • 3D-3V	Partial domains & periodic boundaries & geometrical channel scaling, probabilistic SEE, artificial wall floating potential	[95, 96, 97, 98]
Sydorenko, D. & Smolyakov, A. & Kaganovich, I. & Raitses, Y.	2005	1D(r)-3V PIC-MCC	Plasma slab, Neutral background, artificial anomalous collisions, SEE	[99, 100, 101]
Coche, P.& Garrigues, L.	2011	2D(z-θ)-3V PIC-MCC	Partial domains & periodic boundaries, ϵ_0 scaling, artificial sheath with isotropic reflection of electrons	[102, 103]
`LPPic2D` / Croess, V. & Lafleur, T.	2017	2D(r-θ)-3V PIC-MCC	Neglected curvature effects (large radius), periodic along z, grounded conducting wall boundaries	[104, 105, 106]

Table 1.3: Review of recent Particle near-plume plasma discharge simulation codes

An at-glance compendium of some of the relevant codes reviewed for this work, and their characteristics are shown in Table 1.3 for reference. The reader will find that most codes are devoted to the study of instabilities that arise due to kinetic effects in the discharge of HETs, and the scales associated to them.

Multiple other references have been omitted from this review; the reader may be pointed to the work by Hirakawa[107], Sullivan[108], Liu[109], or to Brophy[110] and Wang[111] (for PIC codes applied to GITs).

Boltzmann-Vlasov models

An alternative approach to the Dirac-delta is to use the n-particle DF, F_{N_S}, which satisfies that the probability of finding an ensemble of particles, N_S, located within a given phase-space volume $\prod_{i=1}^{N_S} d\vec{r}_i d\vec{v}_i$ at a given time by:

$$F_{N_S}\left(d\vec{r}_1, d\vec{v}_1, d\vec{r}_2 d, \vec{v}_2, \ldots, d\vec{r}_{N_S}, d\vec{v}_{N_S}, t\right) \prod_{i=1}^{N_S} d\vec{r}_i d\vec{v}_i \tag{1.11}$$

Multiplying by the Dirac-delta DF and integrating over the phase-space we arrive at the known Velocity Distribution Function (VDF), F_S:

$$F_S\left(\vec{r}, \vec{v}, t\right) = \int F_{N_S}\left(d\vec{r}_1, d\vec{v}_1, d\vec{r}_2 d, \vec{v}_2, \ldots, d\vec{r}_{N_S}, d\vec{v}_{N_S}, t\right) f_{S\delta}\left(\vec{r}, \vec{v}, t\right) \prod_{i=1}^{N_S} d\vec{r}_i d\vec{v}_i \tag{1.12}$$

The VDF represents the number of particles of species S contained at a given time in the phase-space infinitesimal volume $d\vec{r}d\vec{v}$ centered around a certain position $(\vec{r}, \vec{v})$. It allows us to obtain macroscopic quantities from the ensemble by *taking moments* of the VDF over the velocity space, up to an arbitrary order. For the first three, multiplying the VDF by 1, $\vec{v}$ and $1/2 m_S v^2$, and integrating over the velocity space, we can obtain the particle density, n_S, particle flux vector, $\vec{g}_S$, and energy density, e_S:

$$\begin{aligned} n_S(\vec{r}, t) &= \int_{V_{\vec{v}}} F_S\left(\vec{r}, \vec{v}, t\right) d\vec{v} \\ \vec{g}_S(\vec{r}, t) &= \int_{V_{\vec{v}}} \vec{v} F_S\left(\vec{r}, \vec{v}, t\right) d\vec{v} \\ e_S(\vec{r}, t) &= \int_{V_{\vec{v}}} \frac{1}{2} m_S v^2 F_S\left(\vec{r}, \vec{v}, t\right) d\vec{v} \end{aligned} \tag{1.13}$$

Additionally, from the first moment we can obtain the Probability Distribution Function (PDF), f_S, defined as:

$$f_S\left(\vec{r}, \vec{v}, t\right) = \frac{F_S\left(\vec{r}, \vec{v}, t\right)}{n_S(\vec{r}, t)} \tag{1.14}$$

which represents the probability of finding a single particle in the phase-space infinitesimal volume. From the first two moments we can obtain the average, drift or "bulk" velocity of the ensemble, $\vec{u}_S$, as:

$$\vec{u}_S(\vec{r},t) = \frac{\vec{g}_S(\vec{r},t)}{n_S(\vec{r},t)} = \int_{V_{\vec{v}}} \vec{v} f_S\left(\vec{r},\vec{v},t\right) d\vec{v} \tag{1.15}$$

Parting from the Liouville theorem for the n-particle DF and by transformation into the BBGKY chain and subsequent truncation of the equations[112], it is possible to arrive at the known Boltzmann equation[113], which describes the evolution of the VDF for a species S as:

$$\frac{\partial F_S}{\partial t} + \vec{v}_S \cdot \nabla F_S + \frac{q_S}{m_S}\left(\vec{E} + \frac{1}{c}\vec{v}_S \times \vec{B}\right) \cdot \nabla_v F_S = \frac{\delta F_S}{\delta t} \tag{1.16}$$

Where the term in the right-hand-side of the equation represents the change in the VDF due to collisional processes. Since the electromagnetic field appears in the equation, Maxwell's equations, Eq. (1.10), or some subset of them, may be called upon to solve the problem in a self-consistent manner.

From a practical perspective, solving Boltzmann's equation implies tackling a 6-dimensional phase space (unless the some of the spatial or velocity dimensions are neglected) and being able to model the effect of collisions over the DF. Neglecting this last term transforms Boltzmann's equation into the, also well known, and simpler, Vlasov equation.

Neither the Vlasov nor the Boltmann equation lend themselves to being easily resolved[114], which is why there is typically an absence of numerical codes that use this approach for the description of the plasma discharge in an EP device. The codes that do exist are typically lower-dimensionality studies based on the Vlasov equation; a succinct review is gathered in Table 1.4, for codes capable of solving the acceleration region in EP devices with magnetic nozzles. No code was found that reproduces the multi-process physics of a complete thruster.

Code Name/Author	Publication date	Model	Characteristics	References
J. Navarro-Cavalle & M. Martinez-Sanchez	2014	1D(z) Vlasov	Steady state con-di nozzle expansion, quasi-neutral, current-free, fully magnetized, conservation of energy and magnetic moment	[115, 116]
G. Sanchez-Arriaga & J.Zhou	2017	1D(z) Vlasov	Transient divergent nozzle expansion, current-free, fully magnetized, conservation of energy and magnetic moment, particle trapping	[117]

Table 1.4: Review of recent Boltzmann-Vlasov near-plume plasma discharge simulation codes

1.2.2 Fluid models

If macroscopic quantities can be obtained by taking moments of the VDF, as shown in Eq. (1.13), then the evolution of those quantities can be obtained by taking moments of the Boltzmann equation, Eq. (1.16), to obtain the equations for continuity, momentum, energy, stress tensor, etc. These equations are detailed in Section 4.1 for the electron population and for the particular case of a non-isotropic fluid, but can be generalized to any species and particularized for an isotropic case; for the sake of brevity, they will not be reproduced here.

The fluid equations use the framework of the Boltzmann equation to describe the evolution of macroscopic quantities of interest. They have the particularity that each equation always depends on moments whose evolution is given by equations of higher order; therefore, the equations need to be truncated, or "closed", at a certain order. In order to do this, an assumption can made on the shape of the VDF, which is used to derive a closed expression for the moment of the highest order which we wish to conserve in the equations. Boltzmann's H-theorem states that, given enough time (i.e., in equilibrium), an ensemble of particles takes the shape of the isotropic Maxwell distribution:

$$F_S\left(\vec{r},\vec{v},t\right)=\frac{n_S\left(\vec{r},t\right)}{\left(2\pi\right)^{3/2}}\left(\frac{m_S}{k_B T_S\left(\vec{r},t\right)}\right)exp\left(-\frac{m_S\left|\vec{v}-\vec{u}_S\left(\vec{r},t\right)\right|^2}{2T_S\left(\vec{r},t\right)}\right) \tag{1.17}$$

Some simplified closures exist for some of the higher order moments which take into account Maxwell's distribution, such as Fourier's heat-flow equation. In addition, some analytical expressions must be given to model the collisional terms in the transport equations, and, as in other models, certain coupling with Maxwell's equations can be expected. In comparison to the PIC approach, fluid models may necessitate a larger number of "free parameters" if the closure physics, boundary conditions, or some combination of them are not fully understood. The models employed to close the equation chain usually employ a parametric approach, are informed by experimental considerations or require strong assumptions.

In full-fluid model codes, all of the species involved in the plasma discharge (electrons, ions and neutrals) are modeled as fluids with Maxwell distributions or other closures. These approximations can be more or less easily justified depending on the collisional regimes in which we find the various species and how far or close they are expected to be from thermodynamic equilibrium (in consideration of the Maxwellianity premise). The plasma discharge in EP devices is known to host a number of "outlier" species, such as multiply charged ions or ions and neutrals resulting from Charge Exchange Collision (CEX) type collisions[118]; however, due to their relative "rarity", treating these species as Maxwellian fluids can sometimes be called into question.

Fluid models cannot solve for "kinetic" effects, which are those associated to how the various processes in the discharge affect the shape of the VDF and, in turn, how this affects the ultimate response of the plasma. Furthermore, fluid equations distinguish between effects related to the transport of the bulk of the fluid and those related to *averaged* quantities of the dynamic of individual particles; this limits both the breadth of physical effects and the temporal and spatial scales that can be resolved through fluid equations. The scales in the problem also come into play when considering the stability of the numerical methods used to solve the transport equations, such as the Finite Element Method (FEM) or Finite Volume Method (FVM).

Nonetheless, in comparison to the full-PIC approach, the resolution of the fluid transport equations allows for a tremendous reduction in computational resources and times; the latter are typically scaled down from months to somewhere in the order of days. Since the computational load is reduced, the use of physical scaling is uncommon and discouraged (although reduction of the spatial dimensions is still typical) and computational domains and simulated times can also be expanded.

Some notable fluid model codes are reviewed in Table 1.5; perhaps the most prominent example is Hall2De, developed at Jet Propulsion Laboratory (JPL), which has been used to successfully model a wide variety of configurations in HETs, from magnetically shielded[46] to multichannel[119] thrusters.

Code Name/Author	Publication date	Model	Characteristics	References
M. Keidar & I. D. Boyd	2001	2D(r-z) fluid	Stationary results in thruster channel only, purely radial $\vec{B}$, single-parameter SEE yield, 1D collisionless sheath	[120, 121]
Subrata Roy & B. P. Pandey	2002	1D(z) fluid	FEM, neutral/ion dynamics, thruster channel, simplified wall interaction, steady state electrons, experimental T_e	[122]
L. Dorf, V. Semenov & Y. Raitses	2003	1D(z) fluid	T_e imposed, thruster channel results and variability of anode sheath regime	[123]
S. Barral & K. Makowski	2003	1D(z) fluid	Anisotropic T_e, quasi-neutral, neglects anomalous transport, impact on SEE on plasma discharge	[124]
Hall2De / I. G. Mikellides & I. Katz	2012	2D(z-r) fluid	Magnetically aligned mesh, multi-charged-fluid ions, large plume domain, cathode boundary, 2-D electron equations	[125, 126]

Table 1.5: Review of recent Fluid near-plume plasma discharge simulation codes

Other fluid codes can be found in the literature: some of the earliest numerical investigations into HET were based on these models[36], while other EP devices have also been modeled through fluid codes; such is the case, for example, of hollow cathodes, which were modeled self-consistently by the OrCa-2D code[127].

The reader is encouraged to continue learning about fluid modeling throughout the remaining chapters of this thesis, which primarily deal with the fluid treatment of the electron population.

1.2.3 Hybrid models

Hybrid codes are particular in that they employ a combination of the models presented in Sections 1.2.1 and 1.2.2, typically, choosing one of the kinetic approaches for the heavy species populations, and the fluid approach for the electron population. This is done under consideration of the different physical regimes in which these populations may be found: plasmas in typical EP devices are lowly collisional, and the heavy species populations are cold in comparison to electrons, which are normally the "thermal" species (with, perhaps, the exception of the VASIMR rocket[23]). Not all hybrid codes, however, combine kinetic and fluid approaches[12].

In the case of kinetic-fluid hybrids, using the kinetic approach for ions and neutrals allows describing kinetic effects, such as energy dispersion that does not follow the Maxwellian distribution. In parallel, while plenty of sources for non-Maxwellianity have been found for the electron population[13], its modeling as a fluid is advantageous mainly from the perspective of computational resources, while retaining the capacity to describe the physics of the "bulk" population. This is of special importance if one considers that Three Dimensional (3D) or Two Dimensional (2D) kinetic simulations over representative domains and simulated times, are still out of reach of present computational advancements. Thus, hybrid codes offer a good compromise for the study of the near-plume region in EP plasma discharges, which include, based on the literature, thruster performances, thruster wall erosion rates and others.

Hybrid models have special relevance to the work presented in this thesis: first, as seen in Table 1.6, they have been one of the preferred approaches over the past two decades in the simulation of HETs, being able to model some of the high-level physical interactions that are responsible for the behavior of these devices. Secondly, the work carried out in this thesis is based on the legacy and lessons learned from mainly two codes: Hybrid PIC Hall-2 (HPHall-2) and Hall Madrid (HallMa). Throughout the rest of this document, we refer to these specific codes by the general name of *legacy codes*. These were both derived from the original Hybrid PIC Hall (HPHall) by Fife, which boasts some "firsts", such as being able to reproduce "breathing mode" oscillations (see Chapter 7). Fife's work was amongst the first hybrid codes to model HETs, together with the work by Komurasaki & Arakawa[129].

[12] Ref. [128] presents an example of a combination of PIC and Vlasov models.

[13] These include: plasma-wall interaction, highly energetic and non-collisional SEE, anisotropicity, etc., and are reviewed throughout this thesis

Code Name/Author	Publication date	Model	Characteristics	References
HPHALL / J. M. Fife & M. Martinez-Sanchez	1995	Hybrid 2D(r-z) PIC-1D(λ) fluid	DSMC PIC collisions, quasi-neutral, Maxwellian electron fluid, Bohm diffusion	[130, 76]
HPHALL-2, HALLMA / F. I. Parra, E. Ahedo, D. Escobar & R. Santos	2006	Hybrid 2D(r-z) PIC-1D (λ) fluid	MCC for ionization, DSMC for CEX, sheath model with SEE and CSR, kinetic Bohm condition forcing, surface weighting	[131, 132, 133]
J. P. Boeuf & L. Garrigues	1998	1D(z)-1V(z) Hybrid Vlasov-fluid	Quasi-neutral plasma column, electron energy with no temporal evolution	[128]
G. J. M. Hagelaar, J. Bareilles, L. Garrigues & J. P. Boeuf	2002	Hybrid 2D(r-z) PIC-1D(λ) fluid	Quasi-neutral plasma, MCC ionization for singly charged ions, phenomenological expressions for plasma wall interactions	[134, 135, 136]
J. W.Koo & I. D. Boyd	2004	Hybrid 2D(r-z) PIC-1D(λ) fluid	MCC collisions for multiply charged ions, near-wall collisionality and Bohm diffusion	[137, 138]

Table 1.6: Review of recent Hybrid near-plume plasma discharge simulation codes

Table 1.6 compiles references and characteristics of prominent hybrid codes. Most of the hybrid codes use a 1D approximation to the electron fluid, using magnetic field lines as a single spatial coordinate (λ). This approximation, which sometimes is also referred to as perturbed-1D or 1.5D, is tackled in Chapters 3 and 4.

Many other hybrid codes have been developed by various research groups and with various objectives. We point the reader to the works by Sommier[139], for further insight into hybrid PIC-fluid codes, Boniface[140], for a discussion on the origin of anomalous transport, or Fox[141], for another example of a PIC-Vlasov hybrid code.

1.2.4 Plasma-wall interaction and Plasma sheath models

The general interaction between the plasma and material walls can be differentiated in two scales. First, the response of the wall to the impact of each of the species, which generally deposit energy and momentum upon collision. Neutrals are typically considered to go through reflection collisions, with, perhaps, some accommodation factor[142]. Ions, on the other hand, will typically recombine either with electrons from the plasma reaching the walls or having accumulated there, and be can be energetic enough to mechanically erode the wall through the widely studied sputtering phenomenon[143, 144, 145]. While sputtering has been of interest in many studies related to EP thrusters[79, 78], erosion rates can typically be resolved in post-processing, under the assumption that the sputtered material does not significantly alter the overall plasma behavior, and are not the focus of this work.

In the case of electrons, they may be reflected by the wall, but also scattered, absorbed, or, in the case of certain materials, can contribute to the dislocation of other "secondary" electrons, which are released from the internal layers of the material[146]; this last phenomenon is known as SEE. The yields of reflected electrons and SEE have been studied for many materials and impact energies[124].

Electron wall scattering due to microscopic wall roughness, with perhaps some additional scattering due to the existence of secondary electrons, is presumed to be responsible for a phenomenon known as near-wall conductivity[147, 148]. The phenomenon could play a role in the enhanced electron transport of electrons across the magnetic field, in the presence of physical walls, although there is little consensus in the community regarding theories and models associated to this physical phenomenon.

A second, larger scale effect, is the appearance of a thin boundary layer between the bulk plasma and the wall. Conceptually, the boundary layer exists to adapt the flow of either ions or electrons to the electrical properties of the wall. If the wall material is a dielectric, then it may not hold charge in a steady state condition, and thus the plasma self establishes an electric potential gradient in a region of thickness comparable to the Debye length, λ_D, in order to repel one of the charge-carrying populations. If the wall material is a conductor, the sheath limits the amount of current that may be extracted through it. The sheath determines, in part, the energy and momentum deposited to the wall by the plasma, it can be affected by the electron scattering and SEE yield of the material and establishes certain conditions for the plasma bulk, in what is

called the "pre-sheath", such as the Kinetic Bohm condition[149, 150].

A comprehensive review of plasma sheath models was carried out by Taccogna[95]. Some references of interest for the sheath and pre-sheath in representative EP thruster conditions may be found in the work by Ahedo[151], for a 1D-fluid model, Meezan & Capelli[152], for a kinetic Boltzmann model, and Taccogna[153] for a kinetic PIC model. Chapter 5 presents the development of a generalized 1D-fluid sheath model that fits within the scope of this thesis; the reader may find further insight into the physics of plasma sheaths there.

Both the overarching effect of the sheath configuration on the plasma, as well as the presumed existence of near-wall conductivity can have a large impact in the response of the thruster, which has been verified experimentally[154].

1.2.5 Plasma-wave interaction models

The previous sections have alluded to the complete or partial resolution of Maxwell's equations, Eq. (1.10), in conjunction with other models for the plasma discharge. The former situation arises when studying the propagation of electromagnetic waves in the plasma, and thus the characterization of their macroscopic effects becomes very complex.

The study of plasma wave interaction is not the focus of the present work, although it is required if one wishes to simulate the response of certain types of thrusters, such as the HPT or ECR thruster. A brief introduction to plasma-wave interaction can be found in the work by Sercel[155, 156] and Miller[157, 158], in the context of ECR thrusters, or Chen[159, 160], for HPT.

1.3 Scope, objectives and statement of work

The work presented in this thesis is part of an ongoing effort to improve European competitiveness in Space; particularly, funded within the Horizon2020 framework and, specifically, within the EPIC strategy and the CHEOPS[161] project. Included in this framework is the development of simulation tools that will allow for accurately modeling plasma discharges in a variety of different EP thrusters. This is an essential step in order to reduce development time and costs, reveal optimization opportunities and predict operational parameters throughout the thrusters lifetime.

The Electric Propulsion & Plasmas (EP^2) group at Universidad Carlos III de Madrid (UC3M) is responding to this call by building upon more than 15 years of research in simulation of space propulsion plasmas in order to develop a new simulation platform for electromagnetic thrusters. This platform, which we have dubbed HYbrid Plasma-thruster Holistic-simulation ENvironment (HYPHEN), hosts a suite of numerical tools focused on solving 2D(r-z) axisymmetric plasma discharges under the influence of magnetic fields. Special attention has been given to ensuring that the effects over the discharge of a wide variety of magnetic field topologies may be resolved, allowing for a more versatile platform.

Alongside versatility, the platform has been developed following the principles of Test Driven Design (TDD) and modularity. While true computer-aided-design for EP thrusters has not yet been achieved, redoubling efforts on computer simulation with existing and new platforms, such as

HYPHEN, will contribute to the, already significant, pool of qualitative and quantitative knowledge of these devices.

The *core* simulation unit is a hybrid PIC-fluid code that, as mentioned in Section 1.2.3, takes into account the previous experience of the group with hybrid models. The work carried out in this thesis is oriented mainly toward the development of a fluid model for the electron population, its integration alongside the PIC module in the general structure of the code, and the correct interaction between them. The PIC module itself was developed in its entirety by Domínguez-Vázquez[162]; more details on this module can be found in Section 2.2.1.

While the main physical assumptions related to both the electron and heavy-species populations are discussed throughout the following chapters, the plasma regime described in HYPHEN is both informed by, and limited by, the type of Electromagnetic thrusters which we wish to simulate. This regime is characterized by the weak collisionality of the heavy-species populations, the strong magnetization of the electron population and a negligible self-field production by the plasma current. This allows HYPHEN to simulate the response of HETs and derivative types, from SPT to TAL, and, potentially, other types of thruster architectures, such as HEMPTs or applied-field MPDTs. The code is not presently prepared to simulate thrusters that operate in the collisional Magneto Hydro Dynamic (MHD) regime, like the PPT or the self-field MPDT.

The characterization and partial validation of HYPHEN has been initially performed through the simulation of GIT plasma plumes, with ongoing efforts being centered on the simulation of the complex HET discharges. Our hope is that future modules can be seamlessly implemented in order to expand the capabilities of the simulation. An important contribution would be the inclusion of plasma-wave interaction models, focused on ECR or HPT architectures, which operate under a similar plasma regime to the one described previously, or the addition of secondary electron populations; both fall outside of the scope of this work.

Considering all of the above, the objectives for this thesis, and the various chapters in which they are addressed, are:

- To contribute to the creation of a common framework for standardizing code development in the EP^2 group that encouraged continuation and re-usability of the platform and its tools, aided by sufficient documentation and validation. [**Chapter 2**]

- To establish a clear code structure, algorithmic flows and the interface amongst the different modules, from the perspective of code architecture. [**Chapter 2**]

- To develop a fluid model for the electron population, capable of assessing the 2D behavior of the magnetized electron population under arbitrary magnetic topologies (considering the exotic magnetic field variants mentioned in Section 1.1.1). In order to achieve this, we require:

  - Posing of the model equations and various closures required to describe electron transport as well as the numerical methods used to resolve them. The model should be as general as possible, which includes accounting for some sources of anisotropicity

in the Electron Velocity Distribution Function (EVDF), which supposes an important departure from other models found in the literature. [**Chapter 4**]

- Establishing any additional physics models required for the resolution of the fluid models, such as those related to boundary conditions (plasma sheath models) and collisional processes in the plasma; these models should be aimed at reducing the number of assumptions in relation to the important physical mechanisms which they describe. [**Chapter 5**]
- An assessment of the numerical mesh required to best solve the problem at hand, considering its nature, and the development of a mesh generator that explores various alternatives to meshing algorithms and their effect on mesh quality. [**Chapter 3**]
- An investigation into methods for spatial discretization and gradient reconstruction in the proposed mesh. [**Chapter 3**]

- To provide sufficient confidence in the new fluid model, both from the perspective of its numerical implementation, as well as of the physical response that can be resolved. This includes simulations that either explore solely the electron fluid segment or those that allow it to interact with the heavy-species PIC segment. [**Chapter 6**] and [**Chapter 7**]

Lastly, **Chapter 8** provides the conclusions to this work developed in this thesis, as well as some recommendations for future efforts. The document is capped off with an **Annex** section which includes references to publications and conference communications which the author has contributed to, as well as a summary of other achievements made throughout the development of this PhD.

CHAPTER
TWO

The HYPHEN environment

This chapter presents the code which was coauthored throughout the development of this thesis: HYPHEN. We focus on the general development guidelines which were followed, as well as the structure of the code, both from the code architecture and algorithmic perspectives. A brief description of some of the subroutines developed is also provided, as closure to the chapter.

2.1 Code generalities and development methodology

Strict development guidelines were embraced by the EP^2 group as part of an effort to avoid known issues from the development of legacy codes. From the "logistics" perspective, these were related to a lack of sub-version control and traceability and little documentation on code structure, algorithm flows and the different variables used within the code, due to missing developer's comments. A user/developer-oriented approach was taken to ensure that adequate information was available for the future, in the form of user and developer manuals and code repositories[1]. This ensures continuity in the development of the code and encourages re-usability of HYPHEN as a generalistic platform for plasma discharge simulations for various electromagnetic thrusters.

From the development perspective, EP^2 codes now follow three main key guiding principles:

- **Test Driven Design:** TDD is a set of recommendations which constitute a marked development approach. It is based on the idea that adding new code functionality requires it to be independently testable, which helps in structuring the minimum development cycle required to reach the developers' goals, and ensures that each function, subroutine or module meets a known requirement, defined through the aforementioned independent tests. Chapter 6 deals with stress tests performed for the code module dedicated to the electron population (Fig. 2.4).

- **Modularity:** The use of TDD encourages a modular structure for the code, where each part can be validated independently from the others and updated or interchanged without requiring changes in other areas, which is enabled by standardizing the interfaces between modules, functions and subroutines. This approach also allows for a clearer understanding of the program flow, even in cases where the code structure may be complex.

[1] Specifically, we opted for the Mercurial on-line repository, for its extended use amongst the scientific programing community[163].

- **Flexibility:** Following after the concept of modularity, the code must also be oriented towards flexibility: changing or expanding code functionality should be kept as painless as possible and the various modules should be built considering the different simulation scenarios that future users could require and the expected changes to the overall capabilities of the platform. This entails avoiding unnecessary or arbitrary restrictions in the code, which may hinder future applicability; additionally, by considering subsequent developers as "users", we ensure that the environment is both user and developer friendly.

In terms of flexibility and modularity, the first working version of HYPHEN allows for simulation of the polytropic expansion of a plasma in vacuum[162] and also the non-stationary behavior of HETs[164]; however, the platform has been designed with the expectation that future modules will be added.

On the other hand, in an effort to standardize code development and ensure the existence of common code libraries, HYPHEN was designed with the same overall architecture, data structure and interfaces as those of EP2-PLUS, developed by Cichocki[165, 84], including common baseline units and dedicated modules whenever possible.

HYPHEN consists of three independent program units:

- `SET:` Pre-processing unit, coded in common scripted languages `Python/Matlab`. It is composed of different sub-utilities, each of them producing different output files, such as mesh-files (see Chapter 3) or "look-up-table" models (see Chapter 5 for more information on the use of these tables and the interpolation used during simulation run time), which are included into a unique `SimState.hdf5` file. Additionally, the user defines the code input parameters necessary for the `CORE` unit, which are introduced through the `sim_params.inp` file; see Fig. 2.1 for reference.

- `CORE:` Simulation core module, coded in pre-compiled `FORTRAN` language, which carries out the simulation of the plasma discharge in the thruster near-region, as detailed in Section 2.2. It produces a single output files in `HDF5` format, `PostData.hdf5`, and updates the `SimState.hdf5` file with the "exit" status of the simulation. Both files are compatible with various post-processing options and contain the information that is valuable to the user in terms of simulation results.

- `POST:` Post-processing unit, coded in `Python/Matlab`, which takes inputs from the user and the `CORE` output `HDF5` files and generates the required plots, diagrams and simulation statistics.

Industry-level standards for code development were considered, such as the use of the `HDF5`[166] input-output data standard, the `Open-MP`[167] single-machine parallelization standard and others; these are well proven and offer known support from the developers community.

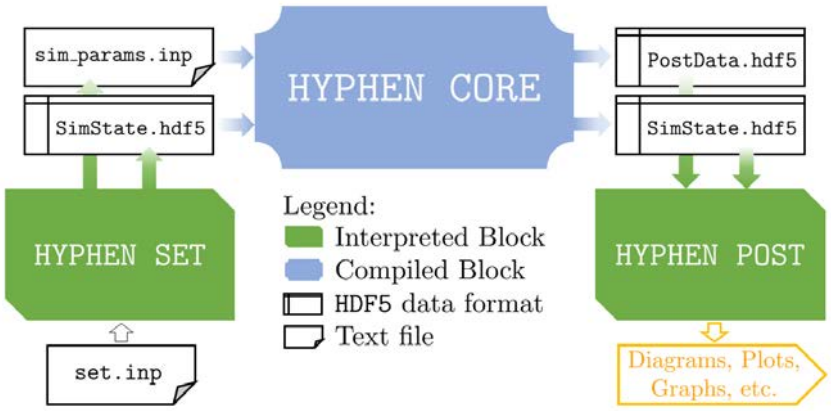

Figure 2.1: HYPHEN platform program units and file flow

2.2 Simulation flow and Code structure

HYPHEN is a hybrid PIC-fluid simulation platform for the analysis of near-region plasma discharges. Its hybrid nature, a legacy from code development in the EP^2 group which presents both advantages and challenges (as described in Section 1.2.3), implies that there are two distinct modules in the `CORE` unit: one related to the Particle-In-Cell approach for the heavy species (neutral and ion populations), and one related to the macroscopic-fluid approach for the electron population.

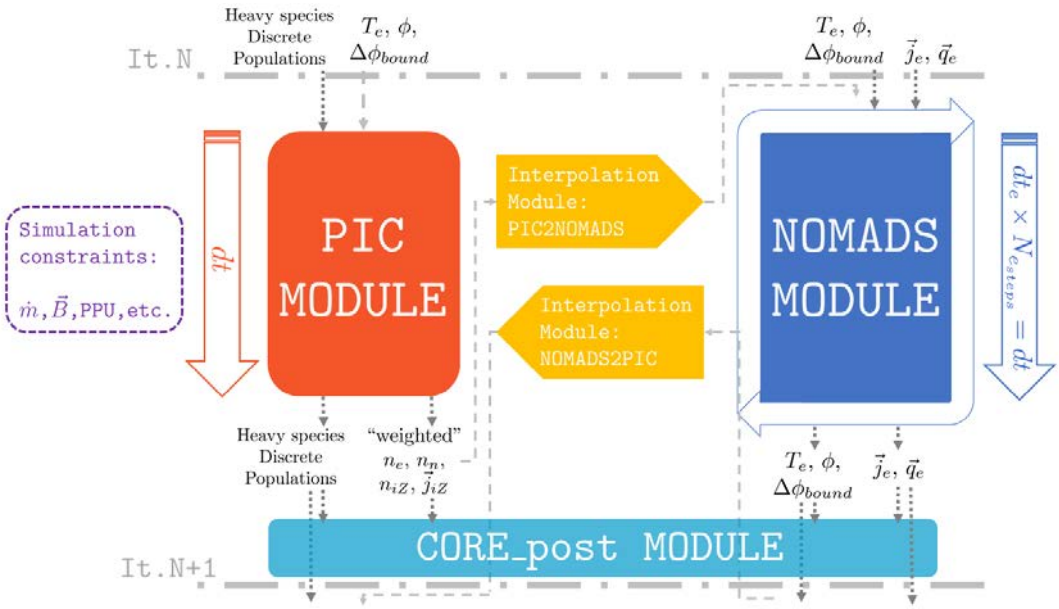

Figure 2.2: HYPHEN `CORE` algorithmic flow

A summary of the algorithmic flow between any two iteration steps in the HYPHEN `CORE` may be found in Fig 2.2. The terms T_e, ϕ, $\Delta\phi_{bound}$ are the electron temperature, the plasma potential and the potential change imposed by any boundary condition. n_e, n_n, n_{iZ} are the particle densities for electrons, neutrals and ions (separated by charge number). $\vec{j}_e$ and $\vec{j}_{iZ}$ are the electron and ion current densities and $\vec{q}_e$ is the electron heat-flow.

From the perspective of simulation time, both modules advance in parallel, iteratively, performing the tasks required to "propagate" the heavy-species (ion and neutral populations) macro-particles and to integrate the electron macroscopic fluid equations; the base unit of time is the time-advanced-per-iteration (dt) in the PIC segment. Certain simulation conditions are kept constant throughout the simulation, such as the injected mass-flow, the magnetic field in the simulation domain (see Section 3.2), the control scheme for the thruster PPU (see Section 4.2.4), etc. A summary of the functions performed by each module, as shown in Fig. 2.2, is detailed next:

2.2.1 The PIC module

The HYPHEN PIC module was developed by Domínguez-Vázquez in conjunction with the one from EP2-PLUS[165, 84] and trialled alongside it[162] to independently demonstrate its modeling capabilities. In particular, this was done by comparing results for the polytropic expansion plume to a Self Similar Method (SSM)[168] result for NASA's NSTAR GIT[169]. The reader may find an in depth discussion on the innovative characteristics of said module in Refs. [170, 164, 162], performed by Domínguez-Váquez and Pérez-Grande.

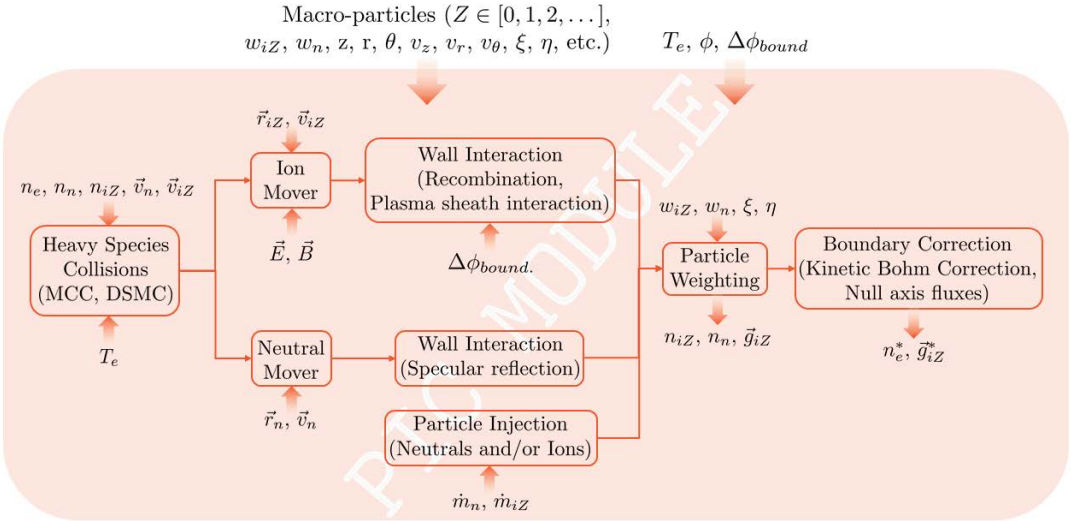

Figure 2.3: HYPHEN PIC module algorithmic flow

In terms of algorithmic flow, the PIC module receives a certain population of *neutral* and *ion* macro-particles, defined both through their positions in the simulation domain as well as in the velocity-space; in addition, macroscopic distributions of electron temperature and electric potential are also given. Both macro-particles and macroscopic distributions may be the result of an ongoing simulation or an initial condition set by the user. Macro-particles are also "sorted" into

the cells of a computational structured PIC mesh[2], based on their positions. The computational mesh coordinates used for the sorting algorithms are (ξ, η), which correspond to the cylindrical coordinates (z, r). This is required for the weighting procedure described next.

First, the PIC segment performs the tasks associated to particle collisions. Ionization, excitation and recombination reactions (see Section 5.2), i.e., those involving the electron population and the various heavy-species, are performed through an ad-hoc MCC method[171, 172]. The method is taken from HPHall[173], with the electron population considered as a "background" macroscopic fluid, and take into account the densities of each species and the electron energy, represented through its temperature (refer to Section 5.2). On the other hand, long-distance CEX type collisions amongst the various populations of heavy-species are performed throughout a DSMC method[89, 174]. No short-range collisions among the heavy-species populations are modeled, since we consider them to be in a non-collisional regime, for the typical densities, temperatures and simulation domains in the EP thrusters we wish to analyze.

Since the treatment of particles in HYPHEN is done through the PIC method, collisions are simulated on a cell-by-cell basis, and only take into account the particles located in a given cell.

Second, macro-particles are propagated, i.e., moved, based on their initial velocity and position and, in the case of particles with electric charge, accelerated due to volumetric forces created by magnetic and electric fields (this last one obtained from gradients of the electric potential).

Third, macro-particles interact with the various physical boundaries in the simulation domain: neutral macro-particles are reflected from the domain walls while ion macro-particles are typically recombined with electrons at the walls. Both deposit energy and momentum at the walls and, in the case of ions, are affected by the plasma boundary layer, a.k.a. plasma sheath (see Section 5.1); Fig. 2.3 exemplifies this through the generic $\Delta\phi_{bound}$ term.

Fourth, macro-particles are injected based on simulation conditions: in the case of EP thrusters, the typical injection profile responds to neutral particles, $\dot{m}_n$, coming from a designated "injector surface" with a mass-flow given by the user. In the case of a plume simulation, the injection profile may represent the exiting Ion Velocity Distribution Function (IVDF) profile from a given thruster, as in Ref. [162], which is exemplified in Fig. 2.3 through the term $\dot{m}_{iZ}$.

Fifth, macro-particles are weighted to their respective cell nodes in the PIC mesh: the procedure implies locating a particle within a given mesh cell (done through its computational coordinates) and distributing its mass and velocity to the nodes of the cell through a "cloud-in-cell" weighting algorithm (similar to a bilinear interpolation scheme) as described by Birdsall[175, 176]. Weighting within a mesh cell is known as *volumetric weighting*; in parallel, particles that cross the domain boundaries may be weighted to boundary nodes based only on information at the surface. The latter is known as *surface weighting* and is performed through linear interpolation. The weighting procedure allows us to define macroscopic variables from the discrete particles, which are passed on to the electron fluid segment.

Last, certain corrections must be carried out at the boundaries; these include imposing null per-

[2]The use of a structured mesh responds to the simplicity it offers in its construction, as well as for the sorting and weighting methods and for the computation of gradient fields, which may be required throughout the simulation. Additionally, it can help in avoiding undesired non-physical effects, which may appear in highly deformed meshes related to the calculation of volumetric forces over the macro-particles[90].

pendicular fluxes at the axisymmetric domain axis or correcting for the Kinetic Bohm condition[149, 150] at the plasma sheaths. The Bohm condition is derived from assuming that the limit of the plasma sheath model, as described in Section 5.1, is that the electric potential fall within the sheath remains monotonic, for which ions need to be at least in sonic conditions at the sheath entrance. The "Bohm correction"[133, 177, 162] algorithm artificially modifies the local plasma density (and in turn the local plasma potential) in order to ensure that said condition is met.

2.2.2 The NOMADS module

The main focus of this thesis is on the electron population module within HYPHEN, which receives its own name: NOn-structured Magnetically Aligned electron-Discharge Simulation (NOMADS). The following Chapters in this thesis describe in detail the way the electrons are modeled from the standpoint of a macroscopic fluid, how its equations are integrated throughout the simulation time and what numerical requirements exist for said task, mainly from the perspective of the method stability and the computational mesh. Particularly, Chapter 3 deals with the non-structured ad-hoc mesh for the electron fluid model: the Magnetic Field Aligned Mesh (MFAM).

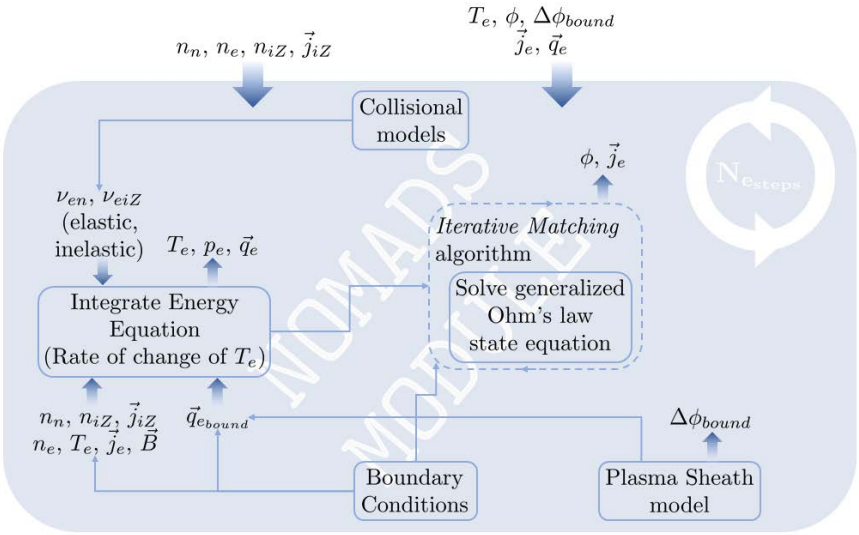

Figure 2.4: HYPHEN NOMADS module algorithmic flow

In terms how the simulation advances, NOMADS receives the output macroscopic quantities from the PIC module, i.e., density and particle fluxes for each heavy-species population, and integrates the electron model equations. A major assumption (treated further in Chapter 4) linking the electron and heavy-species modules is that the plasma is quasineutral: the electron density is equal to the sum of the partial densities of the ion species times their ion charge number.

Regarding the time-advanced-per-iteration, NOMADS has more stringent requirements in terms of the simulation time-step, dt, than the PIC module, due to the stability of the temporal scheme (see Section 6.2). Thus, for each HYPHEN iteration, NOMADS performs a number of "sub-steps" given by $N_{e_{steps}}$; the time-step associated to each sub-iteration of the electron module is $dt_e = {}^{dt}/_{N_{e_{steps}}}$. If the entry quantities result from the initialization of the code, the user

is not required to define the electron current densities; rather, they are obtained by solving a generalized Ohm's law (Section 4.2.1).

The algorithmic flow for each sub-iteration in NOMADS is as follows: first, the rate-of-change in electron temperature (or pressure) is obtained from the entry conditions to the sub-iteration. This is done by solving the energy equations and requires input from the look-up-table models; the plasma sheaths determine the electron energy deposition at the boundaries. On the other hand, the collisional models (Section 5.2) determine the energy sinks due to ionization and excitation reactions, as well as the collision frequencies amongst the various species in the plasma. These frequencies are related to resistive heating in the plasma, which acts as the main energy source for the electron population in HET simulations. The rate-of-change for electron temperature/pressure is used to update said variables for the next sub-iteration.

The temporal evolution of the electron population in our model depends only on the electron energy equation, as shown in Section 4.1. The plasma potential and electron current densities are obtained through the generalized Ohm's law, which acts as a sort of "state equation" in our model; the look-up-table models also factor into said equation. Specifically, the plasma sheath model for conducting walls adds a further level of intricacy: as will be shown in Section 4.2.4 and was detailed in Section 1.1.1, in HETs the plasma closes an electric circuit driven by the PPU. Certain elements may be in charge of injecting or extracting current to and from the plasma; e.g., the anode boundary will extract the discharge current from the plasma, but only does so through a conducting wall boundary layer, which depends on the plasma potential at said boundary. In such cases (and others, which also include electrode type walls or floating potential walls) Ohm's law must be solved recursively, parting from an initial guess for the plasma potential and arriving at a converged solution after a number of sub-iterations; these are performed in a dedicated algorithm called *iterative matching*, based on the Newton-Raphson method.

The exiting quantities of the NOMADS module are the plasma electric potential, the electron temperature and certain conditions at the boundaries: the electric potential drop at the plasma sheaths and electron energy deposition, energy advection at far-field boundaries, etc.

2.2.3 Interpolation module

It is worth noting that the input/output plasma quantities for both the PIC and NOMADS segments are generated in different meshes and thus require interpolation when they are passed from one module to the other. This task is performed in the interpolation module, which is called upon twice per code iteration.

2.2.4 CORE_post module

Finally, the `CORE` may output a number of fields related to the physical properties of the plasma, code statistics, temporal averages or thruster performances. Statistics are mainly related to the PIC module, since controlling the number of macro-particles and their generation rates may be crucial in order to reduce numerical noise typically associated with PIC codes. The data output task is performed at the CORE_post module, although not necessarily in every HYPHEN iteration; the rate of data output is selected by the user.

2.3 SET unit sub-utilities

An array of sub-utilities for the `SET` unit of HYPHEN were also developed as part of the scope of this thesis and are shortly described next; some sub-utilities are described in detail in the referenced chapters:

- **FEMM_MASK** A `Matlab` script was developed for generating magnetic topologies, masking for FEMM, a well known open-source FEM solver for electromagnetic problems in planar and 2D-axisymmetric problems, developed by Meeker[178]; the script was developed by De-Saavedra[179], under supervision from the author. Primarily oriented towards HETs, it facilitates studying the effects of the different elements in the thruster's magnetic circuit over the magnetic field that the plasma is exposed to. Additionally, it outputs an `HDF5` file that contains the information related to a particular magnetic topology, which is then read by MFAM_GEN in order to generate the mesh associated to the NOMADS segment.

- **SHEATH_MODEL** A `Matlab` script was developed for the sheath model described in Section 5.1; it produces a look-up-table `HDF5` file for various wall types and wall material parameters, such as SEE yields, electron backscattering yields, cross-over energies, etc. The look-up-table is in dimensionless form and gives results for sheath quantities such as electric potential drops, energy deposition, electron fluxes, etc. for various input variables such as electron temperatures, magnetic angle, ion fluxes, etc. See the referenced section for further insight into the model.

- **PROPELLANT_CHAR** A `Matlab` script was developed to generate the collisional rates and energy yields for various collision types (ionizing, excitation, elastic, etc.) and different propellant types, based on widely available experimental data and traditional models found in the literature; the data is coded into a look-up-table `HDF5` file. See Section 5.2 for more information.

- **MFAM_GEN** Sections 3.2 and 3.3 address the details for generation of the MFAM: the numerical mesh associated to NOMADS. A `Matlab` script was created to allow the user various meshing strategies and fine-tunning for a numerical domain chosen for the simulation. The selection of boundary types, cathode and potential-reference elements (see Sections 4.2.3 and 4.2.4) and others is also performed in this script. The mesh structure and its various related fields are outputted into an `HDF5` file, organized following the well known open-source Computational Fluid Dynamics (CFD) software OpenFOAM[180, 181].

- **MFAM_QUAL_GR** Sections 3.3 and 3.4 address the geometric quality in the MFAM and the Gradient Reconstruction (GR) performed in the mesh. This `Matlab` script obtains the geometric quality indicators and statistics and allows the user to customize the weighting and stencil selection in the Weighted Least Squares (WLSQR) method. GR error statistics for the various interest points in the MFAM are also obtained for user defined trial functions. The GR coefficients are outputted in the form of sparse matrices in `HDF5`.

- **MESH_INTERP** A `Matlab` script that produces the interpolation matrices between the PIC segment mesh and the NOMADS MFAM, encoding them in `HDF5` in sparse format. It utilizes a combination of the well known Delaunay triangulation method[182] and the WLSQR method proposed in Section 3.4 to correlate nodes in the PIC mesh with element and face centers in the MFAM, and vice-versa. Linear interpolation matrices between boundary-only nodes and face centers, respectively, are also obtained for certain variables that may only be associated to the domain boundaries; interpolation between domains whose boundaries do not coincide is allowed, but it is not recommended. A brief description of the methods used for mesh interpolation can be found in Section 3.5.

- **EFLD_INIT** This `Matlab` script was created for the user to generate and output (onto an `HDF5` file) initial distributions of electron temperature and plasma potential, for the initialization phase in the `CORE`, as well as spatially dependent profiles of the Anomalous Diffusion factor, α_{ano} (see Section 4.1.2).

CHAPTER

THREE

Numerical mesh and spatial discretization in NOMADS

This chapter is focused on the particularities of the numerical mesh used in the NOMADS segment for the electron population modeled as a fluid. The MFAM is presented here, including the rationale behind its use, which is related to the quantifiable existence of *numerical diffusion* in anisotropic mediums, the different meshing strategies and algorithms, and their relation to mesh quality, and the methods by which GR is performed in said mesh, taking into account the scope of our numerical problem, which is detailed in Chapter 4.

A last section is devoted to briefly describing the particularities of the mesh interpolation algorithm, which is used to communicate plasma quantities between the PIC and NOMADS segments.

3.1 Numerical diffusion in anisotropic mediums

A known study by Voloshin[183] reviewed the various sources for anisotropy in fluid-flows; these range from relativistic flows[184, 185] to microfluidic devices[186]. A prime example of anisotropy is the one existing in conducting fluids under the effect of a confining magnetic field[187]; this is the case of the electron flow, which is generally the only magnetized species in plasmas created the EP devices we wish to simulate (as was mentioned in Section 1.1.1), but is not the case for *all* EP thrusters: e.g., the VAriable Specific Impulse Magneto Rocket (VASIMR)[188, 189] rocket presents confined ions in its magnetic nozzle.

In particular, HETs classical plasma transport theory states that the perpendicular electron transport coefficient is up to various orders of magnitude smaller than the parallel transport coefficient [190]. This anisotropicity of the transport coefficients may induce error when numerically solving the flow transport equations, particularly, if the computational mesh is unaligned with the principal magnetic directions. This numerical error is commonly known as *numerical diffusion*.

For the sake of clarity, we may pose a simple problem to illustrate how numerical diffusion can hinder our calculations. Simon[191] established the mathematical formulation for the classic anisotropic diffusion problem in a fully magnetized quasineutral plasma for an infinite 2D slab with fully conducting walls and infinitely straight magnetic field lines (although the problem is easily generalizable to a curved field. Assuming that the diffusion term is uniform across the

domain, the equation for the plasma flow becomes, simply:

$$\frac{dn}{dt} = \begin{bmatrix} D_\perp & 0 \\ 0 & D_\parallel \end{bmatrix} \begin{bmatrix} \frac{\partial^2 n}{\partial x'^2} \\ \frac{\partial^2 n}{\partial y'^2} \end{bmatrix} \tag{3.1}$$

where n is the plasma density, and $D_\perp$ and $D_\parallel$ are, respectively, the diffusion coefficient across the magnetic field and the "free" or natural diffusion coefficient, which make up the diffusion tensor, $\bar{\bar{D}}'$. The tensor quantity is defined in a system of coordinates x' and y' which are associated to the perpendicular, $\vec{1}_\top$[1], and parallel, $\vec{1}_\parallel$, directions with respect to the magnetic field vector, $\vec{B}$, in the 2D plane; we call this system the *aligned* system of coordinates (see Section 3.2).

Numerical diffusion appears when a diffusion equation such as Eq. (3.1) is discretized in a coordinate system which is not aligned with the perpendicular and parallel directions of the magnetic field. In our example, we may assume a Cartesian coordinate system that forms a given angle α with the magnetic field vector, as seen in Fig. 3.1.

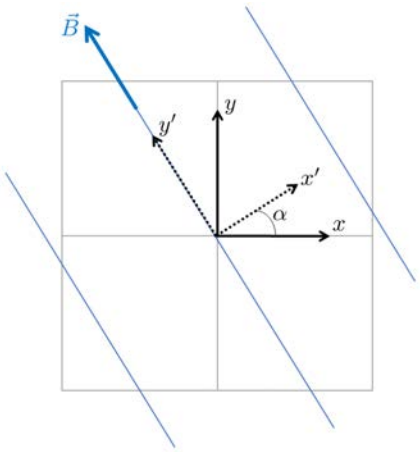

Figure 3.1: Cartesian mesh, Cartesian coordinate system and aligned-to-the-magnetic-field coordinate system

The rotation matrix between the aligned coordinate system, x', y', and the Cartesian one, x, y, is defined as:

$$\mathcal{R} = \begin{bmatrix} \cos\alpha & -\sin\alpha \\ \sin\alpha & \cos\alpha \end{bmatrix}$$

and the gradients for any given variable ψ in the different coordinate systems are related by:

$$\nabla'\psi = \mathcal{R} \cdot \nabla\psi$$

[1]The notation for the perpendicular direction is further detailed in Section 3.2.

Thus, Eq. (3.1) becomes, in the Cartesian coordinate system:

$$\frac{dn}{dt} = \nabla \cdot \left[\mathcal{R}^{-1} \bar{\bar{\mathcal{D}}}' \mathcal{R} \cdot \nabla n \right] \tag{3.2}$$

and the diffusion tensor in the Cartesian coordinate system takes the form:

$$\bar{\bar{\mathcal{D}}} = \mathcal{R}^{-1} \bar{\bar{\mathcal{D}}}' \mathcal{R} = \begin{bmatrix} D_\perp \cos^2\alpha + D_\parallel \sin^2\alpha & \left(D_\parallel - D_\perp\right)\cos\alpha \sin\alpha \\ \left(D_\parallel - D_\perp\right)\cos\alpha \sin\alpha & D_\parallel \cos^2\alpha + D_\perp \sin^2\alpha \end{bmatrix} \tag{3.3}$$

Now, as will be seen in Section 4.2, the preferred numerical method for the resolution of our problem is the FVM. Under said method, Eq. (3.2) may be solved for each of the cell elements in Fig. 3.1 by integrating over its volume, using Gauss' method:

$$\int_V \frac{dn}{dt} = \oint_A d\vec{A} \cdot \begin{bmatrix} (D_\perp \cos^2\alpha + D_\parallel \sin^2\alpha)\frac{\partial n}{\partial x} + \left(\left(D_\parallel - D_\perp\right)\cos\alpha \sin\alpha\right)\frac{\partial n}{\partial y} \\ \left(\left(D_\parallel - D_\perp\right)\cos\alpha \sin\alpha\right)\frac{\partial n}{\partial x} + (D_\parallel \cos^2\alpha + D_\perp \sin^2\alpha)\frac{\partial n}{\partial y} \end{bmatrix} \tag{3.4}$$

Equation (3.4) is equivalent to the one derived for other studies in plasma flows, such as the one portrayed by Wirz[192]. It is easily identifiable that "cross-contamination" of the diffusion terms appears when the diffusion coefficients, $D_\parallel$ and $D_\perp$, take different values, and particularly when $D_\parallel \gg D_\perp$, such as in anisotropic flows of magnetized populations. Continuing with our example, if one imagines a discretized domain such as the one in Fig. 3.2, with an initial distribution of densities such as the one shown there, it may be seen that numerical diffusion appears between elements that do not present differences in density across their common face, under a typical weighting scheme to the mesh's nodes, as seen in Fig. 3.2.

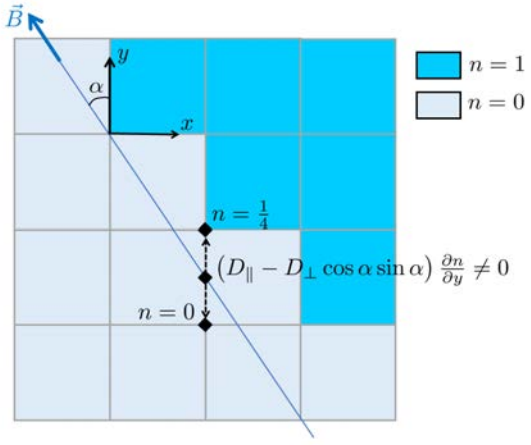

Figure 3.2: Numerical diffusion across a Cartesian mesh face due to density gradients along the face

Furthermore, if one considers the limit case of $D_\perp = 0$, the existence of a discretized domain with elements that are not infinitely small, and the lack of alignment between the mesh and the magnetic field, ensures that mass transport will occur through the mesh cells and across magnetic field lines, even when magnetic field lines should be "impermeable" to mass-flow, as seen in Fig. 3.3.

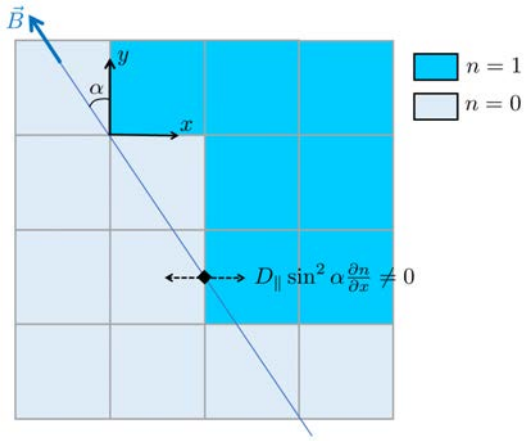

Figure 3.3: Numerical diffusion across a Cartesian mesh face due to density gradients across the face for $D_{\perp} = 0$

Many authors in the literature have discussed this problem at length. Meier[193] analyzed this problem by solving the heat conduction equation with a high-order spectral element code[194]. The study concluded that even small grid misalignments cause significant numerical error and that the error could be reduced by refining the mesh or by increasing the order of the dicretization elements. A similar study was conducted by Anderson[195] demonstrating that numerical diffusion arises when solving the MHD equations in an axisymmetric 2D Cartesian grid with the magnetic field misaligned with respect to the grid directions. The work showed that even in the limit of zero perpendicular transport coefficient, the flow field showed non-zero perpendicular transport. Regarding MHD, and because of this particular reason, codes such as MACH[196] employ Arbitrary Lagrangian Eulerian methods which allow for dynamic grid adaptation, under changing magnetic fields; thrusters such as PPTs[197] or MPDT[198] have been simulated through this approach.

Pérez-Grande et al.[199] tackled the numerical diffusion problem shown in this Section, providing a benchmark for the characterization of this issue. This was done under various conditions of mesh misalignment to the magnetic field and mesh resolution for a Cartesian mesh; the solution for the Cartesian mesh was then compared to one using the MFAM. A more extended account of said study may be found in Ref. [200].

To close this section on the justification of aligned meshes, we would like to end with the following quote from Meier[193]: *"Excessive numerical diffusion due to the large disparity of the transport coefficients in the two directions is avoided by solving the equations on a computational mesh that is aligned with the applied magnetic field. Employment of magnetic field-aligned meshes is a long-standing computational approach for simulating highly anisotropic plasmas, and is widely used nowadays especially by the sustained fusion energy community."*

3.2 The Magnetic Field Aligned Mesh

Numerical diffusion in Catersian meshes, as described in the previous section, may be reduced through mesh refinement or by using higher order numerical methods[195, 193]. A different ap-

proach, which avoids the possibility of numerical diffusion alltogether, is to use a mesh that is aligned with the preferential directions of the problem; in this case, those defined by the magnetic field. These types of meshes are called Magnetic Field Aligned Meshes (MFAM) and have been utilized extensively by the plasma propulsion[125, 132] communities; in particular, HYPHEN makes use of the MFAM solely in the NOMADS segment, since the electron population is the only one treated as a magnetized conducting fluid.

Since the magnetic field in a typical simulation domain cannot be approximated by an infinitely straight one, as in the example shown in Fig 3.1, the MFAM must be defined through a set of curvilinear coordinates that follow the preferent directions of the problem.

Let us assume first that the magnetic field will remain stationary, $^{\partial \vec{B}}/_{\partial t} = 0$ and irrotational, $\nabla \times \vec{B} \approx 0$; in addition, the magnetic field is always solenoidal, $\nabla \cdot \vec{B} = 0$. The first assumption is related to an externally induced magnetic field that does not change in time (a property of the magnetic circuit in the thruster); the second assumption relates to the relative magnetic intensity of the self-field generated by the plasma and the field imposed by a magnetic circuit. The irrorational magnetic field approximation may be discussed by recovering the respective expression from Maxwell's equations:

$$\nabla \times \vec{B} = -\epsilon_0 \vec{j} - \frac{1}{c^2} \frac{\delta \vec{E}}{\delta t}$$

The approximation is valid, within the simulation domain, whenever the effect of the plasma current is negligible compared to the field generated by the magnetic circuit, and for the typical electric field developed by the plasma in an EP device and the smallest temporal scales in which said fields may change (in comparison to the speed of light)[2].

We refer to a magnetic field under the previous assumptions as a *static* one, which allows us to avoid solving Maxwell's equations, Eq. (1.10). Note that only a subset of EP thrusters may be modeled under the static magnetic field approximation: HETs, HEMPTs and possibly applied-field MPDTs, as well as magnetic nozzle thrusters operating in weakly collisional regimes. Other thruster types may require either all or a subgroup of Maxwell's equations to be solved; in particular, plasma-wave interaction requires the solution of the full set of equations.

A solenoidal and irrotational magnetic field, under a cylindrical axisymmetric reference system, must also satisfy:

$$\begin{aligned} &\frac{\partial \vec{B}}{\partial \theta} = 0 \\ &\vec{B} = \{B_z, B_\theta, B_r\} = \{B_z, 0, B_r\} \end{aligned} \tag{3.5}$$

The magnetic field may be posed in an orthogonal-normal (orthonormal) reference system derived from its own relevant directions: the *magnetic reference system*, $\left\{\vec{1}_\parallel, \vec{1}_\theta, \vec{1}_\top\right\}$, in which $\vec{B} = \{B, 0, 0\}$. For clarification, the $\top$ symbol defines the perpendicular direction contained in the $z-r$ cylindrical plane for an axysimmetric magnetic field, whereas the $\perp$ symbol denotes the plane

[2]For a hybrid PIC-fluid code, the smallest temporal scale resolved is the ion transit time.

perpendicular to the magnetic field vector. This contrast must be made since the anisotropicity in our problem only imposes a distinction between the parallel direction and any direction contained within the plane perpendicular to the field; the notation is exemplified by Fig. 3.4.

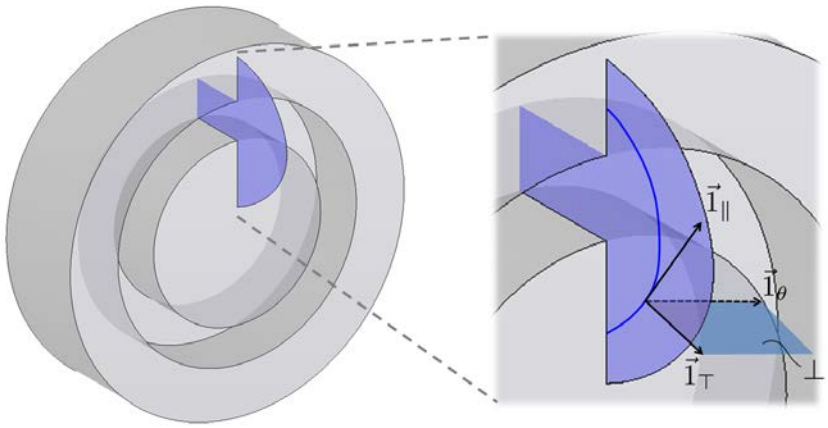

Figure 3.4: Axisymmetric Hall thruster annular geometry and magnetic reference system for a typical $z-r$ plane simulation domain

Now, the irrotational approximation allows us to derive the magnetic scalar potential function, σ:

$$\nabla \times \vec{B} \approx 0 \rightarrow \nabla\sigma = \vec{B} \rightarrow \frac{\partial \sigma}{\partial r} = B_r \,;\, \frac{\partial \sigma}{\partial z} = B_z \tag{3.6}$$

where σ is constant along surfaces perpendicular to the static magnetic field, since:

$$\begin{cases} \nabla\sigma \cdot \vec{1}_{\top} = \vec{B} \cdot \vec{1}_{\top} = 0 \\ \nabla\sigma \cdot \vec{1}_{\theta} = \vec{B} \cdot \vec{1}_{\theta} = 0 \end{cases}$$

Furthermore, we can define the magnetic stream function, λ, through the following:

$$\left.\begin{array}{l} \lambda = -\int r B_z dr \\ \nabla \cdot \vec{B} = 0 \\ \dfrac{\partial \vec{B}}{\partial \theta} = 0 \end{array}\right\} \rightarrow \frac{\partial \left(r B_r\right)}{\partial r} = -r\frac{\partial B_z}{\partial z} \left.\right\} \rightarrow \frac{\partial \lambda}{\partial r} = -r B_z \,;\, \frac{\partial \lambda}{\partial z} = r B_r \tag{3.7}$$

where λ is constant along surfaces parallel to the static magnetic field, since:

$$\nabla\lambda \cdot \vec{B} = 0$$

As an example, let us consider the particular magnetic topology of the SPT-100 thruster (see Section 7.1.1 for more details) and the associated values of λ and σ for a given simulation domain,

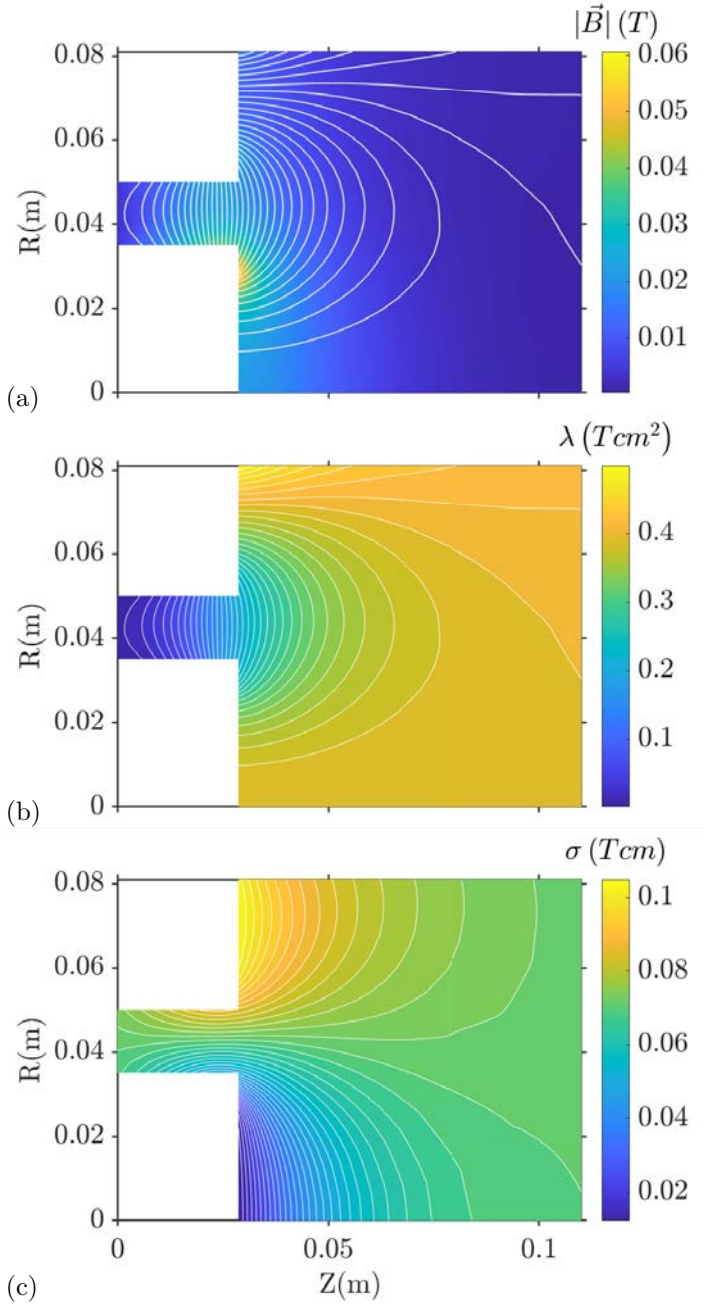

Figure 3.5: SPT-100 (a) magnetic field intensity and magnetic field lines, (b) magnetic stream-line function coordinate λ, (c) magnetic scalar potential coordinate σ

as seen in Fig. 3.5, where both curvilinear coordinates are defined up to a constant, which can be arbitrarily chosen for a given point in the domain.

The intersection of surfaces of constant λ and σ (i.e., contour surfaces), respectively, allows us to split a given simulation domain into toroidal volume elements, where each of the faces is

closely aligned with one of the local directions defined by the magnetic field. Figure 3.6 shows said volume elements and the associated MFAM: *blue faces* represent surfaces of constant magnetic stream function and follow the local parallel direction to the magnetic field, $\vec{1}_{\parallel}$; *red faces* represent surfaces of constant magnetic scalar potential, and are aligned with the local perpendicular-to-the-magnetic-field direction in the $z-r$ plane, $\vec{1}_{\top}$.

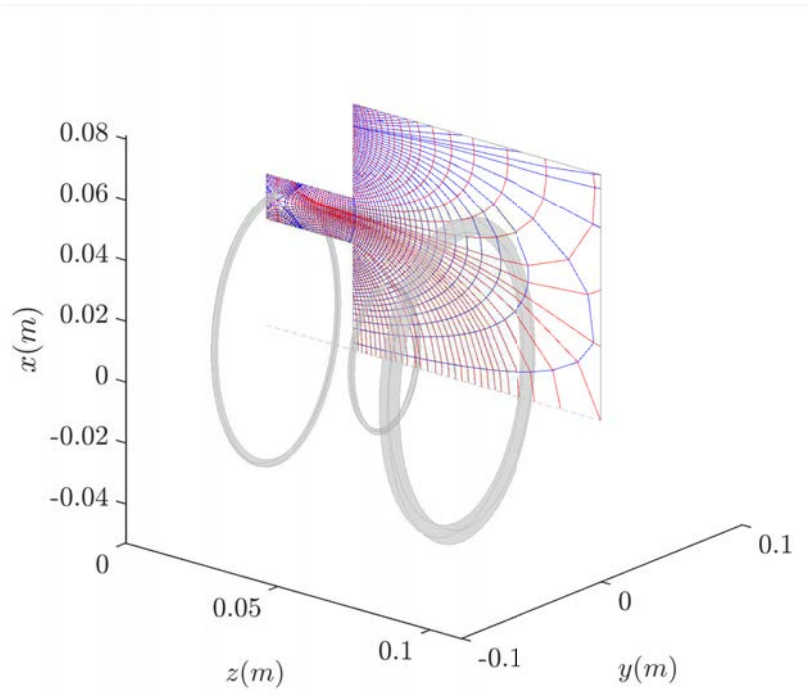

Figure 3.6: 2D-axisymmetric magnetic field aligned mesh and toroidal volume elements

Since we consider our problem to be axisymmetric (see Section 4.1), we typically only consider the MFAM in the $z-r$ plane, as shown in Fig. 3.7.

The MFAM elements shown in Fig. 3.7 and Fig. 3.6 exemplify how the curved surfaces of constant λ and σ are approximated by cone frustrums in the 3D volume, based on the intersection of said surfaces; in the axisymmetric $z-r$ plane this translates into the mesh elements (E_i), faces (F_j) and nodes (N_k) in Fig. 3.7. This implies:

- A spatial deviation of the facets in the mesh from the true "lines" (in the $z-r$ plane) of constant λ and σ, which primarily implies a discrepancy of the face areas and face center coordinates with respect to the same geometrical aspects for the corresponding surface section.
- An angular deviation between the true representative directions of the magnetic field at the center of the surface section and the "resembling" versors in the center of the element faces.

Theoretically, the solution for a highly anisotropic problem posed in the magnetic reference frame should minimize the numerical diffusion caused by anisotropicity, although some numerical

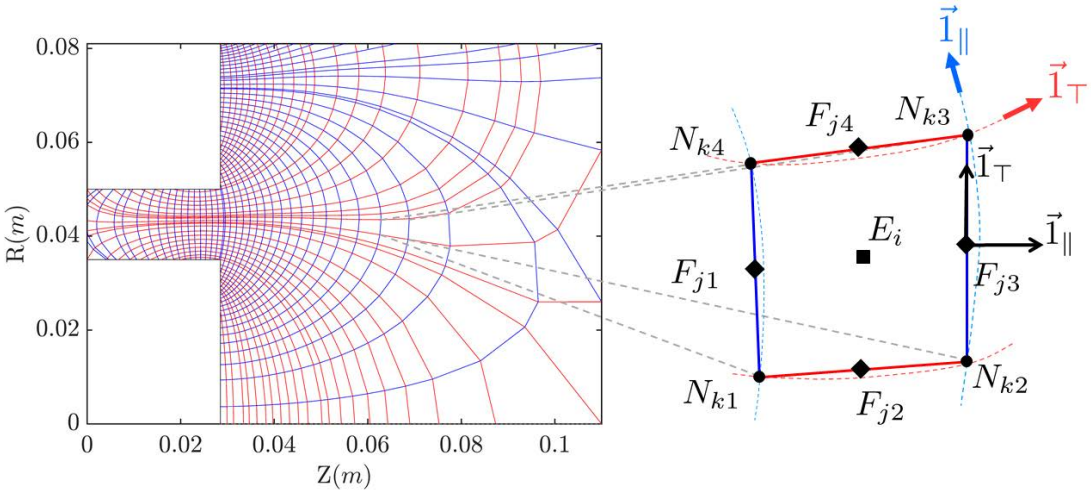

Figure 3.7: Magnetic field aligned mesh in the $z-r$ plane and detail of mesh element, faces and nodes

errors will remain. These include discretization errors and the loss of local curvature information on the MFAM faces, which which depends primarily on the element size.

Finally, the orthonormal magnetic reference system and the curvilinear magnetic coordinates satisfy:

$$\begin{aligned}\vec{1}_{\top} &\equiv \frac{1}{h_\lambda}\frac{\partial}{\partial\lambda};\ h_\lambda = \frac{1}{rB}\\ \vec{1}_{\theta} &\equiv \frac{1}{h_\theta}\frac{\partial}{\partial\theta};\ h_\theta = r\\ \vec{1}_{\parallel} &\equiv \frac{1}{h_\sigma}\frac{\partial}{\partial\sigma};\ h_\sigma = \frac{1}{B}\end{aligned}$$

Where h_λ, h_θ and h_σ are the *scale factors* associated to the orthonormal basis. Some common operations and relations in the orthonormal set are:

$$\nabla f = \frac{1}{h_\lambda}\frac{\partial f}{\partial\lambda}\vec{1}_{\top} + \frac{1}{h_\theta}\frac{\partial f}{\partial\theta}\vec{1}_{\theta} + \frac{1}{h_\sigma}\frac{\partial f}{\partial\sigma}\vec{1}_{\parallel} \rightarrow \begin{cases} \nabla_\perp f = rB\dfrac{\partial f}{\partial\lambda}\vec{1}_{\top} + \dfrac{1}{r}\dfrac{\partial f}{\partial\theta}\vec{1}_{\theta} \\ \nabla_\parallel f = B\dfrac{\partial f}{\partial\sigma}\vec{1}_{\parallel} \end{cases} \tag{3.8}$$

$$\begin{aligned}&\nabla\cdot\vec{v} = \frac{1}{h_\lambda h_\theta h_\sigma}\left(\frac{\partial(h_\theta h_\sigma v_{\top})}{\partial\lambda} + \frac{\partial(h_\lambda h_\sigma v_\theta)}{\partial\theta} + \frac{\partial(h_\lambda h_\theta v_{\parallel})}{\partial\sigma}\right) \rightarrow \\ &\rightarrow \begin{cases} \nabla_\perp\cdot\vec{v} = \dfrac{1}{h_\lambda h_\theta h_\sigma}\left(\dfrac{\partial(h_\theta h_\sigma v_{\top})}{\partial\lambda} + \dfrac{\partial(h_\lambda h_\sigma v_\theta)}{\partial\theta}\right) \\ \nabla_\parallel\cdot\vec{v} = \dfrac{1}{h_\lambda h_\theta h_\sigma}\dfrac{\partial(h_\lambda h_\theta v_{\parallel})}{\partial\sigma} \end{cases}\end{aligned} \tag{3.9}$$

$$\nabla\vec{v} = \begin{cases} (\nabla\vec{v})_{ii} = \dfrac{1}{h_i}\left[\dfrac{\partial v_i}{\partial \xi^i} + \sum\limits_{k\neq i}\dfrac{1}{h_k}\dfrac{\partial h_i}{\partial \xi^k}v_k\right] \\ (\nabla\vec{v})_{ij,i\neq j} = \dfrac{1}{h_i}\left[\dfrac{\partial v_j}{\partial \xi^i} - \dfrac{1}{h_j}\dfrac{\partial h_i}{\partial \xi^j}v_i\right] \end{cases} ; \text{for } i,j,k \text{ taking values 1,2,3 and } \begin{cases} h_1 = h_\lambda; \xi^1 = \lambda \\ h_2 = h_\theta; \xi^2 = \theta \\ h_3 = h_\sigma; \xi^3 = \sigma \end{cases} \tag{3.10}$$

Particularly, the following results are be derived in foresight to the transport equations presented in Section 4.1: considering that $\vec{1}_\parallel = \{0,0,1\}$ in the magnetic reference system and an axisymmetric problem:

$$\nabla\vec{1}_\parallel = \begin{pmatrix} rB^2\dfrac{\partial\left((rB)^{-1}\right)}{\partial\sigma} & 0 & 0 \\ 0 & B\dfrac{\partial(\ln r)}{\partial\sigma} & 0 \\ r\dfrac{\partial B}{\partial\lambda} & 0 & 0 \end{pmatrix} \tag{3.11}$$

$$\nabla\cdot\vec{1}_\parallel = -\frac{\partial B}{\partial\sigma} \tag{3.12}$$

Using the rule for the divergence of a dyad product:

$$\nabla\cdot\left(\vec{1}_\parallel\vec{1}_\parallel\right) = \left(\nabla\cdot\vec{1}_\parallel\right)\vec{1}_\parallel + \left(\vec{1}_\parallel\cdot\nabla\right)\vec{1}_\parallel = r\frac{\partial B}{\partial\lambda}\vec{1}_\top - \frac{\partial B}{\partial\sigma}\vec{1}_\parallel \tag{3.13}$$

Finally, we describe vector projections in the following way:

$$\vec{v} = \left\{v_\top, v_\theta, v_\parallel\right\} \rightarrow \begin{cases} \vec{v}_\perp = \{v_\top, v_\theta, 0\} \\ \vec{v}_\parallel = \left\{0,0,v_\parallel\right\} \end{cases} \tag{3.14}$$

3.3 Meshing strategies and mesh quality

Generating a MFAM for given simulation domain is typically a matter of finding a distribution of values for a chosen number of contours of λ and σ that produces surfaces contributing towards a "good" mesh; the way we find this distribution is what we refer to as a "meshing strategy". However, certain complications arise in aligned meshes:

- Equations (3.7) and (3.6) show that the rate of change of the value for λ and σ in a cylindrical domain depends on the local strength of the magnetic field; hence, the distances between the surfaces defined by two given values of any one of the curvilinear coordinates also depend on the field intensity, and vary over the simulation domain. Typically, areas of high field curvature and low magnetic intensity, such as the bottom right corner area in Fig. 3.7,

present large separation between λ and σ contours and, thus, lead to larger mesh elements and larger deviations between the MFAM and the "true" field curvature. Adding contours in an effort to reduce element sizes in said regions fixes the problem locally, but said surfaces can typically lead to very small elements elsewhere in the domain.

- Domain boundaries are typically chosen to represent the geometry of a given thruster, together with the domain axis and the "exit" boundaries of the domain (see Sections 4.2.3 and 4.2.4). These boundaries, however, do not naturally coincide with contours of λ or σ (except for the domain axis, which is necessarily a λ contour, due to symmetry) and, more generally, cut contour lines at arbitrary positions, making for problematic boundary elements. Araki[201] argued that poor mesh quality in the boundaries of the MFAM led to issues with the calculation of gradients and numerical errors that were, at least, comparable to numerical diffusion. The solution proposed was to sacrifice the MFAM configuration in these type of elements. Araki's approach was not followed in this thesis and we have opted to tackle the order of the GR method instead (see Section 3.4).

- Modern plasma thruster designs may include "exotic" magnetic field topologies containing features such as singular points[3], which refer to regions of $\vec{B} = \vec{0}$. These have been proposed as a means for electron flow control in the near-anode region of HETs[202], or may simply appear as result of back-flow shielding magnets, as in Helicon or ECR thrusters. Regions surrounding singular points have low magnetic field intensity and thus are characterized by large mesh elements. Furthermore, the singular point itself receives its name because more than a single λ or σ surface may cross it, and since the magnetic field is null in said points, contour surfaces are no longer defined; this must be explicitly taken into account by the meshing algorithms[4].

A first requirement for the mesh, which appears due to the complications discussed here, is that the MFAM must be organized in a non-structured manner so that we retain flexibility in the treatment of "non-regular" elements, such as the ones in the boundaries or elements surrounding singular points. The use of a structured "computational mesh", such as in the PIC segment (see Section 2.2.1), is, simply, not possible for the electron population, considering the problem we wish to resolve[5].

In addition, the definition of a "good" mesh is not straightforward. The study performed by Diskin[203] indicates that mesh quality cannot be truly assessed without taking into account the nature of the problem, the numerical discretization approach, and the expected computational output, in addition to purely geometric quality indicators. Since errors in terms of discretization, interpolation and gradient calculation (which can be linked both to geometric properties of the

[3]The term "point" is used here loosely, referring to the $z - r$ plane; in reality they are curved lines in the cylindrical space.

[4]An example of a MFAM which includes a singular point, generated through the meshing strategies presented in this section, is given in Chapter 7.

[5]A structured MFAM was used in legacy codes such as HallMa or HPHall for the perturbed-One Dimensional (1D) solution of the electron fluid. This mesh imposed limitations related to the domain boundaries and magnetic topologies that could be simulated; these were distinctive of said codes and have been sought to be avoided here.

mesh and to the methods used for GR) can never be fully mitigated, the conclusion is that it is best to minimize these issues from the start.

Our initial approach has been to develop a robust meshing strategy that takes into account the particularities of the MFAM and produce an initial assessment based solely on geometric quality indicators. The best strategy is then used to generate a mesh on which GR methods are applied. The trialled meshing strategies are:

- **Inverse-rate-of-change spacing** The values for the magnetic coordinates, λ and σ, are integrated for the whole of the simulation domain; by applying a local regression method, one may find the rate of change for said coordinates. If one were to space out a given number of contour values evenly, more of said values would fall in the regions of low rate-of-change than of high rate of change; thus, the values selected to generate the contour surfaces are spaced with an inverse proportionality with regards to the rate-of-change.

- **Exponential-stretching spacing** This method was proposed by Araki[201] to deal with magnetic field topologies containing singular points and high ratios of maximum-to-minimum field strength. For the magnetic streamline function, λ (the method is equivalent for σ), for a number of contours, n_λ, chosen by the user, the values of said contours, λ_q, are:

$$\begin{aligned} \lambda_q &= \lambda_{min} \frac{\exp\left(\frac{q_0 - q}{q_0 - 1}\alpha_\lambda\right) - 1}{\exp\left(\alpha_\lambda\right) - 1} \text{ for } q < q_0 \\ \lambda_q &= \lambda_{max} \frac{\exp\left(\frac{q - q_0}{n_\lambda - q_0}\alpha_\lambda\right) - 1}{\exp\left(\alpha_\lambda\right) - 1} \text{ for } q > q_0 \end{aligned} \tag{3.15}$$

  where q_0 is defined as:

$$q_0 = \int \left(n_\lambda \frac{\lambda_{min}}{\lambda_{max} - \lambda_{min}} \right) \text{ and } \lambda(q_0) = 0. \tag{3.16}$$

  and α_λ is the "stretching parameter" and is chosen as a parameter in the method. The contour values are obtained, according to Eq. (3.15), by exponentially spacing them from 0 to the maximum and minimum values of the magnetic coordinate found in the domain, λ_{max} and λ_{min}, respectively. The method may be generalized so that the stretching parameter varies in the domain, for example, in the vicinity of singular points, where additional contour surfaces may be added for better mesh quality[199].

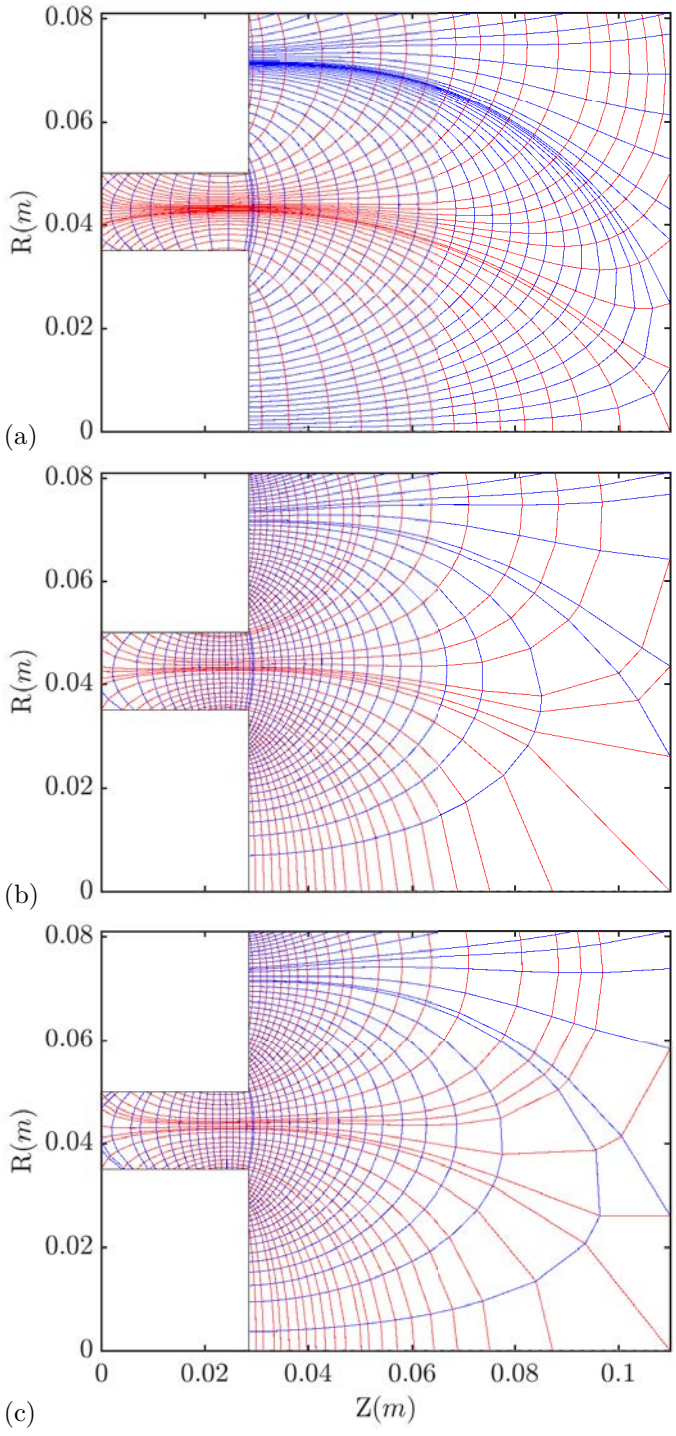

Figure 3.8: (a) Inverse-rate-of-change spacing, (b) Exponential-stretching spacing, (c) Manually corrected Exponential-stretching spacing; blue lines represent axisymmetric surfaces of constant λ and are closely parallel to the magnetic field, red lines represent axisymmetric surfaces of constant σ and are closely perpendicular to the magnetic field

Examples of MFAMs for the magnetic topology of the SPT-100, generated through the different meshing strategies, are shown in Fig. 3.8, for $n_\lambda = 40$ and $n_\sigma = 35$. The term "manually corrected" makes reference to a feature incorporated in the MFAM_GEN sub-utility (Section 2.3). Said feature allows fine tunning of the contour surfaces selection through a Graphical User Interface (GUI) in order to avoid low quality elements in the boundaries. The number of elements on each mesh varies $\pm 5\%$ on the expected value of $35 \times 40 = 1400$ elements; the actual number of elements is difficult to determine solely from the values of n_λ and n_σ, since it strongly depends on the magnetic topology and the position of the boundaries.

These MFAMs can now be assessed through the geometric mesh quality indicators:

$$
\begin{aligned}
smoothness &= \frac{max(A_{element}, A_{adjacents})}{min(A_{element}, A_{adjacents})} \\
aspect\ ratio &= \frac{max(l_{face(element)})}{min(l_{face(element)})} \\
skewness &= max\left[\frac{\theta_{max} - \theta_e}{180° - \theta_e}, \frac{\theta_e - \theta_{max}}{\theta_e}\right]
\end{aligned}
\tag{3.17}
$$

where A represents element areas, l the face length, *element* and *adjacent* refer to, respectively, the element being considered and the elements adjacent to it, θ_{max} is the largest angle in the element polygon and θ_e is the angle in an equiangular polygon with the same number of sides as the element considered. Large aspect ratios and smoothness may be intuitively understood to negatively affect the interpolation of the solution (required when outputting the plasma quantities from NOMADS to the PIC segment. They may also affect gradient reconstruction in the element faces (although this may be offset in part by using the WLSQR method, see Section 3.4). Skewness may be related to large errors for fluxes in facets which are nearly parallel; high skewness elements appear typically in the boundary of the domain. For all indicators, greater values indicate "worse" quality; a visual representation of the indicators is shown in Fig. 3.9.

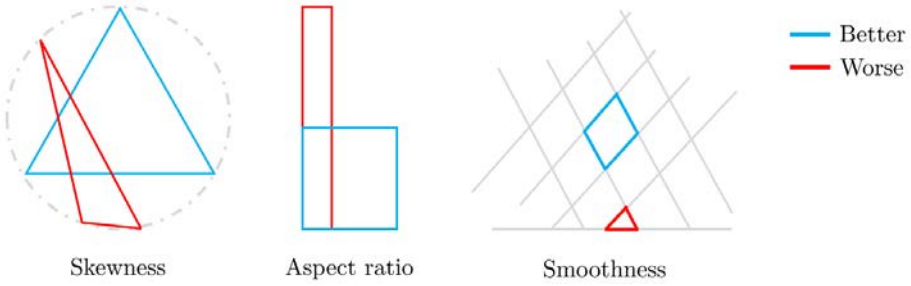

Figure 3.9: Visual representation of mesh quality indicators

Figure 3.10 shows the comparison between statistics of the geometric quality indicators for each of the meshes in Fig. 3.8, as well as the distribution of said indicators for the manually corrected MFAM produced with the exponential-stretching strategy. For the sake of comparison,

we have also added the value of element areas, which serves as a qualitative indicator of how the mesh element faces may not be truly representative of the local curvature in the magnetic field, due to large element sizes. The results were obtained using the MFAM_QUAL_GR sub-utility (see Section 2.3) and may be seen in Fig. 3.10. They show that, with respect to the indicators, the meshes vary mainly with regards to the "minimum" and "maximum" value statistics, which necessarily affect the mean, but not so the most probable values of the distribution. Furthermore, the percentile values are almost mesh independent; this indicates that the major differences reside in the worse quality elements (i.e., the "top" 5%), which typically reside close to the boundaries, as may be seen. The inverse-rate-of-change MFAM seems to present marginally better quality statistics, perhaps with the exception of *aspect ratio*. This meshing approach ensures that the smoothness and element areas in low magnetic field intensity regions are on par with the rest of the domain, at the expense, however, of regions with very high aspect ratio elements.

Careful review of geometric quality properties allows the user to iterate through the different possibilities offered by the previously described meshing strategies, and the fine tuning through manual correction, in order to obtain increasingly better meshes. Nevertheless, low quality elements are intrinsic to the MFAM, due to the use of contour surfaces which are defined by a magnetic topology with varying field intensity, over arbitrary domain boundaries.

An option, not explored in this work, is to introduce local refinement and/or clustering of elements[204, 205] through the use of "hanging-nodes"; the opportunities offered through these method for higher quality meshes are reserved for future work.

3.4 Gradient Reconstruction in aligned meshes

Gradient Reconstruction (GR) in the MFAM must be carried out through a versatile method which takes into account the fact that we are dealing with a non-structured mesh.

The subject treated here presents abundant references in the literature, two recent reviews by Diskin[203] and Sozer[206] considered the use of the Green-Gauss (GG) and the Least Squares (LSQR) (both "weighted", WLSQR and "unweighted", ULSQR) methods in terms of order of accuracy for GR. Sozer also performed analysis on additional methods, showcasing that, while consistency in the GG and LSQR methods might vary with mesh regularity, other methods tend to have lower orders of accuracy. Shima[207] recently tackled the development of a hybrid GG/WLSQR method, which might offer the best compromise between them.

Due to the "cell-centered" FVM discretization approach employed in our problem (Section 4.2), we have chosen to implement the WLSQR method, as presented by Sozer[206], which allows for Face Interpolation (FI) values at the element faces of derivatives up to an arbitrary order, as well as derivatives at the element centers. The method is based on the Taylor series expansion around either the face center or the element center. Since the FVM method is "cell-centered", we may choose a number of "stencils" surrounding our point of interest (e.g., for FI, a face center in the MFAM, see Fig. 3.11), which are, in this case, the element centers in the MFAM, and for which we will obtain the discretized solutions of the fluid variables in our model.

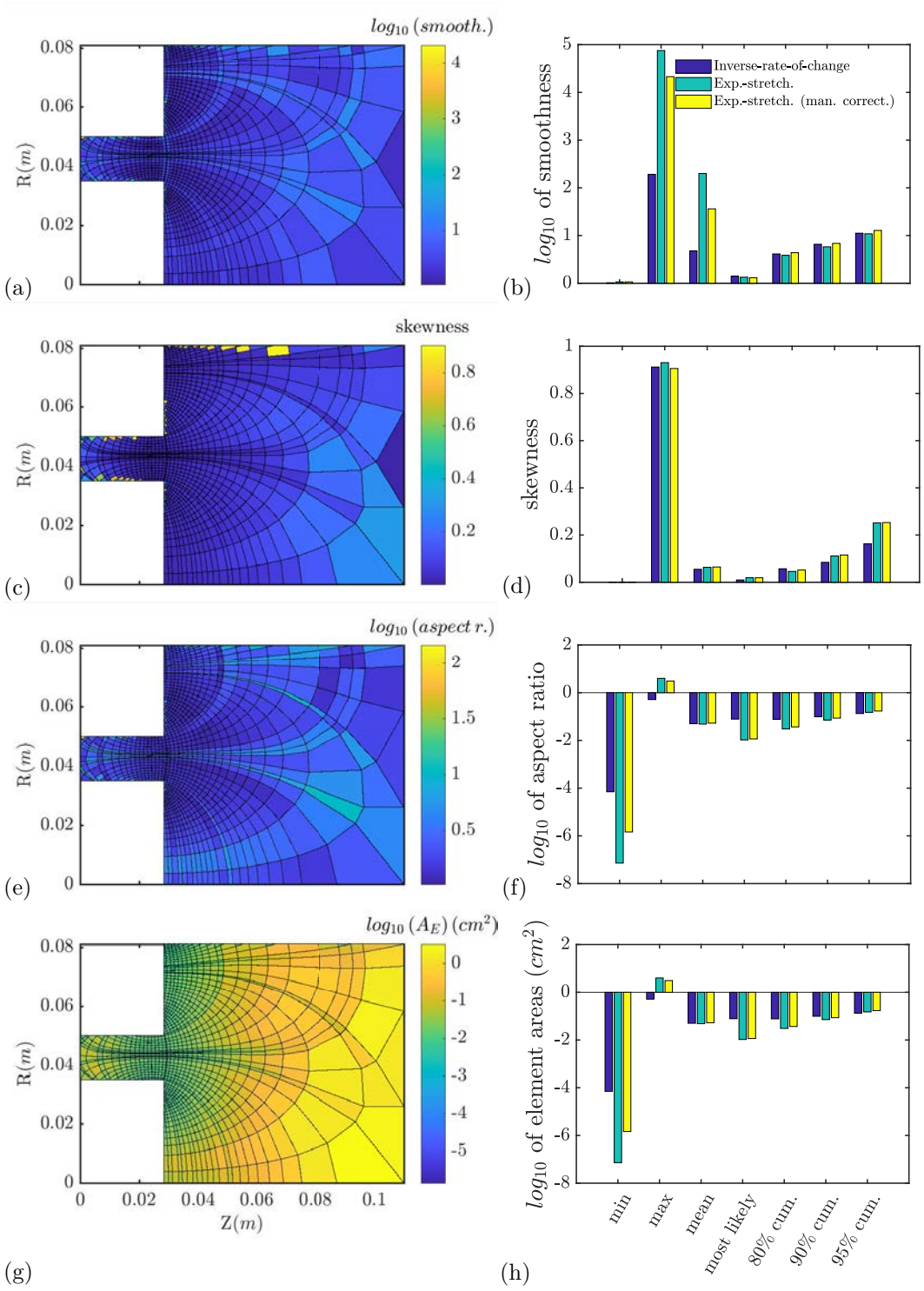

Figure 3.10: Distribution of quality indicators for Exponential-stretching spacing MFAM with manual correction and quality indicator statistics for the trialled meshes for Smoothness [(a),(b)], Skewness [(c),(d)], Aspect Ratio [(e),(f)] and Element Areas [(g),(h)]; Indicator statistics are based on minimum, maximum, mean, most probable and cumulative statistics, i.e., the value *under* which a given percentile of elements exist, for 80%, 90% and 95% percentiles

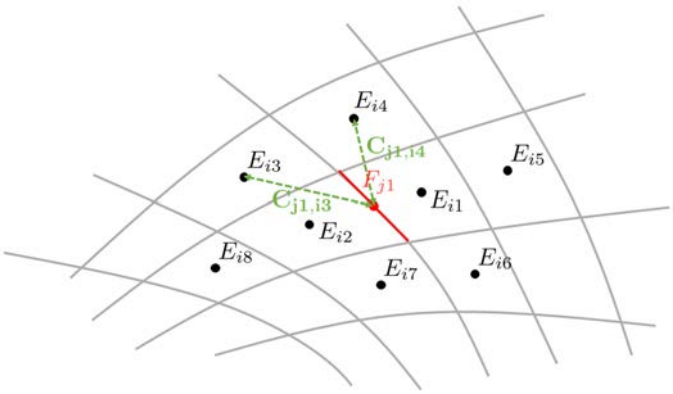

Figure 3.11: Stencils for Face Interpolation using WLSQR method

Following the example set in Fig. 3.11, the Taylor expansion based on the curvilinear magnetic coordinates, λ and σ, around a face center, F_j, for a given stencil element, E_i, and any given fluid variable ψ, follows the given expression:

$$\begin{cases} \psi_{E_i} = \sum_{n=0}^{\infty} \sum_{m=0}^{\infty} \frac{(\Delta\lambda_{E_i})^n (\Delta\sigma_{E_i})^m}{n!\, m!} \frac{\partial \psi^{n+m}}{\partial\lambda^n \partial\sigma^m}(\lambda_F, \sigma_F) \\ \Delta\lambda_{E_i} = \lambda_{E_i} - \lambda_F \,;\, \Delta\sigma_{E_i} = \sigma_{E_i} - \sigma_F \end{cases} \tag{3.18}$$

where n and m represent the order of the derivative with *lambda* and *sigma*, respectively; the 0^{th} derivative represents the actual *value* of ψ at the point of interest. Now, we define a functional which includes the expressions for each of the element stencils; the number of stencils needed, $N_{stencil}$, represents the maximum number of equations we may pose through the LSQR method to obtain the derivatives of ψ at the point of interest:

$$\mathcal{F} = \sum_{i=1}^{N_{stencil}} \omega_{E_i} \left[\psi_{E_i} - \sum_{n=0}^{\infty} \sum_{m=0}^{\infty} \frac{(\Delta\lambda_{E_i})^n (\Delta\sigma_{E_i})^m}{n!\, m!} \frac{\partial \psi^{n+m}}{\partial\lambda^n \partial\sigma^m}(\lambda_F, \sigma_F) \right]^2 \tag{3.19}$$

where ω_{E_i} is the weighting term associated with each stencil element, which factors in the relative importance of each of the stencils. Examples in the literature[208, 209, 210] study the use of the element area, the square of the inverse distance to the point of interest, etc., although the most popular is the inverse distance weighting.

The key to the WLSQR is to find the minimum of the functional defined in Eq. (3.19) with

respect to any of the derivatives:

$$\begin{aligned}
&\frac{\partial \mathcal{F}}{\partial\left(\dfrac{\partial \psi^{n+m}}{\partial \lambda^n \partial \sigma^m}\left(\lambda_F, \sigma_F\right)\right)}=0 \rightarrow \\
&\rightarrow \sum_{i=1}^{N_{stencil}} \omega_{E_i} \frac{\left(\Delta \lambda_{E_i}\right)^n\left(\Delta \sigma_{E_i}\right)^m}{n!\, m!}\left[\sum_{n=0}^{\infty} \sum_{m=0}^{\infty} \frac{\left(\Delta \lambda_{E_i}\right)^n\left(\Delta \sigma_{E_i}\right)^m}{n!\, m!} \frac{\partial \psi^{n+m}}{\partial \lambda^n \partial \sigma^m}\left(\lambda_F, \sigma_F\right)\right]= \\
&=\sum_{i=1}^{N_{stencil}} \omega_{E_i} \frac{\left(\Delta \lambda_{E_i}\right)^n\left(\Delta \sigma_{E_i}\right)^m}{n!\, m!} \psi_{E_i}
\end{aligned} \tag{3.20}$$

By minimizing the functional with respect to each of the derivatives we seek, we land at a system of equations in the form:

$$\begin{cases}
\{\mathbf{A}\}\{\mathbf{\Psi}\}=\{\mathbf{B}\}\left\{\psi_{\mathbf{E}}\right\} \rightarrow\{\mathbf{\Psi}\}=\{\mathbf{A}\}^{-\mathbf{1}}\{\mathbf{B}\}\left\{\psi_{\mathbf{E}}\right\}=\{\mathbf{C}\}\left\{\psi_{\mathbf{E}}\right\} \\
A_{jk}=\sum_{i=1}^{N_{stencil}} \omega_{E_i} \frac{\left(\Delta \lambda_{E_i}\right)^{n_j}\left(\Delta \sigma_{E_i}\right)^{m_j}}{n_j!\, m_j!} \frac{\left(\Delta \lambda_{E_i}\right)^{n_k}\left(\Delta \sigma_{E_i}\right)^{m_k}}{n_k!\, m_k!} \\
\Psi_k=\dfrac{\partial \psi^{n_k+m_k}}{\partial \lambda^{n_k} \partial \sigma^{m_k}}\left(\lambda_F, \sigma_F\right) \\
B_{ji}=\omega_{E_i} \dfrac{\left(\Delta \lambda_{E_i}\right)^{n_j}\left(\Delta \sigma_{E_i}\right)^{m_j}}{n_j!\, m_j!}
\end{cases} \tag{3.21}$$

where ψ_E is a vector containing the values of ψ at each of the chosen stencils. The terms n_j, m_j, n_k and m_k make reference to the particular way in which we order the equations for the various derivative orders; for example, for up to second order:

$$n=\begin{bmatrix} 0 & 1 & 2 & 0 & 1 & 2 & 0 & 1 & 2 \end{bmatrix};$$

$$m=\begin{bmatrix} 0 & 0 & 0 & 1 & 1 & 1 & 2 & 2 & 2 \end{bmatrix}$$

Note that the matrix $\{\mathbf{C}\}$, in the right-hand side of Eq. (3.21), must be at least square, so that the system of equations is not under-determined, but that, in principle, the system may be over-determined if the number of stencil elements is larger than the number of derivatives sought.

The method is equivalent for the derivatives at a certain element center, E_0, when taking into account that the value of any fluid variables is "known" at said center. In this case the following changes apply:

$$\begin{cases}
\{\mathbf{A}\}\{\mathbf{\Psi}\}=\{\mathbf{B}\}\left(\left\{\psi_{\mathbf{E}}\right\}-\psi_{\mathbf{E_0}}\right) \\
\Delta \lambda_{E,i}=\lambda_{E,i}-\lambda_{\mathcal{E}}\ ;\ \Delta \sigma_{E,i}=\sigma_{E,i}-\sigma_{E_0} \\
\Psi_k=\dfrac{\partial \psi^{n_k+m_k}}{\partial \lambda^{n_k} \partial \sigma^{m_k}}\left(\lambda_{\mathcal{E}}, \sigma_{\mathcal{E}}\right)
\end{cases}$$

and the equation for the 0^{th} order derivative is no longer present, which factors into the possible values for n and m, which, again for second order, take the form:

$$n = \begin{bmatrix} 1 & 2 & 0 & 1 & 2 & 0 & 1 & 2 \end{bmatrix};$$

$$m = \begin{bmatrix} 0 & 0 & 1 & 1 & 1 & 2 & 2 & 2 \end{bmatrix}$$

Similarly, the method may be generalized if some derivative is also known, as in the case of the first derivative with λ at the domain axis, which is null due to symmetry.

To showcase the order of WLSQR method, as well as its accuracy in GR, we have chosen to provide results obtained from the MFAM_QUAL_GR sub-utility for three different trial functions and three different meshes. The meshes are generated using the Inverse-rate-of-change approach, with no manual correction, and use the following parameters for contour surface generation:

$$\begin{cases} level1 \rightarrow n_\lambda = 18\,;\; n_\sigma = 20 \sim 360\, elements \\ level2 \rightarrow n_\lambda = 35\,;\; n_\sigma = 40 \sim 1400\, elements \\ level3 \rightarrow n_\lambda = 70\,;\; n_\sigma = 80 \sim 5600\, elements \end{cases}$$

MFAMs *level*1 and *level*3 and are shown in Fig. 3.12, *level*2 is the Inverse-rate-of-change MFAM in Fig. 3.8; the "level" refers to the level of refinement, for the Order Of Accuracy (OOA) analysis (see below). The WLSQR used is based on Inverse-Distance weighting, the Taylor expansion is limited at 1^{st} order derivatives, and the number of stencil elements is fixed at 6 (enough for up to second order gradients).

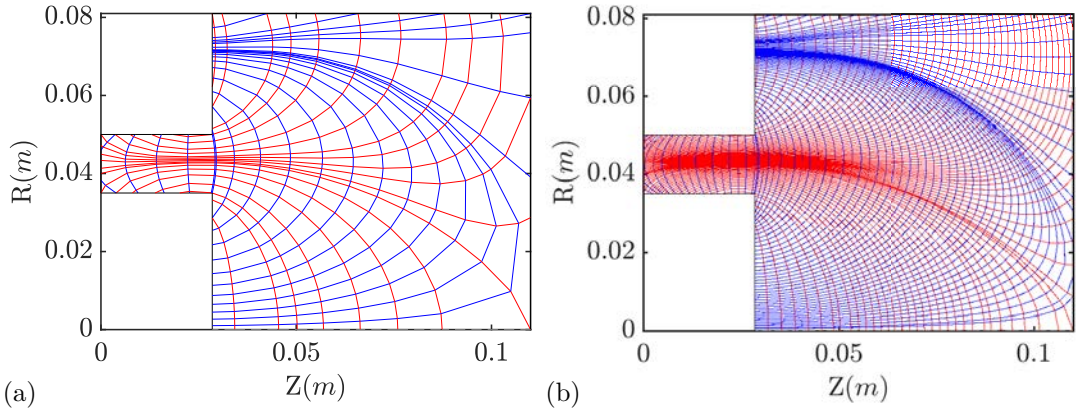

Figure 3.12: Inverse-rate-of-change MFAM with (a) *level*1 refinement $\sim$ 360 elem., (b) *level*3 refinement $\sim$ 5600 elem.

Now, we may compare the analytic derivatives of certain trial functions to the ones obtained using the WLSQR method for GR, particularly for the 1^{st} order derivatives. The proposed trial functions, ψ_1, ψ_2 and ψ_3, are:

$$\begin{aligned} \lambda^* &= \frac{\lambda - \lambda_{min}}{\lambda_{max}} \\ \sigma^* &= \frac{\sigma - \sigma_{min}}{\sigma_{max}} \end{aligned} \rightarrow \begin{cases} \psi_1 = \lambda^* \sigma^* + \lambda + \sigma \\ \psi_2 = (\lambda^*)^2 + (\sigma^*)^2 + \lambda^* + \sigma^* \\ \psi_3 = \sin(2\pi\lambda^*)\cos(2\pi\sigma^*) + \lambda^* + \sigma^* \end{cases}$$

where the linear terms have been included in the trial functions to avoid the possibility of near-zero derivatives, which are problematic from the perspective of relative errors, ϵ, defined as:

$$\epsilon(\psi') = \frac{\left|\psi'_{numerical} - \psi'_{analytical}\right|}{\psi'_{analytical}}$$

where ψ' is the first order derivative of a given trial function with respect to either of the magnetic coordinates.

Figure 3.13 presents the statistics for said errors for each of the trial functions and for the different levels of mesh refinement. Note that the errors include both errors committed on faces and element centers: in constant λ faces only derivatives with λ are calculated, while in constant σ faces only derivatives with σ are calculated; for elements and boundary faces, the worst-case relative error (between derivatives with λ and σ) is shown. We also show the distribution of said errors on the *level*2 MFAM.

These statistics allow us to argue that our ability to reconstruct a given function depends greatly both on the function and on mesh refinement. All trial functions in the *level*2 MFAM present relative errors larger than 1. One possible cause is that the mesh does not provide enough resolution for the 1^{st} order WLSQR method to correctly obtain the function gradients. In the case of ψ_3, for example, only the most refined mesh is capable of producing fractional errors for the 95^{th} percentile. Limitations related to a particular "wavelength" of the trial function are not a specific problem of using non-Cartesian meshes, since a similar issue will arise in a regular structured mesh with low resolution; this error is known as an "aliasing" error. On the other hand, we are utilizing a 1^{st} order Taylor expansion and, thus, some of the errors may be related precisely to the fact that we are neglecting second order terms. A 2^{nd} order Taylor expansion has been avoided here because of numerical issues with the inversion of $\{\mathbf{A}\}$, given by Eq. (3.21), for the *level*3 MFAM. These issues appear due to magnetic coordinates presenting very small values, which produce badly conditioned matrices, and may be avoided by switching to a discretization based on spatial coordinates (see the final comments to this section).

An OOA analysis may be performed, in a similar way to what Sozer [206] presented, although taking into account that the mesh refinement we have performed here does not conserve element centers. For this reason we may obtain a "global" OOA by using qualitative indicators of GR on the MFAM, such as the the 95^{th} percentile value or the L2 norm. For the 3^{rd} and 2^{nd} refinement

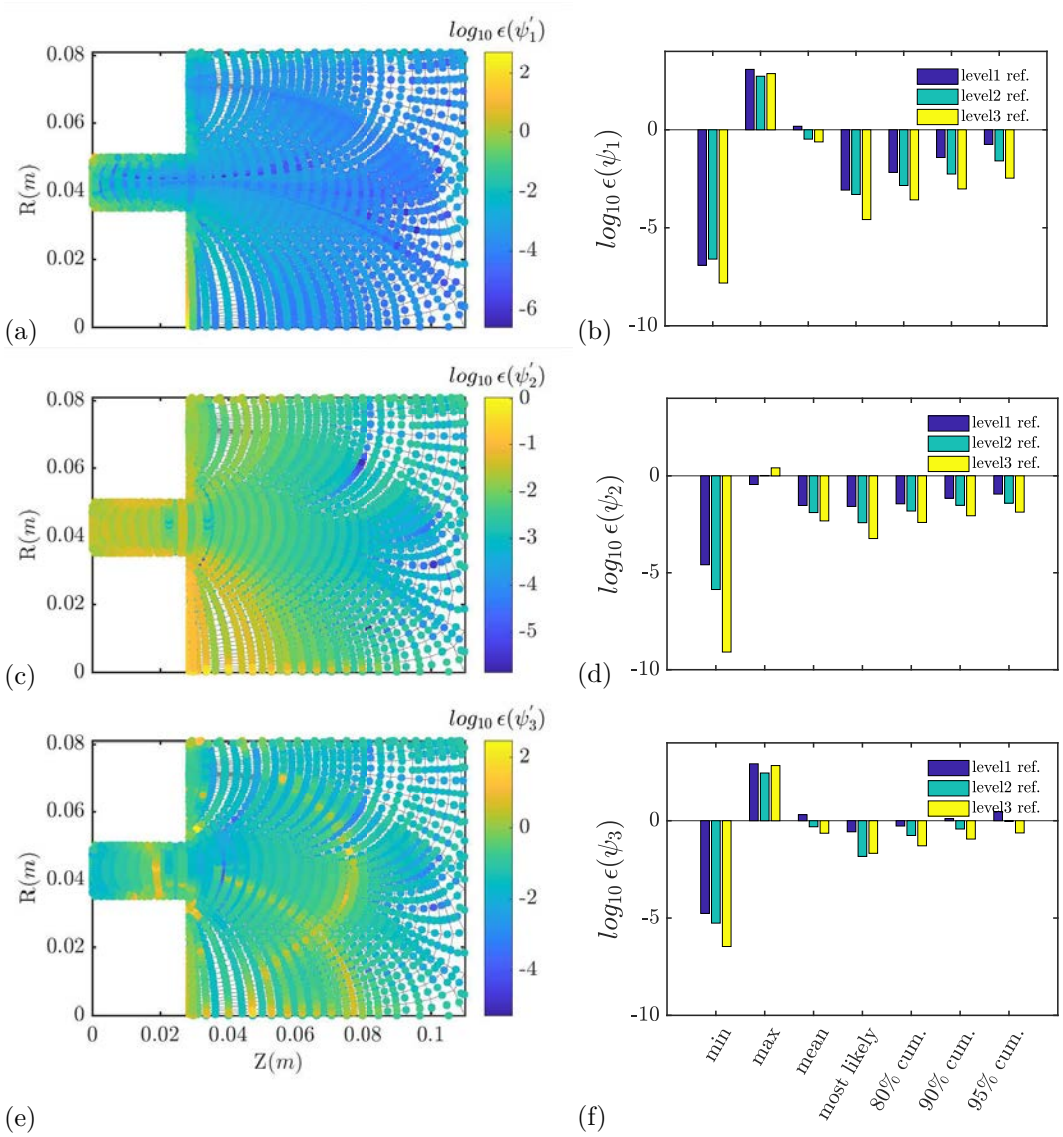

Figure 3.13: Distribution of Gradient Reconstruction relative errors for Inverse-rate-of-change spacing MFAM with *level*2 refinement ~ 1400 and error statistics for different levels of mesh refinement for ψ_1 [(a),(b)], ψ_2 [(c),(d)] and ψ_3 [(e),(f)]. Error statistics are based on minimum, maximum, mean, most probable and cumulative statistics, i.e., the value *under* which a given percentile of elements exist, for 80%, 90% and 95% percentiles; refinement levels are associated to an increasing number of mesh elements: *level*1 ~ 360 elem., *level*2 ~ 1400 elem. and *level*3 ~ 5600 elem.

levels:

$$\begin{aligned}\mathcal{O}^k_{P95}(\psi) &= \frac{\log\left(\mathcal{E}^k_{95}/\mathcal{E}^{k-1}_{95}\right)}{\log 4};\ \mathcal{E}_{95} = P_{95}\left[\epsilon\left(\psi'\right)\right] \\ \mathcal{O}^k_{L2}(\psi) &= \frac{\log\left(\mathcal{E}^k_{L2}/\mathcal{E}^{k-1}_{L2}\right)}{\log 4};\ \mathcal{E}_{L2} = \sqrt{\sum_{i=1}^{N_{elem.}}\left[\epsilon\left(\psi'\right)\right]}\end{aligned} \tag{3.22}$$

where k is the refinement level. The OOA for the trial funcions and MFAMs are shown in Table 3.1.

Trial function	ψ_1	ψ_2	ψ_3
$\mathcal{O}^k_{P95}$	2.34	2.30	2.06
$\mathcal{O}^k_{L2}$	0.71	0.22	0.38

Table 3.1: Global Order Of Accuracy analysis for 95^{th} percentile and L2 norm based error indicators for Gradient Reconstruction

The previous results may be viewed as an optimistic and pessimistic interpretation of the OOA for the WLSQR method, lacking the possibility of showing the OOA for individual elements. It stands for future trials to obtain the evolution of the OOA for further refinement iterations in the mesh. Nonetheless, the literature[206, 208] shows that the method implemented is generally of first or higher order, which provides further confidence in its use.

On a parallel subject, the fact that maximum errors that appear in the GR vary only slightly with mesh resolution indicate that the issue is method-dependent. In particular, large errors appear close to some of the boundaries, which is expected since the derivatives are biased by the fact that the stencils are taken solely from one "side" of the domain boundary. The problem is similar to the one presented by forward or backward centered finite differences schemes, which are widely utilized in the boundaries of structured meshes. Additionally, boundaries are typically regions of "bad" geometric quality, which has a known, although difficult to quantify, effect over the quality of GR. The issue at the boundaries is somewhat downplayed, however, by the fact that gradients at the boundaries are not typically used, since they are replaced by the Boundary Conditions (BCs) (see Section 4.2.3).

As a summary from this section, we may conclude that while GR is both mesh and problem dependent, as mentioned by Diskin[203], the existing literature and our own results point to the WLSQR method as a robust option for a general non-structured mesh such as the MFAM. An analysis of mesh dependency, which, as has been shown, is closely related to the accuracy of GR, is carried out for the electron population model (described in Chapter 4) in Section 6.8.

A few final considerations are worthy of discussion:

- The implementation of other weightings for the WLSQR method have not been found to have significant improvement in error statistics; the inclusion of other mesh-dependent weights, such as the element area, tends to produce larger errors in regions of high smoothness indicator[6], and, thus, is not recommended. A comprehensive parametric analysis on the impact of the various weighting methods and also on the number of recommended stencils is reserved for future studies.

- The use of the curvilinear magnetic coordinates is useful for generating a mesh which reduces numerical discretization. However, since said coordinates are integrated over a discrete mesh which contains the simulation domain, errors can appear in determining their values, both on

[6]Note that the smoothness quality indicator, as defined here, represents lower quality for higher values of the indicator.

the contour lines as well as in different points of interest in the domain, such as element or face centers, if said mesh is not sufficiently refined. Indeed, we have linked problems in coordinate determination to the *resolution* of the magnetic field data provided by FEMM_MASK, or by previous studies (see Section 6.8). These issues carry over into errors committed in GR, which may not be mitigated through the different meshing strategies or GR methods. A possible solution to this problematic is to avoid GR in magnetic coordinates altogether and perform it in the spatial $z-r$ cylindrical coordinates, and then employ the following relation:

$$\nabla_{\top}\psi = \nabla\psi \cdot \vec{1}_{\top} \; ; \; \nabla_{\parallel}\psi = \nabla\psi \cdot \vec{1}_{\parallel}$$

Assuming that the determination of the preferential directions of the problem is consistent, even in low resolution magnetic field data. The implementation of this option into MFAM_QUAL_GR was done by Zhou[164] and tested against the trial functions proposed here; GR errors were significantly lower in these tests, which is promising for a future implementation of this approach into the HYPHEN `CORE`.

3.5 Mesh interpolation

This section briefly describes the mesh interpolation procedures followed in the MESH_INTERP script, which allow us to "translate" the plasma quantities that serve as the interface between the PIC and NOMADS modules (see Chapter 2 for further understanding on the algorithmic flow) between the meshes used in each segment. Note that the PIC mesh and the MFAM are strongly encouraged to share the domain boundaries; while extrapolation based on the WLSQR is possible for positions that fall outside of one of the particular meshes, in case the two do not coincide, this should be avoided.

Interpolation between the meshes is considered point-to-point and various distinct methods have been implemented:

- PIC nodes to MFAM face or element centers: we adapt the WLSQR approach that was trialed for the MFAM in Section 3.4. Each element or face center in the MFAM is sorted within a certain PIC mesh cell; its nodes are then used to construct an inverse-distance WLSQR interpolation, as shown in Fig. 3.14.

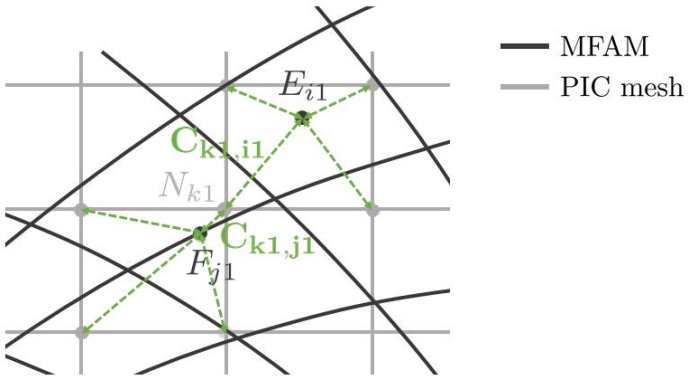

Figure 3.14: Interpolation scheme from PIC mesh nodes to MFAM face and element centers

- MFAM face and element centers to PIC nodes: a Delaunay triangulation[182] is created based on both MFAM element centers and *boundary* face centers, since the plasma quantities are also obtained in the latter through FI, allowing us to triangulate the PIC nodes that are on, or close to, the boundary. This particular arrangement is shown in Fig. 3.15.

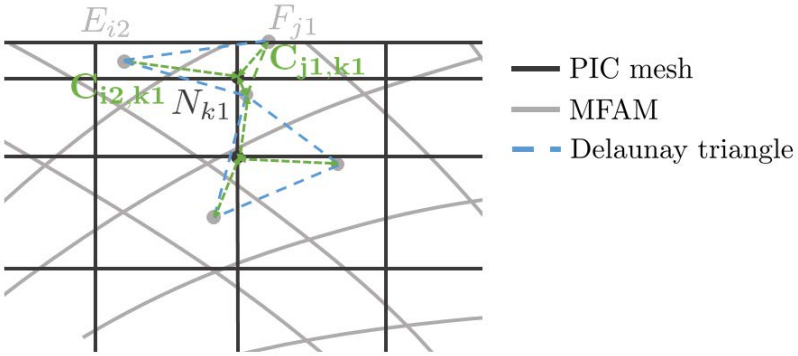

Figure 3.15: Interpolation scheme from MFAM boundary face and element centers to PIC mesh nodes

The Delaunay triangulation ensures that the circumcircle associated with each triangle does not contain any of the other discrete points used for interpolation in its interior; the interpolation itself is linear and based on the *barycentric coordinates* of the particular PIC node within the Delaunay triangle.

- MFAM boundary face centers to PIC boundary nodes and vice versa: an inverse distance weighting[7] interpolation, where the distances are calculated solely along the length of the boundary, as shown in Fig. 3.16.

[7] Also known as Shepard's method[211], where, in this case, we have restricted it to 1D with $p = 1$

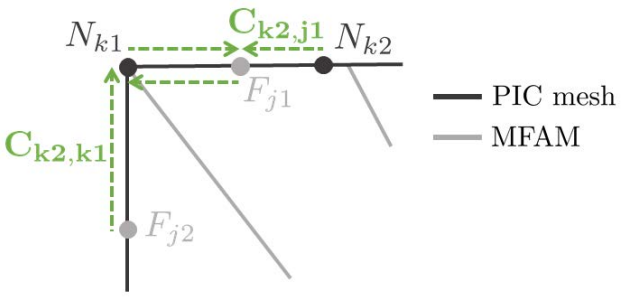

Figure 3.16: Interpolation scheme from MFAM boundary face to PIC mesh boundary nodes and vice versa

Trials similar to the ones shown in Fig. 3.13, and for the same analytical functions, have been performed for accumulated interpolation errors, i.e., the errors committed on the function value when interpolating forth and back between the two meshes. These results, which are not shown here for the sake of brevity, demonstrate that interpolation errors are acceptable and typically very small (less than 1%) for the meshes[8] and functions trialled. It is worth noting that errors are typically larger at the boundaries and, particularly, at the corners of the domain.

[8]The meshes on which consecutive interpolation errors have been obtained are the manually corrected exponential-stretching MFAM shown in Fig. 3.8(c) and the PIC mesh shown in Fig. 6.15

CHAPTER
FOUR

A 2D anisotropic fluid model for the electron population

This chapter presents the main theoretical contribution of this thesis: the macroscopic fluid model for the electron population, and its resolution through the proposed numerical method and spatial (seen in Chapter 3) and temporal discretizations.

4.1 The 12 moment bi-Maxwellian approximation

In this section we present the generalized 2D transport equations for the electron population in weakly collisional plasma discharges in non-uniform, arbitrarily curved magnetic fields, for arbitrary degrees of ionization ratios and rates, in a wide variety of plasma flow conditions. The equations shown here are to be integrated in the NOMADS segment and come as a result of *dismissing* two of the main assumptions made in the electron fluid equations as posed for HallMa and HPHall:

- The description of the electron fluid was quasi-1D: the anisotropicity imposed by magnetic field confinement led to the assumption that the "unbounded" transport of electrons along the magnetic field lines has a thermalizing effect, and thus, magnetic field lines are characterized by a single value of the electron temperature. This assumption allowed to pose the fluid equations as a 1D model, which are solved and then perturbed considering the 2D distribution of plasma density; in particular, this approach obtained the well known *thermalized electric potential*[76, 212].

- The EVDF was assumed to take the form of a Maxwellian description with an isotropic electron temperature, T_e; the assumption was that the anisotropicity of the magnetic confinement over the electron transport equations did not carry over into the distribution function of the electron population.

NOMADS solves a fully 2D-axisymmetric problem instead of the 1D problem initially proposed by Fife[76], which was solved for in the legacy codes HPHall-2 and HallMa. This does not imply, however, that the "isothermal" property of magnetic field lines, typical in HETs, is not recovered in the 2D solution for most of the simulation domain (as will be seen in Chapters 6 and 7). This was demonstrated in simulations of a 6-kW laboratory Hall thruster by Hall2De[125] (which also solves the fully 2D problem), where the 1-D approximation remained valid (as expected) in

the discharge channel, but failed in the near-plume region of the hollow cathode. Furthermore, the approximation of isothermal magnetic lines may also not hold true for regions in which the magnetic confinement is low (e.g., regions far downstream from the thruster, in the vicinity of singular points, etc.).

Additionally, one of the main advantages of discretizing to a 2D MFAM is that it is possible to expand the simulation domain to one that is not only limited to an assortment of magnetic flux "tubes"[1], as in the 1D problem, and may include more complex magnetic topologies (e.g. null magnetic field singular points, magnetically shielded regions, etc.) and extended domain boundaries.

The assumption related to the EVDF is dropped in favor of a more versatile approach, by considering that the anisotropic nature of magnetic confinement establishes preferential directions: those parallel, $\vec{1}_{\parallel}$; and perpendicular, $\vec{1}_{\top}$ and $\vec{1}_{\theta}$, to the magnetic field $\vec{B}$ (what we termed the "magnetic reference system", refer to Fig. 4.1) in both the energy and momentum transport of electrons. This requires two separate electron temperatures, $T_{e\parallel}$ and $T_{e\perp}$, which fit with a bi-Maxwellian distribution description of the electron population. Evidence of anisotropicity (and also of non-Maxwellianity) in the EVDF in HETs exists in the literature[100, 101], which serves as an added rationale for the use of the bi-Maxwellian approximation. Furthermore, we expect that this will allow us to reproduce certain effects present in non-uniform magnetic fields, such as the magnetic mirror effects that may appear in particular configurations (e.g., magnetic nozzles), or, in the future, the anisotropic electron heating that occurs in an ECR discharge[213], for example. Figure 4.1 represents an anisotropic temperature bi-Maxwellian distribution versus an isotropic temperature Maxwellian.

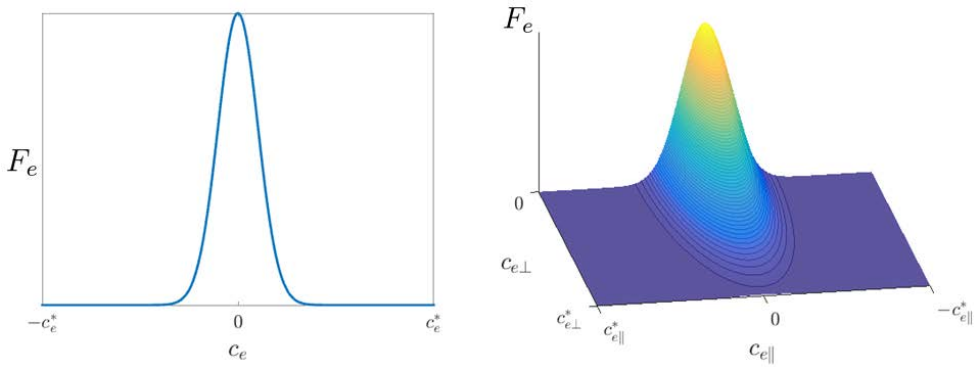

Figure 4.1: Comparison of isotropic mono-Maxwellian and anisotropic bi-Maxwellian EVDF

For the sake of convenience, the equations integrated in NOMADS solve for the *total* macroscopic electron temperature alongside the *parallel* electron temperature. This allows us to either "naturally" obtain the anisotropicity in the system or to assume a relationship between both temperatures, expressed in the form $f\left(T_{e\parallel}, T_e\right) = 0$.

The transport equations are based on the "16 moment approximation" developed by Barakat

[1] In the case of a radial magnetic field, such as in HETs, the volume bounded by two magnetic-flux surfaces can be more correctly described as a "ring".

and Schunk[214] by taking velocity moments of the Boltzmann Equation[113, 215], as presented in Section 1.2.1, for electrons:

$$\frac{\partial F_e}{\partial t} + \vec{v}_e \cdot \nabla F_e + \frac{e}{m_e}\left(\vec{E} + \frac{1}{c}\vec{v}_e \times \vec{B}\right) \cdot \nabla_v F_e = \frac{\delta F_e}{\delta t} \tag{4.1}$$

where $\vec{v}_e$ is the electron particle velocity. As noted in Section 1.2.1, the EVDF, F_e, is such that $F_e\left(\vec{r}, \vec{v}_e, t\right) d\vec{r} d\vec{v}_e$ is the number of electrons in a given instant, t, found in the infinitesimal volume $d\vec{r}$, in the infinitesimal velocity phase space volume $d\vec{v}_e$; $\frac{\delta F_e}{\delta t}$ represents the rate of change of the EVDF in the position-velocity phase space due to collisions.

The following equations[2] present the moments of the Boltzmann Equation up to 12^{th}, order. The corresponding terms for plasma production (ionization) processes, which were absent from the original 16 moment approximation, have been added following the model developed by Bittencourt[215], which is, by nature, compatible with the one by Barakat and Schunk. In addition, the viscous stress tensor for the electron population, $\bar{\bar{\tau}}_e$, is neglected, which is a characteristic assumption of low collisionality plasmas and has been utilized in previous codes under the justification provided by Ramos[216]. Therefore the electron pressure tensor, $\bar{\bar{P}}_e$, is solely diagonal and $\bar{\bar{\tau}}_e = \bar{\bar{0}}$.

Mass continuity equation:

$$\frac{\partial n_e}{\partial t} + \nabla \cdot \left(n_e \vec{u}_e\right) = S_e \tag{4.2}$$

Momentum equation:

$$n_e m_e \frac{D\vec{u}_e}{Dt} + \nabla_\perp p_{e\perp} + \nabla_\parallel p_{e\parallel} + \left(p_{e\parallel} - p_{e\perp}\right) \nabla \cdot \left(\vec{1}_\parallel \vec{1}_\parallel\right) = -e n_e \left(\vec{E} + \vec{u}_e \times \vec{B}\right) + \frac{\delta \vec{M}_e}{\delta t} - S_e m_e \vec{u}_e \tag{4.3}$$

Parallel internal energy equation:

$$\begin{aligned} &\frac{\partial p_{e\parallel}}{\partial t} + \nabla \cdot \left(p_{e\parallel} \vec{u}_e\right) + 2 p_{e\parallel} \nabla_\parallel \cdot \vec{u}_e + \nabla \cdot \vec{q}_e^{\parallel} - \bar{\bar{\bar{Q}}}_e \dddot{:} \nabla \left(\vec{1}_\parallel \vec{1}_\parallel\right) = \\ &= \frac{\delta E_{e\parallel}}{\delta t} - 2\left(u_{e\parallel} \frac{\delta \vec{M}_e}{\delta t} \cdot \vec{1}_\parallel\right) + u_{e\parallel}^2 S_e m_e \end{aligned} \tag{4.4}$$

Perpendicular internal energy equation:

$$\begin{aligned} &\frac{\partial p_{e\perp}}{\partial t} + \nabla \cdot \left(p_{e\perp} \vec{u}_e\right) + p_{e\perp} \nabla_\perp \cdot \vec{u}_e + \nabla \cdot \vec{q}_e^{\perp} + \frac{1}{2} \bar{\bar{\bar{Q}}}_e \dddot{:} \nabla \left(\vec{1}_\parallel \vec{1}_\parallel\right) = \\ &= \frac{\delta E_{e\perp}}{\delta t} - \left(u_{e,\top} \frac{\delta \vec{M}_e}{\delta t} \cdot \vec{1}_\top + u_{e,\theta} \frac{\delta \vec{M}_e}{\delta t} \cdot \vec{1}_\theta\right) + \frac{1}{2}\left(u_{e\top}^2 + u_{e\theta}^2\right) S_e m_e \end{aligned} \tag{4.5}$$

Parallel heat-flow equation:

$$\begin{aligned} &\frac{\partial \vec{q}_{e\parallel}}{\partial t} + \left(\vec{u}_e \cdot \nabla\right) \vec{q}_{e\parallel} + 2\left[\bar{\bar{\bar{Q}}}_e \cdot \nabla \vec{u}_e\right] : \left(\vec{1}_\parallel \vec{1}_\parallel\right) + \vec{q}_{e\parallel} \nabla \cdot \vec{u}_e + \vec{q}_{e\parallel} \cdot \nabla \vec{u}_e + \nabla \cdot \bar{\bar{\mu}}_{e\parallel} + \\ &+ \left[\frac{D\vec{u}_e}{Dt} + \frac{e}{m_e}\left(\vec{E} + \vec{u}_e \times \vec{B}\right)\right] \cdot \left[p_{e\parallel} \bar{\bar{I}} + 2\left(\vec{1}_\parallel \vec{1}_\parallel\right) \cdot \left(p_{e\parallel} \bar{\bar{I}}\right)\right] + \\ &+ \Omega_e \left(\vec{q}_{e\parallel} \times \vec{1}_\parallel\right) - \bar{\bar{\bar{Q}}}_e : \left[\left(\vec{u}_e \cdot \nabla\right)\left(\vec{1}_\parallel \vec{1}_\parallel\right)\right] - \bar{\bar{\bar{R}}}_e \dddot{:} \nabla \left(\vec{1}_\parallel \vec{1}_\parallel\right) = \frac{\delta \vec{H}_{e\parallel}}{\delta t} \end{aligned} \tag{4.6}$$

[2]The notation for the operators in these equations is detailed in Section 3.2.

Perpendicular heat-flow equation:

$$\begin{aligned}&\frac{\partial \vec{q}_{e\perp}}{\partial t}+\left(\vec{u}_e\cdot\nabla\right)\vec{q}_{e\perp}+\left[\dddot{\bar{Q}}_e\cdot\nabla\vec{u}_e\right]:\left(\bar{\bar{I}}-\vec{1}_\parallel\vec{1}_\parallel\right)+\vec{q}_{e\perp}\nabla\cdot\vec{u}_e+\vec{q}_{e\perp}\cdot\nabla\vec{u}_e+\frac{1}{2}\nabla\cdot\bar{\bar{\mu}}_{e\perp}+\\&+\left[\tfrac{D\vec{u}_e}{Dt}+\tfrac{e}{m_e}\left(\vec{E}+\vec{u}_e\times\vec{B}\right)\right]\cdot\left[p_{e\perp}\bar{\bar{I}}+\left(\bar{\bar{I}}-\vec{1}_\parallel\vec{1}_\parallel\right)\cdot\left(p_{e\perp}\bar{\bar{I}}\right)\right]+\\&+\Omega_e\left(\vec{q}_{e\perp}\times\vec{1}_\parallel\right)+\frac{1}{2}\dddot{\bar{Q}}_e:\left[\left(\vec{u}_e\cdot\nabla\right)\left(\vec{1}_\parallel\vec{1}_\parallel\right)\right]+\frac{1}{2}\dddot{\bar{R}}_e\dot{:}\nabla\left(\vec{1}_\parallel\vec{1}_\parallel\right)=\frac{\delta\vec{H}_{e\perp}}{\delta t}\end{aligned}\tag{4.7}$$

In the previous equations, n_e is the electron particle density, $\vec{u}_e$ is the electron drift velocity, $p_{e\parallel}$ and $p_{e\perp}$ are the parallel and perpendicular electron pressures, $\vec{E}$ is the electric field, which can be described, for the irrotational case, through the plasma potential as $\vec{E}=-\nabla\phi$. The term $\frac{\delta\vec{M}_e}{\delta t}$ is the rate of change of the electron momentum due to collisional processes, $\vec{q}_{e\parallel}$ and $\vec{q}_{e\perp}$ are the heat-flows for parallel and perpendicular energies, $\frac{\delta E_{e\parallel}}{\delta t}$ and $\frac{\delta E_{e\perp}}{\delta t}$ are the rates of change of the electron parallel and perpendicular energies due to collisional processes, $\dddot{\bar{Q}}_e$ is the third order heat-flow tensor, $\dddot{\bar{R}}_e$ is the 4^{th} order pressure tensor, $\frac{\delta\vec{H}_{e\parallel}}{\delta t}$ and $\frac{\delta\vec{H}_{e\perp}}{\delta t}$ are the rates of change of the heat-flows for electron parallel and perpendicular energies due to collisional processes, Ω_e is the electron cyclotron frequency and $\bar{\bar{I}}$ is the identity tensor. Finally, S_e is the plasma production contribution, in terms of electron density.

The following relations are observed amongst the different moments:

$$\begin{aligned}&p_{e\parallel}=\bar{\bar{P}}_e:\left(\vec{1}_\parallel\vec{1}_\parallel\right)\ ;\ p_{e\perp}=\frac{1}{2}\bar{\bar{P}}_e:\left(\bar{\bar{I}}-\vec{1}_\parallel\vec{1}_\parallel\right)\\&\vec{q}_{e\parallel}=\dddot{\bar{Q}}_e:\left(\vec{1}_\parallel\vec{1}_\parallel\right)\ ;\ \vec{q}_{e\perp}=\frac{1}{2}\dddot{\bar{Q}}_e:\left(\bar{\bar{I}}-\vec{1}_\parallel\vec{1}_\parallel\right)\\&\bar{\bar{\mu}}_{e\parallel}=\dddot{\bar{R}}_e:\left(\vec{1}_\parallel\vec{1}_\parallel\right)\ ;\ \bar{\bar{\mu}}_{e\perp}=\dddot{\bar{R}}_e:\left(\bar{\bar{I}}-\vec{1}_\parallel\vec{1}_\parallel\right)\end{aligned}\tag{4.8}$$

where $\bar{\bar{P}}_e$ is the electron pressure tensor and $\bar{\bar{\mu}}_{\parallel e}$ and $\bar{\bar{\mu}}_{\perp e}$ are the second order viscous stress tensors associated to parallel and perpendicular energy.

The general state equation for ideal gases is also applicable in this context:

$$T_{e\parallel}=\frac{p_{e\parallel}}{n_e k_B}\ ;\ T_{e\perp}=\frac{p_{e\perp}}{n_e k_B}\tag{4.9}$$

where $T_{e\parallel}$ and $T_{e\perp}$ are the parallel and perpendicular electron temperatures. Finally, some additional considerations for the equations given here are:

- As was mentioned in Chapter 3, the magnetic field is considered static (stationary, solenoidal, and irrotational) within the simulation domain, and, since the presence of electromagnetic waves carried by the plasma is beyond the scope of this thesis, we are spared from solving Maxwell's equations.

- The parallel and perpendicular fluid moments are related to the *total* macroscopic moments

as follows:

$$\begin{aligned} T_e &= \frac{T_{e\parallel} + 2T_{e\perp}}{3} \\ p_e &= \frac{p_{e\parallel} + 2p_{e\perp}}{3} \rightarrow \bar{\bar{P}}_e = \frac{\left(3p_e - p_{e\parallel}\right)}{2}\left[\bar{\bar{I}} - \left(\vec{1}_\parallel \vec{1}_\parallel\right)\right] + p_{e\parallel}\left(\vec{1}_\parallel \vec{1}_\parallel\right) \end{aligned} \tag{4.10}$$

This leads to a "summation law" for the energy and heat-flow equations in order to obtain the Thermal Energy Density[3], $\frac{3p_e}{2}$, and the total heat-flow equation:

$$\begin{aligned} &\text{Thermal Energy Density Eq.} = \frac{1}{2}(\text{Eq. (4.4)} + 2 \cdot \text{Eq. (4.5)}) \\ &\text{Total Heat-Flow Eq.} = \frac{1}{2}(\text{Eq. (4.6)} + 2 \cdot \text{Eq. (4.7)}) \end{aligned} \tag{4.11}$$

Which, in addition, implies that the heat flow terms in the respective energy equations satisfy:

$$\vec{q}_e = \frac{1}{2}\left(\vec{q}_{e\parallel} + 2\vec{q}_{e\perp}\right) \tag{4.12}$$

where $\vec{q}_e$ is the total electron heat-flow.

- The plasma production term is obtained through the following equation:

$$S_e = n_e\left(\nu_{ioniz} - \nu_{recomb}\right) \tag{4.13}$$

where the ionization and recombination frequencies are obtained using the ancillary collisional model detailed in Section 5.2. The terms associated to the plasma production contribution, $S_e m_e \vec{u}_e$, $u_{e\parallel}^2 S_e m_e$ and $1/2\left(u_{e\top}^2 + u_{e\theta}^2\right) S_e m_e$, appear naturally in the equations when $S_e \neq 0$. Particularly, the last two terms, which appear in Eqs. (4.4), and (4.5)) have been introduced by splitting the corresponding term in the thermal energy density conservation equation, as given by Bittencourt[215]. The splitting has been done according to Eq. (4.11):

$$\frac{1}{2}u_e^2 S_e m_e \rightarrow \begin{cases} \text{Parallel Internal Energy Eq.: } u_{e\parallel}^2 S_e m_e \\ \text{Perpendicular Internal Energy Eq.: } \dfrac{1}{2}\left(u_{e\top}^2 + u_{e\theta}^2\right) S_e m_e \end{cases} \tag{4.14}$$

The terms $2\left(\vec{u}_{e,\parallel} \cdot \frac{\delta \vec{M}_e}{\delta t} \cdot \vec{1}_\parallel\right)$ and $\left(\vec{u}_{e,\perp} \cdot \frac{\delta \vec{M}_e}{\delta t} \cdot \vec{1}_\perp\right)$ are obtained analogously to the previous two terms.

- The terms $\frac{\delta E_{e\parallel}}{\delta t} - 2\left(\vec{u}_{e,\parallel} \cdot \frac{\delta \vec{M}_e}{\delta t} \cdot \vec{1}_\parallel\right)$ and $\frac{\delta E_{e\perp}}{\delta t} - \left(\vec{u}_{e,\perp} \cdot \frac{\delta \vec{M}_e}{\delta t} \cdot \vec{1}_\perp\right)$ are given by Barakat and Schunk[214] for various collisional interaction models and the collisionless limit[4]; energy

[3] The thermal energy density is a convenient way of expressing the evolution of the thermal energy in the system, as it may be demonstrated that $\frac{3p_e}{2} = \frac{1}{2}\rho_e\left\langle c_e^2 \right\rangle$.

[4] It is reasonable to question the collisional regime for the electron population, particularly in the direction parallel to the magnetic field, since electrons are unbounded in said direction. This may be of importance for certain magnetic topologies, such as magnetic nozzles and is a topic for future study.

expenditure due to inelastic collisions (which accounts for plasma production and excitation losses) must be added to the model given there. The $\frac{\delta \vec{H}_{e\parallel}}{\delta t}$ and $\frac{\delta \vec{H}_{e\perp}}{\delta t}$ terms are also provided through complex expression, but, for the sake of simplicity, we will model these terms through the Krook relaxation model, or Fourier model (see Section 4.1.4), which has been widely used in legacy codes.

- The momentum equation may be introduced into the parallel and perpendicular Heat flow equations by substituting:

$$\frac{D\vec{u}_e}{Dt} + \frac{e}{m_e}\left(\vec{E} + \vec{u}_e \times \vec{B}\right) = \frac{-1}{n_e m_e}\left(\nabla_\perp p_{e\perp} + \nabla_\parallel p_{e\parallel} + \left(p_{e\parallel} - p_{e\perp}\right)\nabla \cdot \left(\vec{1}_\parallel \vec{1}_\parallel\right) - \frac{\delta \vec{M}_e}{\delta t} + S_e m_e \vec{u}_e\right) \tag{4.15}$$

4.1.1 Model closure and preliminary dimensional analysis

At this point it is necessary to introduce additional assumptions to continue posing the model: the plasma is considered *quasineutral* in the temporal and spatial scales resolved in the simulation: this assumption was briefly discussed in Section 2.2 as a means to link the PIC and fluid segments and allows us to obtain the electron density for a given simulation time as:

$$n_e = \sum_{Z=1}^{2,3,\ldots} Z n_{iZ} \tag{4.16}$$

The assumption is justified since the time-scales at which violation of quasi-neutrality occur (for the plasma frequency and above) are much smaller than any of the other time scales in our problem. Furthermore, the Debye length, λ_D, is much smaller than the spatial scales being resolved by the problem within typical simulation domains[5]; for these we effectively consider that $\lambda_D \approx 0$. Boundary layers in which quasineutrality does not hold, such as plasma sheaths (see Section 4.2.3 and 5.1) are treated externally to simulation domain as infinitely thin layers, meaning that our simulation domains only reach the edge of these boundary layers.

The transport equations presented above do not constitute a closed set due to the fact that in the Boltzmann equation moments, the expression governing a moment of order l contains the moment order $l+1$, as may be appreciated in the set of equations presented. The model is closed by assuming that the EVDF takes the shape of a perturbed two-temperature bi-Maxwellian. The Maxwellian assumption is, in principle, only valid for highly collisional regimes under equilibrium[89] and, in this case, includes the anisotropicity caused by the magnetic field. The perturbation is done over the bi-Maxwellian distribution function in a way which leads to the highest order moments in the equations being expressed as functions of lower order moments. The EVDF takes

[5]Certain low density regions coupled with very small mesh elements might lead to element sizes of the order of the Debye length; in principle, said regions would not necessarily satisfy the quasi-neutrality assumption, although, for lack of a better model, they are resolved as such. Future efforts might be devoted to exploring a different model for these particular elements.

the form $F_e = F_e^{(0)}(1+\Phi_e)$, where:

$$\begin{cases} F_e^{(0)} = \dfrac{n_e}{(2\pi)^{3/2}}\left(\dfrac{m_e}{k_B T_{e\parallel}}\right)^{1/2}\dfrac{m_e}{k_B T_{e\perp}}\exp\left(-\dfrac{1}{2}\dfrac{m_e}{k_B T_{e\perp}}c_{e\perp}^2 - \dfrac{1}{2}\dfrac{m_e}{k_B T_{e\parallel}}c_{e\parallel}^2\right) \\ \Phi_e = f\left(\dfrac{m_e}{k_B T_{e\perp}}, \dfrac{m_e}{k_B T_{e\parallel}}, \bar{\bar{\tau}}_e, \vec{q}_{e\perp}, \vec{q}_{e\parallel}, \vec{c}_e\right) \end{cases} \tag{4.17}$$

where the base bi-Maxwellian is given in terms of the perpendicular and parallel thermal velocities for the electrons, $c_{e\perp}$ and $c_{e\parallel}$; the total thermal velocity is $\vec{c}_e = \vec{v}_e - \vec{u}_e$. Barakat and Schunk[214] proposed a function for Φ_e that leads to the following expressions for the higher order moments:

$$\begin{aligned} \dddot{\bar{\bar{Q}}}_e &= 2\left[\vec{q}_{e\parallel}\vec{1}_\parallel : \nabla\vec{1}_\parallel + \left(\vec{q}_{e\perp}\cdot\vec{1}_\parallel\right)\left(\nabla\cdot\vec{1}_\parallel\right)\right] \\ \nabla\cdot\bar{\bar{\mu}}_e^{\parallel} &= \nabla_\perp\left(\frac{p_{e\parallel}p_{e\perp}}{n_e m_e}\right) + 3\nabla_\parallel\left(\frac{p_{e\parallel}^2}{n_e m_e}\right) + \frac{p_{e\parallel}\left(3p_{e\parallel}-p_{e\perp}\right)}{n_e m_e}\nabla\cdot\left(\vec{1}_\parallel\vec{1}_\parallel\right) \\ \nabla\cdot\bar{\bar{\mu}}_e^{\perp} &= 4\nabla_\perp\left(\frac{p_{e\perp}^2}{n_e m_e}\right) + 2\nabla_\parallel\left(\frac{p_{e\parallel}p_{e\perp}}{n_e m_e}\right) + \frac{2p_{e\perp}\left(p_{e\parallel}-2p_{e\perp}\right)}{n_e m_e}\nabla\cdot\left(\vec{1}_\parallel\vec{1}_\parallel\right) \\ \dddot{\bar{\bar{R}}}_e &= \frac{2}{n_e m_e}\left[\bar{\bar{P}}_e : \left(\nabla\vec{1}_\parallel\right)\vec{1}_\parallel\cdot\bar{\bar{P}}_e + \bar{\bar{P}}_e\cdot\left(\nabla\vec{1}_\parallel\right)\vec{1}_\parallel : \bar{\bar{P}}_e + \bar{\bar{P}}_e : \vec{1}_\parallel\left(\nabla\vec{1}_\parallel\right)\cdot\bar{\bar{P}}_e\right] \end{aligned}$$

The relevant terms in Eqs. (4.4), (4.5), (4.6) and (4.7) become:

$$\begin{aligned} \dddot{\bar{\bar{Q}}}_e &= 2\left[q_{e\parallel\top}r\frac{\partial B}{\partial\lambda} - q_{e\perp\parallel}\frac{\partial B}{\partial\sigma}\right] \\ \left.\begin{aligned} \bar{\bar{P}}_e : \left(\nabla\vec{1}_\parallel\right)\vec{1}_\parallel\cdot\bar{\bar{P}}_e &= \left(\bar{\bar{P}}_e : \nabla\vec{1}_\parallel\right)\left(\vec{1}_\parallel\cdot\bar{\bar{P}}_e\right) = \left(rB^2\frac{\partial\left((rB)^{-1}\right)}{\partial\sigma} + B\frac{\partial\ln r}{\partial\sigma}\right)p_{e\perp}p_{e\parallel}\vec{1}_\parallel \\ \bar{\bar{P}}_e\cdot\left(\nabla\vec{1}_\parallel\right)\vec{1}_\parallel : \bar{\bar{P}}_e &= \left(\bar{\bar{P}}_e\cdot\nabla\vec{1}_\parallel\right)\left(\vec{1}_\parallel : \bar{\bar{P}}_e\right) = \vec{0} \\ \bar{\bar{P}}_e : \vec{1}_\parallel\left(\nabla\vec{1}_\parallel\right)\cdot\bar{\bar{P}}_e &= \left(\bar{\bar{P}}_e : \vec{1}_\parallel\right)\left(\nabla\vec{1}_\parallel\cdot\bar{\bar{P}}_e\right) = p_{e\perp}p_{e\parallel}r\frac{\partial B}{\partial\lambda}\vec{1}_\top \end{aligned}\right\}\rightarrow \\ \rightarrow \dddot{\bar{\bar{R}}}_e &= \frac{2p_{e\perp}p_{e\parallel}}{n_e m_e}\left(r\frac{\partial B}{\partial\lambda}\vec{1}_\top + \left(rB^2\frac{\partial\left((rB)^{-1}\right)}{\partial\sigma} + \frac{\partial\ln r}{\partial\sigma}\right)\vec{1}_\parallel\right) \end{aligned}$$

by using the rules for products of dyadics and vectors and the definition of the double product.

Once the model is given by a closed set of equations, we may introduce dimensional analysis in order to simplify the equations for the conditions expected in electromagnetic plasma thrusters, particularly in HETs. The main assumption here is that, for the electron population, the kinetic energy associated to the drift velocity is much smaller than the thermal energy, that is:

$$\frac{m_e\left|\vec{u}_e\right|^2}{k_B T_e} \ll 1 \tag{4.18}$$

This relation is generally justified: since $\vec{u}_e$ is the average of individual particle velocity vectors over the PDF, f_e, as shown in Eq. (1.15):

$$\vec{u}_e = \langle \vec{v}_e \rangle = \int_{V_{\vec{v}}} \vec{v} f_e \left(\vec{r}, \vec{v}, t \right) d\vec{v} \tag{4.19}$$

When the average is done over the entire distribution function, many individual components will cancel out, until only the drift or bulk velocity remains. On the other hand, T_e represents an average over the modulus of thermal velocity vectors:

$$T_e = \frac{m_e}{k_B} \langle c_e^2 \rangle \tag{4.20}$$

Because no terms cancel out when averaging the modulus of thermal velocity, the thermal energy is typically much higher than the drift kinetic energy. We also assume that this relation is valid for individual components of the macroscopic temperature, in particular, for $T_{e\|}$:

$$O\left(T_{e\|}\right) \sim O\left(T_e\right) \; ; \; \frac{m_e \left|\vec{u}_e\right|^2}{k_B T_{e\|}} \ll 1$$

In some cases however, regions characterized by high magnetic and electric fields, such as the channel exit in HETs, might present an $\vec{E} \times \vec{B}$ drift velocity which is comparable to the thermal velocity of electrons. Said regions have been characterized by various authors[126, 217, 218], demonstrating that the assumption on the drift velocity versus the thermal velocity of electrons, Eq. (4.18), may not hold true. Dropping said assumption would require a change in the resolution of the problem as presented in this chapter, particularly in what refers to the dimensional analysis for the momentum equation in the azimuthal direction, and is outside of the scope of this thesis.

The thermal-to-drift-velocity assumption allows us to obtain the following relations for each of the equations in the model:

- Momentum equation: we may neglect the convective and non-stationary terms in the momentum equation with respect to the pressure terms. This implies that the momentum equation is no longer time-dependent and becomes a "state equation", which must be satisfied at each time in the system's evolution. Considering the relations in Eq.(4.9) and following:

$$\left.\begin{aligned} n_e m_e \frac{D\vec{u}_e}{Dt} = n_e m_e \left(\frac{\partial \vec{u}_e}{\partial t} + \left(\vec{u}_e \cdot \nabla\right) \vec{u}_e \right) \sim \frac{n m_e u^2}{L} \\ \nabla_\perp p_{e\perp}, \; \nabla_\| p_{e\|}, \; \left(p_{e\|} - p_{e\perp}\right) \nabla \cdot \left(\vec{1}_\| \vec{1}_\|\right) \sim \frac{n k_B \mathcal{T}}{L} \end{aligned}\right\} \rightarrow \frac{n m_e u^2 / L}{n k_B \mathcal{T} / L} = \frac{m_e u^2}{k \mathcal{T}} \ll 1 \tag{4.21}$$

  where n, u and $\mathcal{T}$ are, respectively, characteristic electron densities, drift velocities and temperature for the plasma discharge, and L is a characteristic length in the simulation domain. Further discussion is made in Section 4.1.2.

- Energy equations: no terms are dismissed from the energy equation through dimensional analysis; however, we may derive the order of the heat flow terms by comparison with the convective pressure terms. Given the relations expressed by Eq. (4.9) and (4.8) and taking the parallel energy equation as an example (the results are analogous for the perpendicular energy equation):

$$\left.\begin{array}{r} \nabla\cdot\vec{q}_{e\parallel},\ \bar{\bar{Q}}_e\vdots\nabla\left(\vec{1}_\parallel\vec{1}_\parallel\right)\sim\dfrac{q}{L} \\ \dfrac{\partial p_{e\parallel}}{\partial t}+\nabla\cdot\left(p_{e\parallel}\vec{u}_e\right),\ \nabla\cdot\left(p_{e\parallel}\vec{u}_e\right),\ p_{e\parallel}\nabla_\parallel\cdot\vec{u}_e\sim\dfrac{nk\mathcal{T}u}{L} \end{array}\right\}\rightarrow q\sim nk\mathcal{T}u \tag{4.22}$$

  where q is a characteristic electron heat-flow in the plasma discharge. Further discussion is made in Section 4.1.3.

- Heat-flow equations: all convective and non-stationary terms may be neglected from the heat flow equations in comparison to the "pressure product" term, considering the relations given by Eq. (4.22), (4.15) and (4.9), for the parallel heat-flow equation (the results are analogous for the perpendicular heat-flow equation), we have:

$$\left.\begin{array}{l} \left[\dfrac{D\vec{u}_e}{Dt}+\dfrac{e}{m_e}\left(\vec{E}+\vec{u}_e\times\vec{B}\right)\right]\cdot\left[p_{e\parallel}\bar{\bar{I}}+2\left(\vec{1}_\parallel\vec{1}_\parallel\right)\cdot\left(p_{e\parallel}\bar{\bar{I}}\right)\right]\sim\dfrac{n^2k^2\mathcal{T}^2}{nm_eL} \\ \dfrac{\partial\vec{q}_{e\parallel}}{\partial t}+\left(\vec{u}_e\cdot\nabla\right)\vec{q}_{e\parallel},\ \left(\bar{\bar{Q}}_e\cdot\nabla\vec{u}_e\right):\left(\vec{1}_\parallel\vec{1}_\parallel\right),\ \vec{q}_{e\parallel}\nabla\cdot\vec{u}_e,\ \vec{q}_{e\parallel}\cdot\nabla\vec{u}_e,\ \bar{\bar{Q}}_e:\left[\left(\vec{u}_e\cdot\nabla\right)\left(\vec{1}_\parallel\vec{1}_\parallel\right)\right]\sim\dfrac{qu}{L}\sim\dfrac{nk\mathcal{T}u^2}{L} \end{array}\right\}\rightarrow\frac{{}^{nk\mathcal{T}u^2}/_{L}}{{}^{n^2k^2\mathcal{T}^2}/_{nm_eL}}=\frac{m_eu^2}{k\mathcal{T}}\ll1 \tag{4.23}$$

  Further discussion is made in Section 4.1.4.

4.1.2 Discussion for the mass continuity and electron momentum equations

The mass conservation and momentum equations require some further analysis, as some additional arguments are required to complete the model. First, under quasineutrality, we may pose the equation in terms of *current densities*:

$$\vec{j}_e=-en_e\vec{u}_e\ ;\ \vec{j}_{iZ}=Zen_{iZ}\vec{u}_{iZ}\ ;\ \vec{j}_i=\sum_{Z=1}^{2,3,\ldots}Zen_{iZ}\vec{u}_{iZ} \tag{4.24}$$

Equation (4.2) may then be replaced by the current continuity equation, which will be more useful from the perspective of the numerical resolution of the problem (see Section 4.2):

Current continuity equation:

$$\nabla\cdot(\vec{j}_e+\vec{j}_i)=I_d \tag{4.25}$$

where the plasma source term is taken into account in the respective current densities and we include an additional term, the discharge current, I_d, which represents an external current being injected into the domain, like the one provided by a hollow cathode in HETs (see Fig. 1.5).

Now, considering the relations in Eqs. (4.21) and (3.13), and that the electric field in the discharge may be expressed in terms of the electric potential, the resulting momentum equation, in terms of current density, is:

$$\begin{aligned} &rB\frac{\partial p_{e\perp}}{\partial \lambda}\vec{1}_{\top} + \frac{1}{r}\frac{\partial p_{e\theta}}{\partial \theta}\vec{1}_{\theta} + B\frac{\partial p_{e\parallel}}{\partial \sigma}\vec{1}_{\parallel} + (p_{e\parallel} - p_{e\perp})\left(r\frac{\partial B}{\partial \lambda}\vec{1}_{\top} - \frac{\partial B}{\partial \sigma}\vec{1}_{\parallel}\right) = \\ &= en_e\nabla\phi + \vec{j}_e \times \vec{B} + \frac{\delta \vec{M}_e}{\delta t} + \frac{S_e m_e}{en_e}\vec{j}_e \end{aligned} \tag{4.26}$$

which is a "state" equation, in the sense that it only depends implicitly with time, through the electron pressures and densities. The term associated to the plasma production contribution, S_e, represents a sort of "thermalization" term by which bulk of the electron fluid transfers part of its momentum towards newly formed electrons so that they may attain the bulk velocity. The collisional term, $\dfrac{\delta \vec{M}_e}{\delta t}$, models the effects over electron momentum due to collisional events. In Maxwell type molecule interactions (used both by Barakat and Schunk[214] and Bittencourt[215]) these events are defined through collision frequencies without the necessity of assuming specific forms for the VDFs of the different colliding species:

$$\frac{\delta \vec{M}_e}{\delta t} = \sum_{\alpha} m_e n_e \nu_{e\alpha}(\vec{u}_\alpha - \vec{u}_e) \tag{4.27}$$

where α represents the "heavy species" in the plasma, which includes neutrals and ions of various degrees of ionization (typically up to doubly charged) and, potentially, of different atomic elements. The collision frequencies $\nu_{e\alpha}$ take into account both inelastic and elastic collisions, which represent a sort of "drag" term for electrons, reducing the momentum of the electron bulk. Inelastic collisions that are *non-ionizing* and *non-excitation* collisions are disregarded since typical propellants are neither molecules nor diatomic elements, where collisional energy may be spent in breaking chemical bonds or inducing molecular vibration; on the other hand, momentum transfer in ionizing/excitation collisions can be neglected, since the only interacting particles are electrons, which are much less massive than ions. Thus, when considering Maxwell molecule interactions in relation to momentum transfer, we take:

$$\nu_{e\alpha} \approx \nu_{e\alpha_{elastic}} \tag{4.28}$$

Grouping the collision term together with the plasma production term given by Eq. (4.13), we have:

$$\frac{\delta \vec{M}_e^{'}}{\delta t} = \frac{\delta \vec{M}_e}{\delta t} - S_e m_e \vec{u}_e = \sum_{\alpha} m_e n_e \nu_{e\alpha}(\vec{u}_\alpha - \vec{u}_e) - n_e(\nu_{ioniz} - \nu_{recomb}) m_e \vec{u}_e \tag{4.29}$$

A typical assumption is that the velocity of neutrals is negligible in comparison to the electron velocity since neutrals are massive and generally slow throughout the discharge[6]; thus, taking into account that $(\vec{u}_n - \vec{u}_e) \approx -\vec{u}_e$, the previous expression takes the form:

$$\begin{aligned}\frac{\delta \vec{M}_e'}{\delta t} &= m_e n_e \left[\sum_{Z=1}^{2,3,\ldots} \nu_{eiZ}(\vec{u}_{iZ} - \vec{u}_e) - \nu_{en}\vec{u}_e - (\nu_{ioniz} - \nu_{recomb})\vec{u}_e \right] = \\ &= \frac{m_e}{e}\left(\nu_e \vec{j}_e + \sum_{Z=1}^{2,3,\ldots} \frac{n_e}{Z n_{iZ}} \nu_{eiZ} \vec{j}_{iZ} \right)\end{aligned} \tag{4.30}$$

where we have grouped the different collision frequencies into a single term for electrons: the *total electron collision frequency*, ν_e:

$$\nu_e = \nu_{en} + \sum_{Z=1}^{2,3,\ldots} \nu_{eiZ} + (\nu_{ioniz} - \nu_{recomb}) \tag{4.31}$$

If we consider only Maxwellian interaction terms for the collision frequency (which in turn, only account for the elastic collisions, as per Eq. (4.28)), we have the *Maxwellian electron collision frequency*, ν_{eM}:

$$\nu_{eM} = \nu_{en} + \sum_{Z=1}^{2,3,\ldots} \nu_{eiZ} = \nu_e - (\nu_{ioniz} - \nu_{recomb}) \tag{4.32}$$

which formalizes the expression for $\dfrac{\delta \vec{M}_e}{\delta t}$:

$$\frac{\delta \vec{M}_e}{\delta t} = \frac{m_e}{e}\left(\nu_{eM} \vec{j}_e + \sum_{Z=1}^{2,3,\ldots} \frac{n_e}{Z n_{iZ}} \nu_{eiZ} \vec{j}_{iZ} \right) \tag{4.33}$$

Considering all of the above, Eq. (4.26) may now be expressed as:

$$\begin{aligned}\nabla\phi = &\frac{rB\dfrac{\partial p_{e\perp}}{\partial \lambda}\vec{1}_\top + \dfrac{1}{r}\dfrac{\partial p_{e\perp}}{\partial \theta}\vec{1}_\theta + B\dfrac{\partial p_{e\parallel}}{\partial \sigma}\vec{1}_\parallel}{e n_e} + \frac{(p_{e\parallel} - p_{e\perp})}{e n_e}\left(r\frac{\partial B}{\partial \lambda}\vec{1}_\top - \frac{\partial B}{\partial \sigma}\vec{1}_\parallel \right) - \\ &- \left(\eta_e \vec{j}_e + \sum_{Z=1}^{2,3,\ldots} \eta_{eiZ}\vec{j}_{iZ} \right) - \beta_e \eta_e \left(\vec{j}_e \times \vec{1}_\parallel \right)\end{aligned} \tag{4.34}$$

[6]This is not true for "fast" neutrals resulting from a CEX process; however, these particles are rare, and further collisions with electrons would be even more scarce, therefore we consider this assumption as valid for the general neutral population.

where the *resistivity* terms are:

$$\begin{aligned}
&\text{Electron total resistivity: } \eta_e = \frac{m_e \nu_e}{e^2 n_e} \\
&\text{Electron-to-ion-Z resistivity: } \eta_{eiZ} = \frac{m_e \nu_{eiZ}}{Z e^2 n_{iZ}} \\
&\text{Electron-to-neutral resistivity: } \eta_{en} = \frac{m_e \nu_{en}}{e^2 n_e}
\end{aligned} \tag{4.35}$$

And we define the total Hall parameter, β_e, as the value which compares the electron cyclotron and electron total collision frequency:

$$\beta_e = \frac{{}^{eB}/_{m_e}}{\nu_e} = \frac{\Omega_e}{\nu_e}$$

which, as mentioned in Section 1.1.1, is the classical value used to describe magnetic confinement.

Now, projecting the momentum equation, Eq. (4.34), onto each of the directions in the problem, as defined by the magnetic reference system and beginning with the $\vec{1}_\theta$ direction, which requires some additional study:

$$\text{Eq.(4.34)} \cdot \vec{1}_\theta : \ \frac{1}{e n_e}\left(\frac{e n_e}{r}\frac{\partial \phi}{\partial \theta} - \frac{1}{r}\frac{\partial p_{e\perp}}{\partial \theta}\right) = -\left(\eta_e j_{e\theta} + \sum_{Z=1}^{2,3,\ldots} \eta_{eiZ} j_{iZ\theta}\right) + \beta_e \eta_e j_{e\top} \tag{4.36}$$

First, the term associated with azimuthal ion currents may be discarded through dimensional analysis: since ions are considered un-magnetized for the typical magnetic field intensities in HETs, these currents are much smaller than the azimuthal electron current or Hall current which characterizes these devices; furthermore, ion-electron collision frequencies are much smaller than the the total electron collision frequency, primarily due to fact that neutral-electron collisions have a tendency to dominate in the near plume region (as commented by Ahedo[219, 220]). Ion-electron collisions, however, can be dominant once the neutral density drops sufficiently due to ionization or dispersion processes, which occurs in the downstream region of the discharge (in what could be considered the transition zone to the far-plume region). Therefore these terms satisfy:

$$\begin{aligned}
&j_{i_1\theta}, j_{i_2\theta} \ll j_{e\theta} \\
&\frac{\eta_{i_1}}{\eta_e}, \frac{\eta_{i_2}}{\eta_e} \ll 1 \text{(Near Plume)} \ ; \frac{\eta_{i_1}}{\eta_e}, \frac{\eta_{i_2}}{\eta_e} \sim 1 \text{(Far Plume)}
\end{aligned} \tag{4.37}$$

In most EP devices, the first relation in Eq.(4.37) is sufficient to neglect the terms associated to ion azimuthal current, independently of the relative importance of the ion-electron collision frequencies.

Second, the term on the left-hand side of Eq. (4.36) will disappear in a strictly axisymmetric problem, however, it is clear that the existence of azimuthal electric fields and pressure gradients in HETs could be responsible for increased axial electron transport, due to the $\vec{E}\times\vec{B}$ and diamagnetic,

$\nabla p_e \times \vec{B}$, drifts; in particular, a correlation between azimuthal gradients of electron pressure and electron potential must exist in order for net axial transport to appear. The real problem, however, is more complex than what the fluid equations allow us to model. Choueiri[221, 222, 223] worked on characterizing the various oscillatory modes present in HETs, building upon the classic works of Yoshikawa[224] and Janes and Lowder[225]. A variety of mechanisms have been proposed to explain the "anomalous" axial electron current in HET devices: some are related to space-charge effects[226, 227, 218], others to plasma fluctuations[228], such as, for example, the ion-acoustic wave[229, 126], to the short-circuiting of the electron current in the vicinity of the thruster walls[147, 36], or, simply, to the aforementioned drifts. These diffusion mechanisms are categorized as non-classical or "plasma turbulence" and are commonly referred to as the *anomalous* electron transport.

Based on the legacy of previous codes, we may model the azimuthal term as done by Ahedo[220], by considering the correlation of azimuthal perturbation modes in the plasma density and potential as a forcing term in the momentum equations. This *anomalous momentum forcing term* is defined as an average over time and the azimuthal spatial direction of the left-hand side term in Eq. (4.36):

$$\left(\frac{en_e}{r}\frac{\partial\phi}{\partial\theta} - \frac{1}{r}\frac{\partial p_{e\perp}}{\partial\theta}\right) \leftrightarrow \left\langle \frac{en_e}{r}\frac{\partial\phi}{\partial\theta} - \frac{1}{r}\frac{\partial p_{e\perp}}{\partial\theta} \right\rangle_{\theta,t} = en_e F_\theta \tag{4.38}$$

Considering the above, the projected electron momentum equation, in terms of each individual current density component, for total and parallel electron pressure (following the relations given in Eq. (4.10)) is:

$$\text{Eq. (4.34)} \cdot \begin{cases} \vec{\mathbf{1}}_\top\text{:}\ j_{e\top} = \dfrac{1}{\eta_e\left(1+\beta_e^2\right)}\left[-rB\dfrac{\partial\phi}{\partial\lambda} + \dfrac{rB}{2en_e}\dfrac{\partial(3p_e - p_{e\parallel})}{\partial\lambda} - \right. \\ \left. -\dfrac{3(p_e - p_{e\parallel})}{2en_e} r\dfrac{\partial B}{\partial\lambda} - \sum\limits_{Z=1}^{2,3,\ldots} \eta_{eiZ} j_{iZ\top} + \beta_e F_\theta \right] \\ \vec{\mathbf{1}}_{\boldsymbol{\theta}}\ \mathbf{:}\ j_{e\theta} = \beta_e j_{e\top} - \dfrac{F_\theta}{\eta_e} \\ \vec{\mathbf{1}}_\parallel\ \mathbf{:}\ j_{e\parallel} = \dfrac{1}{\eta_e}\left(-B\dfrac{\partial\phi}{\partial\sigma} + \dfrac{B}{en_e}\dfrac{\partial p_{e\parallel}}{\partial\sigma} + \dfrac{3(p_{e\parallel} - p_e)}{2en_e}\dfrac{\partial B}{\partial\sigma} - \sum\limits_{Z=1}^{2,3,\ldots} \eta_{eiZ} j_{iZ\parallel}\right) \end{cases} \tag{4.39}$$

The anomalous forcing term, F_θ, acts a sort of "degree of freedom" in our problem, since we are limited in our capacity to model it self-consistently by the physics implemented in the model and the 2D axisymmetric approach. The work by most authors referenced in Section 1.2.1 delves into the modeling and simulation of the anomalous electron transport; in our case, the in-depth approach to this issue belongs to the category of future work. As a free parameter, the forcing term has been traditionally modeled in relation to an anomalous collision frequency, ν_{ano}, as a fraction of the electron gyrofrequency[128]:

$$\nu_{ano} = \alpha_{ano}\Omega_e$$

where the anomalous collision frequency factor, α_{ano}, is a value in the range $[0, \sim 1]$. The forcing term, F_θ, is modeled as:

$$F_\theta = \frac{\eta_e \left(1+\beta_e^2\right)}{\beta_e} j_{e\top} \left(1 - \frac{\eta_{e^*}\left(1+\beta_{e^*}^2\right)}{\eta_e\left(1+\beta_e^2\right)}\right) \tag{4.40}$$

where we have introduced the electron effective total resistivity, η_{e^*}, the effective total Hall parameter, β_{e^*} and the effective total collision frequency, ν_{e^*}:

$$\begin{aligned} \nu_{e^*} &= \nu_e + \nu_{ano} \\ \eta_{e^*} &= \frac{m_e \nu_{e^*}}{e^2 n_e} \\ \beta_{e^*} &= \frac{\Omega_e}{\nu_{e^*}} \end{aligned} \tag{4.41}$$

If we introduce the previous expression into Eq. (4.39) we have, for the perpendicular and azimuthal directions (the parallel direction remains unaltered):

$$\text{Eq. (4.34)} \cdot \begin{cases} \vec{\mathbf{1}}_\top\text{:}\ j_{e\top} = \dfrac{1}{\eta_{e^*}\left(1+\beta_{e^*}^2\right)} \Bigg[-rB\dfrac{\partial \phi}{\partial \lambda} + \dfrac{rB}{2en_e}\dfrac{\partial (3p_e - p_{e\|})}{\partial \lambda} - \\ -\dfrac{3(p_e - p_{e\|})}{2en_e} r \dfrac{\partial B}{\partial \lambda} - \sum_{Z=1}^{2,3,\ldots} \eta_{eiZ} j_{iZ\top} \Bigg] \\ \vec{\mathbf{1}}_{\boldsymbol{\theta}}\ \mathbf{:}\ j_{e\theta} = j_{e\top}\left[\beta_e - \dfrac{1+\beta_e^2}{\beta_e}\left(1 - \dfrac{\eta_{e^*}\left(1+\beta_{e^*}^2\right)}{\eta_e\left(1+\beta_e^2\right)}\right)\right] \\ \vec{\mathbf{1}}_\|\ \mathbf{:}\ j_{e\|} = \dfrac{1}{\eta_e}\left(-B\dfrac{\partial \phi}{\partial \sigma} + \dfrac{B}{en_e}\dfrac{\partial p_{e\|}}{\partial \sigma} + \dfrac{3(p_{e\|} - p_e)}{2en_e}\dfrac{\partial B}{\partial \sigma} - \sum_{Z=1}^{2,3,\ldots} \eta_{eiZ} j_{iZ\|}\right) \end{cases} \tag{4.42}$$

where the only remaining degree of freedom is now α_{ano}, which is typically given as a certain function of the magnetic coordinates $\alpha_{ano} = \alpha_{ano}(\lambda, \sigma)$ (see Chapter 6).

As a final corollary, it is worth mentioning that the effective total collision frequency in legacy code models included an additional near-wall collisionality term, ν_{wall}, which is simply a separate mechanism for anomalous transport:

$$\nu_{e^*} = \nu_e + \nu_{ano} + \nu_{wall} \tag{4.43}$$

This term has been linked to a multitude of sources, ranging from azimuthal electron momentum exchange in the walls to electron scattering due to microscopic roughness or scattering due to the interactions of bulk and secondary electrons; these phenomena can affect energy and momentum transport in different ways, leading to different flavors of ν_{wall}.

The existence of electron recombination or absorption and the known phenomenon of secondary electron emission (see Section 5.1.1) implies that there a net exchange of plasma azimuthal electron

momentum exists in the walls. Indeed, electrons entering the plasma sheath and reaching the walls are "fully magnetized", presenting the large azimuthal drift characteristic of the Hall current (see Section 1.1.1 or Fig. 7.30, for a comparison of axial and azimuthal currents in simulation results). Secondary electrons leaving the walls, on the other hand, may be considered un-magnetized at their inception, not initially subjected to the $\vec{E} \times \vec{B}$ drift.

This momentum exchange has been linked to an increase in electron cross-field conductivity in HETs, as a possible explanation for the *near-wall conductivity* effect, introduced by Morozov[148, 147] and represented by the near-wall collision frequency term. Ahedo and Gallardo[220] derive a value for ν_{wall} based on dimensional analysis and radial averaging of the azimuthal momentum equation. Escobar[212] obtained this value by integration of said momentum equation in a magnetic tube confined between the walls of a HET. Neither models consider the possibility of microscopic roughness on the wall as a possible source of near-wall conductivity, as was also suggested by Morozov.

These existing models for ν_{wall} cast doubt on the relevance of near-wall conductivity versus the anomalous collision frequency, ν_{ano}, in Eq. (4.43) and its effect on non-classical electron transport in HETs. Ahedo[220] and Garrigues[230] considered it a second order contribution, in an SPT-like and an SPT-100 configurations, respectively, and Hofer[231] found that ν_{wall} was at least one order of magnitude smaller than ν_{ano} at its peak value, in the context of a 6kW laboratory thruster. For these reasons, a near-wall conductivity model has not been presently implemented in NOMADS, remaining an open venue for future developments in the code.

4.1.3 Discussion for the energy equations

Equation (4.5) may be replaced, considering the summation law in Eq. (4.11), the relations in Eq. (4.10), the definition for the electron current density, Eq. (4.24), and the model closure given in Section 4.1.1, by:

Thermal energy density equation:

$$\frac{\partial\left(\frac{3p_e}{2}\right)}{\partial t} - \nabla\cdot\left(\frac{3}{2}p_e\cdot\frac{\vec{j}_e}{en_e}\right) - \bar{\bar{P}}_e\cdot\nabla\cdot\frac{\vec{j}_e}{en_e} + \nabla\cdot\vec{q}_e = \frac{\delta E_e}{\delta t} + \frac{\vec{j}_e}{en_e}\cdot\frac{\delta\vec{M}_e}{\delta t} + \frac{j_e^2}{2e^2n_e^2}S_e m_e \quad (4.44)$$

where,

$$\frac{\delta E_e}{\delta t} = \frac{1}{2}\left(\frac{\delta E_{e\parallel}}{\delta t} + 2\frac{\delta E_{e\top}}{\delta t}\right)$$

The collisional terms in the previous expression can be split in elastic and inelastic contributions:

$$\frac{\delta E_e}{\delta t} = \left.\frac{\delta E_e}{\delta t}\right|_{elastic} + \left.\frac{\delta E_e}{\delta t}\right|_{inelastic}$$

The inelastic collision term, $\left.\frac{\delta E_e}{\delta t}\right|_{inelastic}$, may be further divided into *non-ionizing* and *ionizing/excitation* type collisions. The former are disregarded following the same discussion made for the respective term in the momentum equation. The ionization and excitation terms, on the other hand, represent the main internal energy sink for the electron fluid; thus, the inelastic collisional term in Eq. (4.44) can be approximated to:

$$\left.\frac{\delta E_e}{\delta t}\right|_{inelastic} = \left.\frac{\delta E_e}{\delta t}\right|_{ioniz+excit}$$

The modeling for this last term may be found in Section 5.2. On the other hand, the energy transfer due to elastic collisions may be modeled for Maxwell type molecule interactions[212], as:

$$\left.\frac{\delta E_e}{\delta t}\right|_{elastic} = \sum_{\alpha} m_e n_e \nu_{e\alpha} \left((\vec{u}_\alpha - \vec{u}_e) \cdot \vec{u}_\alpha + \frac{2}{m_\alpha}\frac{3}{2} k_B (T_\alpha - T_e) \right) \tag{4.45}$$

Where we recall that the elastic collision frequency $\nu_{e\alpha_{elastic}}$ is the dominant term in the Maxwell interaction collision frequency $\nu_{e\alpha}$, as per Eq. (4.28)[7].

Furthermore, the previous expression might be simplified through dimensional analysis considering that the electron temperature is dominant over the temperatures of other species ($T_\alpha \ll T_e$). Grouping the rate of change of thermal energy density due to elastic collisions to the contribution of the rate of change of momentum due to collisions, Eq. (4.27), we have:

$$\begin{aligned} &\left.\frac{\delta E_e}{\delta t}\right|_{elastic} + \frac{\vec{j}_e}{e n_e} \cdot \frac{\delta \vec{M}_e}{\delta t} = \\ &\sum_{\alpha} m_e n_e \nu_{e\alpha} (\vec{u}_\alpha - \vec{u}_e) \cdot \vec{u}_\alpha - \vec{u}_e \cdot \sum_{\alpha} m_e n_e \nu_{e\alpha} (\vec{u}_\alpha - \vec{u}_e) - \sum_{\alpha} m_e n_e \nu_{e\alpha} \frac{2}{m_\alpha}\frac{3}{2} k_B T_e = \\ &= \sum_{\alpha} n_e \nu_{e\alpha} \left(m_e \left| (\vec{u}_\alpha - \vec{u}_e) \right|^2 - \frac{2 m_e}{m_\alpha}\frac{3}{2} k_B T_e \right) \end{aligned} \tag{4.46}$$

This expression may be further simplified by comparing the velocity-related and temperature-related terms for each of the collision pairs, taking into account:

$$m_n \sim m_{iZ}$$
$$\left| (\vec{u}_\alpha - \vec{u}_e) \right|^2 \sim \left| (\vec{u}_e) \right|^2$$

[7] It is important to clarify our approach towards those situations in which inelastic collisions may be neglected with respect to elastic collisions and which not: the overall Maxwell interaction collision frequency, $\nu_{e\alpha}$, includes both inelastic and elastic momentum transfer collision frequencies; however, the former are discarded because they are either negligible for the typical propellants in EP devices or because they relate to ionization/excitation collisions where the momentum transfer can be neglected. Thus, we arrive at the approximation in Eq. (4.28), which requires from us only to obtain the elastic collision cross-sections and allows for some convenient groupings in the equations. When considering the electron fluid *energy* equations, however, the principal energy sink for the plasma comes in the form of the less frequent, but costly, ionizing and excitation processes, which are not to be discarded with respect to elastic collisions; thus, inelastic collision (ionizing/excitation) cross-sections need to be obtained. For the an in-depth discussion on the expressions for the various cross-sections refer to Section 5.2.

where m_n is the neutral atom's mass. The relation between velocities is justified in the near-plume region in HETs due to the existence of the Hall current; thus:

$$\frac{\frac{2m_e}{m_\alpha}\frac{3}{2}k_B T_e}{m_e\left|(\vec{u}_\alpha - \vec{u}_e)\right|^2} \sim \frac{\frac{m_e}{m_i}k\mathcal{T}}{m_e u^2} = \left(\frac{u_{i_{sonic}}}{u}\right)^2 \ll 1$$

The temperature term in Eq. (4.46) may thus be dropped if the ion sonic velocity, $u_{i_{sonic}}$, can be considered small versus the characteristic electron drift velocity, which holds true for the mass ratios of typical propellants used in HETs. Therefore, the collisional terms in Eq. (4.44) may be rewritten, in term of electron and current densities, as:

$$\frac{\delta E_e}{\delta t} + \frac{\vec{j}_e}{en_e}\cdot\frac{\delta\vec{M}_e}{\delta t} = \sum_{Z=1}^{2,3,\ldots}\eta_{eiZ}\frac{Zn_{iZ}}{n_e}\left|\left(\vec{j}_e + \frac{n_e}{Zn_{iZ}}\vec{j}_{iZ}\right)\right|^2 + \eta_{en}\left|\left(\vec{j}_e\right)\right|^2 + \left.\frac{\delta E_e}{\delta t}\right|_{ioniz+excit} \tag{4.47}$$

Continuing with the parallel internal energy equation, we may update it, considering the model closure given in Section 4.1.1 and the definition for electron current density, as:

Parallel internal energy equation:

$$\begin{aligned}&\frac{\partial p_{e\|}}{\partial t} - \nabla\cdot\left(p_{e\|}\cdot\frac{\vec{j}_e}{en_e}\right) - 2p_{e\|}\nabla_\|\cdot\frac{\vec{j}_e}{en_e} + \nabla\cdot\vec{q}_{e\|} - 2\left[q_{e\|,\top r}\frac{\partial B}{\partial\lambda} - \left(q_{e\|} - \frac{1}{2}q_{e\|\|}\right)\frac{\partial B}{\partial\sigma}\right] = \\ &= \frac{\delta E_{e\|}}{\delta t} + 2\frac{j_{e\|}}{en_e}\frac{\delta\vec{M}_e}{\delta t}\cdot\vec{1}_\| + \frac{j_{e\|}^2}{e^2n_e^2}S_e m_e\end{aligned} \tag{4.48}$$

The collisional terms for the previous expression are given by Barakat and Schunk[214], for various collisional interactions (and even the collisionless limit); focusing only in the rate of change due to elastic collisions, we have, as before:

$$\begin{aligned}&\left.\frac{\delta E_{e\|}}{\delta t}\right|_{elastic} + 2\frac{j_{e\|}}{en_e}\frac{\delta\vec{M}_e}{\delta t}\cdot\vec{1}_\| = \sum_\alpha\frac{m_e n_e\nu_{e\alpha}}{m_e+m_\alpha}\left\{2k\left(T_{e\|} - T_{\alpha\|}\right) - 2m_\alpha(u_{e\|} - u_{\alpha\|})^2 + \right. \\ &\left. + \frac{m_\alpha}{2}\Lambda\left[2k\left(\left(\frac{T_{e\|}}{m_e} + \frac{T_{\alpha\|}}{m_\alpha}\right) - \left(\frac{T_{e\perp}}{m_e} + \frac{T_{\alpha\perp}}{m_\alpha}\right)\right) - \left|(\vec{u}_e - \vec{u}_\alpha)\right|^2 + 3(u_{e\|} - u_{\alpha\|})^2\right]\right\}\end{aligned} \tag{4.49}$$

where $\Lambda = 1.03318$ and is related to the scattering angle for collisional events in gas mixtures and is given by Chapman and Cowling[232][8].

Equation (4.49) may be simplified through the following relations:

$$\begin{aligned}&m_e + m_\alpha \approx m_\alpha \\ &\frac{T_{e\|}}{m_e} + \frac{T_{\alpha\|}}{m_\alpha} \approx \frac{T_{e\|}}{m_e} \\ &T_{e\|} - T_{\alpha\|} \approx T_{e\|}\end{aligned}$$

[8] In the notation used in Ref. [232], $\Lambda = \frac{A_2(5)}{A_1(5)}$.

Thus, the final expression for the collisional contributions to the parallel internal energy equation is:

$$\begin{aligned}
&\frac{\delta E_{e\parallel}}{\delta t} + 2\frac{j_{e\parallel}}{en_e}\frac{\delta \vec{M}_e}{\delta t}\cdot\vec{1}_\parallel = \\
&= \sum_{Z=1}^{2,3,\ldots} \eta_{eiZ}\frac{Zn_{iZ}}{n_e}\left(\left(2-\frac{3}{2}\Lambda\right)\left(j_{e\parallel}+\frac{n_e}{Zn_{iZ}}j_{iZ\parallel}\right)^2 + \frac{1}{2}\Lambda\left|\left(\vec{j}_e+\frac{n_e}{Zn_{i_Z}}\vec{j}_{iZ}\right)\right|^2\right) + \\
&+\eta_{en}\left(\left(2-\frac{3}{2}\Lambda\right)\left(j_{e\parallel}\right)^2 + \frac{1}{2}\Lambda\left|\left(\vec{j}_e\right)\right|^2\right) - \frac{3}{2}\Lambda\left(p_{e\parallel}-p_e\right)\left(\sum_{Z=1}^{2,3,\ldots}\nu_{eiZ}+\nu_{en}\right) + \left.\frac{\delta E_{e\parallel}}{\delta t}\right|_{ioniz+excit}
\end{aligned} \tag{4.50}$$

where $\left.\frac{\delta E_{e\parallel}}{\delta t}\right|_{ioniz+excit}$ may be related to $\left.\frac{\delta E_e}{\delta t}\right|_{ioniz+excit}$ through the assumption that the energy required for ionization and excitation is extracted from the electron fluid in a non-preferential direction, since the angle of impact for inelastic collisions is essentially random. Under the summation law, Eq. (4.11), we can argue that:

$$\left.\frac{\delta E_{e\parallel}}{\delta t}\right|_{ioniz+excit} = \left.\frac{\delta E_{e\top}}{\delta t}\right|_{ioniz+excit} \rightarrow \left.\frac{\delta E_{e\parallel}}{\delta t}\right|_{ioniz+excit} = \frac{2}{3}\left.\frac{\delta E_e}{\delta t}\right|_{ioniz+excit}$$

4.1.4 Discussion for the heat-flow equations

The heat-flow equations, Eqs. (4.6) and (4.7), also require some additional discussion. First, Eq. (4.7) may be replaced by the "total" heat-flow equation using the summation law in Eq. (4.11), the relations in Eq. (4.10) and the model closure given in Section 4.1.1:

Total heat-flow equation:

$$\begin{aligned}
&\frac{1}{2}\left[\nabla_\perp\left(\frac{(3p_e-p_{e\parallel})^2+p_{e\parallel}{}^{(3p_e-p_{e\parallel})/2}}{n_em_e}\right)+\nabla_\parallel\left(\frac{3p_{e\parallel}^2+p_{e\parallel}(3p_e-p_{e\parallel})}{n_em_e}\right)+\right. \\
&\left.+\nabla\cdot(\vec{1}_\parallel\vec{1}_\parallel)\left(\frac{3p_{e\parallel}^2+p_{e\parallel}{}^{(3p_e-p_{e\parallel})/2}-(3p_e-p_{e\parallel})^2}{n_em_e}\right)\right]- \\
&-\frac{1}{n_em_e}\left(\nabla_\perp\left(\frac{(3p_e-p_{e\parallel})}{2}\right)+\nabla_\parallel p_{e\parallel}+\frac{3(p_{e\parallel}-p_e)}{2}\nabla\cdot(\vec{1}_\parallel\vec{1}_\parallel)\right)\cdot \\
&\cdot\left[(3p_e-\frac{1}{2}p_{e\parallel})(\bar{\bar{I}}-(\vec{1}_\parallel\vec{1}_\parallel))+\frac{3p_e+2p_{e\parallel}}{2}(\vec{1}_\parallel\vec{1}_\parallel)\right]+\vec{\Omega}_e\times\vec{q}_e = \\
&=\frac{\delta\vec{H}_e}{\delta t}-\frac{1}{n_em_e}\frac{\delta\vec{M}_e'}{\delta t}\cdot\left[(3p_e-\frac{1}{2}p_{e\parallel})(\bar{\bar{I}}-(\vec{1}_\parallel\vec{1}_\parallel))+\frac{3p_e+2p_{e\parallel}}{2}(\vec{1}_\parallel\vec{1}_\parallel)\right]
\end{aligned} \tag{4.51}$$

where,

$$\frac{\delta H_e}{\delta t} = \frac{1}{2}\left(\frac{\delta H_{e\parallel}}{\delta t} + 2\frac{\delta H_{e\top}}{\delta t}\right)$$

Now, the collisional terms in the total Heat-flow and the parallel energy Heat-flow equations, $\frac{\delta \vec{H}_e}{\delta t}$ and $\frac{\delta \vec{H}_{e\parallel}}{\delta t}$, may be modeled through the Krook collision model, as proposed by Bittencourt[215], using the maxwellian collision frequency, ν_{eM}:

$$\begin{aligned}\frac{\delta \vec{H}_e}{\delta t} &= -\nu_{eM}\vec{q}_e \\ \frac{\delta \vec{H}_{e\parallel}}{\delta t} &= -\nu_{eM}\vec{q}_{e\parallel}\end{aligned} \tag{4.52}$$

Similarly to the momentum equation, we project Eq. (4.51) onto the azimuthal direction to obtain:

$$\begin{aligned}&\text{Eq. (4.51)}\cdot\,\vec{\mathbf{1}}_{\boldsymbol{\theta}}\,\mathbf{:}\;\; \frac{1}{2m_e}\frac{1}{r}\frac{\partial}{\partial\theta}\left(\frac{\left(3p_e-p_{e\parallel}\right)^2+p_{e\parallel}\dfrac{3p_e-p_{e\parallel}}{2}}{n_e}\right) - \frac{3p_e-\dfrac{p_{e\parallel}}{2}}{n_e m_e}\frac{1}{r}\frac{\partial}{\partial\theta}\left(3p_e-\frac{p_{e\parallel}}{2}\right) = \\ &= \Omega_e q_{e\top} - \nu_{eM}q_{e\theta} - \frac{1}{n_e m_e}\left(3p_e-\frac{p_{e\parallel}}{2}\right)\frac{\delta \vec{M}_e'}{\delta t}\cdot\vec{1}_\theta\end{aligned} \tag{4.53}$$

The left-hand side of Eq. (4.53) is the effect over the electron heat-flow due to correlations in the azimuthal direction similar to the ones that cause anomalous transport. Without loss of generality, we propose an expression for this anomalous heat-flow forcing term as an average over time and the azimuthal spatial coordinate:

$$\left\langle \frac{1}{2m_e}\frac{1}{r}\frac{\partial}{\partial\theta}\left(\frac{\left(3p_e-p_{e\parallel}\right)^2+p_{e\parallel}{}^{3p_e-p_{e\parallel}/2}}{n_e}\right) - \frac{3p_e-\dfrac{p_{e\parallel}}{2}}{n_e m_e}\frac{1}{r}\frac{\partial}{\partial\theta}\left(3p_e-\frac{p_{e\parallel}}{2}\right)\right\rangle_{\theta,t} = \Omega_e Q_\theta$$

and considering the simplification allowed by the relations in Eq. (4.37) and that the electron and ion densities are of the same order (due to quasineutrality), we arrive, after some algebra, at:

$$q_{e\theta} = -\frac{1}{\nu_{e,(Maxw)}}\left(\Omega_e(-q_{e\top}+Q_\theta) + \frac{(3p_e - {}^{p_{e\parallel}}/_2)}{en_e}\nu_e j_{e\theta}\right) \tag{4.54}$$

Following this expression, the parallel and perpendicular projections of the heat-flow equation may be obtained. As in Section 4.1.2, the anomalous forcing term may be replaced by introducing the

anomalous collision frequency into the respective terms for the perpendicular projection (which is equivalent to what was done for the forcing term in the momentum equation):

$$\text{Eq. (4.51)}\cdot\begin{cases}
\vec{\mathbf{I}}_{\top}\text{: } q_{e\top} = \dfrac{1}{1+(\beta_{e^*M})^2}\left[-\dfrac{1}{2}\dfrac{r\beta_{e^*M}}{e}\left(\dfrac{\partial}{\partial\lambda}\left(\dfrac{\left(3p_e-p_{e\parallel}\right)^2+{p_{e\parallel}}^{3p_e-p_{e\parallel}/2}}{n_e}\right)+\right.\right.\\
\left.\left.\dfrac{\partial \ln B}{\partial\lambda}\left(\dfrac{3p_{e\parallel}^2+{p_{e\parallel}}^{3p_e-p_{e\parallel}/2}-\left(3p_e-p_{e\parallel}\right)^2}{n_e}\right)\right)+\right.\\
+\left(\dfrac{3p_e-{}^{p_{e\parallel}/2}}{n_e}\right)\dfrac{r\beta_{e^*M}}{e}\left(\dfrac{\partial}{\partial\lambda}\left(\dfrac{3p_e-p_{e\parallel}}{2}\right)+\dfrac{3(p_{e\parallel}-p_e)}{2}\dfrac{\partial \ln B}{\partial\lambda}\right)-\\
\left.-\dfrac{(3p_e-{}^{p_{e\parallel}/2})}{en_e\eta_{e^*M}}\left(\eta_{e^*}\left(j_{e\top}-\beta_{e^*M}j_{e\theta}\right)+\sum_{Z=1}^{2,3,\ldots}\eta_{eiZ}j_{iZ\top}\right)\right]\\
\vec{\mathbf{I}}_{\parallel}\text{ : } q_{e\parallel} = -\dfrac{1}{2}\dfrac{\beta_{eM}}{e}\left[\dfrac{\partial}{\partial\sigma}\left(\dfrac{3p_{e\parallel}^2+p_{e\parallel}\left(3p_e-p_{e\parallel}\right)}{n_e}\right)-\right.\\
\left.-\dfrac{\partial \ln B}{\partial\sigma}\left(\dfrac{3p_{e\parallel}^2+{p_{e\parallel}}^{3p_e-p_{e\parallel}/2}-\left(3p_e-p_{e\parallel}\right)^2}{n_e}\right)\right]+\\
+\left(\dfrac{3p_e+2p_{e\parallel}}{2n_e}\right)\dfrac{\beta_{eM}}{e}\left(\dfrac{\partial p_{e\parallel}}{\partial\sigma}-\dfrac{3(p_{e\parallel}-p_e)}{2}\dfrac{\partial \ln B}{\partial\sigma}\right)-\\
-\dfrac{\left(3p_e+2p_{e\parallel}\right)}{2en_e\eta_{eM}}\left(\eta_e j_{e\parallel}+\sum_{Z=1}^{2,3,\ldots}\eta_{eiZ}j_{iZ\parallel}\right)
\end{cases} \tag{4.55}$$

where we can define the resistivities and hall parameters as:

$$\nu_{e^*M}=\nu_{eM}+\nu_{ano}\ ;\ \eta_{e^*M}=\frac{m_e\nu_{e^*M}}{e^2n_e}\ ;\ \beta_{e^*M}=\frac{\Omega_e}{\nu_{e^*M}} \tag{4.56}$$

The parallel heat-flow equation may be simplified based on Section 4.1.1 and expressed in terms of total and parallel electron pressures as:

$$\begin{aligned}
&\left[\nabla_{\perp}\left(\frac{p_{e\parallel}(3p_e-p_{e\parallel})}{2n_em_e}\right)+3\nabla_{\parallel}\left(\frac{p_{e\parallel}^2}{n_em_e}\right)+\nabla\cdot(\vec{1}_{\parallel}\vec{1}_{\parallel})\frac{p_{e\parallel}(7p_{e\parallel}-3p_e)}{2n_em_e}\right]-\\
&-\frac{1}{n_em_e}\left(\nabla_{\perp}\left(\frac{(3p_e-p_{e\parallel})}{2}\right)+\nabla_{\parallel}p_{e\parallel}+\frac{3(p_{e\parallel}-p_e)}{2}\nabla\cdot(\vec{1}_{\parallel}\vec{1}_{\parallel})\right)\cdot\left[p_{e\parallel}\bar{\bar{I}}+2p_{e\parallel}(\vec{1}_{\parallel}\vec{1}_{\parallel})\right]+\\
&+\vec{\Omega}_e\times\vec{q}_{e\parallel}-\frac{2}{n_em_e}\left(p_{e\parallel}\frac{(3p_e-p_{e\parallel})}{2}r\frac{\partial B}{\partial\lambda}\vec{1}_{\top}+\left(rB^2\frac{\partial\left((rB)^{-1}\right)}{\partial\sigma}+B\frac{\partial \ln r}{\partial\sigma}\right)\frac{(3p_e-p_{e\parallel})}{2}p_{e\parallel}\vec{1}_{\parallel}\right)=\\
&=\frac{\delta\vec{H}_{e\parallel}}{\delta t}-\frac{1}{n_em_e}\frac{\delta\vec{M}_e^{'}}{\delta t}\cdot\left[p_{e\parallel}\bar{\bar{I}}+2p_{e\parallel}(\vec{1}_{\parallel}\vec{1}_{\parallel})\right]
\end{aligned} \tag{4.57}$$

Taking Eq. (4.57) and projecting it onto the azimuthal direction:

$$\begin{aligned}&\text{Eq. (4.57)}\cdot\vec{1}_\theta:\ \frac{1}{2m_e}\frac{1}{r}\frac{\partial}{\partial\theta}\left(p_{e\|}\frac{3p_e-p_{e\|}}{n_e}\right)-\frac{p_{e\|}}{n_e m_e}\frac{1}{r}\frac{\partial}{\partial\theta}\left(3p_e-\frac{p_{e\|}}{2}\right)=\\&\Omega_e q_{e\|\top}-\nu_{eM}q_{e\|\theta}-\frac{p_{e\|}}{n_e m_e}\frac{\delta\vec{M}_e^{'}}{\delta t}\cdot\vec{1}_\theta\end{aligned}\tag{4.58}$$

Again, the left-hand side of Eq. (4.58) calls for an *anomalous parallel heat-flow forcing* term, which in this case is related to the effects of transport in the parallel internal energy only. We may write:

$$\left\langle\frac{1}{2m_e}\frac{1}{r}\frac{\partial}{\partial\theta}\left(p_{e\|}\frac{3p_e-p_{e\|}}{n_e}\right)-\frac{p_{e\|}}{n_e m_e}\frac{1}{r}\frac{\partial}{\partial\theta}\left(3p_e-\frac{p_{e\|}}{2}\right)\right\rangle_{\theta,t}=\Omega_e Q_{\|\theta}\tag{4.59}$$

Similarly to the total heat-flow equation, we arrive at an expression for the azimuthal component of the parallel heat-flow:

$$q_{e\|\theta}=-\frac{1}{\nu_{e,(Maxw)}}\left(\Omega_e(-q_{e\|\top}+Q_{\|\theta})+\frac{p_{e\|}}{en_e}\nu_e j_{e\theta}\right)\tag{4.60}$$

This last expression lets us obtain the equations for the parallel energy heat flow in the parallel and perpendicular directions. For lack of a better model, the anomalous parallel forcing term is introduced through the anomalous collision frequency, as has been done before:

$$\text{Eq. (4.57)}\cdot\begin{cases}\vec{1}_\top:\ q_{e\|\top}=\dfrac{1}{1+(\beta_{eM^*})^2}\left[-\dfrac{r\beta_{e,^*M}}{e}\left(\dfrac{\partial}{\partial\lambda}\left(p_{e\|}\dfrac{3p_e-p_{e\|}}{2n_e}\right)+\right.\right.\\\left.+\dfrac{\partial\ln B}{\partial\lambda}\left(p_{e\|}\dfrac{7p_{e\|}-3p_e}{2n_e}\right)\right)+\left(\dfrac{p_{e\|}}{n_e}\right)\dfrac{r\beta_{eM^*}}{e}\left(\dfrac{\partial}{\partial\lambda}\left(\dfrac{3p_e-p_{e\|}}{2}\right)+\right.\\\left.\left.+p_{e\|}\dfrac{\partial\ln B}{\partial\lambda}\right)-\ -\dfrac{p_{e\|}}{en_e\eta_{eM^*}}\left(\eta_{e^*}\left(j_{e\top}-\beta_{eM^*}j_{e\theta}\right)+\sum_{Z=1}^{2,3,\ldots}\eta_{eiZ}j_{iZ\top}\right)\right]\\\vec{1}_\| :\ q_{e\|\|}=-\dfrac{\beta_{eM}}{e}\left[\dfrac{\partial}{\partial\sigma}\left(\dfrac{3p_{e\|}^2}{n_e}\right)-\dfrac{\partial\ln B}{\partial\sigma}\left(p_{e\|}\dfrac{7p_{e\|}-3p_e}{2n_e}\right)-\right.\\-\left(\dfrac{3p_{e\|}}{n_e}\right)\left(\dfrac{\partial p_{e\|}}{\partial\sigma}-\dfrac{3(p_{e\|}-p_e)}{2}\dfrac{\partial\ln B}{\partial\sigma}\right)-\left(p_{e\|}\dfrac{3p_e-p_{e\|}}{3n_e}\right)\left(\dfrac{\partial\ln(1/rB)}{\partial\sigma}+\right.\\\left.\left.+\dfrac{\partial\ln(r)}{\partial\sigma}\right)\right]-\dfrac{3p_{e\|}}{en_e\eta_{eM}}\left(\eta_e j_{e\|}+\sum_{Z=1}^{2,3,\ldots}\eta_{eiZ}j_{iZ\|}\right)\end{cases}\tag{4.61}$$

It is worth noting that Eqs. (4.55) and (4.61) are only implicitly dependent with time. This dependency is introduced through the parallel and total electron pressures, but otherwise these represent "state" equations in our problem.

Simplified approach to the electron heat-flow equation

Equation (4.51) is a rather complex expression which arises from moments of the Boltzmann equation being taken with a two-temperature bi-Maxwellian. One may choose to replace said equation by the simpler expression provided by Bittencourt[215], for which missing collisional terms have been added:

$$\frac{5}{2}p_e\nabla\left(\frac{p_e}{n_e m_e}\right)+\Omega_e\left(\vec{q}_e\times\vec{1}_\parallel\right)=\frac{\delta\vec{H}_e}{\delta t}-\frac{1}{n_e m_e}\frac{\delta\vec{M}_e'}{\delta t}\cdot\left(2\bar{\bar{P}}_e+\frac{1}{2}p_{e\parallel}\bar{\bar{I}}+\frac{3}{2}(p_e-p_{e\parallel})(\vec{1}_\parallel\vec{1}_\parallel)\right) \quad (4.62)$$

All of the previous assumptions made for the total heat-flow equation are still valid here and the projection of Eq. (4.62) onto the azimuthal direction is equivalent to the one shown in Eq. (4.54), leading to the contributions for parallel and perpendicular directions of this simplified heat-flow equation:

$$\text{Eq. (4.62)}\cdot\begin{cases}\vec{1}_\top\colon\ q_{e\top}=\dfrac{\beta_{eM^*}}{1+(\beta_{eM^*})^2}\left(-\dfrac{5}{2}r\dfrac{p_e}{e}\dfrac{\partial\left(p_e n_e^{-1}\right)}{\partial\lambda}\right)- \\ -\dfrac{\left(3p_e-\dfrac{p_{e\parallel}}{2}\right)}{en_e\eta_{eM^*}}\dfrac{1}{1+(\beta_{eM^*})^2}\left(\eta_{e^*}\left(j_{e\top}-\beta_{e^*M}j_{e\theta}\right)+\sum\limits_{Z=1}^{2,3,\ldots}\eta_{eiZ}j_{iZ\top}\right) \\ \vec{1}_\parallel:\ q_{e\parallel}=-\beta_{e^*M}\dfrac{5}{2}\dfrac{p_e}{e}\dfrac{\partial\left(p_e n_e^{-1}\right)}{\partial\sigma}-\dfrac{\left(\dfrac{3}{2}p_e+p_{e\parallel}\right)}{en_e\eta_{e^*M}}\left(\eta_{e^*}j_{e\parallel}+\sum\limits_{Z=1}^{2,3,\ldots}\eta_{eiZ}j_{iZ\parallel}\right)\end{cases} \quad (4.63)$$

4.2 Numerical discretization and resolution of the electron fluid model

Equations (4.25), (4.42), (4.44), (4.48), (4.55) (which may be replaced by Eq. (4.63)), (4.54), (4.61) and (4.60) present a closed set of expressions for modeling the electron population as a conducting fluid, which we have dubbed the "12 moment approximation".

This set of equations may, in principle, be modeled through any of the known numerical methods and discretization approaches. For HYPHEN we have chosen to employ a Cell Centered (CC) FVM on a non-structured MFAM, for a given simulation domain in an axisymmetric 2D space (Fig. 3.6). The FVM method was chosen because it provides a conservative or integral approach to the problem (versus the non-integral approach of the Finite Differences Method) in the "strong" formulation (versus the "weak" form of the Finite Element Method). Particularly, the FVM method is referred to by Diskin[203] as being resilient against the effects of non-regularity in unstructured meshes, which provides a good argument favoring its utilization in conjunction with the MFAM approach. The chosen scheme presents an advantage versus legacy codes such as HPHall or HallMa in which issues with energy and current conservation have been reported[212].

The FVM requires spatial discretization of gradients; these have been detailed in Chapter 3, where we presented an ad-hoc solution for the MFAM through the WLSQR FI method. To

summarize the method which was dissected there, the resulting set of equations (based on the Taylor series expansion) determine the value of any fluid quantity ψ at the center of the MFAM element faces, as well as derivatives and cross-derivatives (of up to any given order), from the value of ψ at a number of *stencil points* (the centers of the surrounding elements) and the set of *weights* assigned to them (which are typically functions of the inverse distance, element areas, etc.). This results in a linear equation such as (for example, for a first derivative with an arbitrary spatial variable ξ):

$$\left.\frac{\partial \psi}{\partial \xi}\right|_{F_j(E_i)} = C_i \left.\psi\right|_{E_i} + \sum_k C_k \left.\psi\right|_{E_k} \tag{4.64}$$

where the expression is given for the *jth* face, F_j, of the *ith* control volume in the simulation domain, E_i, and E_k represent the surrounding control volumes (Fig. 3.11). The method may be generalized to also include derivatives at the element centers.

On the other hand, the temporal scheme required for the temporal evolution equations in the problem, i.e., the thermal energy density and parallel internal energy equations, Eqs. (4.44) and (4.48), needs to be chosen based on a trade-off between stability of the method, complexity in its implementation and the toll on numerical resources. The referenced equations are solved using a semi-implicit time-scheme, in line with the one proposed by Mikellides[125] (see Section 4.2.2 and Eqs. (4.72) and (4.73)).

The use of this particular scheme was implemented after trials with fully explicit schemes, which required time-step values for stability in the electron fluid equations that were too restrictive from the point of view of computational resources (see Section 6.2). Likewise, a fully implicit scheme was discarded since this would require either solving simultaneously the momentum, energy and heat-flow equations (which greatly increases the complexity of the numerical method) or doing it iteratively for each particular time-step, which was deemed computationally prohibitive.

Finally, the CC FVM is built on Gauss' theorem and the following approximations:

$$\begin{aligned}
&\text{Gauss' Theorem: } \int_{V_{E_i}} \nabla \cdot \vec{\psi} dV = \oint_{A_{F_j(E_i)}} \vec{\psi} \cdot \vec{n} dA \\
&\oint_{A_{F_j(E_i)}} \vec{\psi} \cdot \vec{n} dA \approx \left(\sum_j \left.\vec{\psi}\right|_{F_j} \vec{n}_{F_j} A_{F_j} \right)\Bigg|_{E_i} \\
&\int_{V_{E_i}} \psi dV \approx \left.\psi\right|_{E_i} V_{E_i}
\end{aligned} \tag{4.65}$$

where $\left.\vec{\psi}\right|_{F_j}$ is a particular vector quantity evaluated at the center of the element face, ψ_{E_i} is a particular scalar quantity evaluated at the element center and $A_{F_j(E_i)}$ and V_{E_i} are, respectively, the lateral area of a face and the volume of a given element. Note that this notation is utilized for the remainder of the chapter to indicate different quantities evaluated throughout the mesh.

The use of the MFAM ensures that for any given element, the normal vectors, $\vec{n}_{F_j}$, which

always point outwards from the element being considered, satisfy:

$$\left.\begin{array}{r}\vec{n}_{F_j}\cdot\vec{1}_{\parallel}=\pm 1\\ \vec{n}_{F_j}\cdot\vec{1}_{\top}=0\end{array}\right\}\text{ for constant }\sigma\text{ faces}$$
$$\left.\begin{array}{r}\vec{n}_{F_j}\cdot\vec{1}_{\top}=\pm 1\\ \vec{n}_{F_j}\cdot\vec{1}_{\parallel}=0\end{array}\right\}\text{ for constant }\lambda\text{ faces} \tag{4.66}$$
$$\vec{n}_{F_j}\cdot\vec{1}_{\theta}=0\text{, for all faces}$$

since each face is considered closely aligned with a constant σ (perpendicular to the magnetic field vector) or λ (parallel to the magnetic field vector) surface, as seen in the detail of an MFAM element in Fig. 3.7.

4.2.1 The generalized Ohm's equation

Equation (4.25) must be satisfied for each position in the simulation domain; particularly, it holds true for each mesh element when integrating over its volume:

$$\int_{V_{E_i}}\nabla\cdot(\vec{j}_e+\vec{j}_i)dV=\int_{V_{E_i}}I_d dV \tag{4.67}$$

this last expression may be transformed, by applying Eq. (4.65), into the following:

$$\left(\sum_j\left(j_{e\top}\vec{1}_{\top}+j_{e\parallel}\vec{1}_{\parallel}+\vec{j}_i\right)\Big|_{F_j}\vec{n}_{F_j}A_{F_j}\right)\Bigg|_{E_i}\approx I_d|_{E_i}\cdot V_{E_i} \tag{4.68}$$

where $I_d|_{E_i}$ is the fraction of the discharge current being introduced into the domain through a particular control volume (see Section 4.2.4); typically, this variable is 0 for the majority of the elements in the simulation domain, but otherwise allows us to introduce the "volumetric cathode", a model first proposed by Maqueda[233].

Combining Eq. (4.68) with the expressions for parallel and perpendicular currents given by the momentum equation, Eq. (4.42), and the GR coefficients for the gradients at element faces, we obtain an equation for each of the control volumes in the simulation domain, with the exception of boundary faces, which are discussed in detail in Section 4.2.3. Each of these equations is a discretized form of a generalized Ohm's equation. The linear system of equations describes the plasma potential at element centers, ϕ_{E_i}, and takes the form:

$$\boldsymbol{\{GR\}\cdot\{\phi_E\}=\{D\}+\{\nabla P\}+\{\nabla B\}+\{J_i\}+\{I_d\}} \tag{4.69}$$

where $\{D\}$ represents a sort of "drag" posed by the heavy species populations, $\{\nabla P\}$ represents the terms associated to electron pressure gradients, $\{\nabla B\}$ the effects of magnetic field non-uniformity, $\{J_i\}$ the ion current density terms in the current continuity equation and $\{I_d\}$ the value of the

current injection term for each of the simulation elements. $\{GR\}$ represents the resulting coefficients *sparse* matrix associated to GR at faces in each element. This set of equations is posed for specific 2D distributions of n_e, n_{iZ} and $\vec{j}_{iZ}$, which are obtained from the corresponding PIC segment time-step, and p_e and $p_{e\parallel}$, which are obtained for a particular NOMADS time-step.

The system of equations in Eq. (4.69) must be posed taking into account BCs (Section 4.2.3) and the existence of current sources external to the simulation domain (Section 4.2.4). When these considerations are taken into account, Eq. (4.69) may be generalized as a sparse system of equations in the form:

$$\boldsymbol{\{S\} \cdot \{\phi_E\} = \{R\}} \tag{4.70}$$

NOMADS employs the PARDISO[234, 235] direct solver for parallelized computation of the solution, although other solvers could be implemented (e.g., LIS[236]). This system of equations requires an electric potential reference imposed within the simulation domain, since the electric potential can only be defined with respect to a given reference[9].

4.2.2 Temporal discretization of the electron fluid model

Equations (4.44) and (4.48) carry the temporal evolution of the problem; as such, the temporal derivatives in the problem are discretized through the temporal scheme. Three different flavors for temporal schemes have been trialled: the *Forward Euler* and *2nd Order Adam-Bashforth* as explicit types and a *Forward-Backward Euler* semi-implicit scheme. For a particular 1st order ODE, we have:

$$\frac{\partial y}{\partial t} = f(t, y, \ldots) \rightarrow \begin{cases} y_{t+\Delta t} = y_t + \Delta t \cdot f(t, y_t) & \text{Forward Euler Method} \\ y_{t+\Delta t} = y_t + \frac{3}{2}\Delta t \cdot f(t, y_t) - \frac{1}{2}\Delta t \cdot f(t - \Delta t, y_{t-\Delta t}) & \text{Adam-Bashforth} \\ y_{t+\Delta t} = y_t + \Delta t \cdot f_i(t + \Delta t, y_{t+\Delta t}) + \Delta t \cdot f_e(t, y_t) & \text{Forward-Backward Euler Method} \end{cases} \tag{4.71}$$

In the Forward-Backward Euler method, f_i groups the part of the equation that may be solved *implicitly*; for the energy equations, this means those contributions in which electron pressure terms appear *explicitly*. On the other hand, f_e represents the part of the equation to be solved explicitly; in our case, those terms that are implicitly dependent with the electron pressure (e.g., the electron current, through Eq. (4.42)).

Before applying the temporal scheme, we integrate the energy equations over an arbitrary

[9] In Section 4.2.4, a potential reference element is addressed in conjunction with externally injected currents; however, the potential reference is needed regardless of if these exist or not.

control volume and apply the relations given in Eq. (4.65), in typical FVM fashion, to obtain:

$$\left.\frac{\partial p_e}{\partial t}\right|_{E_i} = \frac{2}{3V_{E_i}}\left[\left(\sum_j \left.\frac{3}{2}\frac{p_e}{en_e}\vec{j}_e\right|_{F_j}\cdot\vec{n}_{F_j}A_{F_j}\right)\right|_{E_i} + \\ + B^2\left(\frac{3p_e - p_{e\|}}{2e}\frac{\partial\left(rj_{e\top}B^{-1}n_e^{-1}\right)}{\partial\lambda} + \frac{p_{e\|}}{e}\frac{\partial\left(j_{e\|}B^{-1}n_e^{-1}\right)}{\partial\sigma}\right)\Bigg|_{E_i} V_{E_i} - \left(\sum_j \vec{q}_e|_{F_j}\cdot\vec{n}_{F_j}A_{F_j}\right)\Bigg|_{E_i} + \\ + \left(\sum_{Z=1}^{2,3,\ldots}\eta_{eiZ}\frac{Zn_{iZ}}{n_e}\left|\left(\vec{j}_e + \frac{n_e}{Zn_{iZ}}\vec{j}_{iZ}\right)\right|^2 + \eta_{en}\left|\left(\vec{j}_e\right)\right|^2 + \frac{m_e}{2e^2}\frac{S_e\left|\left(\vec{j}_e\right)\right|^2}{n_e^2} + \left.\frac{\delta E_e}{\delta t}\right|_{ioniz+excit}\right)\Bigg|_{E_i} V_{E_i}\Bigg] \tag{4.72}$$

$$\left.\frac{\partial p_{e\|}}{\partial t}\right|_{E_i} = \frac{1}{V_{E_i}}\Bigg\{\left(\sum_j \frac{p_{e\|}}{en_e}\vec{j}_e\Big|_{F_j}\cdot\vec{n}_{F_j}A_{F_j}\right)\Bigg|_{E_i} + B^2\,\frac{2p_{e\|}}{e}\frac{\partial\left(j_{e\|}B^{-1}n_e^{-1}\right)}{\partial\sigma}V_{E_i}\Bigg|_{E_i} - \\ - \left(\sum_j \vec{q}_{e\|}\big|_{F_j}\cdot\vec{n}_{F_j}A_{F_j}\right)\Bigg|_{E_i} + 2\left[q_{e\|\top}r\frac{\partial B}{\partial\lambda} - \left(q_{e\|} - \frac{1}{2}q_{e\|\|}\right)\frac{\partial B}{\partial\sigma}\right]\Bigg|_{E_i} V_{E_i} + \\ + \Bigg\{\sum_{Z=1}^{2,3,\ldots}\eta_{eiZ}\frac{Zn_{iZ}}{n_e}\left[\left(2-\frac{3}{2}\Lambda\right)\left(j_{e\|} + \frac{n_e}{Zn_{iZ}}j_{iZ\|}\right)^2 + \frac{1}{2}\Lambda\left|\left(\vec{j}_e + \frac{n_e}{Zn_{iZ}}\vec{j}_{iZ}\right)\right|^2\right] + \\ \eta_{en}\left[\left(2-\frac{3}{2}\Lambda\right)\left(j_{e\|}\right)^2 + \frac{1}{2}\Lambda\left|\left(\vec{j}_e\right)\right|^2\right] - \frac{3}{2}\Lambda\left(p_{e\|} - p_e\right)\left(\sum_{Z=1}^{2,3,\ldots}\nu_{eiZ} + \nu_{en}\right) + \\ + \left.\frac{\delta E_{e\|}}{\delta t}\right|_{ioniz+excit} + \frac{m_e}{e^2}\frac{j_{e\|}^2}{n_e^2}S_e\Bigg\}\Bigg|_{E_i} V_{E_i}\Bigg\} \tag{4.73}$$

Now, in order to exemplify the semi-implicit approach, we may take Eq. (4.72) together with the simplified heat-flow equation, Eq. (4.63), and apply the temporal scheme as given in Eq. (4.71):

$$p_e|_{E_i}^{t+1} = \frac{2\Delta t}{3V_{E_i}}\Bigg\{\left(\sum_j \left.\frac{3}{2}\frac{p_e}{en_e}\right|_{F_j}^{t+1}\vec{j}_e\Big|_{F_j}^{t}\cdot\vec{n}_{F_j}A_{F_j}\right)\Bigg|_{E_i} + \\ + B^2\left(\left.\frac{3p_e - p_{e\|}}{2e}\right|^{t+1} r\,\frac{\partial\left(j_{e\top}B^{-1}n_e^{-1}\right)}{\partial\lambda}\Bigg|^{t} + \left.\frac{p_{e\|}}{e}\right|^{t+1}\frac{\partial\left(j_{e\|}B^{-1}n_e^{-1}\right)}{\partial\sigma}\Bigg|^{t}\right)\Bigg|_{E_i} V_{E_i} - \\ - \Bigg\{-\left.\frac{5}{2}\frac{p_e}{e}\right|_{F_j}^{t}\sum_j\left[\left.\frac{\beta_{eM^*}}{1+(\beta_{eM^*})^2}\right|_{F_j}^{t}\left(r\,\frac{\partial\left(p_e n_e^{-1}\right)}{\partial\lambda}\Bigg|_{F_j}^{t+1}\right)\vec{1}_\top + \\ + \left(\beta_{e^*M}|_{F_j}^{t}\,\frac{\partial\left(p_e n_e^{-1}\right)}{\partial\sigma}\Bigg|_{F_j}^{t+1}\right)\vec{1}_\|\Bigg]\cdot\vec{n}_{F_j}A_{F_j}\Bigg\}\Bigg|_{E_i} + \\ + \left(\sum_{Z=1}^{2,3,\ldots}\eta_{eiZ}\frac{Zn_{iZ}}{n_e}\left|\left(\vec{j}_e + \frac{n_e}{Zn_{iZ}}\vec{j}_{iZ}\right)\right|^2 + \eta_{en}\left|\left(\vec{j}_e\right)\right|^2 + \frac{m_e}{2e^2}\frac{S_e\left|\left(\vec{j}_e\right)\right|^2}{n_e^2} + \left.\frac{\delta E_e}{\delta t}\right|_{ioniz+excit}\right)\Bigg|_{E_i}^{t} V_{E_i}\Bigg\} + \\ + p_e|_{E_i}^{t}$$

(4.74)

where, for the sake of simplicity in our example, we have only retained the terms from the heat-flow equation associated to gradients of electron pressure. Each of the contributions has been evaluated at different times-steps[10], depending on if its treatment falls onto the implicit or explicit category, hence conferring the scheme its "semi-implicit" nature. In particular, the gradients of $p_e n_e^{-1}$ are the terms that have the most notable impact on the stability of the problem, and hence require the implicit treatment (see Section 6.2).

Equation (4.74), or one like it, may be posed for each of the elements in the simulation domain, leading to a linear system of equations in the form:

$$\boldsymbol{\{p_e\}^{t+1} = \Delta t \left[\left(\{A\}^t + \{Exp\}^t \right) \cdot \{p_e\}^{t+1} + \{Q\}^t \cdot \{GR\} \cdot \{p_e\}^{t+1} + \{CS\}^t \right] + \{p_e\}^t} \tag{4.75}$$

where $\{p_e\}$ represents the electron pressure evaluated at each of domain elements, $\{A\} \cdot \{p_e\}$ represents energy advection, $\{Exp\} \cdot \{p_e\}$ the energy associated with the gas expansion work, $\{Q\} \cdot \{GR\} \cdot \{p_e\}$ the heat-flow terms (where only the gradient of pressure terms are treated implicitly, so that the system of equations remains linear) and $\{CS\}$ the collisional and source terms, which includes the resistive heating term. Again, $\{GR\}$ represents the resulting coefficients *sparse* matrix associated to GR. The terms in the right-hand-side Eq. (4.75) follow the same order as the ones in Eq. (4.74), facilitating the identification of the expressions associated to each term.

4.2.3 Common boundary conditions

Equations (4.69) and (4.75) must be solved taking into account the BCs of the problem since the MFAM is confined by arbitrary domain boundaries which do not, in general, coincide with lines of constant λ and σ, thus truncating MFAM elements, as shown in Fig 4.2.

Boundary elements are treated in a similar way to any other element, with the exception that "face summation" terms ($\sum_j (\ldots)$) now include the boundary face, which must satisfy the BCs for each type of boundary. BC are described in terms of the value of currents and heat-flows at the boundary facet or to the gradients of plasma potential and electron pressure. These are both Neumann type boundary conditions, since fixing the value of currents and heat-flows implies indirectly fixing the value of the associated gradients (of T_e and ϕ) to one that produces the desired value of said vector quantities. Dirichlet type conditions, in this case, would imply directly choosing for values of T_e and ϕ at the boundaries, which does not have a physical rationale.

Boundary conditions may also be coupled to the plasma behavior through plasma sheaths, which exist to self-regulate the plasma flow to the walls (refer to Section 5.1 for an in depth look at the treatment of plasma sheaths in our model). It is worth mentioning that, for these boundaries, the simulation domain only extends to the edge of the plasma sheath, and not to the

[10]The electron density may be evaluated at any given time-step, since NOMADS integrates the electron fluid between two time-steps of the PIC segment, and therefore the density at any position and electron time-step is subject to being linearly interpolated between the entry and exit densities.

physical wall responsible for the existence of the sheath (e.g., the ceramic walls in a HET channel or the conducting wall in the anode).

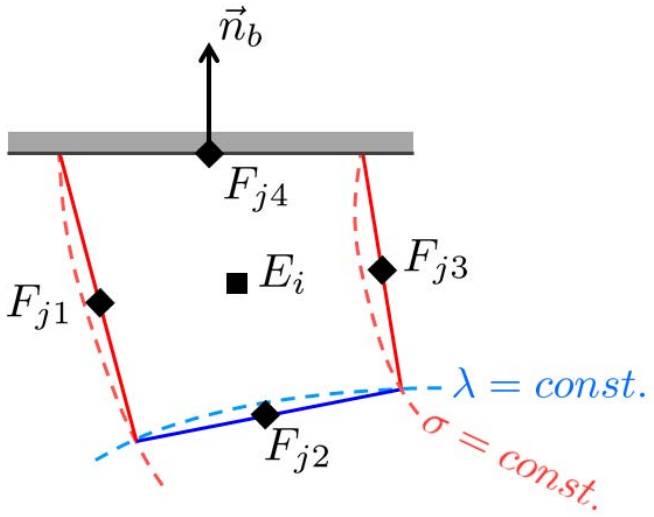

Figure 4.2: MFAM boundary element

Figure 4.3 shows the ensemble of typical BCs the simulation domain for a HET type configuration (the anode boundary and volumetric cathode elements are tackled in Section 4.2.4).

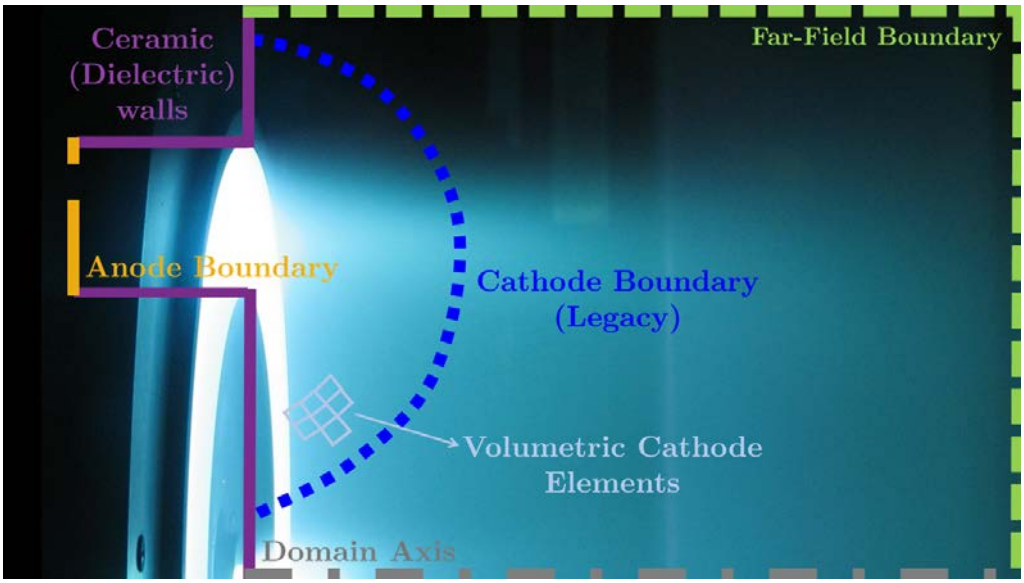

Figure 4.3: Common boundaries used in Hall thruster simulations

We have not included in this work the study of floating (isolated) conducting walls (i.e., passively conducting walls) which can hold electric charge and have sometimes been proposed for HET designs[237]. These boundaries could be treated similarly to anode walls (see Section 4.2.4)

if coupled with a model for the floating potential as a function of the overall current reaching the wall. This topic is left for future efforts.

Far-Field boundaries

The Far-Field boundary (FF) may be considered the "escape" boundary from the domain: it is at these boundaries where the thrust may be computed by recording the momentum of escaping ions and neutrals. A *net* zero-current condition should also be satisfied regardless of the thruster type, as no charging of the space-craft should occur during stationary operation.

On the other hand, these boundaries may be considered sufficiently downstream from the thruster to assume that there is no further variation of the plasma quantities, which can be expressed through a zero-gradient condition. Thus, we may issue either *non-homogeneous Neumann*(1) or *homogeneous Neumann* (2) type boundary conditions for both equation sets:

- Ohm's equation:

$$(1)\quad \left(\vec{j}_e + \vec{j}_i\right)\Big|_{FF} \cdot \vec{n}_b = 0$$

$$(2)\quad \begin{cases} \nabla_b \phi|_{FF} = \vec{n}_b \cdot \nabla\phi|_{FF} = 0 \\ \nabla_b \left(p_e\right)|_{FF} = \vec{n}_b \cdot \nabla \left(p_e\right)|_{FF} = 0 \\ \nabla_b \left(p_{e\|}\right)\big|_{FF} = \vec{n}_b \cdot \nabla \left(p_{e\|}\right)\big|_{FF} = 0 \end{cases}$$

- Thermal energy density and parallel internal energy equations:

$$(1)\quad \begin{cases} \vec{q}_e|_{FF} \cdot \vec{n}_b = 0 \\ \vec{q}_{e\|}\big|_{FF} \cdot \vec{n}_b = 0 \end{cases}$$

$$(2)\quad \begin{cases} \nabla_b \left(\dfrac{p_e}{n_e}\right)\Big|_{FF} = \vec{n}_b \cdot \nabla \left(\dfrac{p_e}{n_e}\right)\Big|_{FF} = 0 \ ; \\ \nabla_b \left(p_e\right)|_{FF} = \vec{n}_b \cdot \nabla \left(p_e\right)|_{FF} = 0 \\ \nabla_b \left(\dfrac{p_{e\|}}{n_e}\right)\Big|_{FF} = \vec{n}_b \cdot \nabla \left(\dfrac{p_{e\|}}{n_e}\right)\Big|_{FF} = 0 \ ; \\ \nabla_b \left(p_{e\|}\right)\big|_{FF} = \vec{n}_b \cdot \nabla \left(p_{e\|}\right)\big|_{FF} = 0 \end{cases}$$

where ∇_b represents the gradient at the boundary and $\vec{n}_b$ the normal vector to the boundary (pointing outwards from the particular element, as in Fig. 4.2).

Note that, for the Ohm's equation, the non-homogeneous Neumann condition is a more restrictive version of the net zero-current condition, as it must be satisfied for each boundary face. The homogeneous Neumann conditions, on the other hand, reflect that the boundary is sufficiently far away from the thruster so that the plasma discharge experiences little change as the domain boundary is crossed. In reality, the plasma plume expansion would drive the behavior of the plasma parameter gradients at the boundary; however this is a sufficiently adequate model for our purposes. It is worth noting that, even with homogeneous Neumann conditions, the fact that the generalized Ohm's law is built upon the current continuity condition ensures that a global net zero-current condition is satisfied.

Domain axis

The axis boundary (Ax), $r = 0$, for an axisymmetric domain carries the "reflection" condition; for *any* given scalar and vector variables we have:

$$\begin{aligned} &(\nabla_b \psi)|_{Ax} = (\vec{n}_b \cdot \nabla \psi)|_{Ax} = \left(\frac{\partial \psi}{\partial \lambda} \right) \Bigg|_{Ax} = 0 \\ &\vec{\psi} \Big|_{Ax} \cdot \vec{n}_b = 0 \end{aligned} \tag{4.76}$$

where, due to symmetry, the domain axis is also a line of constant λ, and thus gradients perpendicular to said boundary are equal to derivatives with respect to λ.

It is worth noting, however, that axis boundary face does not constitute a proper surface in the domain, as the area collapses to zero (i.e. $A_{Ax} = 0$ when $r = 0$). Taking this into account, it is trivial to see that these boundaries, simply, do not contribute to the "face summation" terms $(\sum_j (\ldots) A_{F_j})$ in neither the Ohm's equation nor any of the energy equations. The BCs may be used to calculate fluid properties at the axis, such as the parallel electron currents, for example.

Dielectric wall boundaries

Dielectric or non-conducting walls (D) (typically ceramic type walls in EP devices) have zero current flowing toward the wall in stationary conditions; since electron and ion populations have widely different mobilities and temperatures, a plasma sheath exists to adjust the currents reaching the wall. For a stationary plasma sheath[11], the zero current condition is also carried over to the sheath edge, which represents the limit of the simulation domain. The energy deposited into the sheath and the sheath potential are given by the model governing the sheath response (Section 5.1). A schematic of the dielectric boundary condition can be seen in Fig. 4.4.

For the discretized equations this implies:

- Ohm's equation:

$$\left(\vec{j}_e + \vec{j}_i \right) \Big|_D \cdot \vec{n}_b = 0 \tag{4.77}$$

- Energy deposition in thermal energy density and parallel internal energy equations:

$$\begin{cases} \left(\dfrac{3}{2} \dfrac{p_e}{e n_e} \vec{j}_e \Big|_D + \vec{q}_e|_D \right) \cdot \vec{n}_b = h_{sh_{dielectric}} \left(\vec{j}_i \cdot \vec{n}_b, n_e, \hat{T}_e, T_{e\|}, \alpha_m \right) \\ \left(\dfrac{p_{e\|}}{e n_e} \vec{j}_e \Big|_D + \vec{q}_e|_D \right) \cdot \vec{n}_b = h_{sh\|_{dielectric}} \left(\vec{j}_i \cdot \vec{n}_b, n_e, \hat{T}_e, T_{e\|}, \alpha_m \right) \end{cases} \tag{4.78}$$

where $\hat{T}_e = \dfrac{T_e}{T_{e\|}}$ and α_m is the angle between the magnetic field vector and the normal vector to the wall (see Section 5.1.3). Note that these equations are introduced into Eq. (4.75) and that the sheath energy deposition effectively replaces the advection, $\{A\} \cdot \{p_e\}$, and heat-flow,

[11] The stationary sheath assumption is based on the fact that the response of the sheath is much faster than the time-scales associated to the phenomena in the bulk of the plasma.

$\{Q\} \cdot \{GR\} \cdot \{p_e\}$, terms. Furthermore, since these equations depend on electron temperature in a complex way, they are solved explicitly in the Forward-Backward Euler method from Eq. (4.71) (i.e., using information from the previous electron time-step). The expression for the electron energy deposition at the walls is derived in Section 5.1.

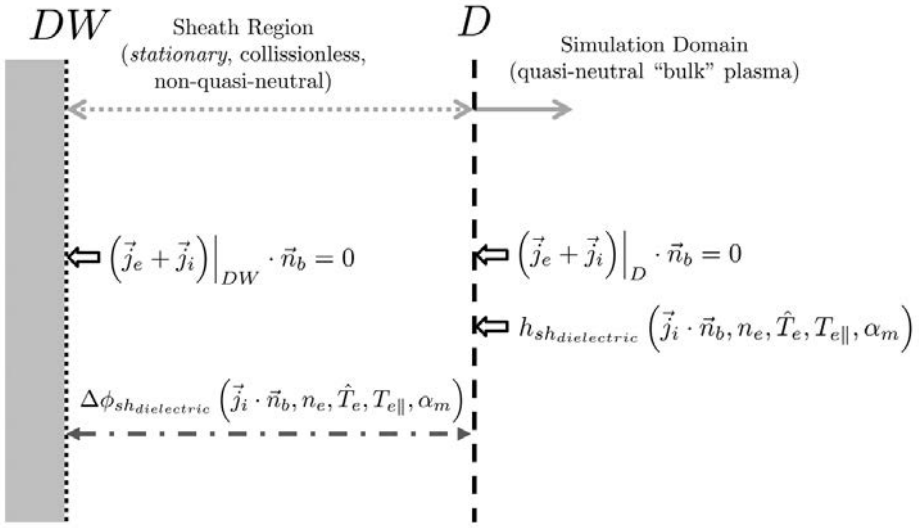

Figure 4.4: Dielectric sheath boundary

An additional output from the sheath model is the potential drop established in the sheath[12], $\Delta\phi_{sh}$:

$$\Delta\phi_{sh}|_D = \Delta\phi_{sh_{dielectric}}\left(\vec{j}_i \cdot \vec{n}_b, n_e, \hat{T}_e, T_{e\|}, \alpha_m\right) \tag{4.79}$$

4.2.4 External current sources

As was discussed in Section 1.1.1, in a HET, the electric circuit (Fig. 1.5) is characterized by a current emitting source (typically a hollow cathode) and a number of conducting surfaces, mainly, the anode.

This section describes the numerical treatment for the elements associated to the electric circuit that drives the operation of a HET. We have not included the study of active electrode surfaces, which appear in what are called multi-stage HETs[132]. These elements, similarly to the PPU control, may be current or potential biased, and they could be simulated by adapting the algorithms for dielectric (Section 4.2.3) and anode walls (Section 4.2.4). This topic is left as future work.

[12]This potential drop is an important value as it determines the acceleration (or deceleration in the case of the, much less likely, repelling sheaths) that ions experience when traversing the plasma sheath, which in turn modifies the energy of impacting ions.

Volumetric cathode

Equation (4.69) allows for a certain discharge current, such as the one provided by the hollow cathode, to be introduced into the equations without the necessity of modeling the cathode response in detail. The injection of current into the plasma may be distributed through multiple mesh elements, which we refer to as the Volumetric Cathode (VC), introduced by Maqueda[233] in HallMa and now adapted for NOMADS. The selection of these "cathode elements" implies that the distribution of volumetric space over which the thruster and cathode plumes interact is known, which is typically not the case (unless the elements selected are located at the physical exit of the cathode); furthermore, the simulation domain must be large enough to capture said interaction, which imposes minimum limits on the size of said domain.

The distribution of discharge current that we have implemented may be done in two ways, either scaled proportionally to the volume of the element, or to its plasma density, with respect to the *total discharge current*:

$$I_d|_{VC} = \frac{V_{E_i}}{\sum_{i\in VC} V_{E_i}} I_d \;;\; I_d|_{VC} = \frac{n_e|_{E_i}}{\sum_{i\in VC} n_e|_{E_i}} I_d \tag{4.80}$$

In addition, the *energy advection*, $\{A\}\cdot\{p_e\}$, and *gas expansion*, $\{Ex\}\cdot\{p_e\}$, terms in Eqs. (4.72) and (4.73) are modified by replacing the electron pressure by one based on a certain "cathode temperature", which is a parameter in the simulation and can be considered isotropic with respect to the directions of the problem:

$$T_{e_{Cath}} = T_{e\|_{Cath}} \tag{4.81}$$

The pressure term is replaced only in those expressions and represents the energy introduced into the domain through the cathode.

Finally, the total discharge current, I_d, may be decided in two ways, depending on the operation mode of the PPU:

- Constant voltage mode: this is the typical operation mode in a HET; a particular element amongst the volumetric cathode elements is designated as the "cathode potential reference element":

  $$\phi_{E_{\phi 0}} = \phi_0$$

  which constitutes a fixed potential within the simulation domain. Typically, a second potential reference is that of the anode wall[13] so that the discharge potential in the simulation is given by:

  $$V_d = \phi|_{AW} - \phi_0 \tag{4.82}$$

[13] Since the anode is made of conducting material, the anode potential represents that of the whole wall.

where $\phi|_{AW}$ represents the electric potential at the anode wall, but not at the anode BC, since the simulation domain only extends up to the sheath edge (see the next subsection for the treatment of said sheath). The total discharge current, I_d, in the simulation appears naturally by integrating the electron and ion current densities at every actively conducting surface, i.e., the anode boundary and the electrodes (see Fig. 1.5).

The equation associated to the cathode potential reference element is substituted in the system of equations portrayed in Eq. (4.70), simply, by:

$$\{s_i\} \cdot \phi_{E_{\phi 0}} = s_i \phi_0 \tag{4.83}$$

where s_i is the coefficient in the sparse matrix associated to the cathode potential reference element, we use it so that the condition number for said matrix remains unaltered when replacing the equation for the said element.

The cathode potential reference element is unique in the MFAM, however, the number elements in the volumetric cathode may be larger than one; in this case, we must operate in the system of equations since the total discharge current is unknown prior to solving Eq. (4.69). The right hand side in Eq. (4.70) for an element belonging to the volumetric cathode takes the form:

$$\{R\}|_{i \in VC} = \alpha_i I_d - \{R^*\}|_{E_i}$$

where α_i represents the fraction of I_d for that particular element, as in Eq. (4.80), and $\{R^*\}$ any term in the electron current density equations that does not depend on the electric potential, plus the ion current density terms. Now, for each element belonging to the volumetric cathode, we subtract a multiple of the equation for the cathode potential reference element, before substituting it by Eq. (4.83), like so:

$$\begin{cases} S^*_{i \in VC} = S_{i \in VC} - \dfrac{\alpha_i}{\alpha_{E_{\phi 0}}} S_{E_{\phi 0}} \\ R^*_{i \in VC} = R_{i \in VC} - \dfrac{\alpha_i}{\alpha_{E_{\phi 0}}} R_{E_{\phi 0}} = \dfrac{\alpha_i}{\alpha_{E_{\phi 0}}} \{R^*\}|_{E_{\phi 0}} - \{R^*\}|_{i \in VC} \end{cases}$$

By doing this we obtain a system of equations that is equivalent to the original and allows for current to be distributed amongst various domain elements when the plasma potential is fixed in one of them.

- Constant current mode: the total discharge current, I_d, is chosen as a parameter in the simulation and distributed in the volume cathode elements as per Eq. (4.80). The discharge

potential in the simulation is given by the difference in electric potential between the chosen anode potential and the average of electric potentials in the volumetric cathode:

$$V_d = \phi|_{AW} - \frac{\sum\limits_{i \in VC} \phi_{E_i}}{\sum\limits_{i \in VC} i} \tag{4.84}$$

Anode wall boundary

In HETs, part of the discharge current emitted by the cathode, together with the electron current generated in the main ionization region of the thruster, travels to the Anode Boundary (AB) and is absorbed by it. The electric potential in the anode wall, $\phi|_{AW}$, is chosen as a simulation parameter, but the current extracted at a certain anode wall face is determined by a plasma sheath that appears in the vicinity of the boundary. This sheath is in charge of permitting a certain electron current through, depending on the potential drop across it:

$$\vec{j}_e\Big|_{AB} \cdot \vec{n}_b = j_{sh_{conducting}}\left(\Delta\phi_{sh}, n_e, \hat{T}_e, T_{e\|}, \alpha_m\right) \; ; \; \Delta\phi_{sh} = \phi|_{AB} - \phi_{AW} \tag{4.85}$$

where, because the sheath is established for a conducting material, the ion current no longer appears as an input into the model. Note that ϕ_{AB}, the electric potential for a particular face belonging to the anode BC, is at the limit of the simulation domain, equal to the potential at the anode sheath edge and different from the electric potential at the anode wall, as seen in Fig. 4.5.

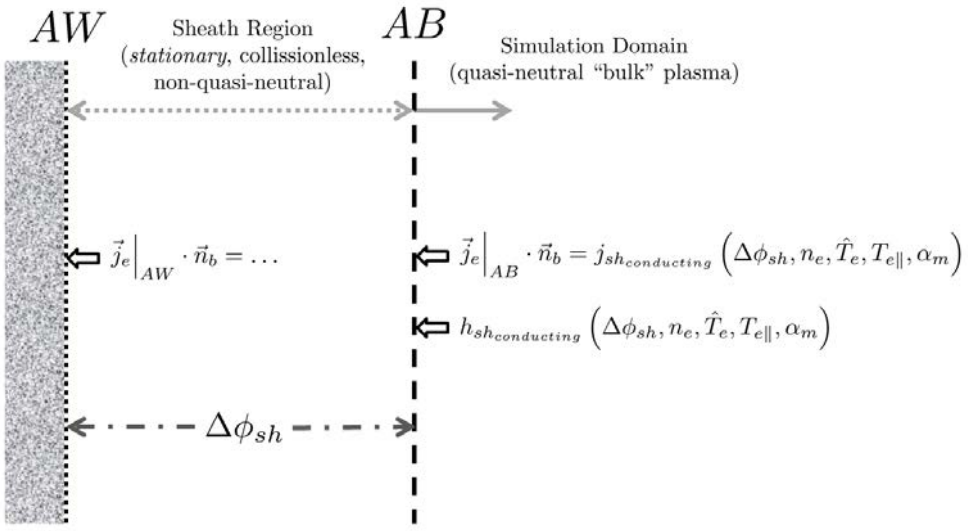

Figure 4.5: Anode sheath boundary

Equation (4.85) may be used to replace the contribution of $\vec{j}_e \cdot \vec{n}_b$ in Eq. (4.68); however, in order to be able to incorporate this condition into Eq. (4.68) in such a way that Eq. (4.69) remains a linear system of equations, $j_{sh_{conducting}}$ must be linear with $\Delta\phi_{sh}$. Since the conducting

sheath model (discussed in Section 5.1) establishes a relation between the previous variables that is generally non-linear, we introduce the BC by linearizing around a certain "guess" or expected value of the sheath potential drop, $\Delta\phi^*_{sh}$:

$$\vec{j}_e\Big|_{AB} \cdot \vec{n}_b = j_{sh_{conducting}}\left(\Delta\phi^*_{sh}, \dots\right) + \frac{\partial j_{sh_{conducting}}}{\partial \Delta\phi_{sh}}\left(\Delta\phi^*_{sh}, \dots\right) \cdot \left(\Delta\phi_{sh} - \Delta\phi^*_{sh}\right) \tag{4.86}$$

The last issue, notwithstanding, is that $\phi|_{AB}$ in Eq. (4.85) is part of the solution and therefore unknown prior to solving the system of equations. This is solved by expressing the value of said potential through GR, as a linear combination of values of ϕ_{E_i} at the surrounding elements, in a similar way to Eq. (4.64).

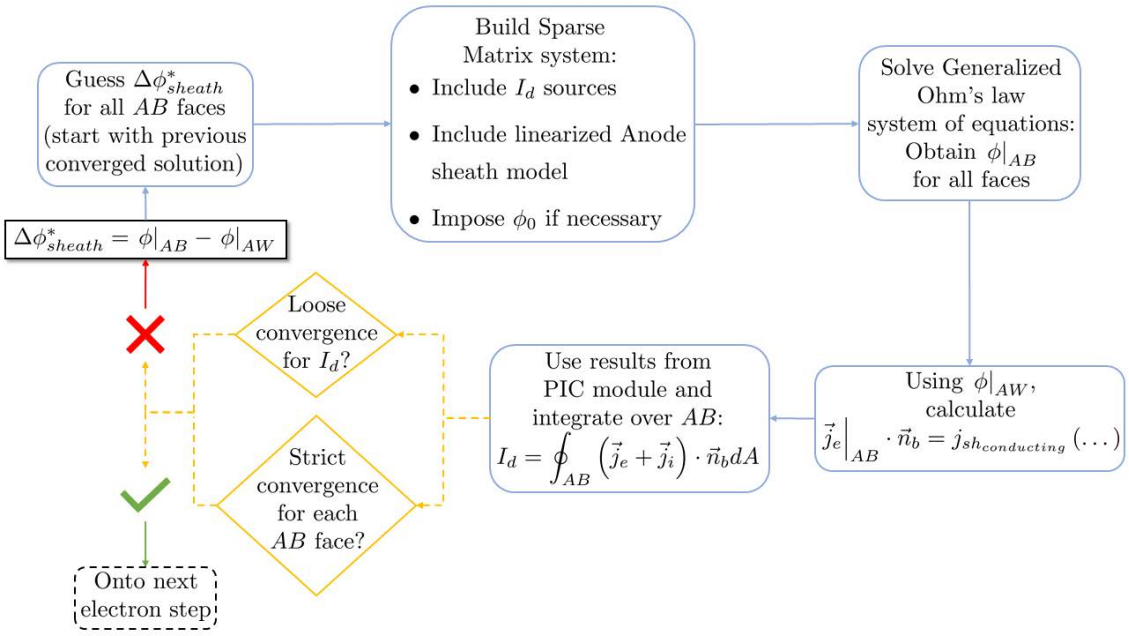

Figure 4.6: Iterative matching algorithm scheme

This methodology lends itself to being tackled through the *Newton-Raphson method*, if the guess value $\Delta\phi^*_{sheath}$ is substituted on each iteration of the method by the value for the sheath potential drop obtained from the solution of the linear system of equations in the previous iteration[14]. We have termed this method the "iterative matching" algorithm, which solves Ohm's system of equations in each iteration in order to find a condition for the anode sheath that is compatible with the current being introduced through the volumetric cathode. The convergence criteria then becomes the *matching* of currents extracted at each anode BC face with the ones traversing the simulation domain (strict convergence) or the *matching* of the total current extracted at the anode and the current injected through the volumetric cathode (loose convergence). This

[14]The initial guess in the simulation is given by assuming that the dimensionless sheath potential drop is equal to 1, i.e. $\frac{e\Delta\phi^*_{sheath}}{T_e\|} = 1$. See Section 5.1.3 for further reference.

is done to a certain tolerance, chosen as a parameter of the simulation. Figure 4.6 provides a schematic of the algorithmic flow in the iterative matching scheme.

This method supposes a major departure from how the anode BC was implemented in codes such as HPHall or HallMa, where the near-anode-region was solved only by approximation. We propose that this new approach could be used to simulate TAL type HETs, although we have not yet trialled this possibility.

Finally, similarly to dielectric walls, the energy equations accept an energy deposition term that replaces heat-flow, while advection due to the normal drift velocity is retained:

- Energy deposition in thermal energy density and parallel internal energy equations:

$$\begin{cases} \left(\frac{3}{2}\frac{p_e}{en_e}\vec{j}_e\Big|_{AB} + \vec{q}_e|_{AB} \right) \cdot \vec{n}_b = h_{sh_{conducting}} \left(\Delta\phi_{sh}, n_e, \hat{T}_e, T_{e\|}, \alpha_m \right) \\ \left(\frac{p_{e\|}}{en_e}\vec{j}_e\Big|_{AB} + \vec{q}_e|_{AB} \right) \vec{n}_b = h_{sh\|_{conducting}} \left(\Delta\phi_{sh}, n_e, \hat{T}_e, T_{e\|}, \alpha_m \right) \end{cases} \tag{4.87}$$

and these terms are solved explicitly in the semi-implicit scheme.

CHAPTER
FIVE

Ancillary physical models

This chapter deals with the ancillary models that complete the electron population fluid model presented in Chapter 4; specifically, the chapter centers on the model for the plasma boundary layer, also known as the plasma sheath, required for BCs associated to material walls in the thruster. Additionally, models for various collisional processes such as ionization, excitation and elastic momentum transfer are reviewed in detail.

The models presented here are coded into the SHEATH_MODEL and PROPELLANT_CHAR `Matlab` scripts and thus share the particularity that the results they provide are stored in `HDF5` look-up-table data format, which are then accessed during processing time by an N-dimensional multi-linear interpolator with no extrapolation, based on a generalization of the well known bilinear interpolation method. This approach spares us from calculating the complex and multivariate solution for these models within the `CORE`, which would imply an additional toll over computational resources employed by the code.

5.1 Arbitrary magnetic angle bi-Maxwellian sheath model

The plasma sheath model for HYPHEN was developed taking into account previous advances made by Ahedo[151, 238] and De Pablo[239, 240], which expanded the model proposed by Hobbs and Wesson[241] by introducing a macroscopic approximation for the electron population in the sheath. These advances allowed to consider the depletion of high energy electrons in the bulk of the plasma, the influence of SEE beams reflecting between sheaths in opposing walls, the effect of the magnetic angle at the wall, and other effects. Particularly, the model presented in Ref. [240] was successfully implemented in HPHall-2[233] and is the basis for the HYPHEN sheath model; its contribution was a considerable step forward in the correct modeling of plasma wall interactions for plasma conditions representative of HETs.

This section does not include a description on the well known Kinetic Bohm condition; the pre-sheath region and its treatment in HYPHEN were discussed briefly in Section 2.2.1.

5.1.1 Introduction

As is made clear in Sections 1.2.4 and 4.2, the plasma boundary conditions for physical walls require special treatment and the introduction of particular models which affect both the electron fluid and ion population.

It has been previously stated that HYPHEN uses a null Debye length approximation, $\lambda_D \approx 0$, and a *quasi-neutral* assumption for the whole of the simulation domain. It is well known, however, that non-quasi-neutral regions appear whenever the plasma is confined by material walls, as boundary layers. These regions are known as plasma sheaths, and exist in order to adjust the total current reaching the wall.

Plasma sheaths play a prominent role in the deposition of electron and ion energy in the walls, as well as ion recombination, which, in the case of EP thrusters, represent sources of inefficiency and take a toll on the overall performances. In the classical problem, due to the high mobility of electrons, the wall potential adjusts itself negatively with respect to the quasi-neutral bulk plasma potential, limiting the electron current reaching the wall[1]. The sheath is thus "negative", and the sheath potential drop, $\Delta\phi_{sh}$, modifies the Ion Energy Distribution Function (IEDF) of the ion population, accelerating the ions and thus, negatively affecting wall erosion and limiting thruster life. Under certain conditions, the sheath can become "positive", repelling ions and accelerating electrons, which can sometimes occur in plasma sheaths around conducting walls; Section 6.8 discusses the matter in the context of a NOMADS simulation.

In the presence of physical walls, as was justified in Section 4.1.1, the simulation domain extends only up to the sheath edge, while the sheath itself represents the transition region between the quasi-neutral domain and the wall, as depicted in Fig. 5.1.

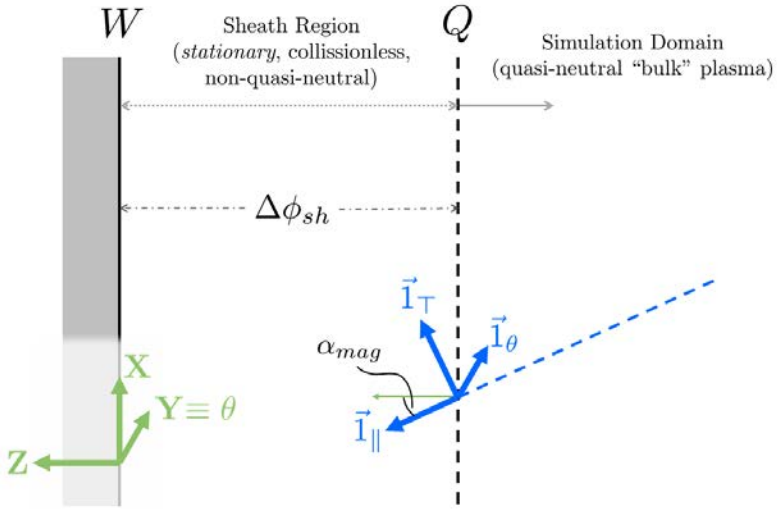

Figure 5.1: Sheath region and reference frame

Note the nomenclature in Fig. 5.1 for positions in the sheath: Q represents the sheath edge, W represents the material wall and α_m represents the angle between magnetic field vector at the wall and the normal vector to the wall. This "magnetic angle" comes into play when considering the anisotropicity of the electron population reaching the sheath edge. If in the sheath reference

[1] In the case of dielectric walls, which admit no electrical charge, the electron current may only be equal and opposite to the ion current. In the case of conducting walls, this current depends on what is absorbed by said wall, either through an external circuit or to the limit imposed by the wall floating potential.

frame (Fig. 5.1) the direction normal to the wall is labeled as z, the magnetic angle can be defined as:

$$\alpha_m = \arcsin\left(|\vec{1}_{\parallel} \times \vec{1}_z|\right) \tag{5.1}$$

The sheath typically retains a thickness of the order of a few Debye lengths, which justifies considering it as a non-quasineutral region. This thickness is smaller than any characteristic length in our problem, L, and also smaller than the typical collision mean free path:

$$\lambda_D \ll L, MFP$$

The sheath can generally be considered planar ($\sim 1D$) and, since the Debye length is negligible in comparison to the MFP, collissionless; for our purposes, it is also considered non-magnetized based on further assumptions in Section 5.1.3 (i.e., the magnetic field does not influence the behavior within the sheath).

5.1.2 Physical mechanisms in plasma sheaths and plasma-wall interaction

This section briefly describes the variety of physical mechanisms taking part in the sheath model. The sheath is non-quasineutral and collisionless and thus the EVDF is unknown. We can make a strong assumption on its form by approximating it to a Maxwellian distribution, which also helps us to visualize some of the mechanisms described here. For the purpose of this section, we also consider the sheath to be negative.

Now, since the sheath is collisionless and its representative spatial scales are negligible, the EVDF only depends on the *constants of motion*, which is the solution from the Vlasov equation, discarding the collisional term in Eq. (1.16). The energy conservation equation may be invoked in the direction perpendicular to the planar sheath, using the notation shown in Fig. 5.1:

$$\frac{1}{2} m_e v_{pz}^2 - e\phi = \text{const.} \tag{5.2}$$

where the subindex p stands for *primary*, and refers to the electron population reaching the wall from the bulk of the plasma. For an electron to reach the wall, its velocity must satisfy $v_{pz}|_W \geq 0$; the velocity at the sheath entry, Q, then satisfies:

$$\left.\begin{array}{l} \Delta\phi_{sh} = \phi_Q - \phi_W > 0 \\ v_{sh} = \sqrt{\dfrac{2e\Delta\phi_{sh}}{m_e}} \end{array}\right\} \rightarrow v_{pz}|_Q - v_{sh} = v_{pz}|_W \geq 0 \tag{5.3}$$

where v_{sh} represents the axial energy "lost"[2] to the sheath potential fall.

[2]For $\Delta\phi_{sh} > 0$, the energy is lost to electrons but added to ions traversing the sheath with a factor that depends on the ion charge number, as: $\sqrt{Z}v_{sh}$.

Electron collection Electrons reaching a physical wall may recombine together with ions to form neutral atoms or be collected by the wall (potentially interacting with other electrons). These mechanisms occur for both dielectric walls (non-conducting materials, e.g., ceramics), and conducting walls (e.g., metallic materials).

Electrons collected at the wall or taking part in the ion recombination process are *removed* from the primary EVDF: since only electrons with velocities sufficient to surpass the sheath potential drop are able to reach the wall (all other electrons being electro-statically reflected by the sheath, see Fig. 5.2). This constitutes a "sink" for the high-energy tails of the primary EVDF, which may become partially or completely depleted, unless a physical mechanism for replenishment of said tails is present. This partial depletion is characterized in the model by the *thermalization fraction* parameter, $\sigma_{th} \leq 1$, which is the fraction of electrons with energies higher than the sheath potential drop that are replenished by some thermalization mechanism in the bulk of the plasma. The concept of depleted tails can be represented by a *truncated* Maxwellian, as seen in Fig. 5.2.

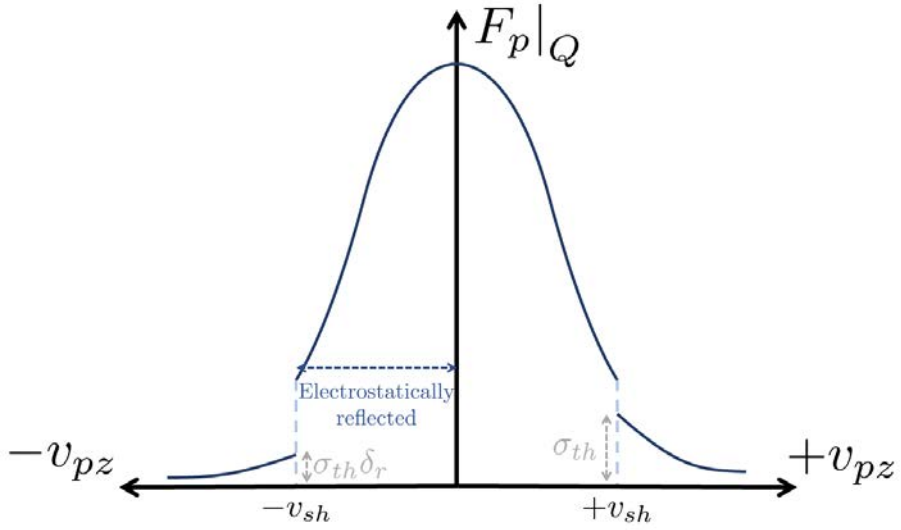

Figure 5.2: Partially depleted high-energy tails on the z-velocity-space for the primary EVDF

Fig. 5.2 only shows the v_z component of the Maxwellian, i.e., the direction normal to the wall; all other directions are not truncated. The negative branch of the velocity space represents the distribution function for electrons either electro-statically reflected or backscattered *from the wall* (addressed next), and includes the fraction of backscattered electrons, δ_r. The positive branch represents the part of the distribution function traveling *towards the wall* and includes the thermalization fraction.

Ahedo and other authors[242, 173] demonstrated that "complete" tails of the EVDF ($\sigma_{th} = 1$) produce excessive energy losses in the discharge of a HET, further making the case for partially depleted tails. The standing theory is that the bulk plasma presents a limited collisionality for high energy electrons, due to the characteristic MFP, which is not sufficient

to fully replenish the high energy tails of the distribution. A certain balance, described by the σ_{th} parameter, is established, based on the capacity of replenishment in the plasma and the high energy electron sink represented by the material wall. Since the high energy tails are never fully refilled, this mechanism can be seen as an energy loss to the sheath, which cools the bulk plasma[243], representing one of the main sources of performance loss in the thruster. The depleted tails of the distribution also imply a non-Maxwellian bulk electron population.

Backscattered or reflected electrons Electron backscattering is present due to a combination of inelastically and elastically reflected[3] electrons at the wall. Taccogna[153] proposed a model for the *yield*, or fraction, of backscattered electrons, δ_r, relative to the incoming electrons, based on experimental results by Schwarz[244]. This model may be simplified, for a *normal incidence angle* of incoming electrons, to an exponentially decaying law:

$$\delta_r \approx \delta_0 \cdot \exp\left(-E/E_r\right) \tag{5.4}$$

where the subindex r stands for *reflected*. The variable E represents the impacting electron energy, and the crossover energy, E_r, and δ_0 are the model parameters for a particular material. For example, for a typical Boron-Nitride ceramic wall, $E_r \approx 40-50eV$ and $\delta_0 \approx 0.4-0.6$ (see Ref. [153]). The model considers no partial accomodation of the impacting electron energy, which would be expected for *inelastic* reflections. In general, inelastic reflections are compounded into a single model together with SEE, as shown by Barral et al.[124]. These effects are considered outside of the current scope of our model, but could be introduced through additional parameters in future iterations.

Secondary Electron Emission (SEE) Secondary Emission refers to those electrons which are released from internal layers of the wall material (typically, dielectric materials) under impact of incoming electrons (and also other particles) with sufficiently high energy[146]. In our model we use the term SEE to refer only to this phenomenon, in principle, excluding backscattered electrons. Historically, this is refered to as "true" secondary electrons or *beam* electrons, due to the *quasi-monoenergetic* nature of the "secondary" population (Fig. 5.3). The model for the SEE yield, δ_b, relative to the incoming electrons, is the one used by Ahedo and De Pablo[240], introduced by Fife[76]:

$$\delta_b = (E/E_b)^p \tag{5.5}$$

where the subindex b stands for *beam*. Again, E is the impacting electron energy, and the crossover energy, E_b, and p are the model parameters for a particular material; for Boron-Nitride, the crossover energy, $E_b \approx 40 - 50eV$ and $p \approx 1$.

The secondary population has been the subject of much study, its existence modifies the sheath potential drop and the energy losses to the walls, and has an effect on the advent of the Charge Saturation Limit (CSL) and CSR. It may be modeled as a low-dispersion

[3] Not to be confused with the *electro-statically* reflected electrons due to the sheath potential drop.

Maxwellian EVDF with a beam temperature $T_b \approx 1 - 3eV$, which is then accelerated by the sheath potential drop to a quasi-monoenergetic beam, as seen in Fig. 5.3.

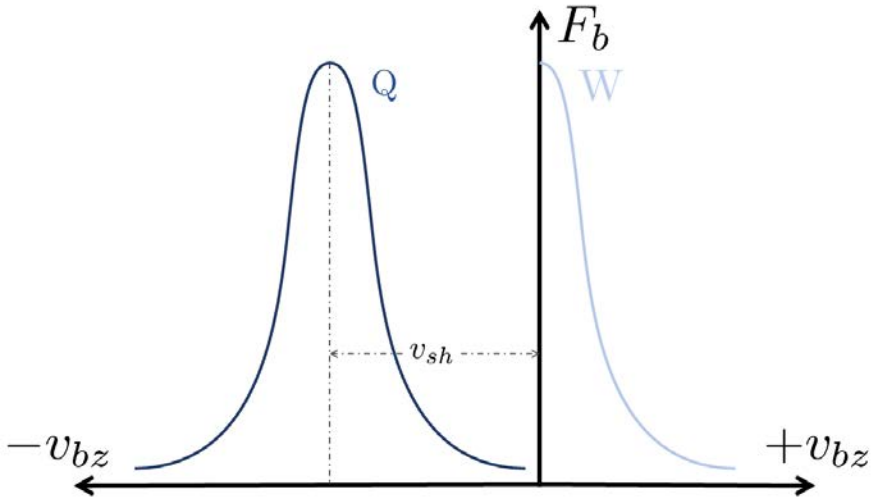

Figure 5.3: Change in the SEE beam z-velocity-space EVDF due to acceleration in the sheath

This high energy beam is weakly collisional and does not thermalize quickly with the bulk plasma, as pointed out by Ahedo and Parra[245], and may be subject to confinement by the magnetic field. Its treatment as a proper secondary population in NOMADS is outside of the scope of this thesis; however, the SEE beam acts as one of the possible sources for replenishment of the primary population tails in the sheath model (the other being the bulk electron population itself) and is partly responsible for the thermalization fraction parameter σ_{th}. Conceptually, the reeincorporation of the SEE beam into the bulk plasma must be taken into account by the thermalization fraction, which should be a *function* of the secondary population MFP, the plasma parameters and the thruster geometry and magnetic topology[100]. Nevertheless, in the absence of a particular treatment for this population, we may assume $\sigma_{th} = \text{cnst.}$, as proposed by Sydorenko et al.[243]

Charge Saturation Limit and Regime Both Riemann[149] and Hobbs and Wesson[241] studied the limit of a monotonic solution for the sheath potential drop: by integrating the Poisson equation,

$$\frac{d^2\phi}{dz^2} = \epsilon_0 \left(n_e - n_i\right) \tag{5.6}$$

across the sheath, for a cold ion population. A null electric field at the wall, $\left.\frac{d\phi}{dz}\right|_W = 0$, which is known as the CSL, represents the limit after which the sheath potential is no longer monotonic and may present particles trapped by an electric potential barrier, from the perspective of the electrons coming the wall (Fig. 5.4). This phenomenon can occur in secondary electron emitting walls when the primary electron flux is much larger than the

ion flux[240] or when the walls are very emissive, and the yield of SEE due to impacting primary electrons becomes so large (comparable to, or larger than, the primary flux[151]) that the sheath potential must trap the emitted secondary electrons to enforce the null current condition.

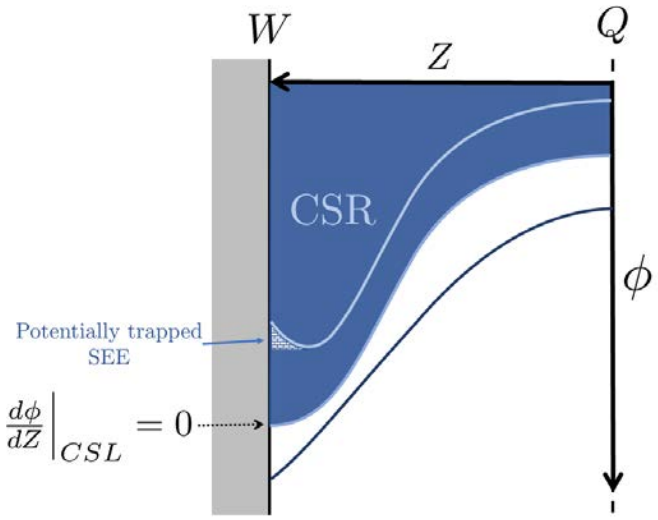

Figure 5.4: Various sheath potential profiles: normal regime, Charge Saturation Limit and Charge Saturation Region

The CSL represents the transition between the "normal" operating regime for the sheath and the CSR, as seen in Fig. 5.4. The condition for the normal regime then can be found to be equivalent, through integration of the Poisson equation, to:

$$\left.\frac{d\phi}{dz}\right|_W \leq 0 \rightarrow \int_{\phi_W}^{\phi_Q} \left(\sum_{Z=1}^{2,3,\ldots} Z n_{iZ} - n_e \right) d\phi \geq 0 \tag{5.7}$$

which takes into account the possibility of multiply charged ions. A particular solution for the CSR is outside of the scope of this simple sheath model: this regime is treated, as was done by Ahedo and De Pablo[240] by extrapolating the conditions under which the CSL is reached, particularly, by assuming that the dimensionless sheath potential drop remains constant:

$$\left.\Delta\hat{\phi}_{sh}\right|_{CSR} = \text{const.} = \left.\frac{e\Delta\phi_{sh}}{T_e}\right|_{CSL} \tag{5.8}$$

5.1.3 Sheath model assumptions and formulation

This section describes the formulation for a 1D (normal-to-the-wall), two-temperature, fluid sheath model. In addition to the planar and collisionless assumptions, we consider the following:

- We assume that the Debye length (i.e., the sheath characteristic size) is small in comparison to the Larmor radius, $\lambda_D \ll r_L$, in addition to the other characteristic lengths in the

problem. This allows us to avoid considering magnetic or kinetic effects in the sheath. Mathematically, this assumption may be expressed, using the thermal velocity definition for the Larmor radius, as:

$$\lambda_D \ll r_L \rightarrow \sqrt{\frac{\epsilon_0 k_B T_e}{n_e e^2}} \ll \frac{m_e \sqrt{\frac{2k_B T_e}{m_e}}}{eB} \rightarrow \sqrt{\frac{2m_e n_e}{B^2 \epsilon_0}} \gg 1$$

and a hierarchy of spatial scales in the problem can therefore be established, considering the characteristic length in the problem, L, as:

$$\lambda_D \ll r_L \ll L$$

Effectively, electrons enter the sheath with a particular velocity vector which depends on the EVDF, the magnetic angle at the sheath edge and the gyro-phase, and are accelerated "instantly" in the perpendicular direction to the sheath, as seen in Fig. 5.5:

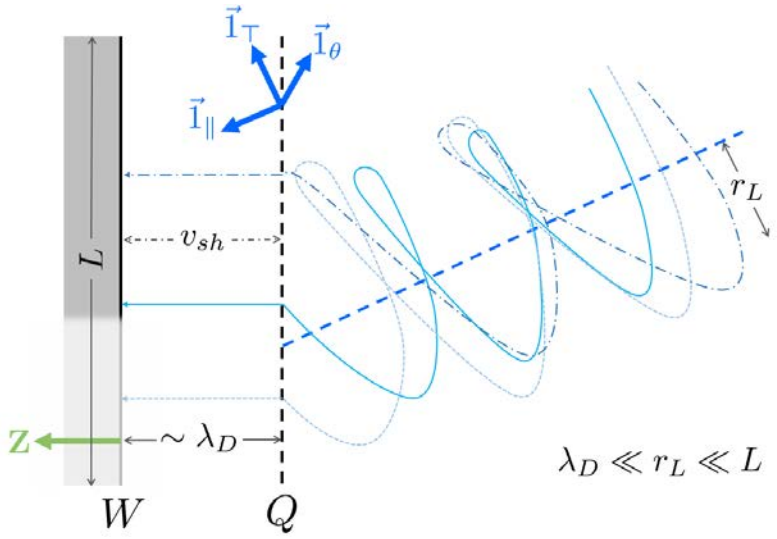

Figure 5.5: Electrons accelerate "instantly" in the planar sheath

- The primary electron population will be modeled as a truncated, non-drifting, bi-Maxwellian EVDF, expanding from the simple Maxwellian used in Section 5.1.2 to take into account the anisotropicity of the bulk electron fluid model, given in Section 4.1. Note that, again, the collisionless and non-quasineutral characteristics of the sheath boundary layer make it difficult to predict the shape of the DF, and therefore this can be considered a *strong* assumption. Backscattered and electro-statically reflected electrons are assumed to return to the primary EVDF with the same properties as before the reflection took place (including anisotropicity).

- We consider that, at the sheath edge, Q, the bulk electron fluid and the sheath fluid model can be linked assuming that the relevant temperatures in the primary and bulk plasma

distributions, the bulk plasma density and total electron density in the sheath, and the perpendicular-to-the-sheath electron particle and energy-fluxes are equal:

$$
\begin{aligned}
&T_e|_Q = T_p|_Q \;\; ; \;\; T_{e\parallel}\big|_Q = T_{p\parallel}\big|_Q \\
&n_e|_Q = \left(n_{p^+} + n_r + n_b\right)\big|_Q = \sum_{Z=1}^{2,3,\ldots} Z n_{iZ}|_Q \\
&g_{ez}|_Q = \left(g_{p^+z} - g_{rz} - g_{bz}\right)\big|_Q \\
&h_{ez}|_Q = \left(h_{p^+z} - h_{rz} - h_{bz}\right)\big|_Q
\end{aligned}
$$

where the subscripts $p+$, r and b stand for, respectively, electrons from the primary distribution with $v_{pz}|_W \geq 0$ (which we also refer to as *impinging* primary electrons), electrons reflected by the wall (or backscattered) and beam secondary electrons (due to the SEE phenomenon). Note that the energy-flux is represented by the quantity h, which was introduced in Section 4.2.3 as the energy deposited by the electron fluid at the sheath boundary.

- Considering the assumption above, the sheath is also *stationary*, for the time scales we wish to resolve (i.e., the sheath reacts instantly to changes in the bulk plasma quantities).

- The limit of the model is $\Delta\phi_{sh} \geq 0$; this means that sheath reversals, which occur mainly in conducting walls[246, 247] are not explicitly part of the sheath model. Nonetheless, sheath reversal is allowed in the HYPHEN `CORE` and is informed by the largest electron current that may be allowed by the sheath, which coincides with the $\Delta\phi_{sh} = 0$ limit.

- The model presented by Ahedo and De Pablo[240] considers the possibility of multiple reflections between opposing material walls (and sheaths) for the non-thermalized fraction of the SEE beam and their effect on the sheath. Since the treatment of secondary electrons and their interaction with the bulk plasma requires more detailed analysis, we have decided to forgo this aspect of the model.

- Various authors[153, 244, 248] explore the effect of the incidence angle of impacting electrons on the various yields: δ_r, δ_b. Amongst them, Schwartz[244] found that this effect is mostly relevant to high impact energies of the order of the cross-over energies. The incidence angle at the wall depends on the magnetic angle at the sheath entry, α_m, and kinetic effects in the sheath, which cannot be neglected if the sheath thickness is comparable to, $\lambda_D \approx r_L$, or larger than, $\lambda_D \gg r_L$, the Larmor radius. Considering our assumption on the hierarchy of spatial scales, the yields used only retain the effects related to *normal incidence*. The inclusion of the incidence angle effect on the yield models may be explored in the future.

The primary distribution function (including reflected electrons) is truncated and described as a *non-drifting* bi-Maxwellian DF. This function may be defined, at the material wall, as:

$$
F_p|_W = \sigma_{th}\left(1 - \delta_r\right)\cdot F \;\; \forall \;\; |v_{pz}|_W \geq 0 \;\; ; \;\; F = \frac{n_p}{\left(2\pi\right)^{2/3}} \left(\frac{m_e}{T_{p\parallel}}\right)^{1/2} \frac{m_e}{T_{p\perp}} \exp\left(-\frac{m_e v_{p\parallel}^2}{2T_{p\parallel}} - \frac{m_e v_{p\perp}^2}{2T_{p\perp}}\right) \quad (5.9)
$$

where n_p is a characteristic density of the primary EVDF which is part of the solution for the model. The truncated form of the distribution function at the wall is determined by the fraction of the population with sufficient energy to reach the wall, represented by σ_{th}, minus the fraction of electrons reflected by the wall, represented by δ_r.

Note that, while the bulk plasma fluid model considers that the bulk electron population exhibits a drift velocity, our sheath model avoids including a drift term. It would be possible to include such a term and consider that both models have the same drift velocity at the sheath edge, Q; however, this would increase the dimensionality of the problem, since said drift velocity would act as a free parameter, enlarging the number of parameters in the "look-up" tables. Since, in any case, the drift velocity in the bulk plasma (and therefore at the sheath edge) can be neglected versus the thermal velocity (as per our assumptions in Section 4.1.1), we also neglect it for the primary population in the sheath. This reduces the parameters in the model that are related to the bulk electron population solely to the electron temperatures and density. Equation (5.9) therefore satisfies:

$$\vec{u}_p \approx \vec{0} \; ; \; \vec{c}_p \approx \vec{v}_p$$

Considering the reference system introduced in Fig. 5.1 and Eq. (5.1), the parallel and perpendicular velocities may be related to:

$$\left.\begin{array}{l} v_{p\parallel} = v_{pz}\cos\alpha_m + v_{px}\sin\alpha_m \\ v_{p\perp}^2 = v_y^2 + \left(v_{pz}\sin\alpha_m - v_{px}\cos\alpha_m\right)^2 \end{array}\right\} F = F\left(v_{px}, v_{py}, v_{pz}, \alpha_m, T_p, T_{p\parallel}\right)$$

which may be accompanied by the constants of motion complementary to Eq. (5.2):

$$v_{px} = \text{const.} \; ; \; v_{py} = \text{const.} \tag{5.10}$$

Equations (5.2) and (5.10) may be linked to a *functional form* of the EVDF used in Eq. (5.9), for the stationary and colissionless solution of the Boltzmann equation:

$$F|_Q \left(v_{px}, v_{py}, v_{pz}|_Q\right) \equiv F|_W \left(v_{px}, v_{py}, v_{pz}|_W \left(v_{pz}|_Q \, , \Delta\phi_{sh}\right)\right) \tag{5.11}$$

The distribution function is referenced at the sheath edge, Q, since temperatures for the primary population are equal to those of the bulk plasma, by assumption. The primary EVDF at the sheath edge is represented in Fig. 5.2.

Now, the primary distribution function may be integrated in the *velocity space* in order to obtain the particle flux *to the wall*, which can be split between the fluxes of primaries reaching the wall, p^+, and reflected, r:

$$g_{p^+z}\big|_W - g_{rz}|_W = \int_{-\infty}^{\infty} dv_{px} \int_{-\infty}^{\infty} dv_{py} \int_{0}^{\infty} v_{pz}|_W \cdot F_p|_W \, dv_{pz}$$

Introducing the following change of variable, known from Eq. (5.2):

$$v_{pz}|_W = \sqrt{v_{pz}^2\big|_Q - {v_{sh}}^2} \; ; \; dv_{pz}|_W = \frac{v_{pz}|_Q}{v_{pz}|_W} \, dv_{pz}|_Q$$

we obtain an expression for the particle flux which may be integrated analytically, taking into account the functional relationship in Eq. (5.11) and the model for δ_r in Eq. (5.4):

$$g_{p^+z}\big|_W - g_{rz}|_W = \\ = \int_{-\infty}^{\infty} dv_{px} \int_{-\infty}^{\infty} dv_{py} \int_{v_{sh}}^{\infty} v_{pz}|_Q \cdot \sigma_{th} \left[1 - \delta_0 \exp\left(\frac{-\frac{1}{2} m_e \left(v_{px}^2 + v_{py}^2 + v_{pz}^2\big|_Q - {v_{sh}}^2 \right)}{E_r} \right) \right] F|_Q \, dv_{pz}$$

This last integral is resolved, after some algebra:

$$\begin{aligned} g_{p^+z}\big|_W - g_{rz}|_W = \sigma_{th} \frac{n_p}{4\pi^{1/2}} \left(\frac{1}{T_{p\parallel}} \right)^{1/2} \frac{m_e}{T_{p\perp}} \cdot \left[\sqrt{\frac{T_{p\perp}}{a}} \frac{1}{c'} \exp\left(-c' {v_{sh}}^2 \right) - \right. \\ \left. - \delta_0 \sqrt{\frac{1}{a' \left(1/E_r + 1/T_{p\perp} \right)}} \frac{1}{c''} \exp\left(\frac{m_e {v_{sh}}^2}{2E_r} - c'' {v_{sh}}^2 \right) \right] \end{aligned} \tag{5.12}$$

with:

$$\begin{aligned} a &= \frac{m_e}{2T_{p\parallel}} \sin^2 \alpha_m + \frac{m_e}{2T_{p\perp}} \cos^2 \alpha_m & a' &= a + \frac{m_e}{2E_r} \\ b &= \frac{m_e}{2T_{p\parallel}} \cos^2 \alpha_m + \frac{m_e}{2T_{p\perp}} \sin^2 \alpha_m \quad ; & b' &= b + \frac{m_e}{2E_r} \\ c &= \left(\frac{m_e}{2T_{p\parallel}} - \frac{m_e}{2T_{p\perp}} \right) \sin 2\alpha_m & c' &= b - \frac{c^2}{4a} > 0 \\ & & c'' &= b' - \frac{c^2}{4a'} > 0 \end{aligned}$$

The two main terms in the Eq. (5.12) represent the thermalized fraction of primary electrons that reach the wall and the corresponding reflected electrons, dependent on their impacting energy.

Equation (5.12) may be rewritten in the, much preferred, dimensionless form, which we will use for the remainder of this section:

$$\begin{aligned} \hat{g}_{p^+z}\big|_W &= \frac{g_{p^+z}\big|_W}{n_p \sqrt{T_{p\parallel}/m_i}} = \frac{\sigma_{th}}{4\pi^{1/2}} \sqrt{m_r} \left[\sqrt{\frac{1}{\hat{T}_{p\perp} \hat{a}}} \frac{1}{\hat{c}'} \exp\left(-\hat{c}' 2\Delta\hat{\phi}_{sh} \right) \right] \\ \hat{g}_{rz}|_W &= \frac{g_{rz}|_W}{n_p \sqrt{T_{p\parallel}/m_i}} = \frac{\sigma_{th}\delta_0}{4\pi^{1/2}} \sqrt{m_r} \left[\sqrt{\frac{1}{\hat{T}_{p\perp} \hat{a}' \left(1 + \hat{T}_{p\perp}/\hat{E}_r \right)}} \frac{1}{\hat{c}''} \exp\left(\frac{\Delta\hat{\phi}_{sh}}{\hat{E}_r} - \hat{c}'' 2\Delta\hat{\phi}_{sh} \right) \right] \end{aligned} \tag{5.13}$$

with the following terms in dimensionless form:

$$\begin{aligned} \hat{T}_{p\perp} &= \frac{T_{p\perp}}{T_{p\parallel}} \\ \hat{T}_p &= \frac{T_p}{T_{p\parallel}} = \frac{2\hat{T}_{p\perp} + 1}{3} & \hat{a} &= \left(\frac{\sin^2 \alpha_m}{2} + \frac{\cos^2 \alpha_m}{2\hat{T}_{p\perp}} \right) & \hat{a}' &= \hat{a} + \frac{1}{2\hat{E}_r} \\ \Delta\hat{\phi}_{sh} &= \frac{e\Delta\phi_{sh}}{T_{p\parallel}} \quad ; & \hat{b} &= \left(\frac{\cos^2 \alpha_m}{2} + \frac{\sin^2 \alpha_m}{2\hat{T}_{p\perp}} \right) \quad ; & \hat{b}' &= \hat{b} + \frac{1}{2\hat{E}_r} \\ \hat{E}_r &= \frac{E_r}{T_{p\parallel}} & \hat{c} &= \left(\frac{1}{2} - \frac{1}{2\hat{T}_{p\perp}} \right) \sin 2\alpha_m & \hat{c}' &= \hat{b} - \frac{\hat{c}^2}{4\hat{a}} > 0 \\ m_r &= \frac{m_i}{m_e} & & & \hat{c}'' &= \hat{b}' - \frac{\hat{c}^2}{4\hat{a}'} > 0 \end{aligned}$$

The electron energy-flux to the wall may be obtained in a similar way, by integrating:

$$h_{p^+z}\big|_W - h_{rz}|_W = \int_{-\infty}^{\infty} dv_{px} \int_{-\infty}^{\infty} dv_{py} \int_{v_{sh}}^{\infty} v_{pz}|_Q \, \frac{1}{2} m_e \left(v_{px}^2 + v_{py}^2 + v_{pz}^2\big|_Q - {v_{sh}}^2 \right) \cdot \sigma_{th} \, (1 - \delta_r) \, F|_Q \, dv_{pz}$$

which, at this moment, does not take into account the possibility of partial energy deposition in reflected electrons. This last equation produces the following expression, in dimensionless form:

$$\hat{h}_{p^+z}\Big|_W = \frac{h_{p^+z}\big|_W}{n_p T_{p\parallel} \sqrt{T_{p\parallel}/m_i}} = \frac{\sigma_{th}}{4\pi^{1/2}} \sqrt{m_r} \sqrt{\frac{1}{\hat{T}_{p\perp}}} \exp\left(-\hat{c}' 2\Delta\hat{\phi}_{sh}\right) \left[\frac{1}{4\hat{a}^{5/2}} \left(\frac{\hat{a}}{\hat{c}'} + \frac{\hat{c}^2}{2\hat{c}'^2} \left(1 + \hat{c}' 2\Delta\hat{\phi}_{sh} \right) \right) + \right.$$
$$\left. + \frac{1}{\sqrt{\hat{a}}} \frac{1}{\hat{c}'} \left(\frac{\hat{T}_{p\perp}}{2} + \frac{1 + \hat{c}' 2\Delta\hat{\phi}_{sh}}{2\hat{c}'} - \Delta\hat{\phi}_{sh} \right) \right]$$

$$\hat{h}_{rz}\Big|_W = \frac{h_{rz}|_W}{n_p T_{p\parallel} \sqrt{T_{p\parallel}/m_i}} = \frac{\sigma_{th}\delta_0}{4\pi^{1/2}} \sqrt{m_r} \sqrt{\frac{1}{\hat{T}_{p\perp} \left(1 + \hat{T}_{p\perp}/\hat{E}_r \right)}} \exp\left(\frac{\Delta\hat{\phi}_{sh}}{\hat{E}_r} - \hat{c}'' 2\Delta\hat{\phi}_{sh} \right) \cdot$$

$$\cdot \left[\frac{1}{4\hat{a}'^{5/2}} \left(\frac{\hat{a}'}{\hat{c}''} + \frac{\hat{c}^2}{2\hat{c}''^2} \left(1 + \hat{c}'' 2\Delta\hat{\phi}_{sh} \right) \right) + \frac{1}{\sqrt{\hat{a}'}} \frac{1}{\hat{c}''} \left(\frac{\hat{T}_{p\perp}}{2 \left(1 + \hat{T}_{p\perp}/\hat{E}_r \right)} + \frac{1 + \hat{c}'' 2\Delta\hat{\phi}_{sh}}{2\hat{c}''} - \Delta\hat{\phi}_{sh} \right) \right] \tag{5.14}$$

Equations (5.13) and (5.14) may be used to define an *average energy* deposited by the primary EVDF at the wall:

$$2\hat{T}_1 = \frac{2T_1}{T_{p\parallel}} = \frac{\hat{h}_{p^+z}\Big|_W - \hat{h}_{rz}\Big|_W}{\hat{g}_{p^+z}\big|_W - \hat{g}_{rz}|_W} \tag{5.15}$$

In a similar way, the parallel electron energy-flux may be derived by integrating:

$$h_{p^+z\parallel}\big|_W - h_{rz\parallel}\big|_W = \int_{-\infty}^{\infty} dv_{px} \int_{-\infty}^{\infty} dv_{py} \int_{v_{sh}}^{\infty} v_{pz}|_Q \, \frac{1}{2} m_e \left(\sqrt{v_{pz}^2\big|_Q - v_{sh}^2} \cos\alpha_m + v_{px} \sin\alpha_m \right)^2 \cdot \sigma_{th} \, (1 - \delta_r) \, F|_Q \, dv_{pz}$$

This expression has not been found to have an analytic solution and thus must be integrated numerically. Some analytical reduction is possible though: e.g., for the energy-flux associated to the primary distribution reaching the wall:

$$\hat{h}_{p^+z\parallel}\Big|_W = \frac{h_{p^+z\parallel}\big|_W}{n_p T_{p\parallel} \sqrt{T_{p\parallel}/m_i}} = \frac{\sigma_{th}}{4\pi^{1/2}} \sqrt{m_r} \sqrt{\frac{1}{\hat{T}_{p\perp}}} \exp\left(-\hat{c}' 2\Delta\hat{\phi}_{sh}\right) \left[\frac{\cos^2\alpha_m}{2\hat{c}'^2\sqrt{\hat{a}}} - \right.$$
$$- \frac{\hat{c} \sin 2\alpha_m}{2\hat{a}'^{3/2} \exp\left(-\hat{c}' 2\Delta\hat{\phi}_{sh}\right)} \int_{v_{sh}}^{\infty} \frac{m_e^2}{T_{p\parallel}^2} \, v_{pz}^2\big|_Q \sqrt{v_{pz}^2\big|_Q - {v_{sh}}^2} \exp\left(-c' \, v_{pz}^2\big|_Q\right) dv_{pz}|_Q + \tag{5.16}$$
$$\left. + \frac{\sin^2\alpha_m}{4\hat{a}^{5/2}} \left(\frac{\hat{a}}{\hat{c}'} + \frac{\hat{c}^2}{2\hat{c}'^2} \left(1 + \hat{c}' 2\Delta\hat{\phi}_{sh} \right) \right) \right]$$

Alternatively, and for the sake of simplicity, one could assume that the energy-flux is isotropic and follows the same summation laws as shown in Eq. (4.11):

$$\hat{h}_{p^+z\parallel}\Big|_W - \hat{h}_{rz\parallel}\Big|_W = \frac{2}{3}\left(\hat{h}_{p^+z}\Big|_W - \hat{h}_{rz}\Big|_W\right) \tag{5.17}$$

To continue, the SEE flux may be obtained from the following integral, using the model in Eq. (5.5):

$$g_{bz}|_W = \int_{-\infty}^{\infty} dv_{px} \int_{-\infty}^{\infty} dv_{py} \int_{v_{sh}}^{\infty} v_{pz}|_Q \cdot \sigma_{th}\,(1-\delta_r) \left(\frac{\frac{1}{2} m_e \left(v_{px}^2 + v_{py}^2 + v_{pz}^2\big|_Q - {v_{sh}}^2 \right)}{E_b} \right)^p F|_Q \, dv_{pz}$$

Since, typically, $p \approx 1$, we can obtain an exact solution for $p = 1$ and an approximate one for $p \neq 1$, using the average impacting electron temperature in Eq. (5.15), as:

$$\begin{cases} \forall p = 1 \rightarrow \hat{g}_{bz}|_W = \dfrac{g_{bz}|_W}{n_p \sqrt{T_{p\parallel}/m_i}} = \dfrac{\hat{h}_{p^+z}\Big|_W - \hat{h}_{rz}\Big|_W}{\hat{E}_b} \\ \forall p \neq 1 \rightarrow \hat{g}_{bz}|_W \approx \left(\dfrac{\hat{T}_1}{\hat{E}_b}\right)^p \cdot \left(\hat{g}_{p^+z}\Big|_W - \hat{g}_{rz}|_W\right) \end{cases} \tag{5.18}$$

And the SEE energy-flux may be obtained considering the *beam* temperature, T_b, introduced in Section 5.1.2, as:

$$\hat{h}_{bz}\Big|_W \approx 2\hat{T}_b \; \hat{g}_{bz}|_W \tag{5.19}$$

where the dimensionless terms used in relation to SEE are:

$$\hat{E}_b = \frac{E_b}{T_{p\parallel}}$$
$$\hat{T}_b = \frac{T_b}{T_{p\parallel}}$$

The expression in Eq. (5.19) includes the thermalization fraction and, therefore, represents the heat added back into the bulk plasma by the secondary population. This does not necessarily mean, however, that the SEE has a *net* diminishing effect on the deposited heat at the wall, since it also modifies the sheath structure in terms of electric potential drop, altering the primary population heat deposition. The combination of these effects is explored in the following section.

Regarding the SEE parallel energy-flux, one may argue that, since the SEE are unmagnetized at their inception, and we are in the limit of zero Debye length, the SEE energy-flux is isotropic, which implies:

$$\hat{h}_{bz\parallel}\Big|_W = \frac{2}{3}\,\hat{h}_{bz}\Big|_W \tag{5.20}$$

Now, in order to complete the model, we must seek the expressions for the densities of the various EVDFs, which will allow us to derive the CSL condition and obtain the primary population

density as a function of density at the sheath edge: $n_p = n_p\left(n_e|_Q\right)$. The CSL condition in Eq. (5.7) requires that we obtain density as a function of the electric potential in the sheath; for this, we may focus on an arbitrary section of the sheath, R, depicted in Fig. 5.6.

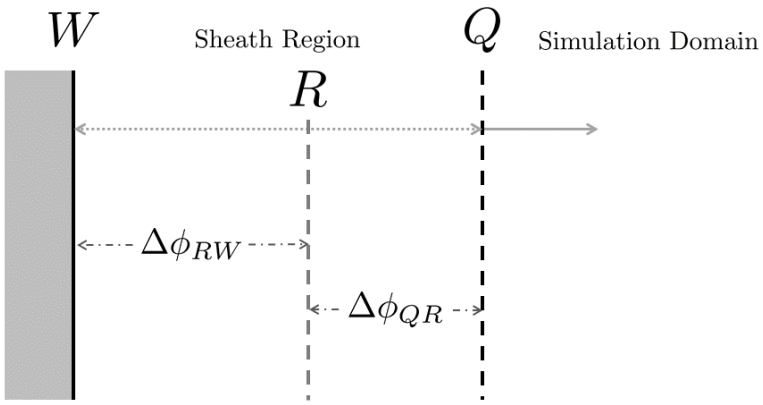

Figure 5.6: Arbitrary section in the sheath, R

For the EVDF, we can expand the functional form given in Eq. (5.11) to:

$$F|_R\left(v_{px}, v_{py}, v_{pz}|_R\right) \equiv F|_Q\left(v_{px}, v_p, v_{pz}|_Q\left(v_{pz}|_R, \Delta\phi_{QR}\right)\right) \tag{5.21}$$

and, in a similar way to Eq.(5.9), the primary and reflected EVDF can be defined by parts as:

$$F_p|_R = \begin{cases} \sigma_{th}\cdot F \;\forall\; v_{pz} \geq v_{RW} \\ F \;\forall\; v_{pz} < v_{RW} \\ \sigma_{th}\delta_r\cdot F \;\forall\; v_{pz} \leq v_{RW} \end{cases} \tag{5.22}$$

with

$$\begin{aligned} v_{RW} &= \sqrt{\frac{2e\Delta\phi_{RW}}{m_e}}\;;\; \Delta\phi_{RW} = \phi|_R - \phi|_W \;;\; \Delta\hat{\phi}_{RW} = \frac{e\left(\phi|_R - \phi|_W\right)}{T_{p\parallel}} \\ v_{QR} &= \sqrt{\frac{2e\Delta\phi_{QR}}{m_e}}\;;\; \Delta\phi_{QR} = \phi|_Q - \phi|_R \;;\; \Delta\hat{\phi}_{QR} = \frac{e\left(\phi|_Q - \phi|_R\right)}{T_{p\parallel}} \end{aligned} \tag{5.23}$$

The density of primaries at an arbitrary sheath section, R, can be obtained by doing the integral:

$$n_p|_R = \int_{-\infty}^{\infty}\int_{-\infty}^{\infty}\int_{-\infty}^{\infty} F_p|_R\, dv_{px}dv_{py}\, dv_{pz}|_R$$

using the functional form in Eq. (5.21), and the variable change:

$$v_{pz}|_Q = \text{sign}\left(v_{pz}|_R\right)\sqrt{v_{pz}^2|_R + v_{QR}^2}$$

The final expression, for an arbitrary sheath section, becomes:

$$\begin{aligned} \hat{n}_p|_R = \frac{n_p|_R}{n_p} &= \frac{1}{4}\sqrt{\frac{1}{4\hat{a}\hat{c}'\hat{T}_{p\perp}}}\exp\left(-\hat{c}'2\Delta\hat{\phi}_{QR}\right)\left[\sigma_{th} + (2-\sigma_{th})\,\text{erf}\left(\sqrt{\hat{c}'2\Delta\hat{\phi}_{RW}}\right)\right] + \\ &+\frac{\delta_0\sigma_{th}}{4}\sqrt{\frac{1}{4\hat{a}'\hat{c}''\hat{T}_{p\perp}\left(1+\hat{T}_{p\perp}/\hat{E}_r\right)}}\exp\left(\frac{\Delta\hat{\phi}_{RW}}{\hat{E}_r} - \hat{c}'''2\Delta\hat{\phi}_{QR}\right)\left[1 - \text{erf}\left(\sqrt{\hat{c}''2\Delta\hat{\phi}_{RW}}\right)\right] \end{aligned} \tag{5.24}$$

with

$$\hat{c}''' = \hat{b} - \frac{\hat{c}^2}{4\hat{a}'} > 0$$

Now, the SEE density at an arbitrary section of the sheath may be obtained considering its EVDF, taking into account the shift in the velocity space due to the acceleration caused by the sheath potential fall and the fact that electrons are *emitted from* the wall, with particle flux $g_{bz}|_W$ from Eq. (5.18):

$$F_b|_R = \begin{cases} g_{bz}|_W \sqrt{\dfrac{2\pi m_e}{T_b}} \left(\dfrac{m_e}{2\pi T_b}\right)^{3/2} \exp\left(-\dfrac{m_e\ v_{bz}^2|_W}{2T_b} + \dfrac{e\Delta\phi_{RW}}{T_b}\right) \ \forall\ v_{bz} \leq -v_{RW} \\ 0 \ \forall\ v_{bz} > -v_{RW} \end{cases} \tag{5.25}$$

The secondary population distribution function is, analogous to the primary electrons, referenced to the material wall, W, since the emission temperature, T_b, is known there (imposed as a parameter for the model).

The SEE density at an arbitrary sheath section results in:

$$\hat{n}_b|_R = \frac{n_b|_R}{n_p} = \hat{g}_{bz}|_W \sqrt{\frac{\pi}{2\hat{T}_b}} \exp\left(\frac{\Delta\hat{\phi}_{RW}}{\hat{T}_b}\right) \left[1 - \operatorname{erf}\left(\sqrt{\frac{\Delta\hat{\phi}_{RW}}{\hat{T}_b}}\right)\right] \tag{5.26}$$

Finally, the ion density in the sheath may be obtained by invoking mass continuity, the energy conservation equation for ions, analogous to Eqs. (5.2) and (5.10) :

$$\left.\begin{array}{l} g_{iZz}|_Q = n_{iZ}|_Q\ u_{iZz}|_Q = \text{cnst.} \\ u_{iZz}^2|_R = u_{iZz}^2|_Q + \dfrac{2Ze\Delta\phi_{QR}}{m_i} \end{array}\right\} \hat{n}_{iZ}|_R = \frac{n_{iZ}|_R}{n_p} = \frac{\hat{g}_{iZz}|_Q}{\sqrt{\left(\hat{g}_{iZ}/\hat{n}_{iZ}|_Q\right)^2 + 2Z\Delta\hat{\phi}_{QR}}} \tag{5.27}$$

where the ion particle flux has been made dimensionless in the same way as for the various electron particle fluxes.

Equations (5.24), (5.26) and (5.27) may be integrated using the dimensionless form of the condition given in Eq. (5.7) to find the limit for the monotonic sheath potential function, which represents the CSL. It is worth observing this integral is the only expression in the dimensionless model where the mass ratio between ions and electrons, m_r, appears explicitly; therefore, it is the only term dependent on the propellant type.

Additionally, the value at the sheath edge, Q, for the densities of each of the distinctive species in the EVDF: primaries, reflected and secondaries, may be obtained by simply substituting $\phi_R = \phi_Q$ in the expressions referenced here. Since the bulk plasma density at the sheath edge is, by definition, equal to the sum of these partial densities, we can obtain the following relation:

$$\frac{n_p}{n_e|_Q} = \frac{1}{\hat{n}_p|_Q + \hat{n}_b|_Q} \tag{5.28}$$

which provides closure to the proposed sheath model. In particular, this expression may be factored into the expressions derived in this section so that they are made dimensionless through

$n_e|_Q$, which is more convenient from the perspective of its implementation into the global electron fluid model.

The expressions in Eqs. (5.13), (5.18), (5.14), (5.16) (or (5.17)), (5.19) and (5.20) provide a consistent model for particle fluxes and energy-fluxes at physical walls in the thruster, for a combination of model parameters: σ_{th}, δ_0, E_r, E_b, T_b, and as a function of the dimensionless sheath potential fall, $\Delta\hat{\phi}_{sh}$, and $\hat{T}_{p\perp}$, $T_{e\|}$ and α_m. As was commented in Section 4.2, this model may be implemented either as a direct problem, if $\Delta\hat{\phi}_{sh}$ is indeed the independent variable, or as an inverse problem, if the particle flux becomes the independent variable.

As a final comment, we can say that deposition values at the wall are important from the performance perspective or, for example, for the thruster thermal models in the case of energy-fluxes. The expressions for the various fluxes derived here have been, thus, obtained for the material wall, W; however, from the perspective of the bulk plasma model, we require said fluxes at the sheath edge, Q. Therefore, mass and energy continuity are used to derive the following relations:

$$\begin{aligned}
&\hat{g}_{ez}|_Q = \hat{g}_{ez}|_W = \left(\hat{g}_{p^+z} - \hat{g}_{rz} - \hat{g}_{bz}\right)\big|_W \\
&\left(\hat{h}_{p^+z} - \hat{h}_{rz}\right)\Big|_Q \approx \left(\hat{h}_{p^+z} - \hat{h}_{rz}\right)\Big|_W + \left(\hat{g}_{p^+z}|_W - \hat{g}_{rz}|_W\right)\Delta\hat{\phi}_{sh} \\
&(\hat{h}_{p^+z\|} - \hat{h}_{rz\|})\Big|_Q \approx (\hat{h}_{p^+z\|} - \hat{h}_{rz\|})\Big|_W + \left(\hat{g}_{p^+z}|_W - \hat{g}_{rz}|_W\right)\Delta\hat{\phi}_{sh}\cos\alpha_m \\
&\hat{h}_{bz}\Big|_Q \approx \hat{h}_{bz}\Big|_W + \hat{g}_{bz}|_W\,\Delta\hat{\phi}_{sh} \\
&\hat{h}_{bz\|}\Big|_Q \approx \hat{h}_{bz\|}\Big|_W + \frac{\hat{g}_{bz}|_W\,\Delta\hat{\phi}_{sh}}{\cos\alpha_m}
\end{aligned} \tag{5.29}$$

where the relation between energy-fluxes is permitted by the assumption that the Larmor radius is much larger than the sheath thickness and no kinetic effects are present. The average energy gained in the parallel direction takes into account the magnetic angle at the wall.

5.1.4 Sheath model characterization

Finally, we wish to characterize the sheath model developed in the previous section, providing insight into how the various physical mechanisms and parameters will affect the solution. We can do this by solving the model self-consistently for the marginal Bohm condition or by providing values for the ion current and plasma density reaching the sheath edge to obtain dimensional results:

Marginal Bohm criteria solution

A self-consistent solution for a dielectric material wall exists by introducing the Bohm criteria at the sheath edge, Q. From Riemann[149]:

$$\frac{d}{d\phi}\left[n_e\left(\phi\right) - n_i\left(\phi\right)\right]\big|_Q \geq 0$$

In particular, taking the *marginal* case of the previous expression (i.e., for it to be exactly equal to 0 and the derivatives of both electron and ion densities to be equal at the sheath edge) implies that

ions are sonic at the sheath entrance. The expression in (5.27), for a single-ion species ($Z = 1$), becomes, after some algebra:

$$u_{i1z}|_Q = \sqrt{\frac{e\, n_e|_Q}{m_i} \frac{1}{dn_e/d\phi|_Q}}$$

Considering the dielectric wall condition, which implies no net charge density at the wall, for a single-ion species:

$$g_{iz}|_Q = g_{ez}|_Q$$

we reach a final self-consistent expression which leads to a solution for the potential drop in the sheath, and therefore the characterization of other terms such as heat and particle fluxes, as a function of each of the parameters and variables in the model; in dimensionless form:

$$\hat{g}_{ez}|_Q = \hat{n}_e^{3/2}\Big|_Q \sqrt{\frac{1}{d\hat{n}_e/d\hat{\phi}|_Q}} \tag{5.30}$$

The derivative term in this expression may be obtained simply by deriving Eqs. (5.24) and (5.26) with respect to ϕ_R and substituting $\phi_R = \phi_Q$.

The following figures show the main results for the sheath model: $\Delta\hat{\phi}_{sh}$, $\hat{g}_e$ and $\hat{h}_e$, for the marginal Bohm condition. The crossover energies and emission temperature for SEE are:

$$E_b = 40eV \; ; \; E_r = 40eV \; ; \; T_b = 2eV \tag{5.31}$$

and the remaining parameters in the sheath model, σ_{th}, δ_0, together with the magnetic angle, α_m, are referenced in Table 5.1 for each of the figures shown next. The magnetic angle has been limited to $5\pi/12$ since the model's limit is at $\alpha_m = \pi/2$, which does not represent the typical situation in HETs. The results shown here are made dimensionless through the relation shown in Eq. (5.28). Note that, for the sake of clarity, the figures showing results for the eletron particle flux are scaled differently for each combination of model parameters.

Fig.	5.7 (a)	(b)	(c)	5.8 (a)	(b)	(c)	5.9 (a)	(b)	(c)	5.10 (a)	(b)	(c)
$\alpha_{\mathbf{m}}$	0	$\frac{\pi}{4}$	$\frac{5\pi}{12}$	0	$\frac{\pi}{4}$	$\frac{5\pi}{12}$	0	$\frac{\pi}{4}$	$\frac{5\pi}{12}$	0	$\frac{\pi}{4}$	$\frac{5\pi}{12}$
$\sigma_{\mathbf{th}}$	0.1	0.1	0.1	0.5	0.5	0.5	0.1	0.1	0.1	0.5	0.5	0.5
$\delta_{\mathbf{0}}$	0	0	0	0	0	0	0.4	0.4	0.4	0.4	0.4	0.4

Table 5.1: Model parameters for the sheath model characterization (using marginal Bohm criteria)

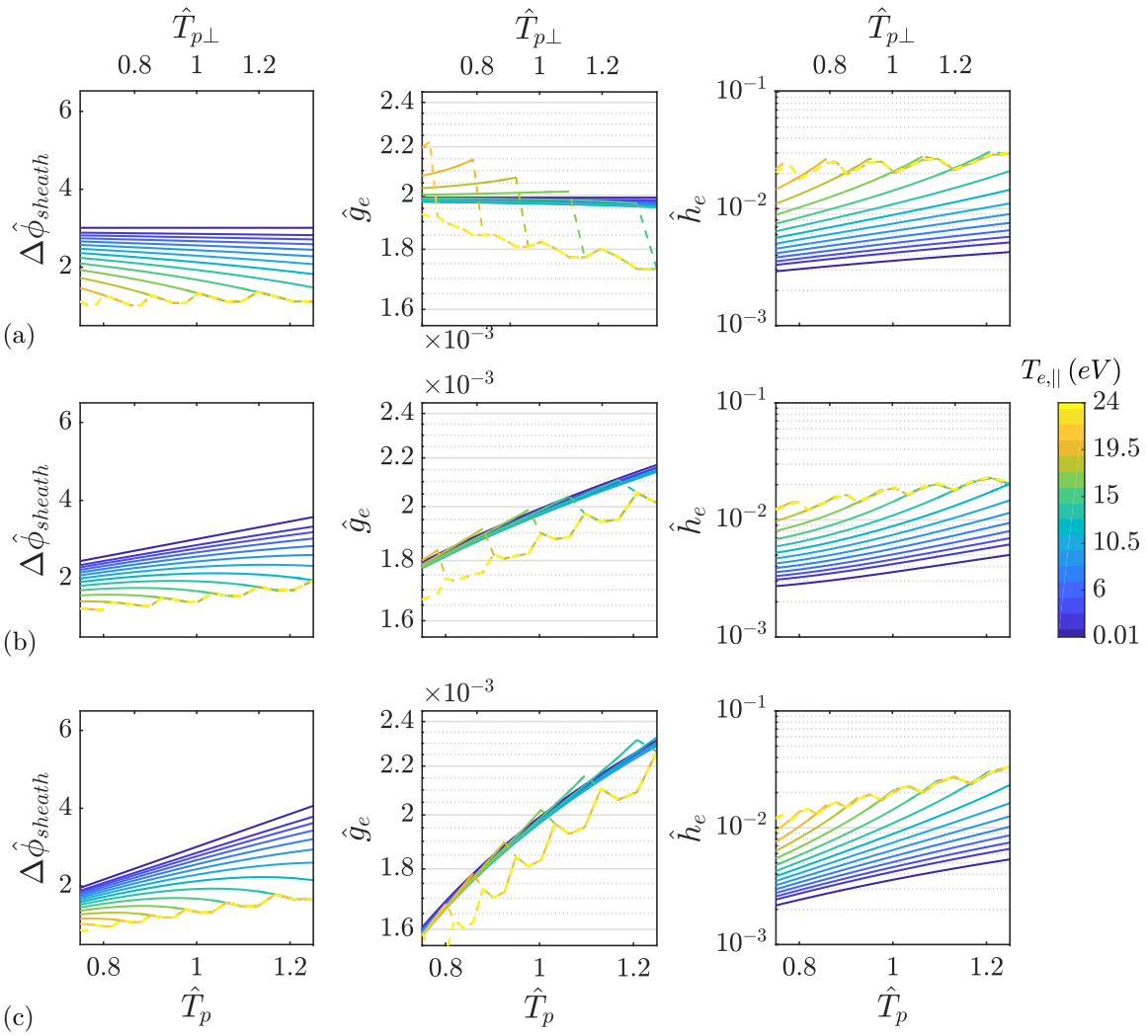

Figure 5.7: Sheath model results for σ_{th}= 0.1, δ_0 = 0 and (a) α_m= 0, (b) α_m= $\pi/4$, (c) α_m= $5\pi/12$; straight lines represent the "normal" operating regime, dashed lines represent the CSR

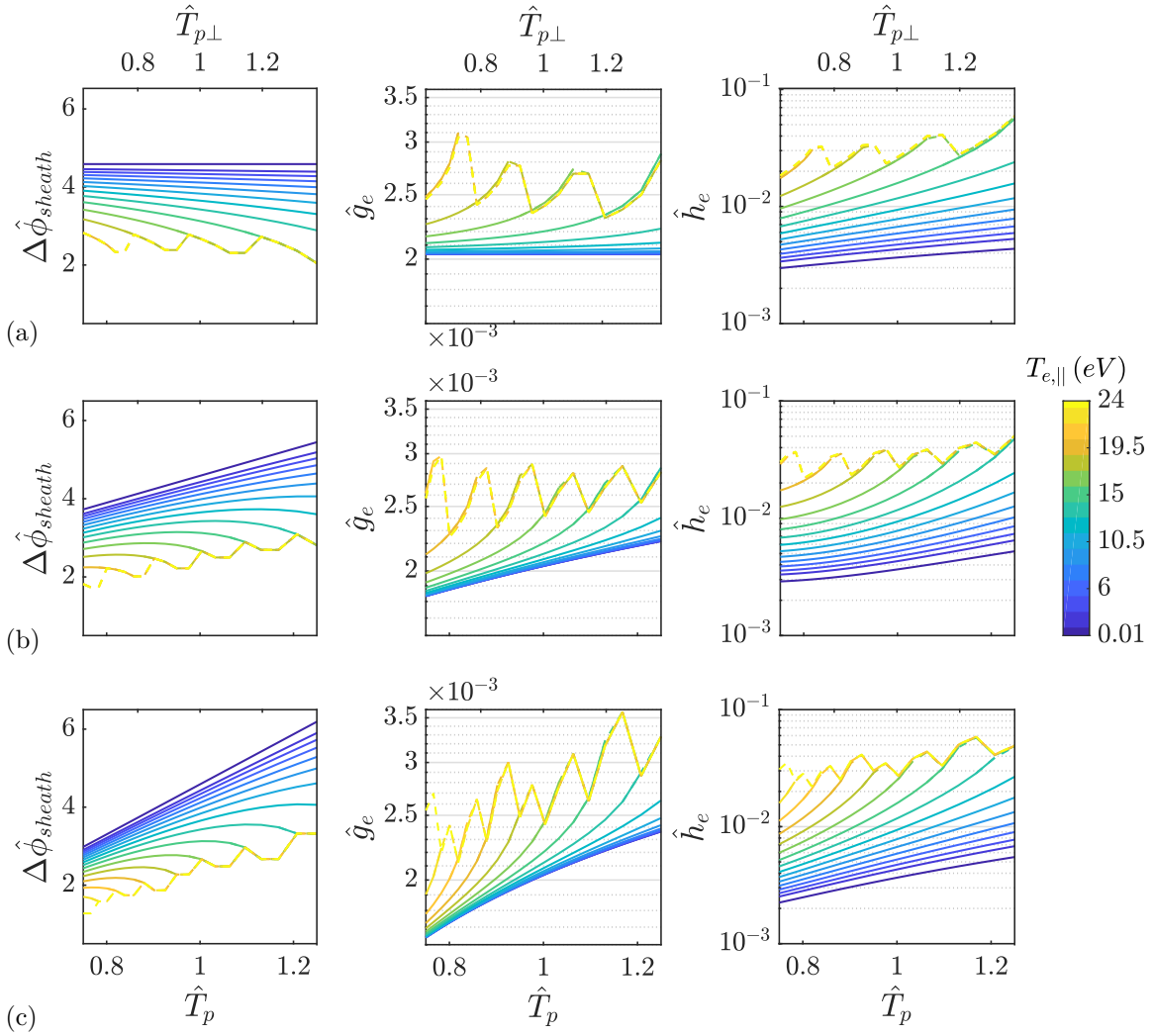

Figure 5.8: Sheath model main results for σ_{th}= 0.5, $\delta_0 = 0$ and (a) α_m= 0, (b) α_m= $\pi/4$, (c) α_m= $5\pi/12$; straight lines represent the "normal" operating regime, dashed lines represent the CSR

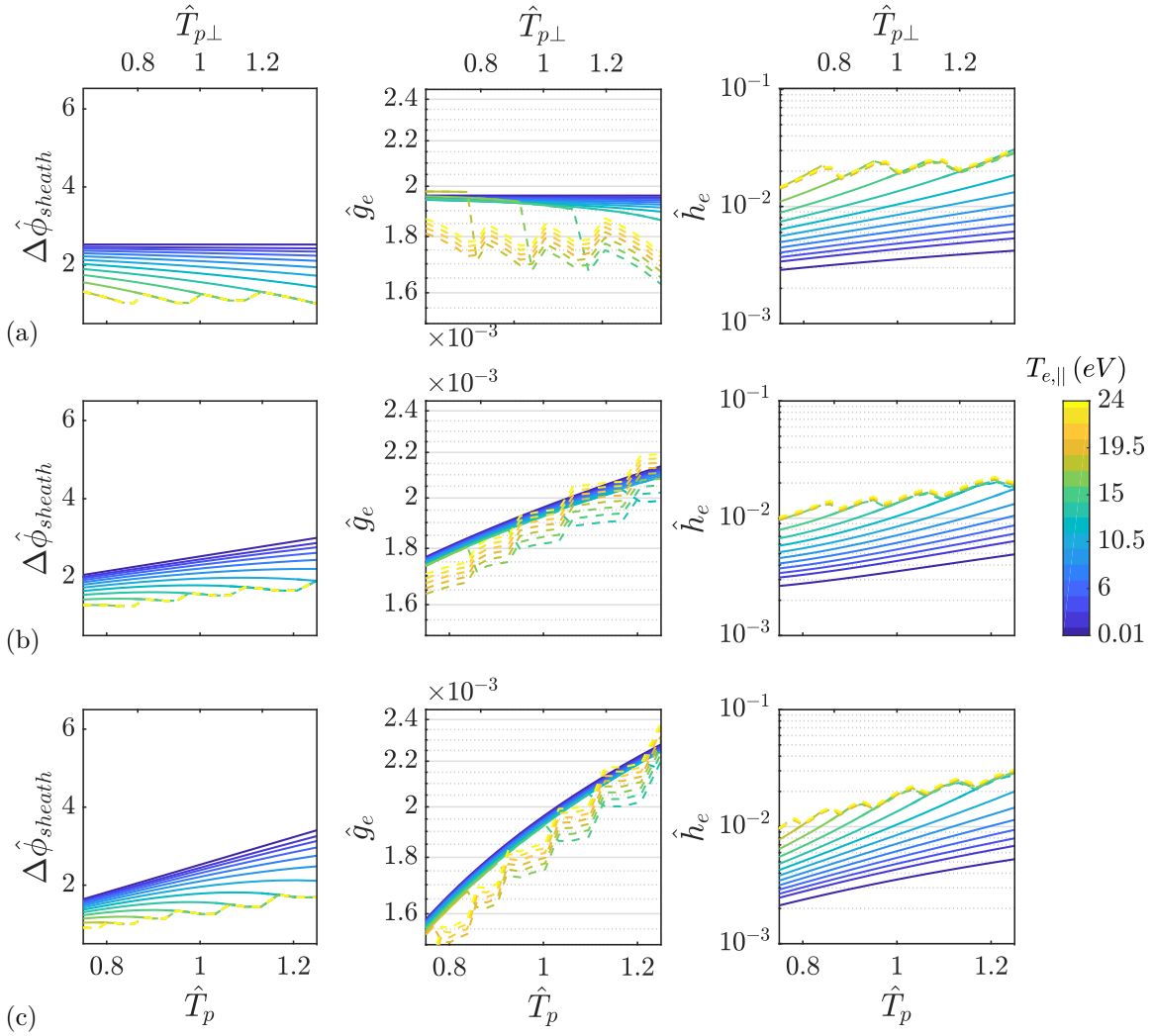

Figure 5.9: Sheath model main results for σ_{th}= 0.1, δ_0 = 0.4 and (a) α_m= 0, (b) α_m= $\pi/4$, (c) α_m= $5\pi/12$; straight lines represent the "normal" operating regime, dashed lines represent the CSR

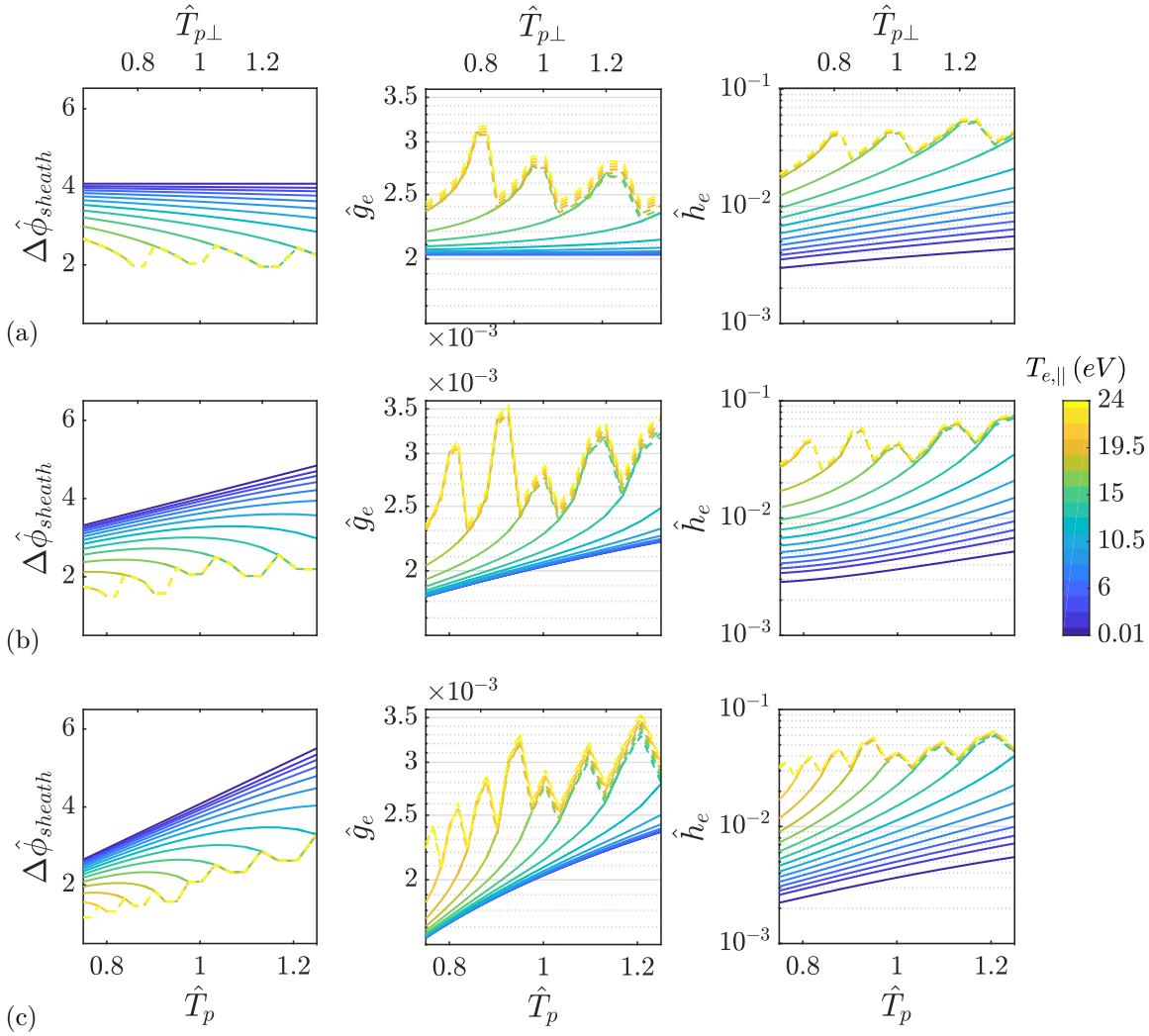

Figure 5.10: Sheath model main results for σ_{th}= 0.5, δ_0 = 0.4 and (a) α_m= 0, (b) α_m= $\pi/4$, (c) α_m= $5\pi/12$; straight lines represent the "normal" operating regime, dashed lines represent the CSR

The results shown in Figs. 5.7, 5.8, 5.9 and 5.10 are coherent with the ones shown by Ahedo and De Pablo[240], taking into account that the crossover energies and the emission temperature for SEE are introduced, not as a fixed dimensionless ratio as was done there, but as particular values, due to which, the dimensionless results depend on the dimensional quantity $T_{e\|}$. Moreover, the results show the non-negligible effects of generailizing the model for arbitrary magnetic angles and anisotropic mediums, which are further coupled with the thermalization fraction and SEE and reflection models.

For further reference, the impinging primary flux and the flux ratios for reflected-to-impinging-primary and secondary-to-impinging-primary are shown next, for the model parameters corresponding both to Figs. 5.9 and 5.10:

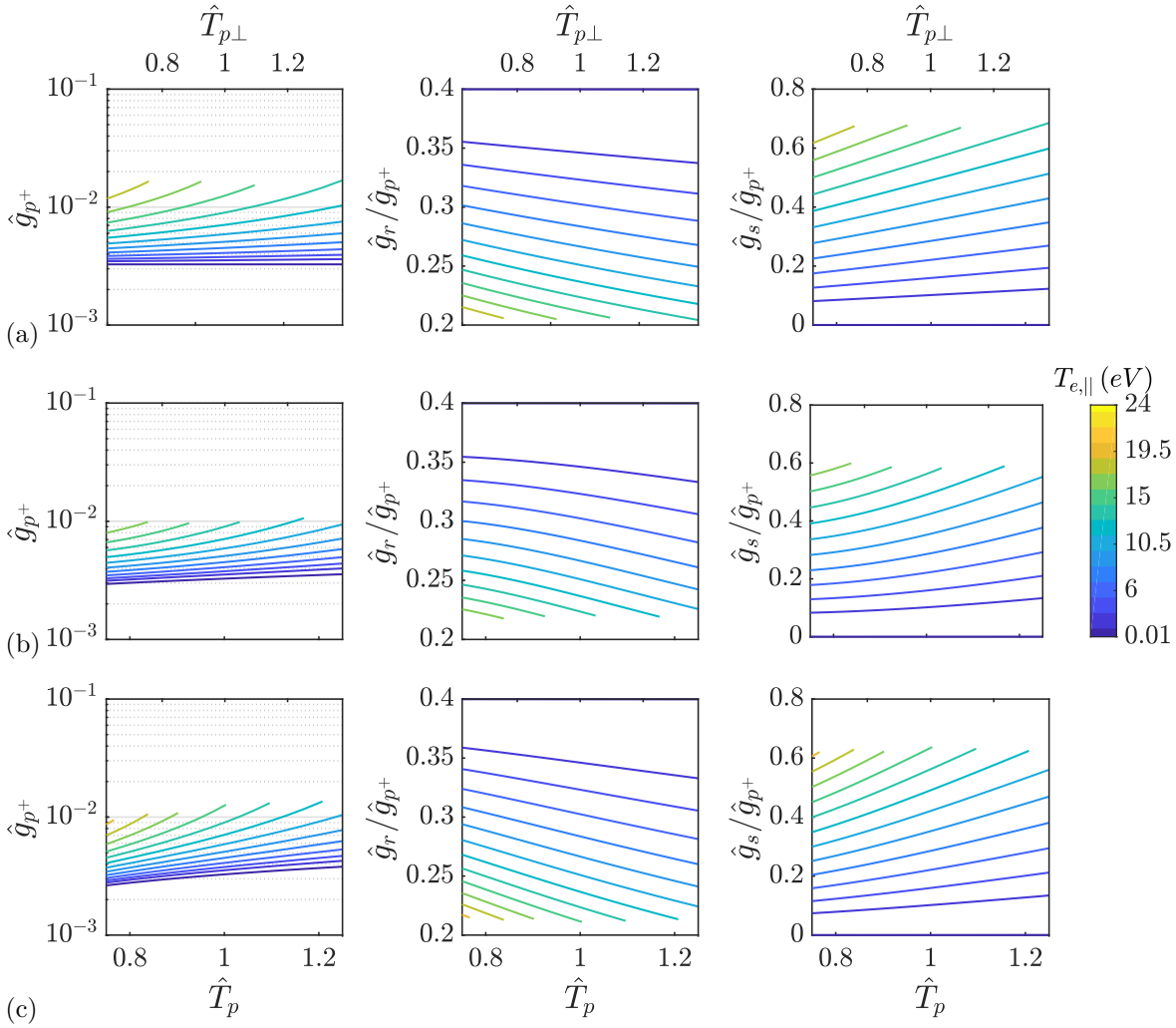

Figure 5.11: p^+ flux and $r-\text{to}-p^+$ and $b-\text{to}-p^+$ flux ratios for σ_{th}= 0.1, $\delta_0 = 0.4$ and (a) α_m= 0, (b) α_m= $\pi/4$, (c) α_m= $5\pi/12$; results end at the CSL (CSR not shown)

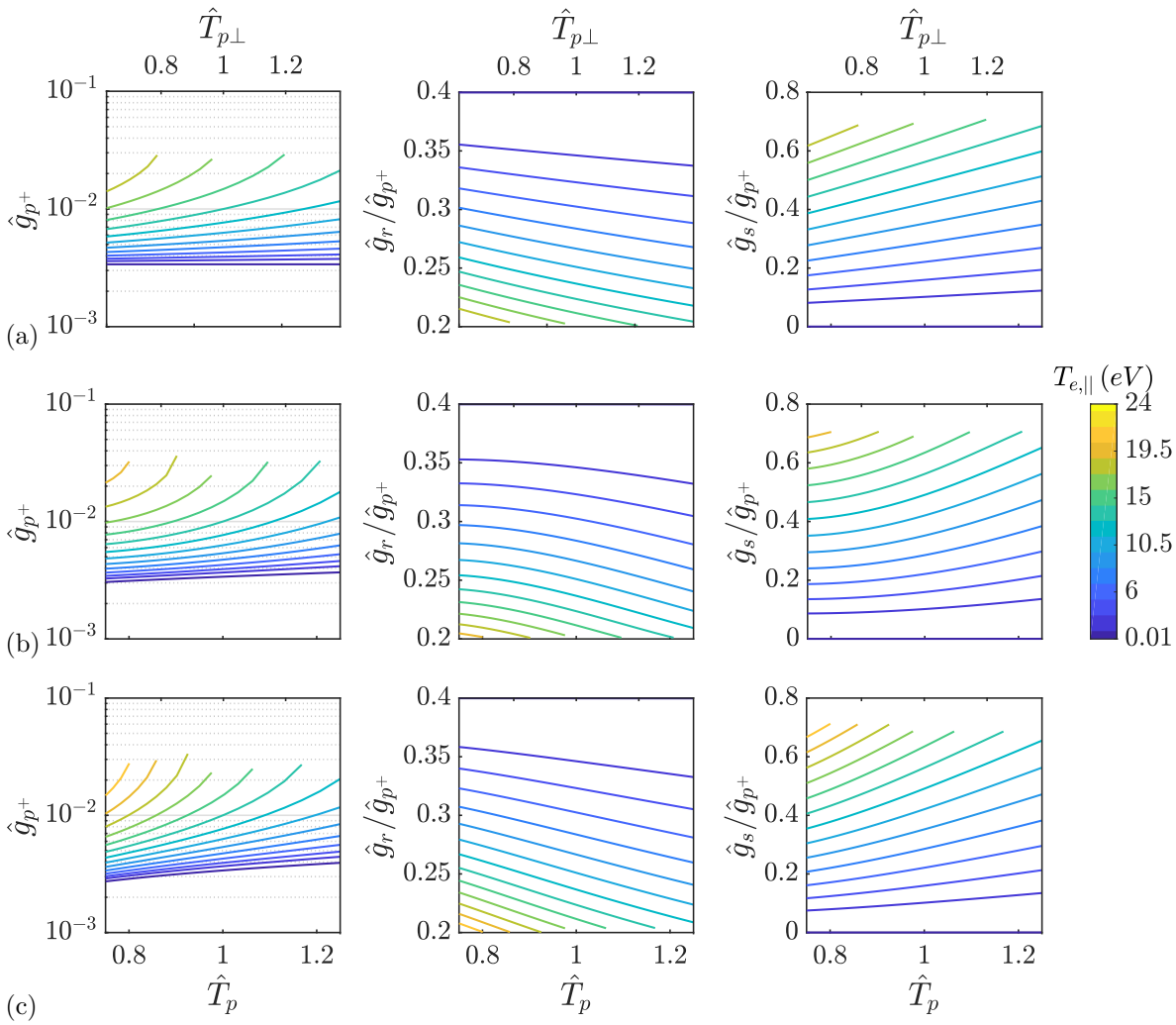

Figure 5.12: p^+ flux and $r-\text{to}-p^+$ and $b-\text{to}-p^+$ flux ratios for σ_{th}= 0.5, $\delta_0 = 0.4$ and (a) α_m= 0, (b) α_m= $\pi/4$, (c) α_m= $5\pi/12$; results end at the CSL (CSR not shown)

The results for the sheath model, at the marginal Bohm condition, are complex and show a strong coupling in the model variables; some conclusions are summarized as follows:

- The solutions for the sheath model are symmetric in α_m with respect to 0, in the $[-\pi/2, \pi/2]$ range, by definition.
- The $T_{e\|}$ range used for the model solutions presented here was chosen so that the CSR was not the dominant regime shown. Higher temperatures are incompatible with a non-CSL regime and the sonic ion condition imposed by the marginality of the Bohm criteria.
- The CSR is extrapolated from the "normal" regime by using the condition in Eq. (5.8). Numerically, since the solution has two independent variables: $T_{e\|}$ and $\hat{T}_p$ or $\hat{T}_{p\perp}$, the extrapolation can be done following lines that have constant values of either variables. We have chosen to start with extrapolating through lines of constant $T_{e\|}$ and, if this is not

possible, then through lines of constant anisotropy ratio. This produces the somewhat peculiar shapes in the results for the CSR. As is also mentioned in Ref. [240], the CSL represents both the lower limit for the dimensionless potential fall and the upper limit for the dimensionless electron energy-flux.

- The δ_0 parameter reduces $\Delta\hat{\phi}$, which is understood in the context of an electron repelling sheath: since the flux of electrons reflected on impact at the wall is subtracted from the total electron flux, $\Delta\hat{\phi}$ becomes lower to accommodate the need for less electrons to be reflected electro-statically in the sheath. The $\hat{g}_e$ which satisfies the marginal Bohm condition and the respective $\hat{h}_e$ are both diminished with increasing δ_0. It is expected that a reduction in the crossover energy, E_r, would have a similar effect to an increase in δ_0, considering the model in Eq. (5.4).

- The thermalization fraction, σ_{th}, increases $\Delta\hat{\phi}$, as a larger population is present in the truncated Maxwellian EVDF of primaries, which needs to be repelled by the sheath. Understandibly, increasing σ_{th} also leads to larger $\hat{h}_e$. Its effect on the $\hat{g}_e$, however, is more complex: the major difference lies in the monotonic increase of $\hat{g}_e$ with $T_{e\parallel}$, for the high σ_{th} limit, versus a non-monotonic or partially decreasing trend for the low σ_{th} limit. Since the variation of reflected and secondary fluxe ratios is very subtle, the global tendency in $\hat{g}_e$ is primarily an effect of the variation in $\hat{g}_{p^+}$, which depends on both the $\Delta\hat{\phi}$ and also on the ${}^{n_e|_Q}/_{n_p}$ ratio, given by (5.28). The wide differences in results for the different values of the thermalization fraction serve to ratify its importance as a parameter in the sheath model; while the implications of introducing σ_{th} as a variable in the model, instead of as a pre-selected parameter, are outside of the scope of this thesis.

- The effect of anisotropy ratios, $\hat{T}_{p\perp} = {}^{T_{e\top}}/_{T_{e\parallel}}$ or $\hat{T}_p = {}^{T_{e\parallel}}/_{T_e}$, must be understood in the context of, primarily, values of $T_{e\parallel}$, but also of α_m. Increasing values of $\hat{T}_{p\perp}$ (also increasing values of $\hat{T}_p$) imply larger total electron temperatures, T_e for a constant value of $T_{e\parallel}$. This has an effect over the reflected and SEE fluxes: the former decreases with the total energy of impinging primary electrons, while the latter increases. This effect may be appreciated in Figs. 5.9 and 5.10. Larger electron energies, both for increasing $\hat{T}_{p\perp}$ (increasing $\hat{T}_p$) and $T_{e\parallel}$ are eventually responsible for the outset of the CSR, coinciding with minimum $\Delta\hat{\phi}$, as was also confirmed by Ahedo and De Pablo[240]. The effect of the magnetic angle, α_m, adds an additional layer of complexity since it alters the distribution of $v_{pz}|_Q$ with respect to T_e and $T_{e\parallel}$. This makes it dificult to identify a trend decoupled, particularily, from the anisotropy ratios; in general, it emphasizes the role of $T_{e\perp}$ in the EVDF of the population entering the sheath, accounting for higher or lower energy distributions in the sheath reference frame (Fig. 5.1).

It is important to note that the characterization of the model through the marginal Bohm condition, as per Eq. (5.30), imposes a constraint on the ion population to be both sonic and single species. The model implemented in HYPHEN for dielectric walls uses the ion fluxes, g_{iZ}, as input variables for the "inverse" problem, together with $T_{e\parallel}$, $\hat{T}_p$ and α_m, meaning that the constraint is not present and ions may be sonic or supersonic. The characterization shown in this

section remains relevant however, and allows for results from a 3-dimensional variable space ($T_{e\|}$, $\hat{T}_p$, α_m) to be shown, instead of the 4-dimensional variable space (which includes ion fluxes) that the model draws from when the marginal Bohm constraint is not imposed.

Representative dimensional results

In addition to the non-dimensional results, the sheath model may be further characterized through its dimensional results, continuing with the example of the dielectric wall. These dimensional results may be obtained for fixed values of the plasma density and the impacting ion current (assuming that only singly-charged ions are present); we have chosen to explore the following combination of entry parameters in the model:

- Constant plasma density: $n_e = 10^{17}\frac{1}{m^3}$; $j_i \in \left[0.005\frac{A}{cm^2}, 0.05\frac{A}{cm^2}\right]$
- Constant ion current: $j_i = 0.05\frac{A}{cm^2}$; $n_e \in \left[10^{17}\frac{1}{m^3}, 10^{18}\frac{1}{m^3}\right]$

The wall parameters are the same as in Eq. (5.31), and the remaining dimensionless entry parameters are:

$$\sigma_{th} = 0.3 \; ; \; \delta_0 = 0.4 \; ; \; \alpha_m = 0 \; ; \; \hat{T}_e = \hat{T}_{e\perp} = 1 \; ; \; \hat{g}_i \in \left[3 \cdot 10^{-4}, 5 \cdot 10^{-2}\right]$$

The dimensionless ion-flow parameter was chosen in order to recover most of the dimensional parameter space we wish to characterize. Figure 5.13 shows the results for the constant density and constant current for various values of the parallel electron temperature.

These results follow the general conclusions for the dimensionless case, while providing actual values for the sheath response, which are in line with results from Barral[124]. It is clear that the sheath response is very non-linear: the CSR can be clearly spotted for $T_{e\|}$ larger than $\sim 18eV$. This implies that the CSL depends mostly on the SEE and backscattering characteristics of the wall, and somewhat on the current reaching the sheath and the plasma density. The CSR region is clearly the result of being approximated by the use of the condition in Eq. (5.8), and, as expected, presents low $\Delta\phi_{sh}$ and high h_{sh} and secondary electron currents, j_b; note that the latter are much larger than the incident ion current, and must therefore be compensated by a large primary electron current in order to satisfy the null current condition.

Variations with density for a fixed ion current also present a non-linear response: for the $\Delta\phi_{sh}$, the solution is more sensible to changes in density in the non-CSR region, whereas the energy and secondary particle fluxes exhibit the opposite behavior.

The "complete" 4-dimensional sheath model is used in the NOMADS module and will be further characterized in the following chapters from a "macroscopic" perspective, focusing on the electron energy deposition into the sheath and wall and the self-consistent sheath potential drop. HYPHEN also uses the model results for a conducting anode wall, which have not been explored in this chapter.

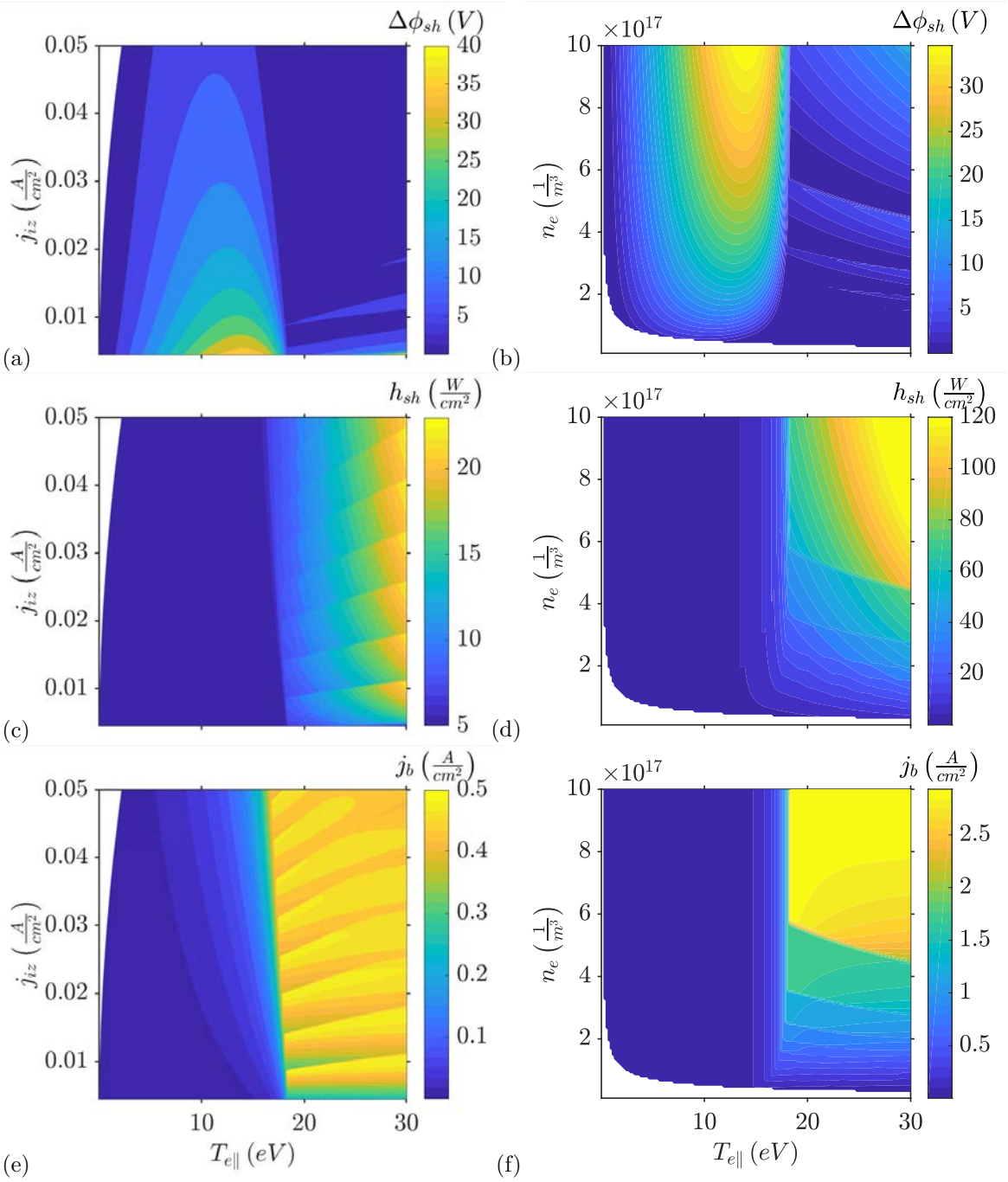

Figure 5.13: (a) $\Delta\phi_{sh}$, (c) h_{sh} and (e) j_b for constant density $n_e = 10^{17}{}^1/_{m^3}$ and (b) $\Delta\phi_{sh}$, (d) h_{sh} and (f) j_b for constant sheath entry ion current $j_i = 0.05^A/_{cm^2}$

As a final note, regarding the multiple ion charge number, the model implemented in HYPHEN uses the following approximation to avoid dealing with it in an explicit manner:

$$j_{ez}|_W = \sum_{Z=1}^{2,3,\ldots} j_{iZz}|_W \rightarrow g_{ez}|_Q \approx \sum_{Z=1}^{2,3,\ldots} Z g_{iZz}$$

Future versions of the sheath model may include explicit treatment of multiply charged ions at the cost of adding multiple ion flux input variables.

5.2 Collisional models

Collisional processes in the plasma underpin the physical response is simulated in HYPHEN. Frequencies associated to collisions appear throughout Chapter 4 in Maxwell type molecule interactions and for the plasma production terms, which are considered short-distance interactions. Elastic collisions are responsible for the resistivity associated to the plasma, as per Eq. (4.41), and also play a major role in terms such as the resistive (or Ohmnic) heating term, appearing in Eq. (4.47). Inelastic collisions, on the other hand, represent a large energy sink for the electron population since they may lead to ionization or excitation of neutral atoms.

A third type of collisions is also considered in HYPHEN: resonant CEX[249, 118], which vary in nature with respect to elastic and ionization collisions, since they are considered long distance processes. The Xenon cross-sections for CEX were obtained from the work by Miller[250], but will not be reviewed here, since they belong, in scope, to the PIC segment. Ion and neutral scattering in the PIC are neglected based on the comparison between the collisional MFP, for the typical densities of the various heavy species, and the simulation domain sizes.

Finally, it is worth noting that plasma recombination models, i.e. an electron recombining with an ion within the bulk of the plasma, are neglected. This assumption is based on the recombination rate for single-ion-to-neutral given by Mitchner & Krueger[251], which is $\mathcal{O}\left(10^{-20}\right)$ for typical near-plume electron densities of $\mathcal{O}\left(10^{17}\right)$; these values are many orders of magnitude smaller than the values obtained for the first ionization of typical propellants such as Xenon or Argon, as will be seen in this section, and thus may be neglected.

Collisional processes in HYPHEN are modeled in a similar way to HPHall[76] or HallMa[132, 133], by employing the collision cross-section, σ. The cross section represents the effective area of collision between an "incoming" particle and an agregate of "quasi-stationary" particles. This mathematical construct is valid between populations with largely disparate velocities, which is the case if we compare the electron thermal velocity to the velocity of ions or neutrals in the plasma. As per Ref. [27], the cross section satisfies:

$$\begin{aligned} \nu &= \frac{1}{\tau} = n_\alpha \sigma v \\ R &= \frac{\nu}{n} \end{aligned} \tag{5.32}$$

where n_α is the density of the stationary species, v the velocity of the incoming particle, τ the mean time between collisions and, thus, ν the frequency of collisions, and R is the collision *rate*.

The previous expression may then be averaged over the PDF of the incoming population in order to obtain a representative value of the collisional rate between two species. In our case, we employ a bi-Maxwellian Electron Probability Distribution Function (EPDF), obtained by dividing $F_e^{(0)}$ in Eq. (4.17) by the electron density, integrated in cylindrical space, since the DF only distinguishes between parallel and perpendicular velocities (Fig. 3.4):

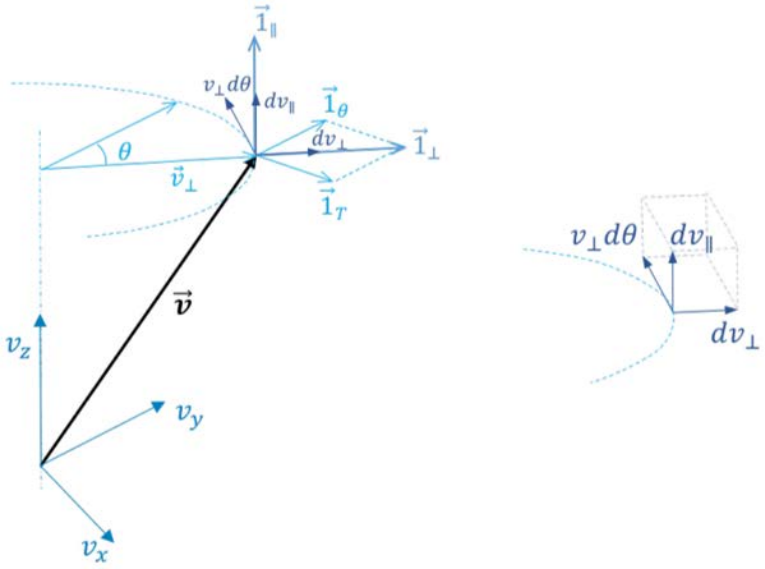

Figure 5.14: Cylindrical integration space for bi-Maxwellian EPDF

$$f_e = \frac{F_e^{(0)}}{n_e} = \left(\frac{m_e}{2\pi k_B}\right)^{3/2} \frac{1}{T_{e\perp}\sqrt{T_{e\parallel}}} \exp\left(-\frac{m_e c_{e\perp}^2}{2k_B T_{e\perp}} - \frac{m_e c_{e\parallel}^2}{2k_B T_{e\parallel}}\right)$$
$$\langle R \rangle = \int_0^{2\pi} d\theta \int_{-\infty}^{\infty} dc_{e\parallel} \int_0^{\infty} c_e \sigma f_e c_{e\perp} dc_{e\perp} \tag{5.33}$$

where the integration limits pertinent to the integration space considered. Note that the electron particle velocity in the collision rate integral average, $\langle R \rangle$, has been approximated by the thermal velocity[4], $\vec{c}_e \approx \vec{v}_e$.

The key aspect here are the models used for the cross-sections of the various collisions considered; typically, these models respond either to experimental data or to mechanistic models of particle collisions.

Regarding the latter, Gryzinski[252] derived a model for obtaining ionization and excitation cross-sections based on classical mechanics. Gryzinski's model allows for obtaining ionization and excitation cross-sections, although it assumes that the electrons only impact with the outer orbitals of the atom, neglecting the case in which an electron may impact with inner orbitals, which may

[4]The dimensionality of the model could be increased by adding the electron drift velocity as an additional parameter, if it were considered that the drift kinetic energy could play a significant role in the integrals for collisional rates; this may be considered for future work.

excite the atom and lead to an auto-ionization process known as the Auger effect[5][253].

Other classical models include Lotz's formulation[254], which provide similar values to those obtained through the Drawin model[255], which has been extensively used in legacy codes.

Regarding experimental results for cross-sections, there are multiple sources where the values for different possible collisions can be found, such as the works by Mathur & Badrianthan[256] and Borovik[257], both presenting data for single and multiple ionization reactions and excitation-auto-ionization processes. Perhaps one of the most prolific authors in the field, which has been proposed for some of the models employed in HYPHEN, is Hayashi[258, 259], which obtained experimental cross-sections for a multitude of atomic reactions.

Experimental results have been compiled in the well-known database of the Plasma Data Exchange Project[260], which includes freely accessible data for cross sections by a multitude of researchers, including Hayashi, Puech[261], Phelps, etc. The cross-sections for the Xenon atom were compared by Bordage et al.[262]. Another useful database for cross-sections is OPEN-ADAS[263], which, however, does not include data for Xenon.

Finally, an alternative to experimental results for the calculation of cross-sections are numerical codes that are able to compute values for elastic or ionization and excitation collisions based on the fine structure and atomic constants of a large number of atomic elements. Some examples of such codes are the open source Los Alamos National Laboratory (LANL) Atomic Physics Codes suite[264] or the Magboltz code by Biagi[265, 266].

The following sections offer a review of the models and experimental data that have been integrated in HYPHEN, particularly for the Xenon and Argon atoms. Some of these models have been previously employed on legacy codes and others seek to update cross-sections with more accurate descriptions.

5.2.1 Elastic collisions

Momentum exchange elastic collisions take a central role in the electron population transport equations and thus the modeling approach can have distinct effects over the simulation results (see Chapter 7). Consider that the collision rates derived here are translated into collision frequencies through the following expression:

$$\nu_{en} = n_n \langle R_{en} \rangle$$
$$\nu_{eiZ} = n_{iZ} \langle R_{eiZ} \rangle$$

Starting with electron-neutral collisions, legacy codes such as HallMa have utilized a constant cross-section for the Xenon elastic neutral collisions, obtained from the work by Mitchner & Krueger[251], of $\sigma_{en} = 3 \cdot 10^{-19} m^2$. This approach yields a high collision rate in comparison to experimental results obtained by Hayashi. A separate model by McEachran& Stauffer[267] produces even higher collisional rates than the Drawin model and was implemented in a modified

[5]This process may be of importance in high electron temperature plasmas, which may be present in certain EP technologies and high powered thrusters.

version of HPHall-2[231] by the EP group at JPL. The collision rates for these models and the bi-Maxwellian approximation to the PDF are compiled in Fig. 5.15 for representative values of $T_{e\|}$ and expected values of $\hat{T}_e$.

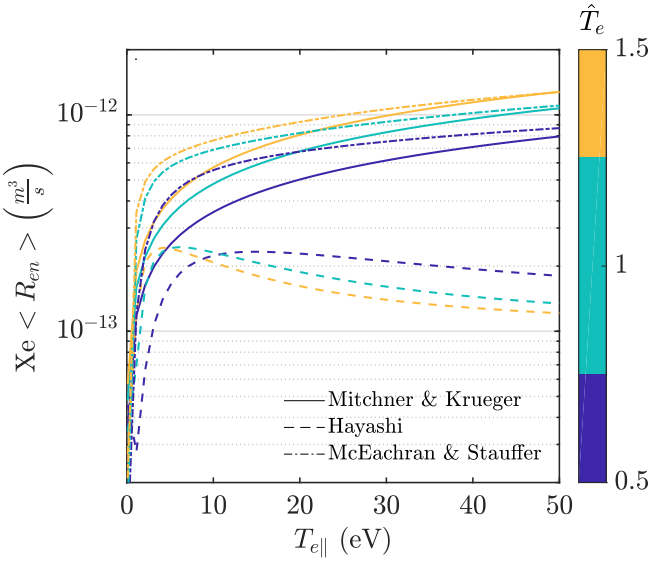

Figure 5.15: Xenon electron-neutral elastic collision cross-section, integrated from the models proposed by Mitchner & Krueger[251] and McEachran& Stauffer[267] and the experimental data compiled by Hayashi[259]

The electron-neutral elastic scattering cross-section for Argon was obtained from the experimental data produced by Hayashi[268], which is fractionally smaller than the experimental cross-section for Xenon; the collision rate can be seen in Fig. 5.16.

It stands for future work to update these cross-sections with further models found in the literature, particularly for Argon.

Secondly, elastic electron-ion collisions were neglected in HallMa since they present cross-sections that are at least an order of magnitude smaller than electron-neutral collisions; however, the collision frequencies can still become comparable in the plume region sufficiently downstream from the thruster channel, and therefore should not be discarded a priori.

Elastic electron-ion collisions are approached using a Coulomb interaction model as described by Goldston[269], whose development will not be reproduced here, for brevity. The model takes into account the importance of small-angle deflections versus the effect of strong deflections due to the potential energy of the Coulomb interaction. The expression for the cross-section results in:

$$\sigma_{eiZ} = \frac{Z^2 e^4 ln\Lambda}{4\pi\epsilon_0^2 m_e^2 v_e^4} \tag{5.34}$$

where $ln\Lambda$ is the well known Coulomb logarithm, which typically takes values $10 - 20$ for the

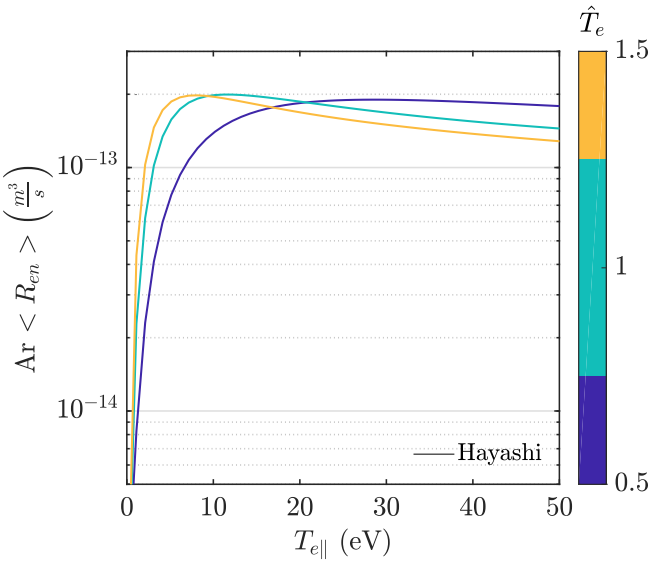

Figure 5.16: Argon electron-neutral elastic collision cross-section, integrated from the experimental data compiled by Hayashi[259]

near plume region. The expression for σ_{eiZ} can be introduced in the integral in Eq. (5.33) by approximating the electron particle velocity by the thermal velocity.

5.2.2 Ionization and excitation inelastic collisions

The inelastic collisions that have been considered in HYPHEN are the following:

$$\begin{aligned} &X + e^- \rightarrow X^* + e^- \\ &X + e^- \rightarrow X^+ + 2e^- \\ &X + e^- \rightarrow X^{++} + 3e^- \\ &X^+ + e^- \rightarrow X^{++} + 2e^- \end{aligned} \tag{5.35}$$

where X is an arbitrary atomic element. Triply charged ions are not considered, since cross sections for Xenon are at least an order of magnitude smaller[270] than the smallest of the cross-sections considered here (specifically, the $0 \rightarrow 2$ reaction).

Each of these ionization or excitation processes is characterized by the energy deposited in the collision and the cross-section. The source terms related to ionization in Eq. (4.13) are given by:

$$\begin{aligned} &S_{i1} = n_e \nu_{i01} = n_e n_n \langle R_{i01} \rangle \\ &S_{i2} = n_e \left(\nu_{i02} + \nu_{i12}\right) = n_e \left(n_n \langle R_{i02} \rangle + n_{i1} \langle R_{i12} \rangle\right) \\ &S_e = n_e \left(n_n \langle R_{i01} \rangle + 2 n_n \langle R_{i02} \rangle + n_{i1} \langle R_{i12} \rangle\right) \end{aligned} \tag{5.36}$$

The models that have been implemented for each of the various cross-sections of Xenon and Argon are compiled in Table 5.2 and are reviewed next:

Element	Reaction	Models
Xe	$0 \rightarrow *$	Hayahsi
	$0 \rightarrow 1$	Drawin
	$0 \rightarrow 2$	Drawin
	$1 \rightarrow 2$	Drawin, Bell
Ar	$0 \rightarrow *$	Hayashi
	$0 \rightarrow 1$	Drawin, Hayashi
	$0 \rightarrow 2$	Drawin
	$1 \rightarrow 2$	Drawin

Table 5.2: Ionization and Excitation cross-section models for Xenon and Argon

The energy deposition *rate* per volume, or energy *yield*, $Y\left(\frac{eV}{m^3 s}\right)$, represents the energy spent in inelastic collisions per unit of volume; it can be obtained by averaging the energy deposited per collision, ϵ, over the DF, alongside the cross-section as:

$$\langle Y \rangle = \int_0^{2\pi} d\theta \int_{-\infty}^{\infty} dc_{e\parallel} \int_0^{\infty} c_e \epsilon \sigma F_e c_{e\perp} dc_{e\perp} \tag{5.37}$$

On first approximation, this value depends solely on the final atomic state, however, the problem grows in complexity if one considers that, for example, a multitude of excited states can appear before ionization occurs, or that ionization may occur through the more complicated Auger effect[253]; thus, the energy deposited may also depend on the energy of the impacting electron.

Starting with the excitation reactions, this happens to be the case for Argon as per the Hayashi database[259], where each excited state responds to a different excited configuration in the electron orbitals, as shown in Fig. 5.17, and is onset by a different energy deposition and cross-section.

In this case, we are interested in an overall "engineering" cross-section and energy yield: this can be obtained by performing a weighted average based on the cross-section values for each instance of impacting electron energy, considering only the excited states that require an energy deposition equal or greater than the impact energy being considered.

In general however, one may consider a single value for the energy deposited in the inelastic collision process. These figures, together with the average value for the excited state of neutral Argon, are shown in Table 5.3:

Element	ϵ_{i01}	ϵ_{i02}	ϵ_{i12}	ϵ_{ex}
Xe	12.13	20.98	32.12	8.32
Ar	15.75	27.62	40.74	$\langle 13.61 \rangle$

Table 5.3: Impacting electron energy deposition per inelastic collision type for Xenon and Argon (all values in eV); the Argon excitation energy has been averaged for the surveyed data in Ref.[259]

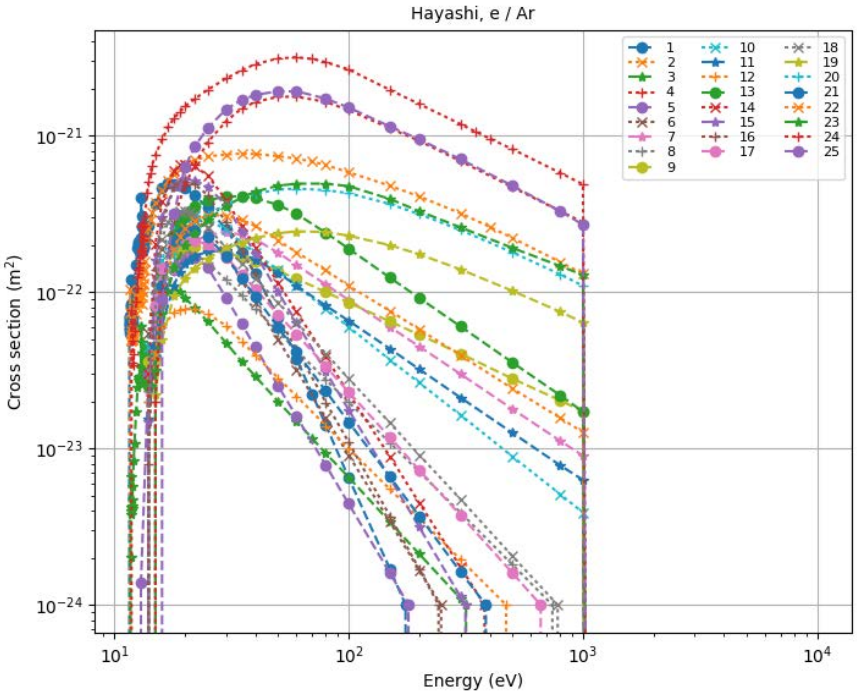

Figure 5.17: Cross sections for various excited states in neutral Argon, obtained from the Plasma Data Exchange Project[260]

The excitation cross-section for Xenon has been obtained from Hayashi[258], which offers a single relation for the most probable excited state.

Regarding the ionization cross-sections, we have mainly utilized the Drawin model, which is a commonly used approach to obtain the cross-section of simple and double ionization[76, 142, 212]. We have also implemented data from the Hayashi database for the first ionization of Argon, yielding much smaller cross-sections than the Drawin model.

The Drawin model uses a semi-empirical method based on classical mechanics; the formulation is described by Mitchner & Krueger[251] and provides the following expression for an arbitrary ionization cross-section:

$$\sigma_i = 2.66\pi a_0^2 \beta_1 \left(\frac{\epsilon_i^H}{\epsilon_i}\right)^2 \eta g\left(u\right) \;\; ; \; g\left(u\right) = \frac{u-1}{u^2} ln\left(1.25\beta_2\right) \tag{5.38}$$

Where a_0 is the radius of the first Bohr orbit for Hydrogen (i.e., the fine structure constant), η is the equivalent number of electrons in the outer shell, ϵ_i^H is the ionization energy of Hydrogen and $u = \dfrac{m_e c_e^2}{2\epsilon_i}$ is the electron non-dimensional energy. The parameters β_1 and β_2 depend on the ionization process and are used to adjust the results to fit those obtained experimentally. The values in Table 5.4 have been used in the literature when applying the Drawin model:

Element	Reaction	β_1	β_2	η
Xe	$0 \rightarrow 1$	1.0	0.8	6
	$0 \rightarrow 2$	1.0	0.8	6
	$1 \rightarrow 2$	1.0	0.8	5
Ar	$0 \rightarrow 1$	0.82	1.0	6
	$0 \rightarrow 2$	0.82	1.0	6
	$1 \rightarrow 2$	0.82	1.0	5

Table 5.4: Drawing model parameter values for various ionization reactions in Xenon and Argon

In the case of Xenon, for the three ionization reactions studied, the Drawin model results in an underestimation of the cross-sections at electron energies larger than $\sim 60eV$. Because of this, Smith[270] proposed a revised fit in which the $g(u)$ function is modified by adding a third parameter β_3:

$$g(u) = \frac{u-1}{u^{\beta_3}} ln(1.25\beta_2)$$

This modified fit has better correlation with the experimental data obtained by Mathur & Badrianthan[256] for single and double ionization of Xe at higher energies, although since it is only relevant at very high energies, it has not yet been incorporated in HYPHEN.

For the lower energy range, on the other hand, the Drawin model for the $0 \rightarrow 1$ reaction underestimates the ionization rates found in experimental results. For this reason, legacy codes implemented the fit proposed by Bell[271], which is based on experimental results. The Bell fit targets $\langle R_{12} \rangle$ and adjusts to the experimental results using a Chebyshev polynomial expansion, assuming a maxwellian PDF; the fit is given by the following expression:

$$\langle R_{12} \rangle|_{Bell} = \frac{1}{2}\sqrt{\hat{T}_e T_{e\|}} \exp\left(\frac{\epsilon_{i12}}{\hat{T}_e T_{e\|}}\right)(b_0 - b_2) \cdot 10^{-6}\frac{m^3}{s} \tag{5.39}$$

where b_0 and b_2 are parameters which depend on T_e and are given by the Clenshaw algorithm[272]. The expression for the Bell fit has been modified to take into account the variables considered here.

To finish, the ionization and excitation collision rates for the reactions contemplated here, for the various models for Xenon and Argon atoms are shown inf Figs. 5.18 and 5.19.

It is worth noting that, in the case of Xenon, the excitation rate and energy yield are of the same order as the ones for the $0 \rightarrow 1$ ionization, which will be reflected in the energy expenditure due to inelastic collisions (refer to Chapter 7). Since the excited state is frequent, its is arguable that the ionization reaction $X^* + e^- \rightarrow X^+ + 2e^-$ should also be included; however, this would imply tracking the excited neutral state as a separate population in the PIC segment, which is not currently contemplated, and possibly a matter of future work.

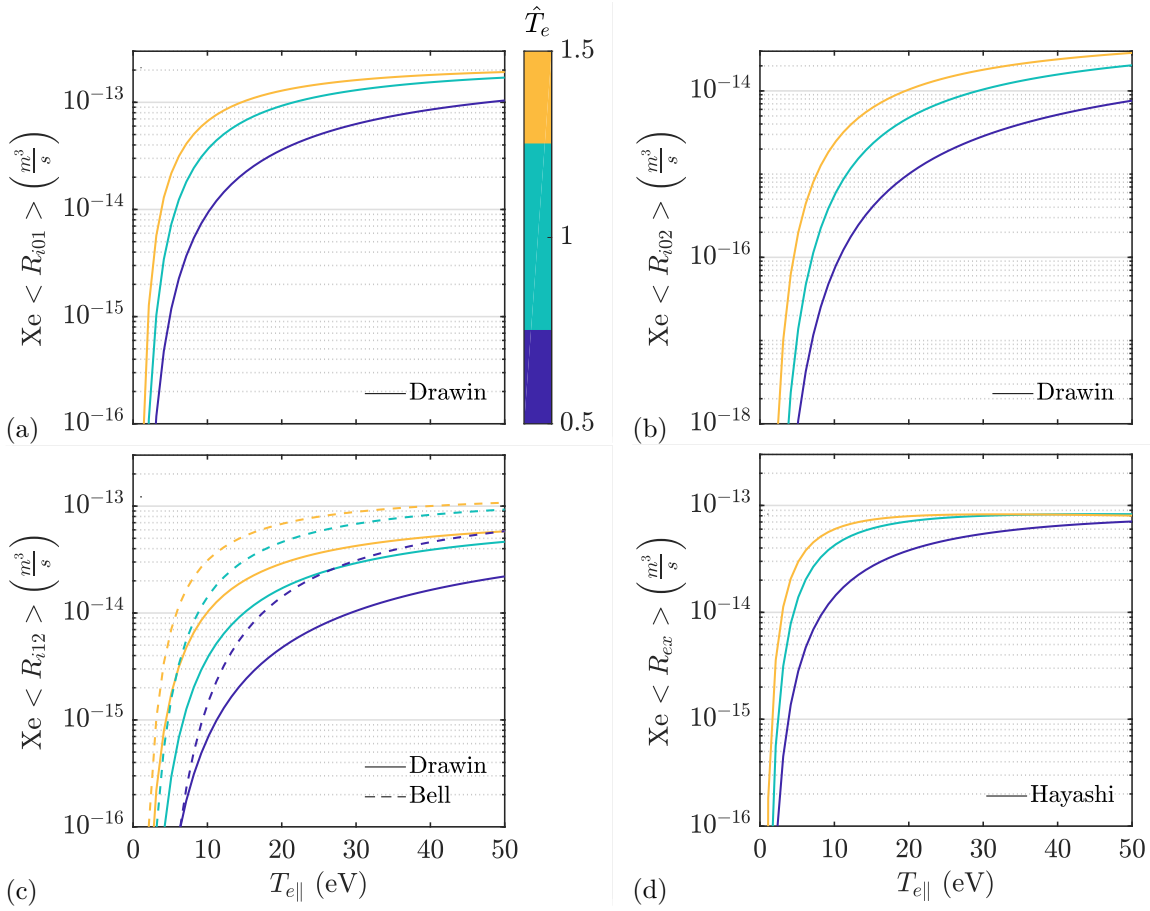

Figure 5.18: Xenon ionization and excitation collision cross-sections, integrated from various models and experimental results[255, 271, 259]

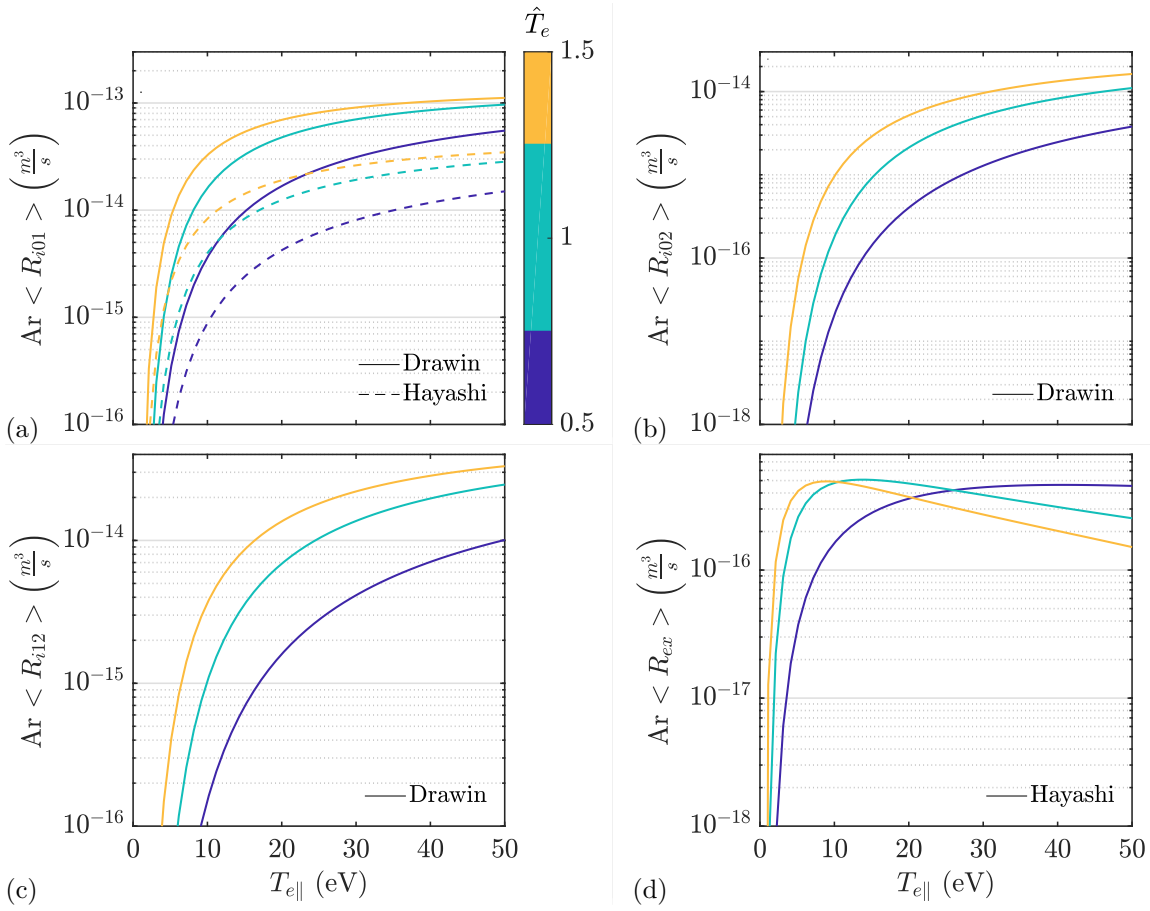

Figure 5.19: Argon ionization and excitation collision cross-sections, integrated from various models and experimental results[255, 259]

CHAPTER
SIX

NOMADS stress test results

This chapter is centered on the results obtained from the NOMADS module under the conditions set by frozen entry PIC 2D maps[1]. In particular, the PIC maps used in this chapter are obtained from a stable HallMa simulation for the SPT-100 thruster, in an effort to prove that the NOMADS module is capable of providing a solution which is consistent with the former code; as an exception, Section 6.8 uses PIC maps obtained from HYPHEN, for the reasons detailed there.

6.1 Foreword to NOMADS stress test

Focusing solely on the results of the electron fluid module allows us to explore the physics of the electron population as well as the various options in the simulation pertaining to the electron model. In particular, different temporal schemes, initial conditions, time-steps, current injection types, mesh refinement and other variants are examined.

The results obtained in this chapter are viewed, partly, from the perspective of convergence of the electron solution; for this we use two indicators: simulation volume balances of thermal energy density in the FVM (see Section 6.2) and "residual" values (both for temperature and plasma potential) throughout the simulation. The residual is an indicator of the average change of a particular quantity between two consecutive time-steps and is based on the following expression:

$$R_{\psi}^{t} = \frac{\sqrt{N_E \sum_{i=1}^{N_E} \left(\Psi_{E_i}^{t} - \Psi_{E_i}^{t-1}\right)^2}}{\sum_{i=1}^{N_E} \Psi_{E_i}^{t-1}} \tag{6.1}$$

where N_E is the number of elements in the MFAM and Ψ_{E_i} is any given quantity defined at a particular control volume.

The MFAM and PIC meshes used for the simulations in this chapter (unless specified otherwise), together with the magnetic field in the simulation domain, are presented in Fig. 6.1. The MFAM was generated using the exponential-stretching method (Section 3.3) and the PIC mesh was taken directly from the mesh utilized in HallMa. The configuration of the magnetic circuit used to obtain the magnetic field and MFAM is akin to the one shown in Fig. 7.1(a).

[1]NOMADS offers options so that these fields are be obtained either from the entry or exit conditions for a particular PIC time-step, or from a mid-point condition (averaged between entry and exit).

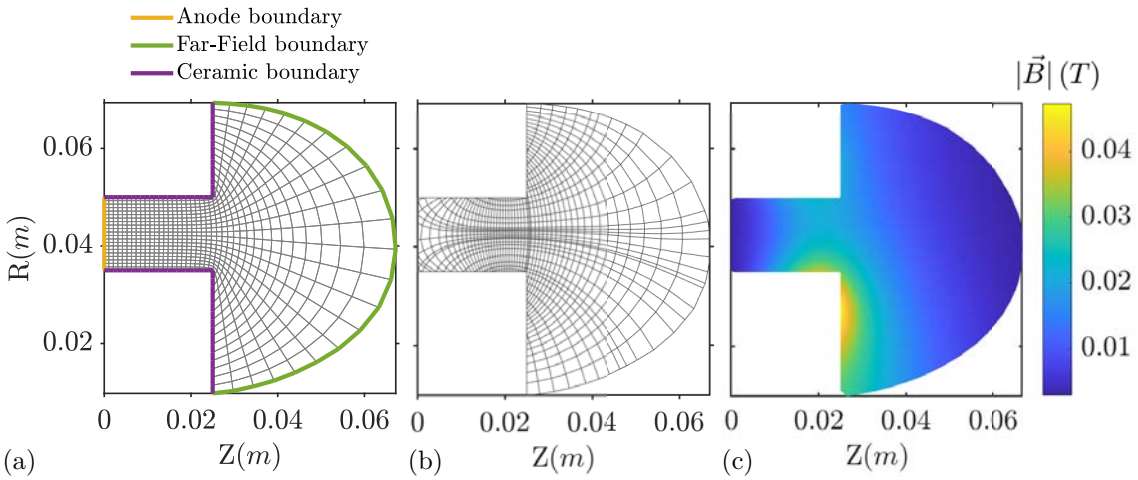

Figure 6.1: (a) PIC mesh, (b) MFAM and (c) magnetic field for NOMADS stress test (except mesh-refinement analysis)

Note that, unless specified otherwise, when showing 2D maps, a fine "plotting" mesh has been utilized, with both results from the PIC segment and the NOMADS segment being interpolated to it; this avoids bias in representation due to different plasma quantities being obtained in different meshes, although it cannot account for low quality elements in the origin meshes (e.g., regions of low smoothness or very large element areas).

The PIC solution utilized here may be characterized through its "interface" variables with the NOMADS module: plasma density, ion currents and partial densities for each heavy species. Representative maps are shown next, together with the electron temperature and plasma potential maps obtained from HallMa. These constitute an *initial condition*[2] for the electron fluid (unless specified differently in a particular section) and are shown in Fig. 6.2.

Furthermore, the anomalous collisional frequency factor, α_{ano}, is chosen to be a two-region parameter (with the exception of the results shown in Section 6.6) and is shown in Fig. 6.3. The necessity of various distinct regions for this parameter was proposed by Koo[137], partially based on the work by Hagelaar[136, 273]. The latter made the case for regions influenced either by "Bohm type" diffusion, or by wall-collisionality, rather than regions with varying values of α_{ano}, similarly to what was originally proposed by Kaufman[37]. The two-region approach been implemented by various other authors[231, 233, 142] both for different thrusters and different simulation codes that make use of this approach towards modeling of the non-classical electron transport. Nonetheless, other authors have recently challenged the idea that the problem should be resolved through distinct regions of anomalous collisionality or the existence of Bohm-like regions. In particular, Mikellides & Ortega[126, 229] showed that the values of α_{ano} can differ greatly from the ones traditionally reported in the literature in the region downstream from the thruster[3].

[2]Since the generalized Ohm's equation, Eq. (4.69), is a state equation which depends on plasma density, ion currents and electron temperature, the initial condition for the electron fluid may be described solely through the electron temperature, for a given PIC map; nonetheless, we show the plasma potential solution from HallMa for comparison with our own solution.

[3]This has been addressed in Chapter 7.

Following the above, and for the particular results obtained in this chapter (considering both the simulation domain utilized and the results from legacy codes to which we wish to compare), we employ a "step-out" type function (or "mixed outer", in Koo's terminology), which depends only of the magnetic streamline function coordinate, λ, and a *traditional* value for α_{ano} outside the thruster channel (and no anomalous collisionality within it).

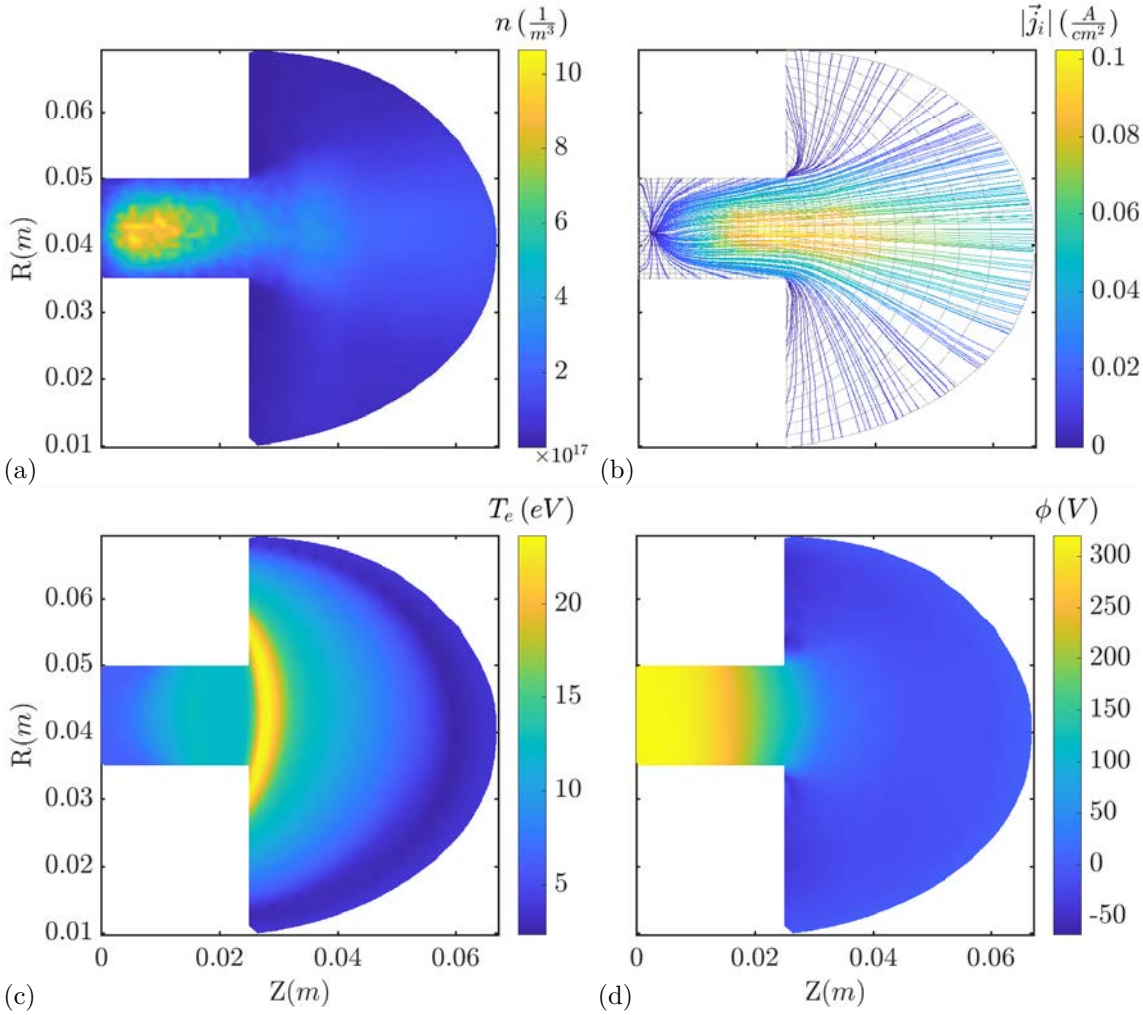

Figure 6.2: (a) Plasma density, (b) Total ion currents, (c) T_e and (d) ϕ initial conditions for NOMADS stress test (except mesh-refinement analysis)

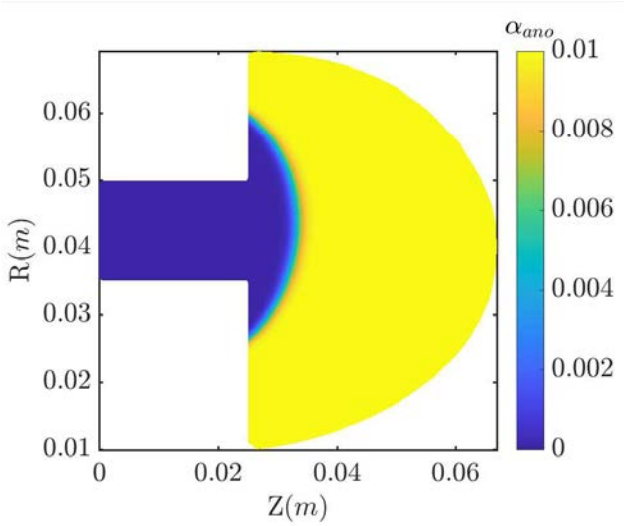

Figure 6.3: Anomalous collisionality factor for NOMADS stress test (except mesh-refinement analysis)

The operating parameters for the thruster, unless specified otherwise, are:

PPU control	$\mathbf{V_d}$	$\dot{\mathbf{m}}$ **(Xe)**	**Cath. type**
Constant voltage	$300V$	$5\frac{mg}{s}$	Volume proportional (single elem.)

Table 6.1: SPT-100 operating parameters for NOMADS stress test

The specifics of PPU control and cathode type can be seen in Section 4.2.4. The collisional models used for Xenon are as follows (more details on these models may be found in Chapter 5):

- Elastic collisions use the model by Hayashi[259] for electron-neutral pairs and the Coulomb interaction model from Goldston[269] for electron-ion pairs.
- Inelastic collisions use the Drawin[274] model for ionization reactions $Xe \rightarrow Xe^{+}$ and $Xe \rightarrow Xe^{++}$, the Bell[271] model for $Xe^{+} \rightarrow Xe^{++}$ and the Hayashi[258] model for the excitation reaction $Xe \rightarrow Xe^{*}$. Recombination reactions were neglected.
- Presently, CEX are neglected in the simulations.

Finally, the sheath models implemented were generated under the following parameters (refer to Section 5.1):

sheath type	**material**	δ_0	σ_{th}	$\mathbf{E_r}$	$\mathbf{E_b}$	$\mathbf{T_b}$
Dielectric	BN	0.4	0.3	$40eV$	$40eV$	$2eV$
Conducting	$\sim$	0.0	0.3	$\sim$	$\sim$	$\sim$

Table 6.2: Sheath model parameters for NOMADS stress test

The Far-Field BC was chosen to be non-homogeneous Neumann both for electron currents and heats (refer to Section 4.2.3), i.e., null-heat flow at the boundary and normal electron current equal and opposite to the total ion current. The mesh boundaries can be seen in Fig. 6.1(a).

6.2 Explicit and Semi-implicit time schemes: stability and convergence analysis

Section 4.2.2 provides various temporal discretizations for the thermal energy density, Eq. (4.72), and parallel internal energy, Eq. (4.73), equations, which, together with plasma density changes from the PIC segment, are responsible for the temporal evolution of the electron fluid in the present model. The main difference in the discretization is the explicit vs. implicit nature of the *pressure terms* in the equations.

Initial trials with NOMADS, solving only for the total electron temperature and assuming isotropic electron temperatures, showed that the explicit equation required an unreasonably large number of electron time-steps to achieve stable convergence in the results. The reason being that transport in the parallel direction is unbounded by the magnetic field and thus may take values that are various orders of magnitude larger than other terms in the equation.

In order to reduce the large number of iterations required by the explicit time-scheme, a numerical limiter which capped the change in the energy contribution to a particular element due to the parallel heat-flow term was implemented. The limiter existed as a multiple of the maximum change in energy-per-volume present in the simulation domain for a particular time-step due to all of the other terms in Eq. (4.72), including the perpendicular heat-flow term:

$$
\begin{aligned}
&\left\{ q_{e\parallel}\big|_{F_j} \cdot \frac{A_{F_j}}{V_{E_i}} \right\}_{lim} \propto \underset{i}{max} \left\{ \frac{2}{3} \left[\sum_{j(E_i)} \frac{3}{2} \frac{p_e}{e n_e} \vec{j}_e \Big|_{F_j} \cdot \vec{n}_{F_j} \frac{A_{F_j}}{V_{E_i}} + \right.\right. \\
&+ B^2 \left(\frac{3p_e - p_{e\parallel}}{2e} \frac{\partial \left(r j_{e\top} B^{-1} n_e^{-1} \right)}{\partial \lambda} + \frac{p_{e\parallel}}{e} \frac{\partial \left(j_{e\parallel} B^{-1} n_e^{-1} \right)}{\partial \sigma} \right) \Bigg|_{E_i} - \\
&- \sum_{j(E_i)} \left(q_{e\top} \vec{1}_\top \right)\big|_{F_j} \cdot \vec{n}_{F_j} \frac{A_{F_j}}{V_{E_i}} + \left(\sum_Z \eta_{i_Z} \frac{Z n_{i_Z}}{n_e} \left| \left(\vec{j}_e + \frac{n_e}{Z n_{i_Z}} \vec{j}_{i_Z} \right) \right|^2 + \right. \\
&\left.\left. \left. + \eta_{en} \left| \left(\vec{j}_e \right) \right|^2 + \frac{m_e}{2e^2} \frac{S_e \left| \left(\vec{j}_e \right) \right|^2}{n_e^2} + E_{ioniz+excit} \right) \Bigg|_{E_i} \right] \right\}
\end{aligned}
\tag{6.2}
$$

The use of the limiter is not preferred since it artificially modifies the physics encoded into the energy equations, although precedents exist in the literature. Section (6.2.2) presents differences in the overall electron energy balances and the residuals and comments on the general difficulties encountered when using the explicit temporal scheme.

6.2.1 Stability and convergence considerations

In relation to the FVM method on non-structured meshes, Barth & Ohlberger[275] have proposed a generalization for stability and convergence conditions in integral conservation law schemes of

the type:

$$\int_{V_{E_i}} \frac{d\psi}{dt} dV = \oint_{A_{F_j(E_i)}} f\left(\psi, \dots\right) d\vec{A} \tag{6.3}$$

where the evolution for any quantity ψ can be described, approximating using Eq. (4.65), by:

$$\left.\frac{d\psi}{dt}\right|_{E_i} = \frac{1}{V_{E_i}} \sum_{F_j(E_i)} \left[C_{ji}\left(\psi, \dots\right) \cdot f\left(\left.\psi\right|_{E_i}\right) + C_{jk}\left(\psi\right) \cdot f\left(\left.\psi\right|_{E_k}\right)\right] \tag{6.4}$$

where the coefficients associated to fluxes depend on both the particular element being treated as well as the surrounding elements, denoted by k; note that these surrounding elements do not need to be immediately adjacent, as they depend on the stencils used for gradient reconstruction.

The previous description only takes into account the temporal change in ψ due to fluxes at the control volume faces. Equations (4.72) and (4.73), however, also include changes in the total and parallel electron pressures due to volumetric terms, particularly, the resistive heating and the gas expansion work. This means that, for the following considerations, the quantity ψ takes the form:

$$\psi \equiv \{p_e\} + \{Exp\} \cdot \{p_e\} + \{CS\} \tag{6.5}$$

Barth & Ohlberger[275] propose a condition for stability based on local maxima and minima being bounded in the temporal evolution; the condition is known as Local Extremum Diminishing (LED) and can be described mathematically by:

$$min\left(\left.\psi\right|_{E_i}^{t}, \left.\psi\right|_{E_k}^{t}\right) \leq \left.\psi\right|_{E_i}^{t+1} \leq max\left(\left.\psi\right|_{E_i}^{t}, \left.\psi\right|_{E_k}^{t}\right) \tag{6.6}$$

which implies that local minima are non-decreasing and local maxima are non-increasing. This condition can be extended into an L^{∞}-stable condition if absolute bounds may be found for all elements at any time-step in the scheme.

Additionally, a Courant Fredrich Levy number (CFL) type condition for the coefficients associated to flux terms can be used to ensure convergence, imposing a constraint on the time-step, Δt:

$$1 - \frac{\Delta t}{V_{E_i}} \sum_{F_j(E_i)} C_{ji}\left(\mathrm{GR}, \left.\beta_{e^*M}\right|^{t}, \left.\vec{j}_e\right|^{t}, \dots\right) \leq 0 \tag{6.7}$$

Note that this condition only appears if the fluxes across the control volumes in the mesh are treated explicitly, which only occurs in the fully explicit scheme. C_{ji} represents those coefficients associated to GR for first order derivatives, appearing in the heat-flow terms, as well as function value reconstruction coefficients, for advection terms, times the factors associated to each of those. As exemplified by Eq. (4.74), the factors depend on the Hall parameter, electron currents, etc.,

and are always evaluated explicitly. It is worth noting that, while the gradient reconstruction coefficients do not vary throughout the simulation, the aforementioned factors do, which means that the CFL condition must be checked at each time-step.

For the explicit scheme, the CFL condition imposes a restriction over Δt based mainly in the coefficients associated to the direction parallel to the magnetic field, which are much larger than those related to the perpendicular direction, due to the anisotropicity of the problem. In particular, the restriction is primarily due to the heat-flow term, which justifies the use of the numerical limiter for that term.

For the semi-implicit scheme, the flux terms are treated implicitly for every control volume face that does not belong to the boundary. The boundary fluxes are treated explicitly in the code only in the case of plasma sheath BC, although their contribution to the CFL condition is difficult to quantify.

As a summary, the condition for stability may only be checked during simulation run-time and must be checked for each element and temporal step. The condition for convergence is a CFL type condition which must be checked for each element and time-step in the explicit scheme, imposing hard constraints in the Δt used in the simulation. In the semi-implicit scheme, the CFL condition exists solely for boundary elements, meaning that the Δt constraints are less strict. The Δt or, more precisely, the number of electron time-steps in NOMADS, must be chosen in consideration of these conditions, although the violation of stability or convergence may only be checked a-posteriori.

6.2.2 Temporal scheme comparison

Results from the simulations confirm that the use of the semi-implicit discretization allows for an electron time-step which is a few orders of magnitude larger than the minimum required for convergence in the explicit discretization. The following figures compare two NOMADS simulations with equal initial conditions, BCs (equal anode and ceramic sheath models and "far-field" non-homogeneous Neumann condition, as per Section 6.1) and anomalous collisionality factor (α_{ano}) maps. The time-steps chosen for the semi-implicit Euler and explicit Euler results are, respectively, $10^{-9}s$ and $10^{-11}s$; the simulation time is $2{\cdot}10^{-5}s$ in both cases[4].

Each of the terms in Eq (4.74) is integrated over the simulation domain to obtain the partial contributions to an electron *energy balance* in the system (the expressions for each of the partial contributions presented in Fig. 6.4 may be found in Section 4.2.2, in Eqs. (4.74) and (4.75)). Notice that the contribution due to the perpendicular and parallel heat-flow terms in the simulation volume adds to zero, by definition; additionally, the sum over the whole simulation volume of the energy advection term amounts only to the value for said contribution at the Far-Field boundary.

[4] A convergence criteria based on the residuals value was not selected for these simulations.

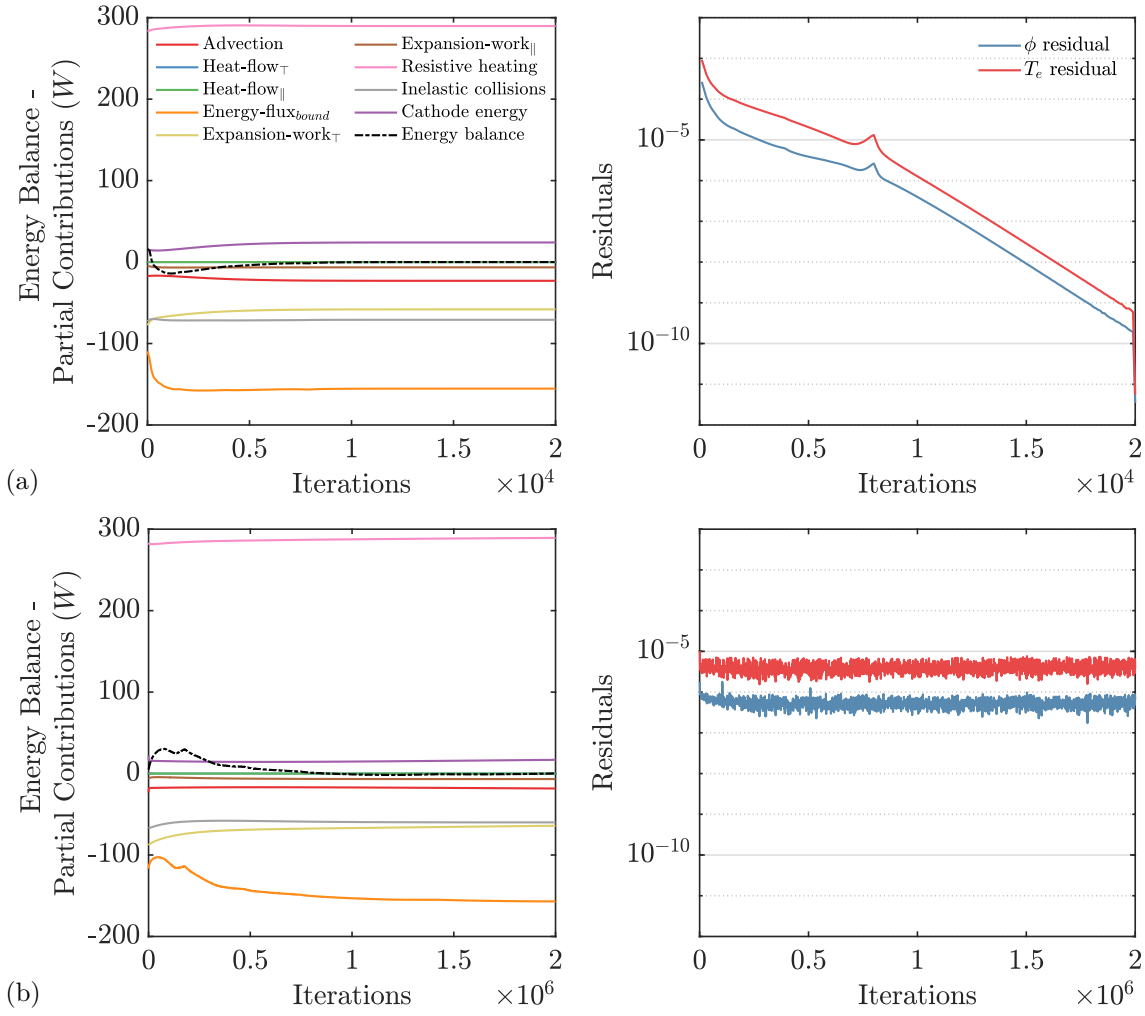

Figure 6.4: Electron energy Balance and T_e and ϕ residuals for (a) Semi-implicit Euler discretization and (b) Explicit Euler discretization

Discretization	$\mathbf{P_{adv}}\vert_{\mathbf{FF}}$	$\mathbf{P_{bound}}$	$\mathbf{P_{exp\top}}$	$\mathbf{P_{exp\parallel}}$	$\mathbf{P_{heat}}$	$\mathbf{P_{inel}}$	**Err**	$\mathbf{P_{cath}}$
explicit	−18.3	−151.0	−59.1	−3.8	289.3	−59.9	−2.8	16.8
semi-implicit	−15.1	−145.4	−58.1	−6.5	290.8	−65.8	−0.1	24.1

Table 6.3: Partial contributions to *electron energy balance* and cathode energy, P_{cath}, for explicit and semi-implicit temporal discretizations; all values provided in W

Table 6.3 shows the exit balances, split between each of the different contributions. Note that the power balances presented in this chapter refer exclusively to the electron population; power balances for the heavy-species as well as integral balances for the whole plasma are presented in Chapter 7. Also, take notice that the cathode energy in these power balances simply represents the

sum of the contributions due to energy advection and gas expansion work at the cathode elements and must not be summed separately to the total energy balance; the electron temperature related to said terms is a *fixed* cathode temperature, selected by the user.

Equation (4.74) shows that the only terms to be calculated completely in an explicit manner are those related to collisions. The change in resistive heating between the explicit and semi-implicit schemes shown in Table 6.3 is inappreciable, meaning that the effect over the electron currents (which can only appear through varying gradients of electron pressure) is small. The difference between the remaining terms, however, is less subtle: more energy is lost to the walls and lost to the gas expansion work in the explicit scheme, which implies that the reached temperatures will be lower and, in turn, the energy lost to ionization and excitation will also be smaller. These differences can have a profound effect on the overall results of a simulation in which NOMADS runs alongside the PIC segment; however, as is discussed in the remainder of this section, the explicit discretization also presents other problems, which prevented us from displaying results for the plasma quantities in the simulation domain.

Regarding the convergence criterion, it is clear that an arbitrarily low residuals cannot be met by the explicit discretization solution, shown in Fig. 6.4(a), since residuals for both the electron temperature and plasma potential oscillate around an average value. This is due to the fact that the explicit solution can be oscillatory in nature, even when the time-step chosen is below the stability or convergence limits. Lower residual values may be achieved by lowering the value of the time-step, at the cost of further increasing the number of iterations. On the contrary, for the semi-implicit case, shown in Fig. 6.4(b), it is a reasonable assertion that arbitrarily low convergence criteria could be met simply by increasing the simulation time, for this particular configuration.

Further numerical complications and stability issues due to the use of the explicit discretization and the numerical limiter were noticed, including nonsensical gradient reconstruction results, due to the existence of highly non-smooth temperature fields for certain values of the electron time-step.

For the reasons exposed in this section, use of the explicit discretization was discarded in favor of the semi-implicit method. Every other simulation result shown in this document corresponds to that particular discretization scheme.

6.3 Semi-implicit discretization results

Once the semi-implicit discretization was chosen as the default, we wished to characterize the electron fluid results obtained from the NOMADS segment. These results offer a fully 2D reconstruction of the electron fluid, in comparison to the "perturbed" 1D model that was implemented in legacy codes (refer to Sections 1.2.3 and 4.1). The following figures correspond to the "end-state" for the simulation whose convergence was presented in Fig. 6.4(a).

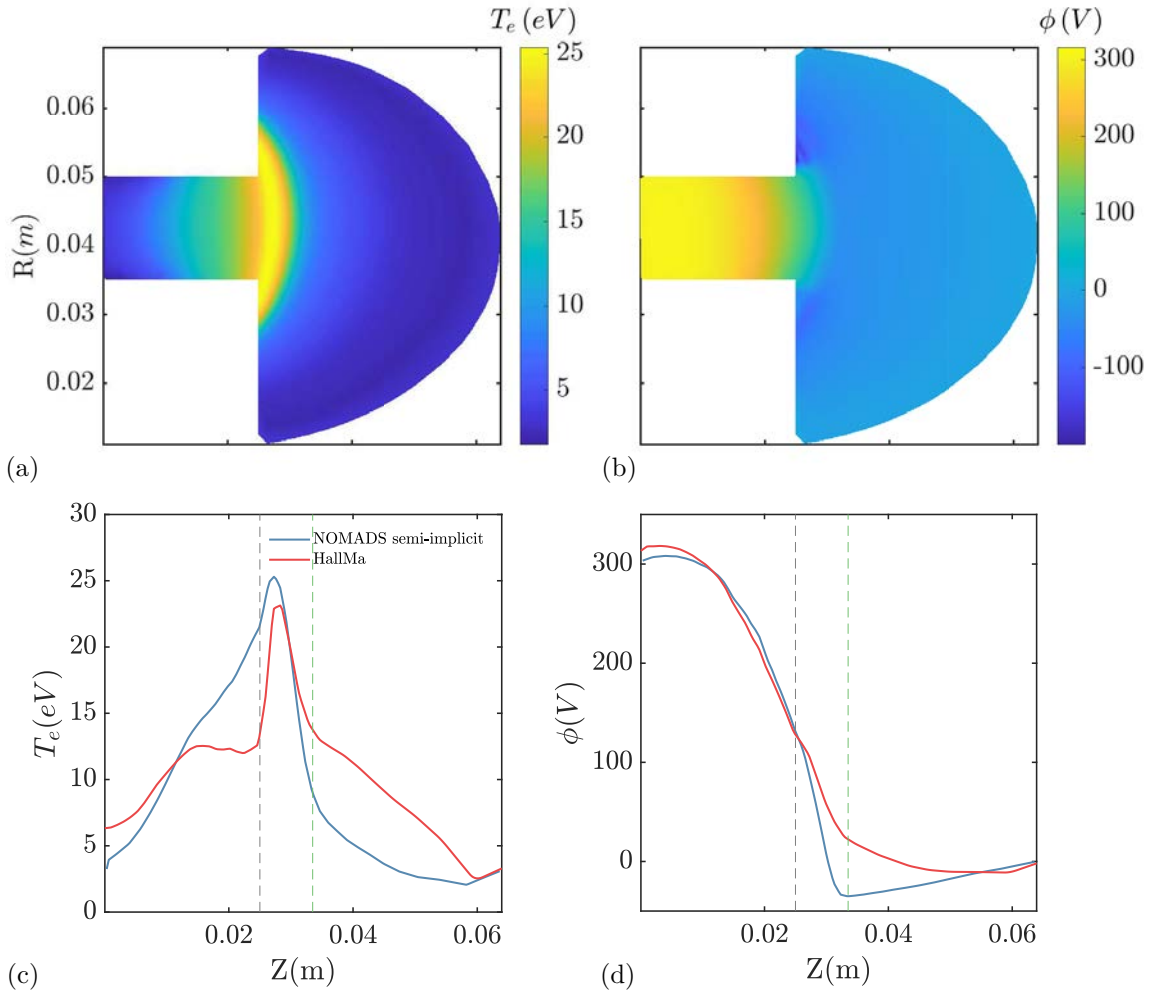

Figure 6.5: 2D maps in semi-implicit NOMADS for (a) T_e and (b) ϕ and TCL profiles (HallMa vs. semi-implicit NOMADS) for (c) T_e and (d) ϕ; (- - -) marks the channel exit and (- - -) the step change in α_{ano}

The most obvious difference, in comparison to the initial conditions (shown in Fig. 6.2) appears in the electron temperature. The main difference between HallMa and NOMADS is in the implementation of the thermal energy equation and the ancillary physical models such as the collisional or sheath models (Chapter 5), as well as the other BCs implemented. In particular, the following items summarize some major changes, that help to illustrate the differences between solutions:

- The energy expenditure due to inelastic collisions in HallMa (first and second ionization and excitation collisions) was approximated by a factor multiplying the first ionization yield, and the electron-neutral elastic collision rate employed the Mitchner-Krueger model[274], which is based on a constant cross-section; in contrast, HYPHEN employs updated and separate models for each of the collisional processes in the simulation (Section 5.2), which may play a role in lower electron temperature presented the near-anode channel region and in the plume region. Chapter 7 explores the energy expenditure due to various collisional models.

- The sheath model implemented in HallMa is very similar to the one developed in Section 5.1, although the former neglected the influence of the magnetic field and considered multiple reflections of the energetic electron beams between the dielectric wall sheaths.

- HallMa resorted to an approximate solution for the NAR[212], instead of solving the region consistently with the rest of the simulation domain as does NOMADS; this may also play a role in the electron temperature in the NAR.

- The exit boundary condition for the energy equation in HallMa was a Dirichlet condition which imposed a temperature on the "closing" magnetic streamline; in comparison, we have implemented non-homogeneous Neumann BCs together with a fixed temperature only in the advection and gas expansion terms for the volumetric cathode (refer to Section 4.2.4).

Contrary to the electron temperature, the plasma potential presents relatively smaller differences between the two solutions. This is in line with the dependency of the potential with the electron *pressure* in the generalized Ohm's equation, Eq. (4.39), which is related to both temperature and density, the latter bring equal in both simulations. The larger potential drop in the NOMADS solution may be linked to a lower electron temperature past the channel exit. Nonetheless, the main differences in the electric potential solution appear in the 2D nature of the solution, which are influenced by the also 2D distribution of the Hall parameter and electron resistivity as well as by the use of a true 2D MFAM, versus the 1D version used in HallMa.

For completion, we present the 2D maps of the Effective total Hall parameter, β_{e^*}, and Effective total electron resistivity, η_{e^*} (both on logarithmic scale for convenience); terms which play a main role in the response of the electron fluid:

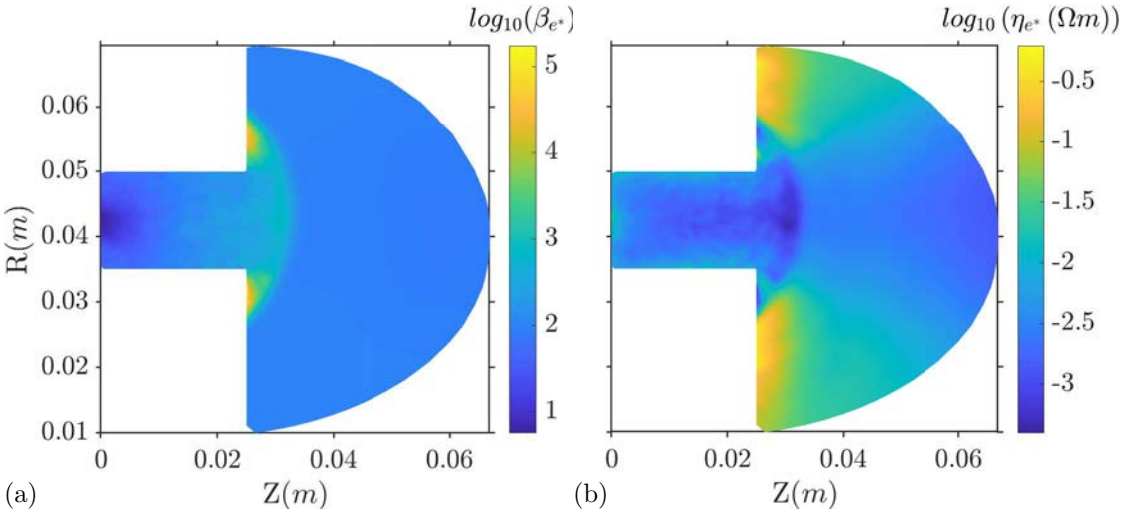

Figure 6.6: 2D maps of (a) β_{e^*} and (b) η_{e^*} in semi-1implicit Euler NOMADS scheme

It is clear that the anomalous collision frequency has a large effect over both physical quantities, seen here as the obvious step in their values after the thruster channel exit. It is worth reminding

the reader that both quantities offer a view of the compounded effect of various collisional processes, including: elastic electron-to-heavy-species collisions, inelastic collisions (ionization and recombination) and non-classical terms such as the anomalous or near-wall collision frequency (Section 4.1.2), which depend on the electron and heavy species densities. For a segregated comparison of the various collision frequencies in the problem, please refer to the results in Chapter 7.

The role of the α_{ano} over the coupled response of the plasma is explored briefly in Section 6.6. As can be inferred from Chapter 4, α_{ano} has an overarching effect in relation to the electron temperature, since it affects the electron total resistivity, the Hall parameter (Fig. 6.6) and the perpendicular and azimuthal electron current densities. In turn, these modify the resistive heating term, Eq. (4.72), which has a major influence over the resulting electron temperature.

Finally, Fig. 6.7 presents the electron current density in the domain. Note that the current streamlines are derived only from the axisymmetric $z-r$ solution, whereas the current density *modulus* also takes into account the value of the azimuthal current. This result is native to HYPHEN, and not to previous codes, since the parallel electron current density field is now obtained as part of the solution.

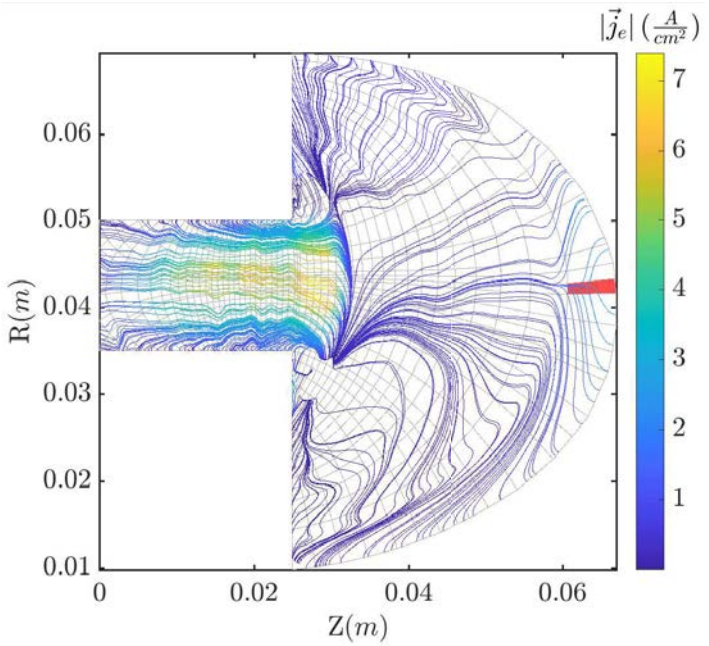

Figure 6.7: Electron currents in semi-implicit NOMADS (volumetric cathode element in red)

A few comments can be made regarding this last figure:

- The electron current density solution can only be, by definition, consistent with the electric potential, density and temperature fields and ion current maps, since the generalized Ohm's law is solved by imposing current continuity over the momentum equation (Section 4.2).
- All BCs, except for the anode wall, impose $\vec{j}_e \cdot \vec{n}_b = -\vec{j}_i \cdot \vec{n}_b$. The electron current in the direction *along* the boundary is obtained through extrapolation from the inner simulation

domain. This fixes the way the streamlines behave at the boundaries.

- Electron current density is up to two orders of magnitude larger than ion current densities (Fig. 6.2(b), mind the different scales). This is mainly due to the azimuthal Hall current typical of HETs, which appears mainly around the channel exit, where the $\vec{E}\times\vec{B}$ drift is largest.

- The streamlines surrounding the volumetric cathode element show that the cathode current tends to disseminate in the parallel direction to the magnetic field; this current is split between the neutralization current and a part which flows back to the anode.

- The anomalous collisionality factor also exhibits a large influence on electron currents, as it does on every other fluid result. The developed electric potential, which presents a local minimum $\sim 0.05m$ downstream from the channel exit, as seen in Fig. 6.5, together with the electron resistivity and Hall parameter are responsible for the particular electron current distribution near the channel exit.

- In comparison to ion currents, electron current streamlines are much less uniform. This is reasonable considering the large electron mobility, and the fact that they are subject to non-uniform electron pressure, electric potential and resistivity fields and different degrees of magnetic confinement. Note that the source of these non-uniformities for a given time-step may also arise from numerical noise derived from the PIC solution. In particular, the streamlines are subject to a sort of "rippling" effect which is more prevalent in regions with very low current densities. A possible explanation is that this is related to a sort of high "noise-to-signal-ratio" in said regions, where local and larger scale effects are equally relevant.

  Alternatively, streamline representation becomes difficult for non-structured meshes due to plotting artifices that may be present in meshes with varying cell size, and mesh quality, such as the MFAM. This must be kept in mind when considering electron streamline results shown in this work.

As a last remark, it can be said that the obtained results are reasonably in line with what was obtained from HallMa and may be explained through the characteristics of the model implemented in NOMADS. Chapter 7 will provide a deeper look into results from complete simulations, which present the transitory nature of the thruster physics.

6.4 Initial conditions sensitivity analysis

It is important to characterize the effects of different initial conditions over convergence, since it provides a clue on the time-scales associated with the electron physics. Thus, instead of using the initial temperature map from HallMa, shown in Fig. 6.2(c), we may impose a constant temperature, e.g. $T_e = 10eV$, while the ion currents and plasma density maps remain as per Fig. 6.2. Simulation convergence results for an electron time-step value of $10^{-9}s$ are shown in Fig. 6.8.

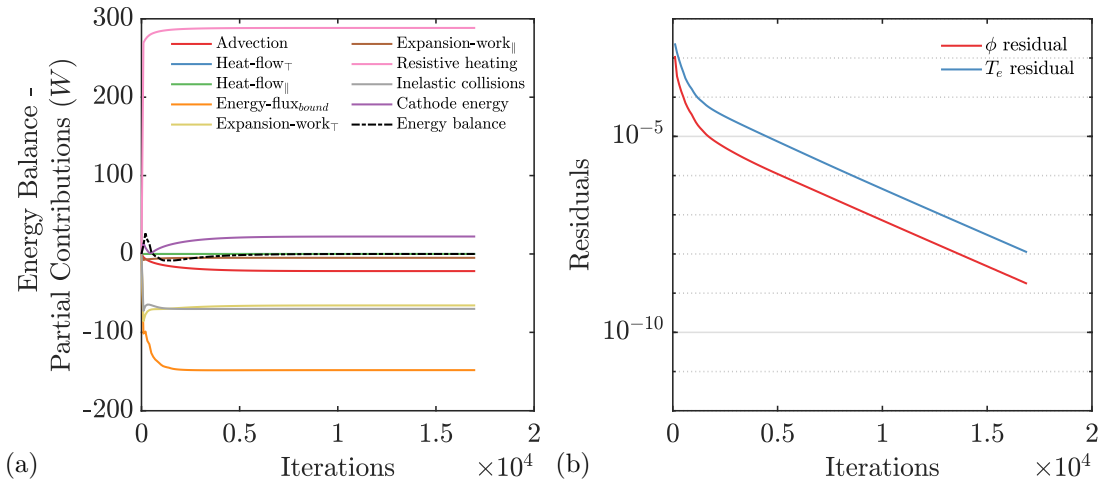

Figure 6.8: (a) Electron energy balance and (b) T_e and ϕ residuals for Semi-implicit Euler discretization ($dt_e = 10^{-9}s$) with constant initial T_e map

Note that the convergence criteria was selected for the T_e residual to be under 10^{-8}, which is why the results are cut-off after the criteria is met. The *Iterations axis* is scaled as per the results in Fig. 6.4(a) for comparison: both initial condition simulations would achieve the same convergence criteria for a number of iterations in the order of $1.7 \cdot 10^4$.

Init cond	$\mathbf{P_{adv}}\vert_{\mathbf{FF}}$	$\mathbf{P_{bound}}$	$\mathbf{P_{exp\top}}$	$\mathbf{P_{exp\parallel}}$	$\mathbf{P_{heat}}$	$\mathbf{P_{inel}}$	**Err**	$\mathbf{P_{cath}}$
constant T_e	−16.8	−145.2	−60.7	−6.9	293.4	−65.0	−1.3	22.3
2D T_e map	−15.1	−145.4	−58.1	−6.5	290.8	−65.8	−0.1	24.1

Table 6.4: Partial contributions to electron energy balance and cathode energy, P_{cath}, for semi-implicit temporal discretization with constant initial T_e map and 2D T_e map obtained from the HallMa output; all values provided in W

Table 6.4 shows that some slight variation of $\sim 1W$ exists for some values, although thi. These changes are linked to the fact that the exit time-step is 3000 iterations earlier than in the case shown in Fig. 6.4, due to the exit criteria.

For the sake of brevity, the simulation results are not shown here, since they are identical to the ones presented in Fig. 6.5. This similarity is expected, as the electron temperature is only dictated by the constraints for the simulation (ion densities and currents, boundary conditions, various collisionalities etc.), which are exactly the same for both initial conditions.

6.5 Time-step sensitivity analysis

Regarding the chosen time-step for a particular simulation, it is not only important to understand what the method's limit for stability and convergence is, as shown at the beginning of the chapter, but also if and how sensitive the solution is to different electron time-steps.

The following figure presents the convergence results for simulations with a constant initial temperature field ($T_e = 10eV$, as in Section 6.4) for electron time-step values of $10^{-8}s$ and $10^{-10}s$:

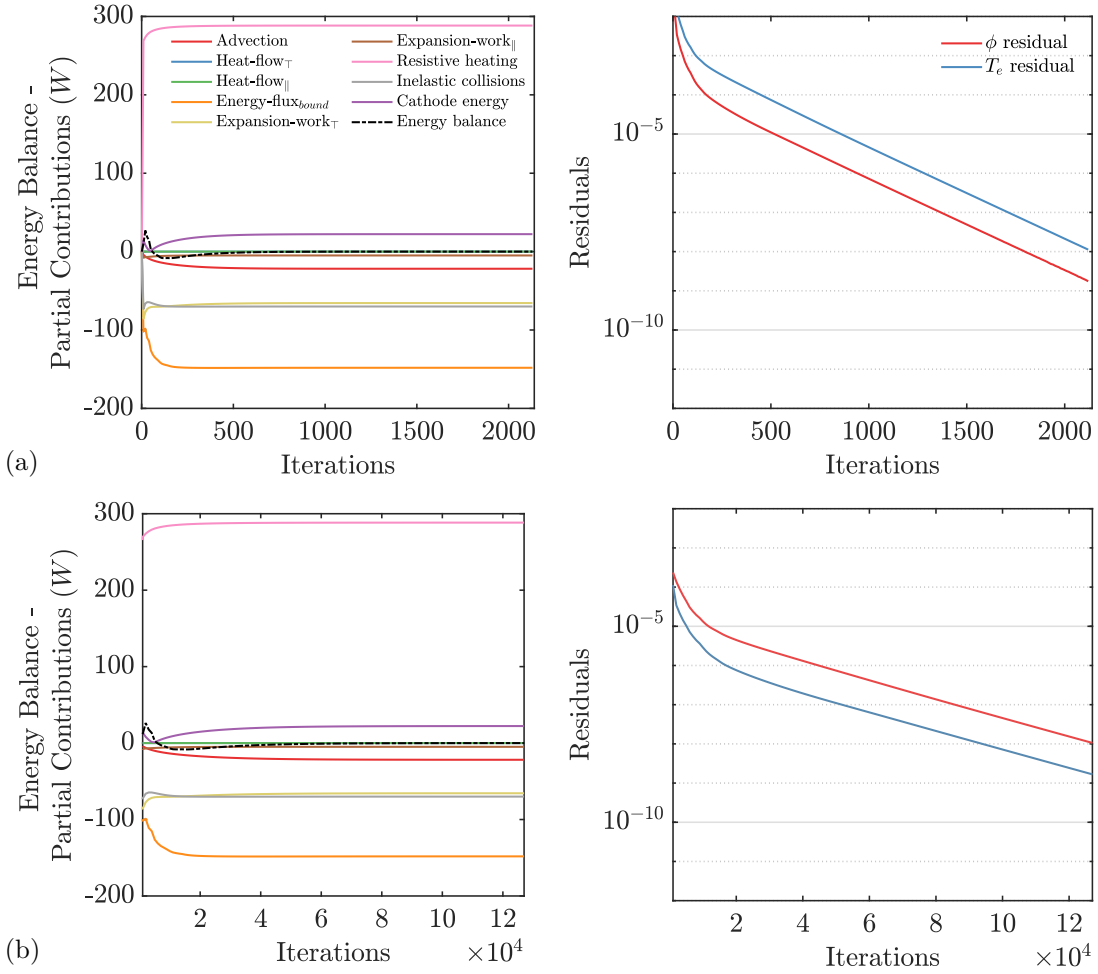

Figure 6.9: Electron energy balance and T_e and ϕ residuals for Semi-implicit Euler discretization with (a) $dt_e = 10^{-8}s$ and (b) $dt_e = 10^{-10}s$

Again, the convergence criterion chosen for all simulations was for the T_e residual to be under 10^{-8}. The converged fluid states as well as the contributions to the energy balances, shown in Table 6.5, are identical for both of the electron time-steps trialled (and identical to the ones shown in Fig 6.5), signaling that when we are above the stability and convergence limits the solutions are not dependent on the dt_e.

dt_e	$\mathbf{P_{adv\|_{FF}}}$	$\mathbf{P_{bound}}$	$\mathbf{P_{exp\top}}$	$\mathbf{P_{exp\parallel}}$	$\mathbf{P_{heat}}$	$\mathbf{P_{inel}}$	**Err**	$\mathbf{P_{cath}}$
$10^{-8}s$	-16.9	-145.3	-60.6	-6.9	293.4	-65.0	-1.3	22.2
$10^{-10}s$	-16.8	-145.2	-60.7	-6.9	293.4	-65.0	-1.2	22.2

Table 6.5: Partial contributions to electron energy balance and cathode energy, P_{cath}, for semi-implicit temporal discretization with constant initial T_e map various dt_e; all values provided in W

The convergence iteration as a function of the dt_e used, for the simulations presented above, is shown next:

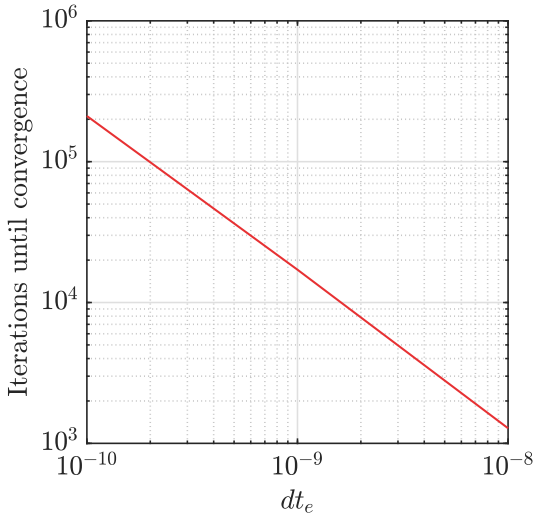

Figure 6.10: Iterations until convergence vs. dt_e for Semi-implicit Euler discretization

6.6 Brief sensitivity analysis for the anomalous collisionality factor

The anomalous collisionality is intricately coupled to the plasma physics modeled in HYPHEN: perpendicular and azimuthal electron current densities and heat-flow are affected by it, which in turn has an effect on the resistive heating term, which then cascades over to the PIC segment through the electron temperature and dependent collision rates. The plasma production, which in turn determines plasma density, influences the electron current densities, and so forth. The sensitivity of solutions in hybrid codes which employ this parameter to account for non-classical axial electron mobility has been studied by various authors[276, 231, 277, 278].

This section presents a short comparison of two different α_{ano} maps: the one shown in Fig. 6.3 and a constant anomalous collision frequency factor $\alpha_{ano} = 0.005$. This comparison cannot take into account the compounded effect over the ion populations, but will allow the reader insight into the physical mechanisms pertaining the electron fluid, which are influenced by this parameter.

Figure 6.11 shows the perpendicular and azimuthal components of electron current density and the electron current density modulus: a lack of anomalous transport in the thruster channel and downstream from it leads to lower perpendicular current densities[5] for the 2D map. However, the opposite is true in the case of azimuthal current densities, as per Eq. (4.42), in which the added anomalous collision frequency transfers momentum in the azimuthal direction to the perpendicular one in an asymmetric way. The transfer of momentum between azimuthal and perpendicular directions carries over to the electron current density module, where the azimuthal current (also known as Hall current) provides it's largest contribution, and then, to the resistive heating term, in Eq. (4.75).

Notice that the volumetric cathode (Fig. 6.7) condition for the plasma potential (described in Section 4.2.4), together with the non-homogeneous Neumann BC for the exit boundary, can be clearly noticed in the electron current, including the required reversal in the perpendicular current direction after neutralization. Additionally, the perpendicular current density for the constant α_{ano} remains larger than its counterpart for the extent of the Thruster Center Line (TCL), even in the region where the 2D map presents a larger anomalous collisionality factor. This is due to the fact that currents ultimately depend on electron pressure and plasma potential gradients (which are shown to clearly differ in Fig. 6.12), and must conserve total current continuity.

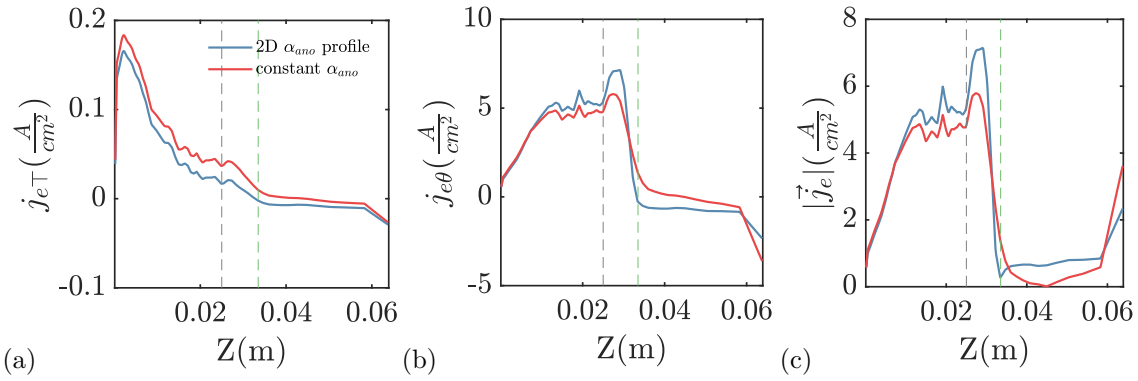

Figure 6.11: TCL profiles of (a) $j_{e,\top}$, (b) $j_{e,\theta}$ and (c) $\left|\vec{j}_e\right|$ for constant α_{ano} vs. 2D α_{ano} map; (- - -) marks the channel exit and (- - -) the step change in α_{ano}

[5]Due to the magnetic topology of the SPT-100, perpendicular currents generate the largest contribution to the axial electron current, since the magnetic field is mostly radial.

Table 6.7 provides a comparison for the exit state in both simulations, in terms of the discharge current in the simulation and the partial contributions to the energy balance.

α_{ano}	$\mathbf{I_d}$	$\mathbf{P_d}$
2D	$3.2A$	$960W$
cnst.	$3.7A$	$1110W$

Table 6.6: Discharge current and power for constant α_{ano} vs. 2D α_{ano} map; cathode energy, P_{cath}, shown for reference

α_{ano}	$\mathbf{P_{adv}}_{\vert\mathbf{FF}}$	$\mathbf{P_{bound}}$	$\mathbf{P_{exp\top}}$	$\mathbf{P_{exp\parallel}}$	$\mathbf{P_{heat}}$	$\mathbf{P_{inel}}$	**Err**	$\mathbf{P_{cath}}$
2D	-21.8	-143.2	-60.6	-4.9	290.8	-61.2	-0.9	22.3
cnst.	-20.5	-101.5	-45.4	-2.3	230.2	-61.2	-0.7	20.6

Table 6.7: Partial contributions to electron energy balance and cathode energy, P_{cath}, for constant α_{ano} vs. 2D α_{ano} map; all values provided in W

While the discharge current and power is greater for the constant α_{ano} case, the achieved heating power is less, which produces a lower exit state electron temperature (Fig. 6.12, to be compared with Fig. 6.5). Note that the perpendicular heat-flow also takes into account the anomalous collisionality factor and its effects are implicit in the electron temperature results.

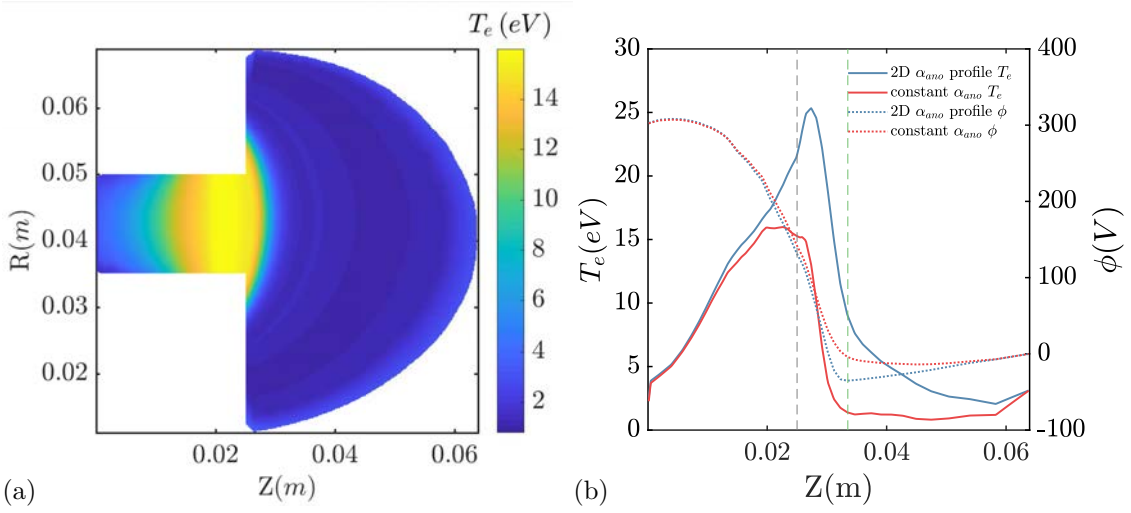

Figure 6.12: (a) 2D T_e map for constant α_{ano} and (b) TCL T_e profiles (constant α_{ano} vs. 2D α_{ano} map); (- - -) marks the channel exit and (- - -) the step change in α_{ano}

The previous analysis implies that the α_{ano} parameter has profound effects on the electron physics, not only affecting the axial currents in the thruster but also the energy balances, as was already expected due to the considerable literature on the topic, which has been referenced throughout this chapter. These effects will carry over onto the heavy species side of the simulation,

further complicating its mark onto the full response of the plasma. The selection of a particular distribution for α_{ano} must therefore be based on a wide parametric investigation which is informed either by experimental or expected performance values and plasma characteristics from a particular thruster. As such, a parametric investigation exploring the effects of α_{ano} on full simulations in HYPHEN is presented in Chapter 7.

6.7 PPU Control and Current injection variants

NOMADS offers the user the possibility of varying both the PPU Control type, the selection of elements on which the discharge current is "injected" in the domain and the way said current is distributed along the injection elements, i.e., what we have termed the *cathode type*. This section offers a comparison to the previously shown results by presenting a simulation in which we have used a volumetric cathode with currents distributed proportionally to the plasma density and a PPU control based on constant discharge current. The thruster operating parameters for this simulation are:

PPU control	$\mathbf{I_d}$	$\dot{\mathbf{m}}$ **(Xe)**	**Cath. type**
Constant current	$3.2A$	$5\frac{mg}{s}$	Density proportional (multiple elements)

Table 6.8: SPT-100 operating parameters for variant PPU Control and Current injection options

The discharge current, I_d, was chosen as per the one obtained from the simulation with a 2D anomalous collisionality factor, as shown in Table 6.7. This was done to demonstrate that both thruster operation modes are equivalent for the same frozen PIC maps. Indeed, the discharge voltage for the exit state, obtained by averaging the plasma potential over the volumetric cathode elements (shown in red in Fig. 6.13), is $V_d = 300.91V$, which differs only 0.3% from the input discharge voltage in the previous simulations. The exit state electron temperature and plasma potential are identical to the ones shown in Fig. 6.5, and are not shown here for brevity; similarly, the partial contributions to the energy balance present negligible differences between simulations.

Figure 6.13 shows electron current density streamlines for the variant operation. Comparing this plot and Fig. 6.7 one may notice that the streamlines are only different over the section of the simulation domain closest to the exit boundary, where the cathode current is injected. For additional insight, Fig. 6.14 presents the difference for parallel current density over the simulation domain and a comparison of the perpendicular current density over the TCL, between the two operational modes in the thruster.

The most relevant distinction between operating modes resides in the distribution of elements over which current is injected: in the case of the "single element injection", the current is rapidly distributed along the parallel direction, which explains the large difference between parallel current density between both solutions. Note that the parallel current density over the lower half of the simulation domain is larger than over the upper half. This is due to the fact that, as we approach $r = 0$, the areas become smaller, and thus the current density must be larger to distribute a given injection total current.

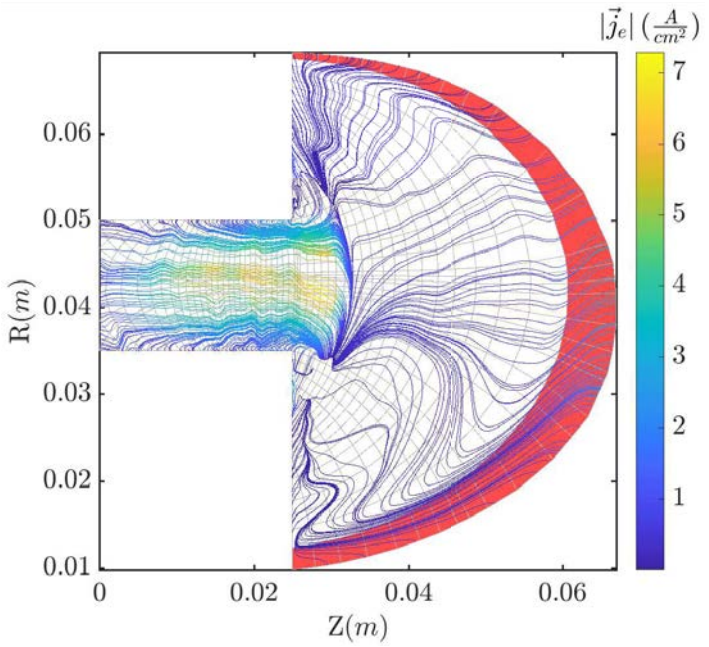

Figure 6.13: Electron currents for variant operating parameters (volumetric cathode elements in red)

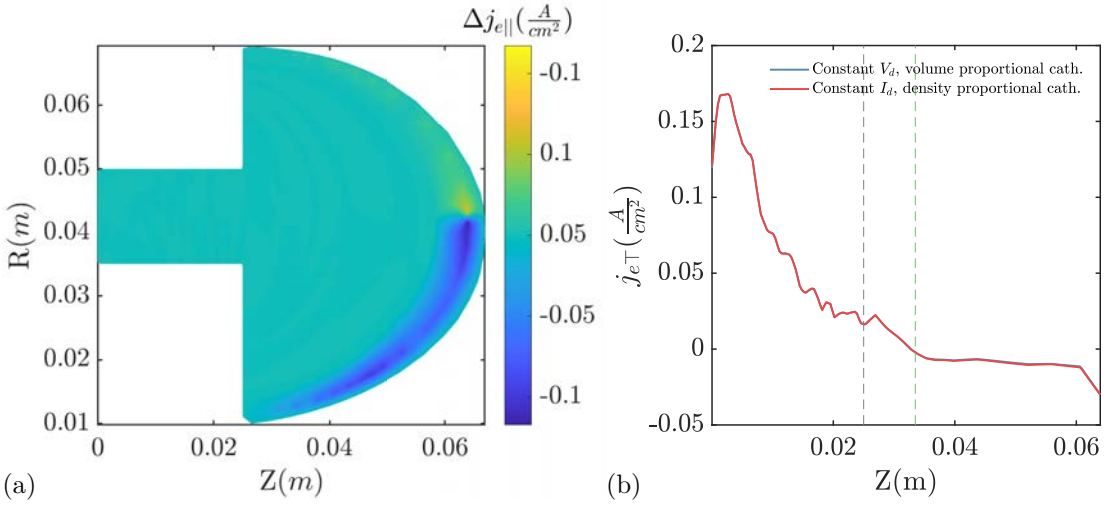

Figure 6.14: (a) Differences between 2D maps of $j_{e\|}$ and (b) TCL comparison of $j_{e\top}$ for variant and base operating parameters; (- - -) marks the channel exit and (- - -) the step change in α_{ano}

6.8 MFAM mesh refinement sensitivity analysis

Sections 3.3 and 3.4 were devoted to the study of the geometric quality of the mesh and the influence of mesh refinement on GR; both indicators are associated with the overall quality of the mesh which, nevertheless, cannot be truly assessed without considering the problem under

scrutiny, as proposed by Diskin[203] and Sozer[206].

This section is oriented towards comparing results for a single NOMADS time-step for a stable simulation carried out by HYPHEN, similar to the ones shown in Chapter 7. The initial temperature and plasma potential maps are equal for all cases, but will not be shown here for brevity, since we are interested only in the converged state.

The operating parameters for the simulations, as well as the sheath model parameters and collisional models, are the same as described in the introduction to this chapter. Additionally, we have selected for no anomalous transport in this case, to avoid potential effects related to this simulation parameter. The volumetric cathode has been restricted to a single element[6] for all three simulations, following the results from Section 6.7. For this purpose, a single element closest to both the TCL and an axial position of $Z = 0.065m$ has been chosen. This approach lends itself to some variability in the reconstruction of the plasma potential, as can be appreciated in Fig 6.19.

The PIC mesh used is shown in Fig. 6.15, where the imposed domain boundary types are also displayed.

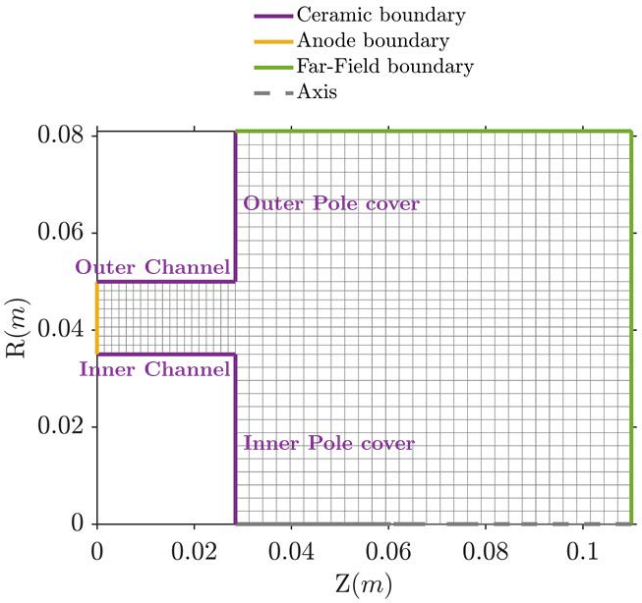

Figure 6.15: Structured PIC mesh used in MFAM refinement sensitivity analysis

It is worth noting that the PIC mesh is kept the same for the comparison carried out in this section, with the intention of focusing solely on the variability that may arise due to the MFAM. Some unavoidable differences will appear, however, due to interpolation from the PIC mesh to the different MFAMs. For completion, the instantaneous PIC maps used are also presented in the PIC mesh, specifically, in terms of plasma density and ion currents:

[6]Since the PPU is set to Constant Voltage mode, this means that said element is also the plasma potential refence.

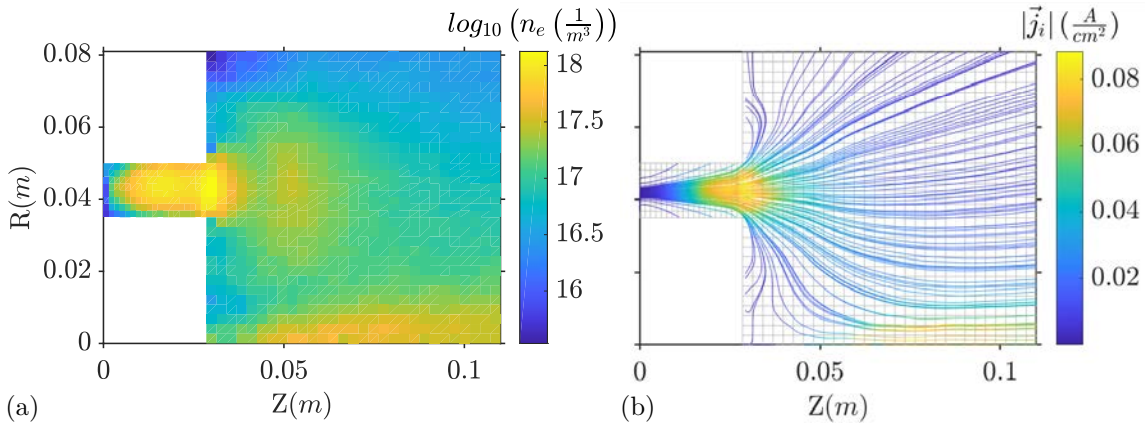

Figure 6.16: (a) Plasma density and (b) total ion current density at the PIC mesh for MFAM refinement sensitivity analysis

The rationale for not employing the PIC solution from HallMa, as in the previous sections, was that mesh refinement proved difficult due to the very coarse mesh in which the magnetic field data was provided. As mentioned in the closing comments of Section 3.4, this induces inaccuracy in magnetic coordinate determination, which then leads to unavoidable errors in GR. For this reason we have employed newly generated and readily trialed MFAMs; in particular, the meshes obtained using the Inverse-rate-of-change meshing strategy and compared in Section 3.4 (Fig. 3.8(a) and Fig. 3.12).

In this case, we have not used a particular convergence criteria based on the exiting residual; instead, we have used a fixed time-step, $dt = 10^{-12}s$, and number of iterations, $N_{it} = 2 \cdot 10^6$, for all of the simulations. The chosen time-step is within the stability and convergence limits, based on the results obtained. The number of iterations is chosen so that the output state has been allowed to converge comfortably. The energy balances and residuals for each simulation are shown in Fig. 6.17. The exit iteration energy balances are compiled in Table 6.9 for clarity.

Refinement lev.	$\mathbf{P_{adv}}\vert_{\mathbf{FF}}$	$\mathbf{P_{bound}}$	$\mathbf{P_{exp\top}}$	$\mathbf{P_{exp\parallel}}$	$\mathbf{P_{heat}}$	$\mathbf{P_{inel}}$	**Err**	$\mathbf{P_{cath}}$
*level*1	−28.2	−233.2	−131.7	63.3	394.5	−65.1	−0.4	31.1
*level*2	−21.8	−223.4	−114.6	17.5	415.3	−73.5	−0.5	27.4
*level*3	−34.6	−184.8	−117.2	26.6	380.6	−70.3	0.3	26.5

Table 6.9: Partial contributions to electron energy balance for various levels of Inverse-rate-of-change MFAM refinement; all values provided in W

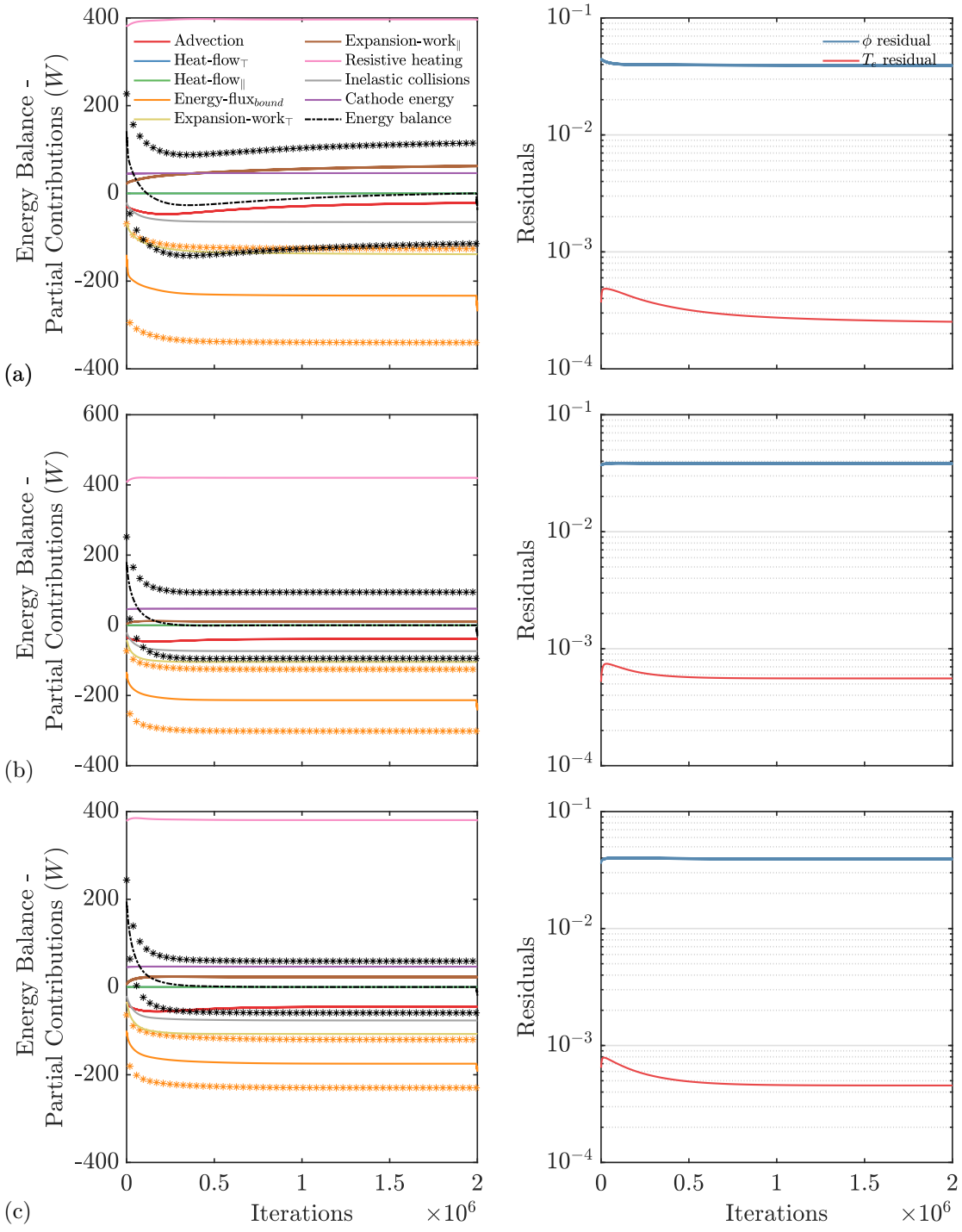

Figure 6.17: Energy Balance and T_e and ϕ residuals for various levels of Inverse-rate-of-change MFAM refinement (a) $level1 \sim 360 elements$, (b) $level2 \sim 1400 elements$, (c) $level3 \sim 5600 elements$. For the wall energy deposition and the total energy balance, both the moving average and the upper and lower limits of the oscillating values are provided; the limits are shown using starred dots

As a first comment, it is notable that, from the perspective of residuals, the results are more similar to the ones shown for the Explicit Euler discretization (Section 6.2) than for the Semi-implicit results in the remainder of the chapter. Although less "noisy" than in the explicit case, the residuals plateau to a given value, instead of dropping to arbitrarily lower values as the simulation progresses. The origin of this behavior is shown in the energy balances and is related to largely oscillating values of the contribution due to energy deposition at the wall, which in turn affects the total energy balance (a moving average, as well as the upper and lower limits of these oscillating values are presented in Fig. 6.17).

This oscillating behavior ultimately appears because of the anode boundary condition: the linearized sheath model in Eq. (4.86) is limited by a null sheath potential drop at the anode; particularly, the sheath drop *guess* value, $\Delta\phi^*_{sh}$, is limited to 0. This limitation exists in the model because the $\Delta\phi^*_{sh} = 0$ condition implies that the anode is accepting the largest electron current that it can, since a sheath reversal condition, given by $\Delta\phi_{sh}|_A = \phi_{AB} - \phi_{AW} < 0$, cannot increase the electron flux to the wall. The anode sheath reversal, which has been studied in prior works by Ahedo[279, 280], can appear in the Iterative Matching algorithm, even considering the $\Delta\phi^*_{sh} = 0$ limit, since the resulting potential in the anode boundary (obtained from solving for the generalized Ohm's law) can be lower than the anode wall potential. Indeed, we have observed in simulations that, under certain conditions (typically when the axial electron current is low, which occurs for null anomalous collisionality, or when the plasma density in the NAR is small) the anode BC can become unstable or present continuous sheath reversal during a number of simulation steps.

The unstable anode is partly due to the fact that the derivative term in Eq. (4.86) becomes very large near a null sheath potential drop, since the current in the anode presents an asymptote-like behavior as $\Delta\phi_{sh}|_A$ becomes smaller. This breaks the stability of the Newton-Raphson approach, although over-relaxation of the method could potentially solve this issue. The sheath reversal mode is not expected for typical operation regimes in HETs but can occur for certain simulation parameters; in this case, the unstable mode may be triggered by the null anomalous transport. Further insight into results for no anomalous collision frequency is presented in Chapter 7.

A consequence of anode sheath reversal is that the energy lost to the sheath boundary must be smaller than that lost to the wall. Eq (5.29) provides the expression for the energy deposition at the sheath boundary and it is trivial to see that, when sheath reversal does occur, $h_e|_Q < h_e|_W$.

The average anode face sheath behavior for the simulation, corresponding to the *level*3 MFAM, is shown in Fig. 6.18, which provides the rationale for the oscillatory nature of the wall energy deposition in Fig. 6.17 and also for the high plasma potential residual. Nevertheless, the electron temperature residual plateaus at relatively small values (less than 0.1% in the trialed MFAMs), and, thus, we consider that the simulations can present a valid "converged" state. Said state can be characterized through the 2D maps for electron temperature and plasma potential, shown in Fig. 6.20 for each of the MFAMs, and the 1D profiles, shown in Fig. 6.19.

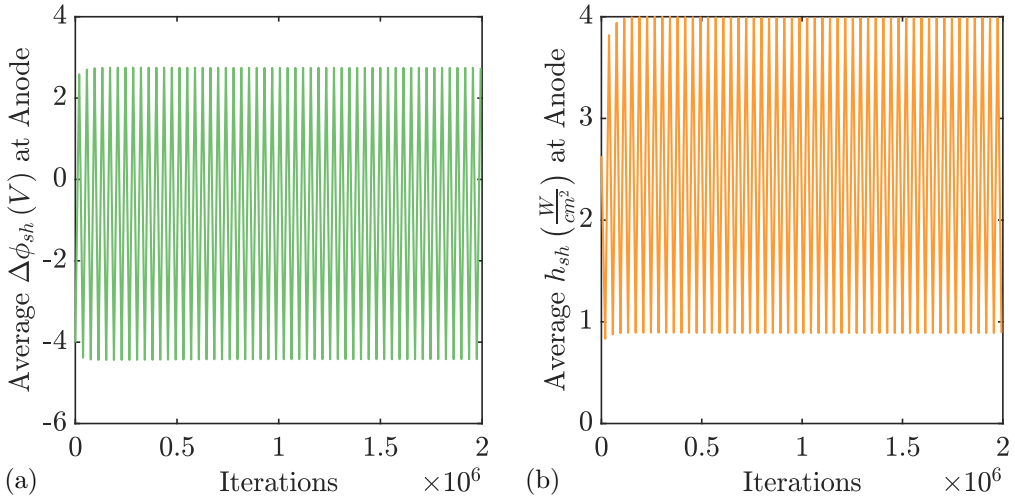

Figure 6.18: Average anode face response in terms of $\Delta\phi_{sh}$ and electron energy deposition for the *level*3 mesh refinement level ($\sim$ 5600 elem.) of the Inverse-rate-of-change MFAM

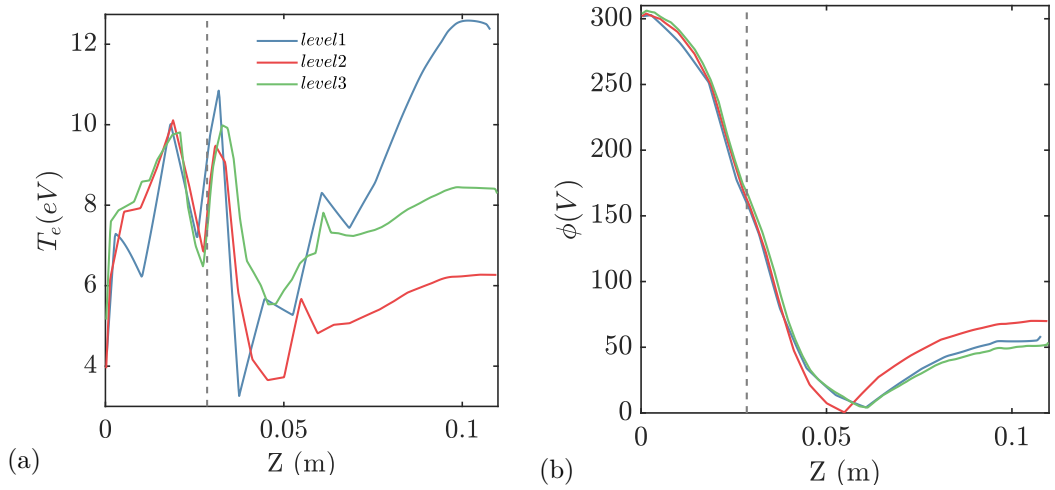

Figure 6.19: 1D profiles of (a) T_e and (b) ϕ for various levels of Inverse-rate-of-change MFAM refinement; (- - -) marks the channel exit

The converged results provide insight into the importance of mesh refinement in the simulation and the quality of the mesh within the context of a representative problem. It is clear that the solution for the plasma potential is almost identical for all three MFAMs, save for slight variation in the potential reference position (which also represents the sole volumetric cathode element in these simulation), and is due to the fact that it was imposed by choosing the closest mesh element to a given spatial position. The *level*2 mesh plasma potential does differ significantly from the other solutions downstream from the potential reference point, which can be related to the very different temperature distributions.

Indeed, while the electron temperature maps follow similar trends for all solutions in the

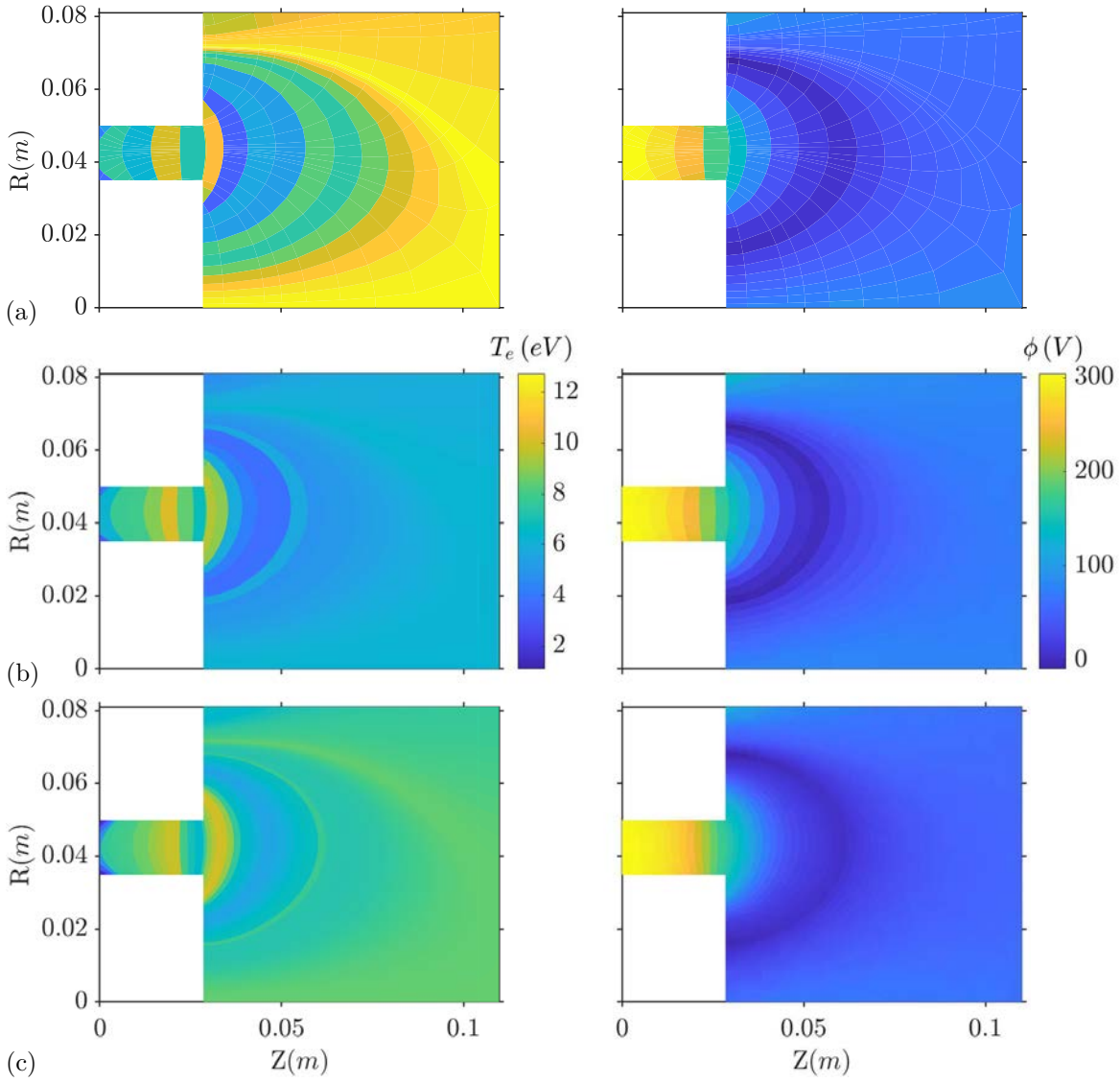

Figure 6.20: T_e (left) and ϕ (right) 2D maps for various levels of Inverse-rate-of-change MFAM refinement (a) $level1 \sim 360 elements$, (b) $level2 \sim 1400 elements$, (c) $level3 \sim 5600 elements$

channel region (with, perhaps, the exception of the NAR), the maps vary significantly once past the channel exit and more so past the neutralization region; in particular, the cathode position and the near-axis region seem to have a large influence in these. The former is apparent from the slight variation in the cathode element position between the *level*2 MFAM and the other two meshes; the latter is apparent in the 2D maps, for the magnetic field lines that graze the domain axis.

When comparing the meshes, shown in Figs. 3.12 and Figs. 3.8(a), it is clear that the axis domain region is characterized by the lowest quality mesh elements, and that it is also an "active" region from the perspective of the plasma, presenting a relatively large plasma and ion current

densities (Fig. 6.16). The low quality of the mesh will impact the GR performed there. In principle, this can affect both the values of electron currents as well as the gas expansion work terms in Eq. (4.72). Changes in electron currents can have a dramatic effect on the resistive heating term, although the near-axis region is expected to have currents with low modules, since it is a low β_e region and the axis forces currents to be mainly in the parallel direction, preventing a strong azimuthal drift (which is the main contributor to the electron current module, and thus to the resistive heating term) from developing. The currents for the *level*2 mesh are shown in Fig. 6.21.

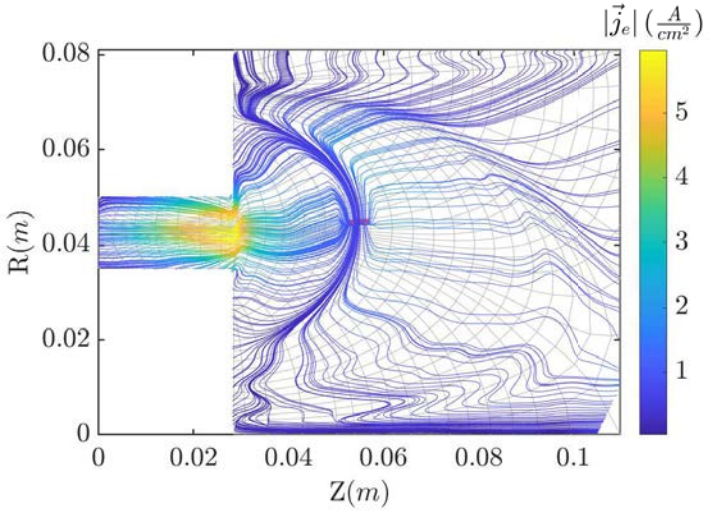

Figure 6.21: Electron current streamlines for the *level*2 refinement Inverse-rate-of-change MFAM ($\sim$ 1400 elem.); the volumetric cathode element (also potential reference element) is marked in red

Considering the previous rationale, the impact of resistive heating in the domain axis region is limited. The variation in the resistive heating term, shown in Table 6.9 for the three simulations can only be related then to the regions where this term is important: in the channel and channel exit areas and in the region immediately downstream from the neutralization area.

On the other hand, Table 6.9 shows off a large change in the gas expansion terms, which is in line with a varying quality of GR. These terms will play the central role in the shifting electron temperature maps downstream from the neutralization region.

In addition to varying quality of GR, a major caveat was found related to the mesh interpolation procedure carried out by the MESH_INTERP script as a result of using meshes with different refinements. As mentioned in Section 3.5, mesh interpolation is based on the Delaunay triangulation and WLSQR methods: both approaches are point-to-point interpolation, which in principle should be valid whenever intensive quantities, such as temperature, electric potential or density are interpolated, as is done in HYPHEN. Since both the Delaunay and WLSQR methods are based on distance, the error committed here will be small for meshes with similar element sizes; however, it may lead to an aliasing error for interpolation of any quantity in regions with disparate mesh element sizes: e.g., a large MFAM element will only "see" the density of the nearest PIC mesh cell, however small that cell may be, and therefore the interpolation would be less

representative of the information encoded in the PIC mesh. This error was not spotted in the trials referred to in Section 3.5 because the functions used there are continuous. In the case of the PIC segment, on the other hand, the variables to be interpolated contain numerical noise (specially since they are instantaneous variables), which will be amplified by this issue.

The error due to interpolation on meshes with disparate sizes is difficult to quantify since it depends both on the meshes and quantities being interpolated; however, it is clear that it may affect the solution for the electron temperature and cannot be discarded as one of the main causes for its variability. The MESH_INTERP script could be easily updated so that interpolation takes into account whether multiple cells of the PIC overlap with a MFAM element's volume of influence (or vice-versa). This would suppose a certain "smoothing" of the interpolated fields of one solution to the other, but would conserve more of the information stored in the meshes. This update is reserved for future work.

Lastly, regarding the boundary energy deposition (whose values are given in Table 6.9), Figs. 6.20 and 6.19 show that the NAR in the simulations presents substantial differences, in terms of electron temperature. This is deemed to be a fully mesh-dependent effect: as mesh refinement increases, smaller elements appear closer to the anode and since, even in this region, the magnetic confinement hinders heat-flux across magnetic field lines, the energy deposition to the anode boundary has a larger effect in these smaller elements. Ultimately, this reduces the temperature in the elements facing the anode, as well as the energy deposited there. Figure 6.22 clearly shows a decreasing anode temperature with mesh refinement. Note that the values for energy flux in the dielectric material boundaries appear to be comparable, while the ones for the anode boundary are not[7].

To summarize, the solution dependency on mesh refinement has been explored in this section. It was found that results, particularly those for electron temperature, can be largely affected, even within a single electron time-step, by mesh refinement, due to GR effects, volumetric cathode position, element size near the boundaries and mesh interpolation (notably for those plasma quantities which are extensive). It is unclear whether this would have a large effect over the overall thruster operation, since temperatures are comparable inside the channel region, which is where most of the ionization occurs, and the plasma potential solutions are nearly identical. It is recommended that simulations are carried out taking into account potential variability in the solution due to mesh refinement. Some of the future work mentioned throughout this thesis and in Chapter 8 is also oriented towards reducing mesh-dependency effects.

[7]Keep in mind that the values shown in Fig. 6.22 are at the boundary, i.e., at the sheath edge, for each of the different material wall sections, they do not represent the values of those quantities at the walls themselves.

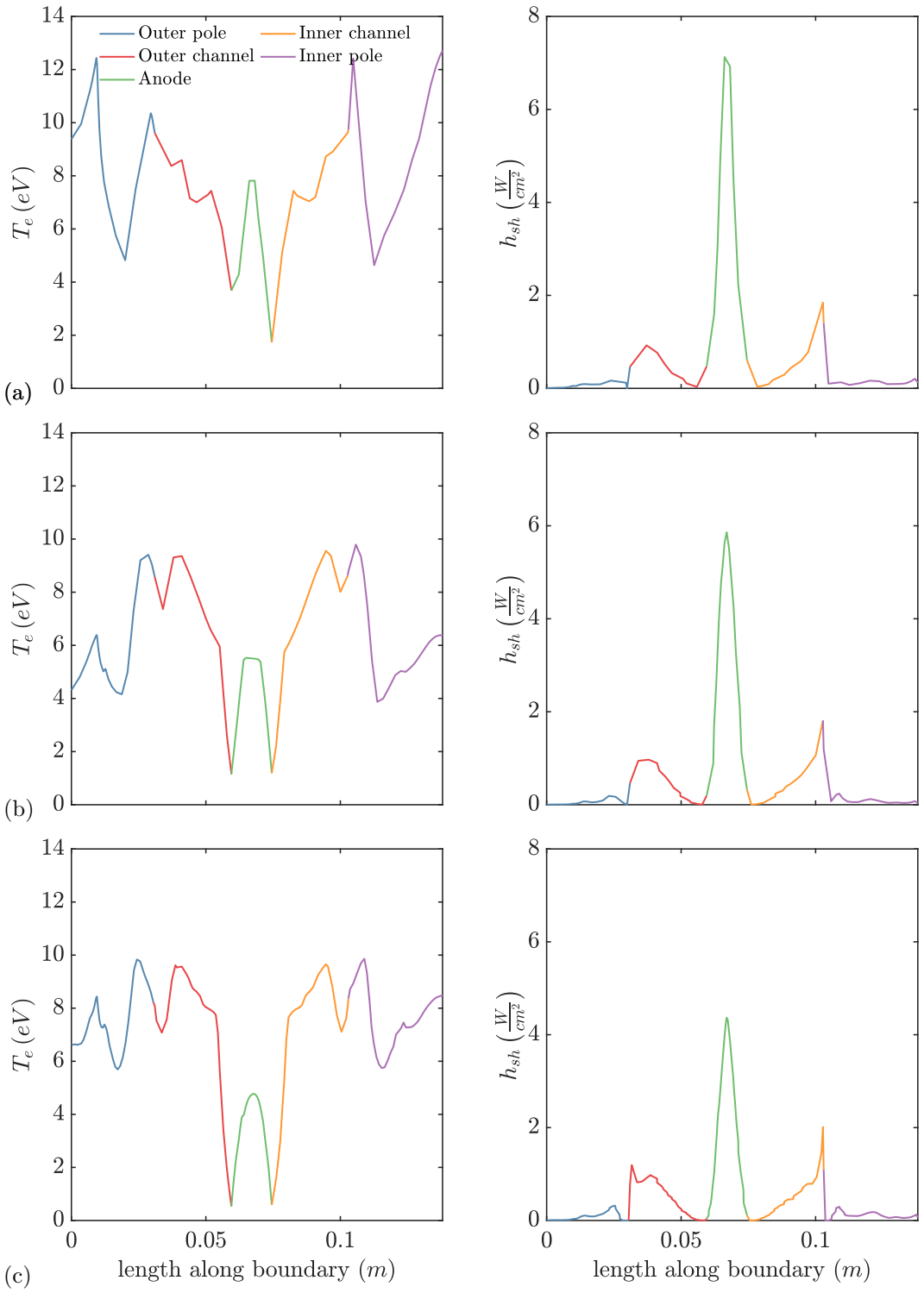

Figure 6.22: T_e and electron energy-flux along material wall boundary sections: Outer pole cover, Outer channel, Anode, Inner channel and Inner pole cover, for various levels of Inverse-rate-of-change MFAM refinement (a) $level1 \sim 360 elements$, (b) $level2 \sim 1400 elements$, (c) $level3 \sim 5600 elements$

CHAPTER
SEVEN

HYPHEN results

This chapter describes the results obtained from the integrated HYPHEN code, allowing for the PIC heavy species to respond in simulation time to the results produced by the NOMADS segment and vice-versa. The results are mainly explored from the perspective of the electron fluid, but global results are also provided. The results produced by HYPHEN for this chapter would have been impossible to obtain without the contribution of the PIC module, which, as mentioned in Chapter 2, was fully developed and implemented by Domínguez-Vázquez[162], with whom we share authorship.

A thruster with a magnetic and geometric configuration mimicking the SPT-100 HET has been simulated, carrying out a parametric investigation focused mainly on the effects of the anomalous collisional frequency factor, α_{ano}, on the global response of the thruster. Other parameters explored include the thermalization fraction, σ_{th}, for the sheath model of the dielectric walls and the model used for elastic momentum transfer electron-neutral collisions.

An in-depth discussion is carried out for a case with no anomalous transport and a case where the anomalous collision frequency factor has been fine tuned to obtain results that are in line with experimental results of the SPT-100, both from the perspective of global performance figures and also plasma quantities throughout the length of the simulation domain; the former presented less variability to the anomalous frequency factor than the latter. The case with no anomalous transport presents a non-physical solution which will be addressed. For the remaining cases, a broader comparison section has been included, which includes various power balances: the electron energy balance, a global energy balance for the thruster and an electric energy balance; the expressions for the latter two are derived here.

In addition, the results for an SPT-100 thruster configuration that includes a trim magnet to generate a magnetic singular point in the NAR have also been included. The purpose of these results is to demonstrate that HYPHEN is able to tackle such "exotic" magnetic topologies.

7.1 Foreword to HYPHEN results

7.1.1 SPT-100 design and performances

The SPT-100 is, perhaps, one of the most widely studied HETs in the literature, which is unsurprising considering its historical relevance. The thruster's magnetic circuit and geometric characteristics are not typically disclosed in the literature, potentially due to contractual obligations. However, some publications as well as previous studies in the EP^2 group have reported

some representative quantities: the inner and outer channel radii, r_i and r_o, the length of the channel, l_c and the maximum field intensity in the TCL were, respectively, $35mm$, $50mm$, $25mm$ and $0.023 - 0.025T$ in the design simulated by Escobar[212]. Kim[281] reported only values of r_i and r_o of $28mm$ and $50mm$, correspondingly; Nackles[282] reported radii values and also the channel length: $r_i = 25mm$, $r_o = 50mm$ and $l_c = 21mm$.

The work carried out by De-Saveedra[179] considered the available information towards producing various designs for an SPT-100 type thruster magnetic circuit, modeled in FEMM[178] through the FEMM_MASK tool developed for the `SET` unit of HYPHEN. The designs considered an additional limitation that had not been addressed in previous works regarding the manufacturability of the magnetic circuit. FEMM allows for un-checked or "virtual" values of coil wire currents that may not be compatible with wire *ampacity*, i.e., the maximum electric current intensity to be carried with no immediate or progressive degradation to the wire. FEMM does consider, however, the packing factor of wires being wrapped in the magnetic circuit coils. This leads to an iterative approach toward the design of a magnetic circuit, capable of delivering a certain field intensity, which takes into account the physical space occupied by the coils and the electrical current through the wires.

The final magnetic circuit design for the "base" SPT-100 and the magnetic field intensity may be seen in Fig. 7.1; the ferromagnetic poles are made of pure iron, while the coils are made of copper wiring with a certain packaging factor.

Table 7.1 gathers the chosen geometric characteristics of the design, as well as some quantities related to the magnetic circuit. The channel length was chosen in order to limit the influence of the front poles over the numerical calculation of the magnetic coordinates.

$r_i\,(mm)$	$r_o\,(mm)$	$r_{thr}\,(mm)$	$l_c\,(mm)$	$l_{thr}\,(mm)$	$B_{max}@TCL\,(T)$
35	50	85	28	52	~ 0.025

Table 7.1: Geometric and magnetic circuit parameters for base SPT-100

where r_{thr} and l_{thr} represent the outer radius of the complete thruster and its length along z, i.e., the thruster width.

The magnetic field shown in Fig. 7.1 and the geometric characteristics of the thruster channel are used in the following simulations, as well as for the results of Section 6.8.

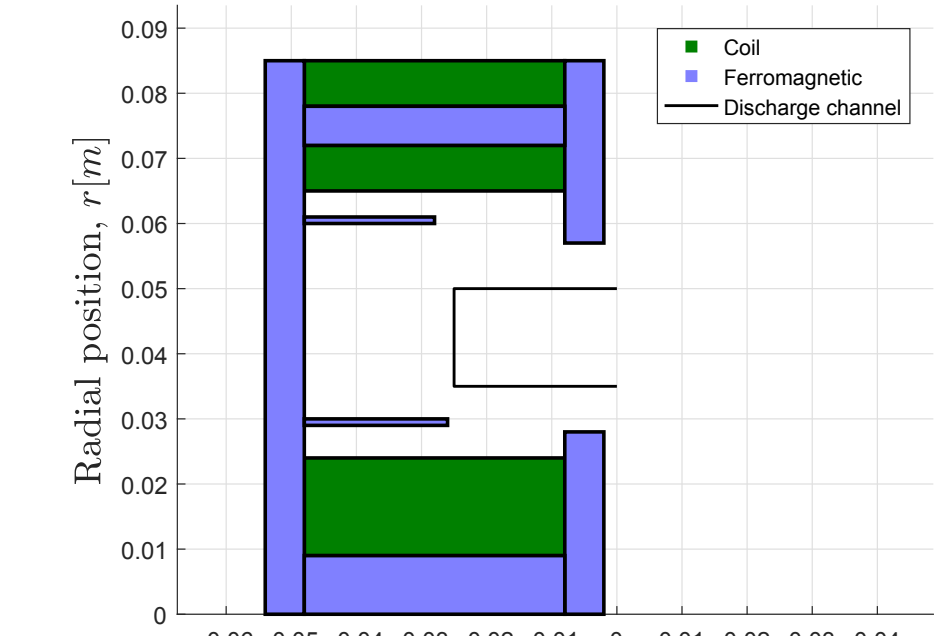

(a)

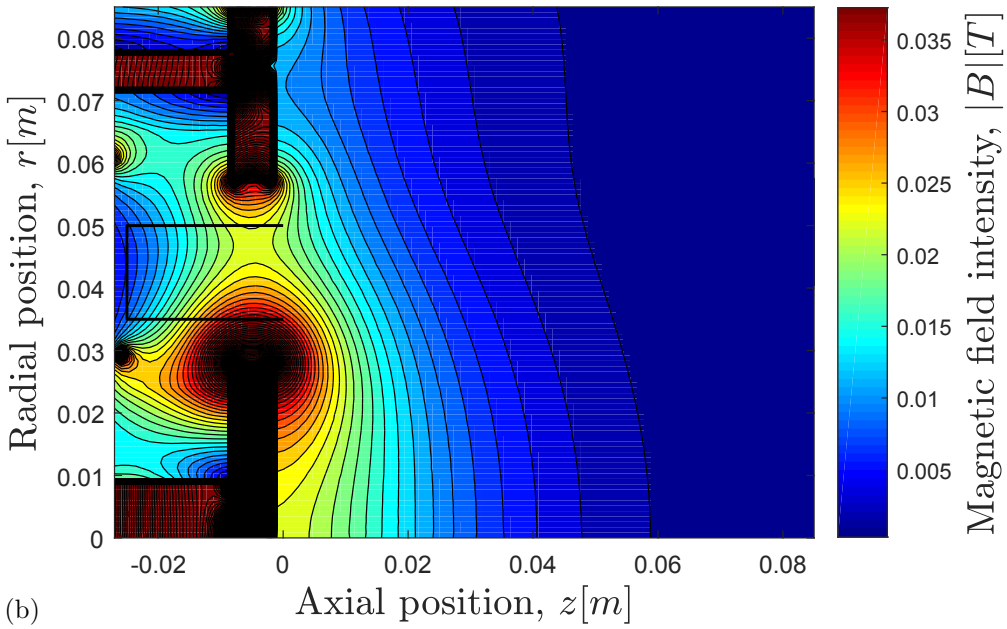

(b)

Figure 7.1: Base SPT-100: (a) magnetic circuit design and geometry and (b) magnetic field intensity from Ref. [179]

Contrary to the actual *design* of the SPT-100, the nominal operating point and overall performances are well known and, generally public, further cementing the SPT-100 as a valid target for study of simulated thruster performances and plasma quantities. A short literature review of the various performance values of the SPT-100 is given in Table 7.2:

Reference	$\dot{m}_{anode}\,(mg/s)$	$I_d\,(A)$	$P_d\,(W)$	$T\,(mN)$	$I_{sp}\,(s)$	η_T
Brophy[38]	5.0	4.5	1350	80	1600	0.5
Absalamov[283]	5.21	4.5	1350	85	1630	0.5
Sankovik[284]	5.12	4.5	1350	85.7	1550	0.484
Garner[285, 286, 287]	5.5	4.5	$1330 - 1350$	$80 - 86$	$1450 - 1560$	~ 0.48
Kim[288]	4.27	4.28	1495	84	2006	0.55

Table 7.2: Published performance values for the SPT-100

The performance values are commented further in Section 7.1.2. The reviewed publications show a certain level of variability around the nominal operating points of the thruster and the performances that may be derived from them. We have chosen to compare the results obtained in this chapter against the ones published by Brophy[38], which historically, represent the "nominal" operating point of the thruster.

Regarding the plasma quantities that may be obtained from experimental results on the thruster, on its various configurations, or on thrusters similar to the SPT-100, a wide breath of publications and dissertations exist, based on a number of experimental techniques. The results shown in this chapter are in good agreement, albeit with some short-falls that will be addressed in the following sections, with the ones produced by Raitses[289, 290], Meezan[291], Dorval[292], Kim[288, 293], Kim[294, 281] or King[295, 296, 297].

Additionally, plasma discharge simulations of the SPT-100 have been performed by many authors previous to this work; references may be found in the works by Hofer[298], Ahedo et al.[173, 80], Garrigues[230, 202], Hagelaar[273] and in the original work on hybrid codes by Fife[130].

In addition to the base SPT-100 we have also simulated an alternate configuration that adds a singular point in the magnetic topography of the NAR, in order to test the capabilities of HYPHEN for such configurations. The magnetic circuit configuration, which in this case also includes a NdFeB 32 MGOe permanent trim magnet behind the anode wall, as well as the resulting magnetic field in the simulation may be seen in Fig. 7.2. Note that, while the thruster magnetic circuit geometry remains unaltered, a larger coil power would have to be dedicated in order to maintain the chosen maximum value of magnetic field intensity in the TCL.

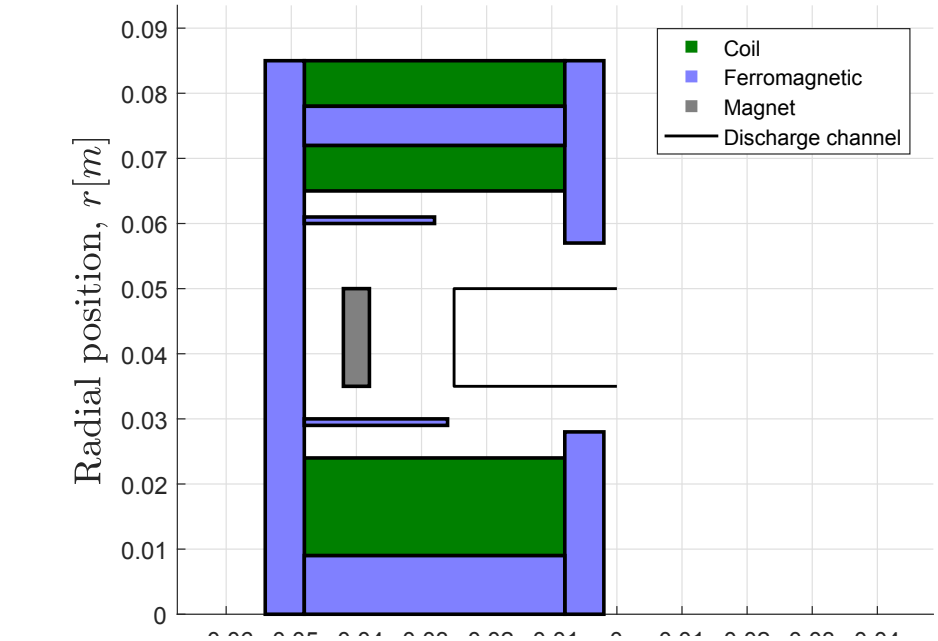

(a)

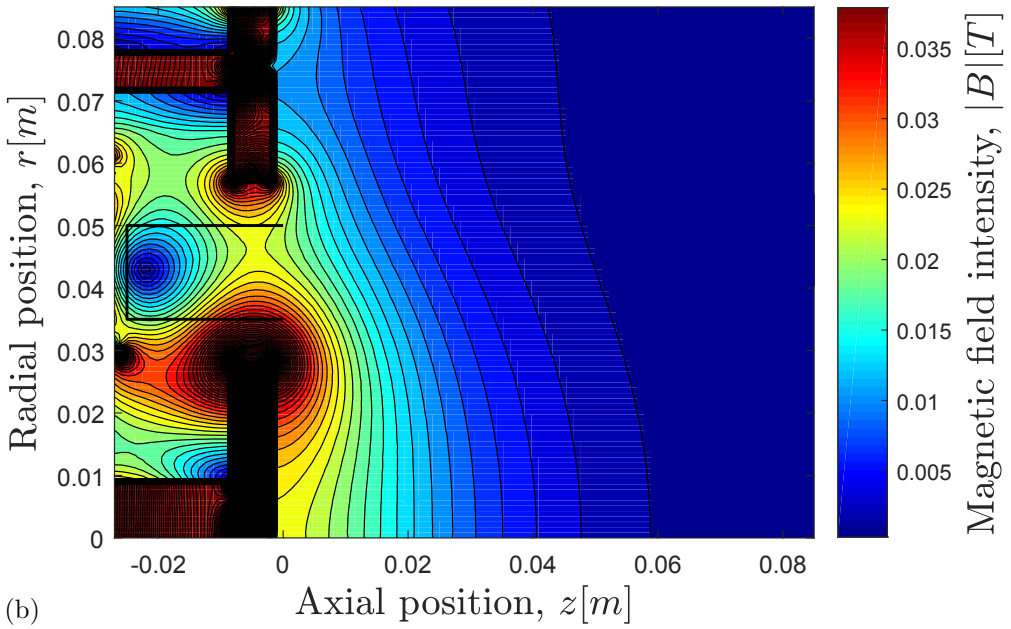

(b)

Figure 7.2: SPT-100 with singular point: (a) magnetic circuit design and geometry and (b) magnetic field intensity from Ref. [179]

7.1.2 Performance evaluation

Thrust, T, and specific impulse, I_{sp}, were addressed in Section 1.1 from the perspective of their overall impact in a spacecraft's mission. How thrust may be measured in the simulation environment, and what other performance values may be derived is addressed next.

Mathematically, thrust can be easily divided between the thrust calculated at the escape boundaries versus the thrust calculated due to volumetric forces plus momentum deposition at the thruster walls, as such:

$$\begin{aligned} T_{FF+inj} &= \oint_{FF+inj} \Bigg[m_n n_n \left(\vec{1}_Z \cdot \vec{u}_n\right)\left(\vec{u}_n \cdot \vec{n}_b\right) + \sum_{Z=1}^{2,\ldots} m_{iZ} n_{iZ} \left(\vec{1}_Z \cdot \vec{u}_{iZ}\right)\left(\vec{u}_{iZ} \cdot \vec{n}_b\right) + \\ &+ \left(\vec{1}_Z \cdot \vec{n}_b\right)\left(p_n + \sum_{Z=1}^{2,\ldots} p_{iZ} + p_e\right)\Bigg] dA \\ T_{V+D+AW} &= \vec{1}_Z \cdot \int_V \left(\vec{j}_e + \vec{j}_i\right) \times \vec{B} dV - \oint_{D+AW} \Big[m_n n_n \left(\vec{1}_Z \cdot \vec{u}_n\right)\left(\vec{u}_n \cdot \vec{n}_b\right) + \\ &+ \sum_{Z=1}^{2,\ldots} m_{iZ} n_{iZ} \left(\vec{1}_Z \cdot \vec{u}_{iZ}\right)\left(\vec{u}_{iZ} \cdot \vec{n}_b\right) + \left(\vec{1}_Z \cdot \vec{n}_b\right)\left(p_n + \sum_{Z=1}^{2,\ldots} p_{iZ} + p_e\right)\Big] dA \end{aligned} \tag{7.1}$$

where inj represents the surface integral over the injector. These expressions may be approximated by considering the most relevant terms associated to the ion and neutral populations or to the electron population. Neglecting the surface integral over the injector surfaces, the effect of the ion swirl on the Lorentz force, the momentum transfer in the axial direction deposited by the heavy species over the material walls and the electron pressure over the Far-Field boundaries, we have:

$$\begin{aligned} T_{FF+inj} \approx \mathbf{T_{hs}} &= \oint_{FF+inj} \Bigg[m_n n_n \left(\vec{1}_Z \cdot \vec{u}_n\right)\left(\vec{u}_n \cdot \vec{n}_b\right) + \sum_{Z=1}^{2,\ldots} m_{iZ} n_{iZ} \left(\vec{1}_Z \cdot \vec{u}_{iZ}\right)\left(\vec{u}_{iZ} \cdot \vec{n}_b\right) + \\ &+ \left(\vec{1}_Z \cdot \vec{n}_b\right)\left(p_n + \sum_{Z=1}^{2,\ldots} p_{iZ}\right)\Bigg] dA \\ T_{D+AW} \approx \mathbf{T_e} &= \vec{1}_Z \cdot \left(\int_V \vec{j}_e \times \vec{B} dV - \oint_{D+AW} p_e \vec{n}_b dA\right) \end{aligned} \tag{7.2}$$

These last two expressions recover the argument made in Section 1.1.1 regarding thrust in HETs, which can be accounted for either by considering the *electrostatic* force imparted over the ions plus the momentum of the exiting neutrals, T_{hs} (where hs stands for "heavy species"), or the *electromagnetic* Lorentz force that couples the magnetic circuit and the Hall current in the plasma, T_e, which is mostly due to the *electron* current. It can be demonstrated that both forces are equal[27], thus opening two venues for the calculation of thrust in the simulation.

The heavy species thrust is obtained in the PIC for each iteration simply by doing a summation over the momentum flux of macro-particles that cross each of the Far Field boundary faces, while the hall current thrust is obtained in NOMADS by employing the approximations in Eq. (4.65).

The two definitions for thrust allow us to obtain independent values of the specific impulse using Eq. (1.5), and, also, of the Thrust efficiency, also known "anode efficiency" for HET, defined

as[27]:

$$\eta_a = \frac{T^2}{2\dot{m}_a P_d} \tag{7.3}$$

where the discharge power, P_d, can be evaluated as:

$$P_d = I_d V_d \tag{7.4}$$

This expression is different from the total thruster efficiency in that it doesn't consider the power used in the coils of the magnetic circuit or the fraction of propellant required to feed the cathode, but represents the efficiency of the thruster only in relation to the thrust being generated, through plasma production and subsequent acceleration. The $\dot{m}_a$ term used in Eq. (7.3) refers to the fact that in typical HETs the injector doubles as the thruster anode; this is not necessarily the case in all HET designs.

Certain partial efficiencies also allow us to discern the merits of each of the processes involved separately. In particular, we will be using:

- Propellant utilization efficiency: provides a measure of the fraction of injected propellant that becomes exiting ion mass-flow, $\dot{m}_{iZ}|_{FF}$.

$$\eta_{utiliz} = \frac{\sum_{Z=1}^{2,\ldots} \dot{m}_{iZ}|_{FF}}{\dot{m}_a} \tag{7.5}$$

- Current efficiency: compares the exiting ion beam current, $\sum_{Z=1}^{2,\ldots} I_{iZ}|_{FF}$, to the current required to establish the discharge, I_d.

$$\eta_{curr} = \frac{\sum_{Z=1}^{2,\ldots} I_{iZ}|_{FF}}{I_d} \tag{7.6}$$

- Production efficiency: compares ion current lost to the thruster walls, $\sum_{Z=1}^{2,\ldots} I_{iZ}|_{D+AW}$ to the exiting ion beam current.

$$\eta_{prod} = 1 - \frac{\sum_{Z=1}^{2,\ldots} I_{iZ}|_{D+AW}}{\sum_{Z=1}^{2,\ldots} I_{iZ}|_{FF}} \tag{7.7}$$

- Divergence efficiency: gives a measure of the fraction of exiting heavy species energy that is axial kinetic energy, i.e., contributing to Thrust.

$$\eta_{div} = \frac{\oint_{FF} \left(m_n n_n v_{nz}^2 \vec{v}_n + \sum_{Z=1}^{2,\ldots} m_{iZ} n_{iZ} v_{iZz}^2 \vec{v}_{iZ} \right) \cdot \vec{n}_b dA}{\oint_{FF} \left(m_n n_n v_n^2 \vec{v}_n + \sum_{Z=1}^{2,\ldots} m_{iZ} n_{iZ} v_{iZ}^2 \vec{v}_{iZ} \right) \cdot \vec{n}_b dA} \tag{7.8}$$

where $\vec{n}_b$ is the vector normal to the boundary, pointing outwards from the simulation domain.

Whereas all of the expressions in this section may be evaluated for each time-step in the simulation, the values offered in Sections 7.2 and 7.3 make reference to time-averaged values.

7.1.3 Power balances

Complete simulations allow us to establish certain energy balances that must be met for the individual species as well as for the complete operation of the thruster, linking both the heavy species and the electron population.

The discharge power, P_d, can be evaluated by taking into account the work developed by the electric field established in the plasma over the electron and ion populations, together with the total energy deposited by the ion and electron populations at the plasma sheaths; the expression is thus:

$$P_d = \int_V \left(\vec{j}_e + \vec{j}_i\right) \cdot \vec{E} dV + \oint_{AB} \Delta\phi_{sh}|_{AB} \left(\vec{j}_e + \vec{j}_i\right) \cdot \vec{n}_b dA + \oint_D \Delta\phi_{sh}|_D \left(\vec{j}_e + \vec{j}_i\right) \cdot \vec{n}_b dA \quad (7.9)$$

where the term associated to the dielectric type material walls, D, is, by definition, equal to zero; AB denotes the "anode boundary", as mentioned in Section 4.2.4. The expression in Eq. (7.9) represents the electrical energy balance, which can be compared to Eq. (7.4) to ensure that energy in the simulation is conserved. Equation (7.9) can be averaged in time in order to obtain a representative balance for the thruster operation, which, as will be seen in the following sections, develops in a stable, but not stationary, way[1].

We label the time-averaged contributions in Eq. (7.9) as:

$$\begin{aligned} P_{elec_e} &= \left\langle \int_V \vec{j}_e \cdot \vec{E} dV \right\rangle_t \\ P_{elec_i} &= \left\langle \int_V \vec{j}_i \cdot \vec{E} dV \right\rangle_t \\ P_{elec_a} &= \left\langle \oint_{AB} \Delta\phi_{sh}|_{AB} \left(\vec{j}_e + \vec{j}_i\right) \cdot \vec{n}_b dA \right\rangle_t \end{aligned} \quad (7.10)$$

Separately, we can establish energy balances for each of the independent heavy species populations; for this task we employ the total energy equation instead of the thermal energy density equation used for the electron population, since it is easier to evaluate from the perspective of the PIC segment:

$$\frac{\partial}{\partial t}\left(\frac{3}{2}p_\alpha + \frac{1}{2}m_\alpha n_\alpha u_\alpha^2\right) + \nabla\cdot\left(\frac{3}{2}p_\alpha \vec{u}_\alpha + \frac{1}{2}m_\alpha n_\alpha u_\alpha^2 \vec{u}_\alpha + \vec{q}_\alpha\right) + \nabla\cdot\left(\bar{\bar{P}}_\alpha \cdot \vec{u}_\alpha\right) = \vec{j}_\alpha \cdot \vec{E} + \frac{1}{2}u_\alpha^2 m_\alpha S_\alpha \quad (7.11)$$

[1] HETs present periodic oscillations of global plasma parameters and performances; thus, "correct" time averaging refers to ensuring that an even number of periods are taken when averaging or, alternatively, averaging over large simulation times also helps in reducing the influence of each individual period.

where α represents any of the heavy species in the simulation. The $\frac{1}{2}u_\alpha^2 m_\alpha S_\alpha$ term is a *source* or *sink* term that represents the energy lost to species transitioning from one state to another: for example, in the case of a single ion being ionized into a double ion, the energy of the first particle is lost into the second population, since said particle is no longer considered part of the single ion population. While we do not consider recombination reactions in the simulation (as was argued in Section 5.2), the aforementioned term does include the energy lost due to wall recombination.

Time-averaging of Eq. (7.10) allows us to neglect the non-stationary term in the equation: integrating over the volume and adding the equation for each of the heavy-species populations in the simulation provides us with a general energy balance for the PIC segment. However, since we are interested in the interaction between both the PIC and NOMADS segments, we can also add the thermal energy density equation for the electron population, Eq. (4.44), in terms of the electron drift velocity (instead of current density) and integrated over the volume:

$$\begin{aligned}
\sum_{Z=1}^{2,\dots} \Bigg\langle \oint_b \left(\frac{3}{2} p_{iZ} \vec{u}_{iZ} + \frac{1}{2} m_{iZ} n_{iZ} u_{iZ}^2 \vec{u}_{iZ} + \vec{q}_{iZ} + \bar{\bar{P}}_{iZ} \cdot \vec{u}_{iZ} \right) \cdot \vec{n}_b dA = \\
= \int_V \vec{j}_{iZ} \cdot \vec{E} dV + \int_V \frac{1}{2} u_{iZ}^2 m_{iZ} S_{iZ} dV \Bigg\rangle_t \\
\left\langle \oint_b \left(\frac{3}{2} p_n \vec{u}_n + \frac{1}{2} m_n n_n u_n^2 \vec{u}_n + \vec{q}_n + \bar{\bar{P}}_n \cdot \vec{u}_n \right) \cdot \vec{n}_b dA = \int_V \frac{1}{2} u_n^2 m_n S_n dV \right\rangle_t \\
\left\langle \oint_b \left(\frac{3}{2} p_e \vec{u}_e + \vec{q}_e \right) \cdot \vec{n}_b dA + \int_V \bar{\bar{P}}_e \cdot \nabla \cdot \vec{u}_e dV = \int_V \{CS\}_e \, dV \right\rangle_t + \\
\hline
P_{elec_i} + P_{inj_n} + P_{heat_e} + P_{inel_e} + \\
= P_{jet_i} + P_{sh_i} + P_{jet_n} + P_{sh_n} + P_{adv_e}|_{FF} + P_{sh_e} + P_{exp_e}
\end{aligned} \tag{7.12}$$

where the subscript *sh* refers to the sheath edge and we have used Eq. (4.65) to obtain the surface integrals. The time-derivative term in Eq. (4.44) has also been neglected in the time-averaged equation and, for the sake of brevity, we have used the notation from Eq. (4.75) for the resistive heating terms and the energy sinks and sources due to electron collisions, $\{CS\}_e$. Note that all of the heavy-species "state transition" source or sink terms cancel out when adding over all of the populations.

The partial contributions to this *global* power balance are defined as:

$$
\begin{aligned}
P_{jet_i} &= \sum_{Z=1}^{2,\dots} \left\langle \oint_{FF} \left(\frac{3}{2} p_{iZ} \vec{u}_{iZ} + \frac{1}{2} m_{iZ} n_{iZ} u_{iZ}^2 \vec{u}_{iZ} + \vec{q}_{iZ} + \bar{\bar{P}}_{iZ} \cdot \vec{u}_{iZ} \right) \cdot \vec{n}_b dA \right\rangle_t \\
P_{sh_i} &= \sum_{Z=1}^{2,\dots} \left\langle \oint_{AB+D} \left(\frac{3}{2} p_{iZ} \vec{u}_{iZ} + \frac{1}{2} m_{iZ} n_{iZ} u_{iZ}^2 \vec{u}_{iZ} + \vec{q}_{iZ} + \bar{\bar{P}}_{iZ} \cdot \vec{u}_{iZ} \right) \cdot \vec{n}_b dA \right\rangle_t \\
P_{jet_n} &= \left\langle \oint_{FF} \left(\frac{3}{2} p_n \vec{u}_n + \frac{1}{2} m_n n_n u_n^2 \vec{u}_n + \vec{q}_n + \bar{\bar{P}}_n \cdot \vec{u}_n \right) \cdot \vec{n}_b dA \right\rangle_t \\
P_{sh_n} &= \left\langle \oint_{AB+D} \left(\frac{3}{2} p_n \vec{u}_n + \frac{1}{2} m_n n_n u_n^2 \vec{u}_n + \vec{q}_n + \bar{\bar{P}}_n \cdot \vec{u}_n \right) \cdot \vec{n}_b dA \right\rangle_t \\
P_{adv_e}|_{FF} &= \left\langle \oint_b \left(\frac{3}{2} p_e \vec{u}_e + \vec{q}_e \right) \cdot \vec{n}_b dA \right\rangle_t \\
P_{sh_e} &= \left\langle \oint_b \left(\frac{3}{2} p_e \vec{u}_e \cdot \vec{n}_b + h_{sh} \right) dA \right\rangle_t \\
P_{exp_e} &= \left\langle \int_V \bar{\bar{P}}_e \cdot \nabla \cdot \vec{u}_e dV \right\rangle_t \\
P_{elec_i} &= \sum_{Z=1}^{2,\dots} \left\langle \int_V \vec{j}_{iZ} \cdot \vec{E} dV \right\rangle_t \\
P_{inj_n} &= \left\langle \oint_{inj} \left(\frac{3}{2} p_n \vec{u}_n + \frac{1}{2} m_n n_n u_n^2 \vec{u}_n + \vec{q}_n + \bar{\bar{P}}_n \cdot \vec{u}_n \right) \cdot \vec{n}_b dA \right\rangle_t \\
P_{heat_e} &= \left\langle \int_V \left(\sum_{Z=1}^{2,3,\dots} \eta_{eiZ} \frac{Z n_{iZ}}{n_e} \left| \left(\vec{j}_e + \frac{n_e}{Z n_{iZ}} \vec{j}_{iZ} \right) \right|^2 + \eta_{en} \left| \left(\vec{j}_e \right) \right|^2 + \frac{m_e}{2e^2} \frac{S_e \left| \left(\vec{j}_e \right) \right|^2}{n_e^2} \right) dV \right\rangle_t \\
P_{inel_e} &= \left\langle \int_V \left. \frac{\partial E_e}{\partial t} \right|_{ioniz+excit} dV \right\rangle_t
\end{aligned}
\tag{7.13}
$$

Note that all of the surface and volume integrals may be approximated using the expressions in Eq. (4.65).

For the heavy-species terms we note that heat-flow may be neglected since we have considered that ions (and neutrals) are cold and lowly collisional; the remaining terms, related to pressure and drift kinetic energy, can be evaluated by simply adding the kinetic energy flow for each of the macro-particles, M_α, traversing a particular boundary:

$$
\frac{3}{2} p_\alpha \vec{u}_\alpha + \frac{1}{2} m_\alpha n_\alpha u_\alpha^2 \vec{u}_\alpha + \bar{\bar{P}}_\alpha \cdot \vec{u}_\alpha \approx \sum_{M_\alpha} \frac{1}{2} m_{M_\alpha} n_{M_\alpha} v_{M_\alpha}^2 \vec{v}_{M_\alpha} \tag{7.14}
$$

For the power lost to the sheath edge by the electron population in Eq. (7.13), we have used the notation for the sheath energy deposition obtained in Section 5.1.3.

For simplicity, we may combine the power due to neutrals reaching the boundaries into a single

term:

$$P_{b_n} = P_{jet_n} + P_{sh_n} \tag{7.15}$$

The resulting expression in Eq. (7.12) may be put in terms of the energy reaching the walls, instead of the sheath edges, which is a more natural balance if one considers the output variables from HYPHEN. Going from one expression to the other is trivial, since the energy lost to the sheath by electrons is always gained by the ions, and neutrals are not affected by the sheath:

$$P_{elec_i} + P_{inj_n} + P_{heat_e} + P_{inel_e} = P_{jet_i} + P_{w_i} + P_{b_n} + P_{adv_e}|_{FF} + P_{w_e} + P_{exp_e} \tag{7.16}$$

This last expression provides a useful view of the energy flows in the plasma discharge: the work of the electric field over the ion populations, together with the resistive heating power in the electrons (which is mostly due to the Hall current and appears due to the effect of both the electric and magnetic fields), and the power contained in the injected neutral population, is "spent" either as power deposited to the walls, power of the plasma beam exhausted by the thruster or power lost in the "fluid" expansion of the electron population.

7.1.4 Simulation conditions and Parametric investigation

HYPHEN presents a wide range of parameters, both numerical and physical, as well as various models that may be "tweaked" or turned on or off in each simulation. In the PIC segment, different populations may be selected for tracking (single and double ions, CEX, etc.), with their respective collisional processes, as well as minimum, maximum, and target statistics for the macro-particles associated to each population. Other options include forcing the Bohm criterion for the pre-sheath, the type of weighting associated to particles traversing boundaries, etc. On the NOMADS segment, the various options include the type of PPU control simulated, tolerances for the solver and iterative matching algorithms, the cathode type and the specific volumetric cathode elements, the way the anomalous collisional frequency factor, α_{ano}, is implemented, certain parameters related to the sheath models, etc.

The number of variables in the simulation amount to a large dimensional space that cannot be realistically explored in a full parametric sweep; the results in this section aim to provide a limited, though comprehensive, parametric investigation that provides insight into the various physical mechanisms at play in the plasma discharge of a HET; in particular, from the perspective of the electron population physics.

Some general simulation settings and PIC segment settings are shown in Table 7.3:

dt (**s**)	$1.5 \cdot 10^{-8}$
simulated time (**ms**)	$\mathcal{O}(1)$
$\mathbf{N_{e_{steps}}}$	150
steps-to-average	50
steps-to-output	100
min,target,max MPs per-cell	$75, 125, 150$
Background $\mathbf{n_n}, \mathbf{n_{i1}}, \mathbf{n_{i2}}$ $(1/\mathbf{m^3})$	$10^{15}, 10^{14}, 10^{14}$
Propellant mass-flow $(mg/\mathbf{s})$	$5\,(Xe)$
Position of cathode/potential-reference element (**m**)	$z = 0.055, r = 0.0425$
Bohm kinetic correction	OFF
Extended surface weighting	ON

Table 7.3: General and PIC simulation settings

The "background" density is a rarely used value chosen for each of the heavy species that ensures that a null density cannot be passed to the NOMADS segment, in the case that, for example, no macro-particles exist in a given cell in a particular time-step. More information on the Bohm kinetic correction and the surface weighting algorithm may be found in in Refs. [170, 164, 162]. The position of the cathode/potential-reference element was chosen somewhat arbitrarily but kept constant for all the results; some additional commentary on the volumetric cathode is made in Chapter 8.

The simulations have been run on a proprietary server dedicated for single-machine parallel processing, with 20 CPU cores at $1.2GHz$. Each simulation requires a time in the order of days to complete, for the simulated times and dt, which somewhat justifies the limited parametric investigation.

Regarding the NOMADS segment, the results shown in this chapter are obtained for the same PPU control scheme, discharge voltage and cathode type shown in Table 6.1; the boundary conditions used are also non-homogeneous Neumann. The collisional models employed are also the same as the ones described in Section 6.1, with the exception of the elastic electron-neutral collisions, where we have compared both the model proposed by Mitchner & Krueger[251] and the experimental data gathered by Hayashi[259]; again, no CEX collisions have been considered at this time. Regarding the sheath model parameters, we have employed the ones we proposed in Table 6.2 for a nondescript conducting material in the anode, and the BN ceramic material covering the thruster walls, with the exception of the thermalization fraction parameter, σ_{th}, for which we have compared values of 0.3 and 0.1.

The main physical parameter in the parametric investigation is the anomalous collisional frequency factor, α_{ano}, which is responsible for the large variability between the various results; the parameter can be introduced either as a fixed quantity in the simulation domain or through a spatially dependent function, typically: $\alpha_{ano} = f(\lambda, \sigma)$. While a number of physical processes and models have been proposed as tied to anomalous diffusion, as commented in Section 4.1.2,

the actual values used and the shape of the function are still an open question. Typically, an initial reference to these values lies in the early work by Janes[299], where a low β_{e^*} parameter[2], between 3 and 10, was required to allow sufficient mobility for the measured electron current to be established. However, traditional values and scaling of the anomalous transport factor seem unable to represent the IVDF measured experimentally, as shown by Garrigues[300]. The breadth of possible values for the α_{ano} parameter is, therefore, large, and the proposed vales have varied over time. Recent contributions by Mikellides & Ortega[126, 229] suggest, for example, that very large values of α_{ano} can exist downstream from the thruster channel, possibly close to 1. The practical reality, is that we will typically require some form of parametric analysis and experimental insight in most simulations, in order to inform the α_{ano} parameter.

On the other hand, as mentioned in Section 6.1, we have favored the "step-out" function for α_{ano}, with little or no anomalous transport in the thruster channel; this is partly because, similarly to Hagelaar[273], simulation results are unreasonable in any other case. We have not trialled the "quenching" or "three region"[231] type functions found by Meezan[278], where the anomalous transport is quenched in the region of higher magnetic field intensity (or higher Hall parameter and azimuthal drift). Based on the results shown in this chapter, this type of functions would be interesting to explore in future work.

In addition to the anomalous collision frequency factor, NOMADS admits an alternative anomalous collisionality parameter solely for the heat-flow equation, Eq. (4.55), α_Q; the parameter replaces α_{ano} in the expressions for the effective Maxwellian collision frequency, resistivity and Hall parameter, ν_{e^*M}, η_{e^*M} and β_{e^*M}, respectively. This parameter, was added as an extra degree of freedom in the simulation since Eqs. (4.59) and (4.38) do not necessarily admit the same anomalous transport model parameter. Typically, a minimum value of α_Q is required in regions of $\alpha_{ano} = 0$ to ensure smoother temperature profiles, which favor higher ionization rates in the channel.

Table 7.4 presents the electron fluid model parameters for the various cases that are compared in this final results chapter. Additionally, the 1D profiles of α_{ano} are provided in Fig. 7.3 for further reference. The length-scale for the rise in the step functions was arbitrarily selected to be 20% of the channel length. The purpose was to ensure that the transition from one step value to the next takes place smoothly over a number of magnetic streamline function contour lines (lines of constant λ). The sensitivity to this length-scale has not been assessed in the parametric investigation.

[2]In some of the works referenced here, the effective hall parameter was directly referenced as the Bohm diffusion coefficient.

Case	α_{ano}	$z_{\alpha_{step}}$ (m)	α_Q	$< R_{en} >$ model	σ_{th} dielectric	Trim magnet
1	0.0 – 0.2	0.03	0.04	Mitchner & Krueger	0.3	NO
2	0.0	∼				
3			0.0			
4	0.0 – 0.2	0.043	0.04			
5	0.01 – 0.2	0.03				
6	0.0 – 0.1					
7	0.01 – 0.1					
8	0.0 – 0.2			Hayashi		
9				Mitchner & Krueger	0.1	
10				Hayahshi		
1SP				Mitchner & Krueger		YES

Table 7.4: Case reference for HYPHEN results

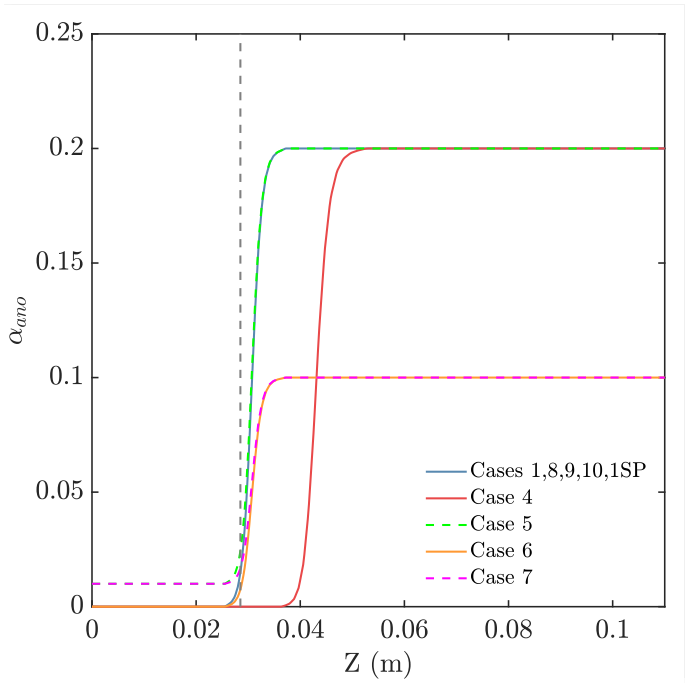

Figure 7.3: 1D profiles of anomalous collisional frequency factor along the TCL; (- - -) marks the channel exit

Case 1 was chosen as the "reference" case because it presents performance values that are closest to the nominal expected operation of the SPT-100[38]. Cases 2 and 3 were run in contrast to Case 1, to demonstrate the type of solutions that are obtained if anomalous transport is neglected; however, they differ in the anomalous collision frequency factor applied in the heat-flow equations. Cases 4 to 7 explore changes in the values of α_{ano}, as well as the position of the step-out function. Case 8 serves to compare the use of the Hayashi model for electron-neutral collision frequency with

the Mitchner & Krueger model used in Case 1 (Fig. 5.15 compares these two models, alongside the one by McEachran & Stauffer, which was not tested in a simulation). Cases 9 and 10 were simulated with a lower thermalization fraction parameter for the dielectric sheath model[3] than all other cases, and they differ in the electron-neutral collision frequencies employed; they are comparable to Cases 1 and 8, respectively. Finally, Case 1SP provides results for the SPT-100 magnetic circuit that includes the trim magnet. The other simulation parameters are as for Case 1, bar some slight variation due to the differing MFAM (shown in Fig. 7.5).

Cases 1 to 10 have been simulated using the manually corrected Exponential-stretching MFAM shown in Fig. 3.8, which contains ~ 1300 elements. The magnetic field in the simulation domain presents the following field lines and intensity, provided for reference:

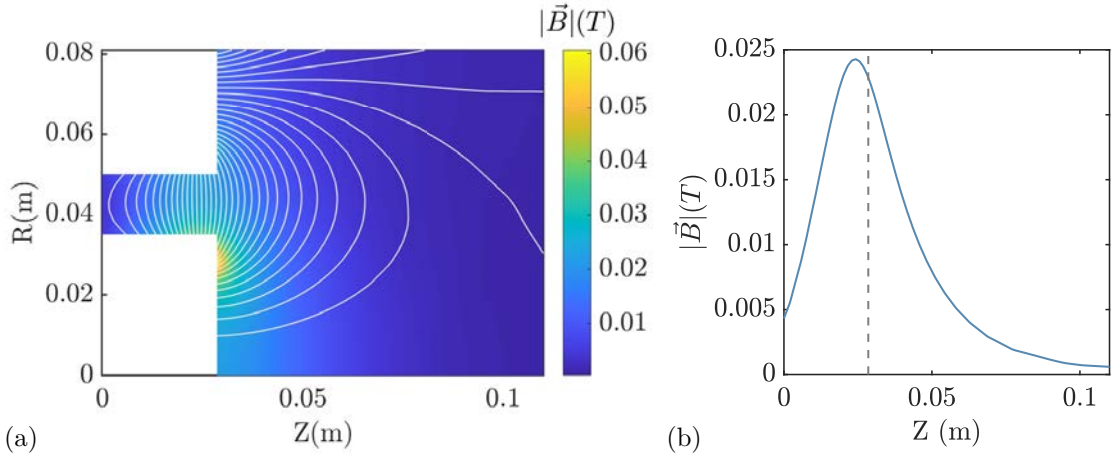

Figure 7.4: (a) Magnetic field intensity and magnetic field lines in the simulation domain and (b) magnetic field intensity at the TCL for Cases 1-10 of HYPHEN results (Table 7.4); (- - -) marks the channel exit

Case 1SP, on the other hand, was simulated using a MFAM corresponding to its magnetic geometry. The MFAM was constructed using the Exponential-stretching method, with additional lines to account for the singular point, and manually corrected; it is shown in Fig. 7.5.

[3]The conducting sheath model for the anode boundary retains its value of $\sigma_{th} = 0.3$ for all simulations; since the sheath potential drop in this conducting wall is typically the lowest for all sheaths, it is reasonable to think that the tails of the EVDF that attain sufficient energy to surpass the electric potential drop are replenished more easily; it is possible that an even higher value would be more fitting for this type of sheath.

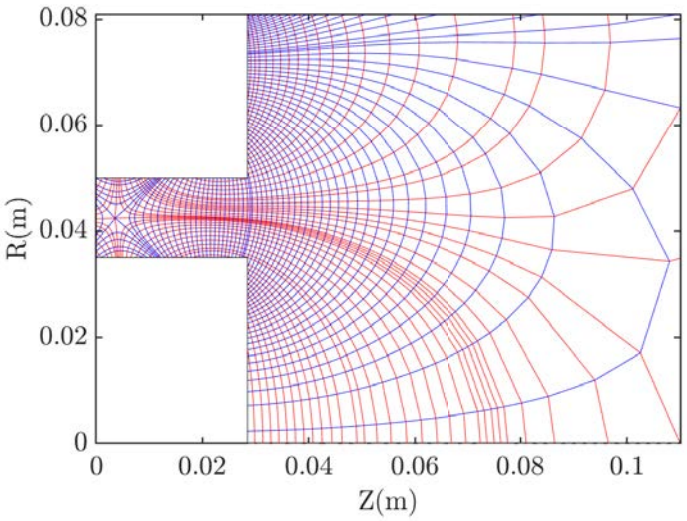

Figure 7.5: MFAM for Case 1SP of HYPHEN results (Table 7.4); lines in blue represent lines of constant magnetic stream-line function and coincide with the magnetic field lines, lines in red represent lines of constant scalar magnetic potential and are locally perpendicular to the magnetic field

The magnetic field lines and intensity for the singular point simulation are shown in Fig. 7.6; note that the 1D magnetic field intensity plot does not show a nil value for this quantity, but that that characteristic "X" shape of the magnetic lines in the NAR denote the existence of the singular point.

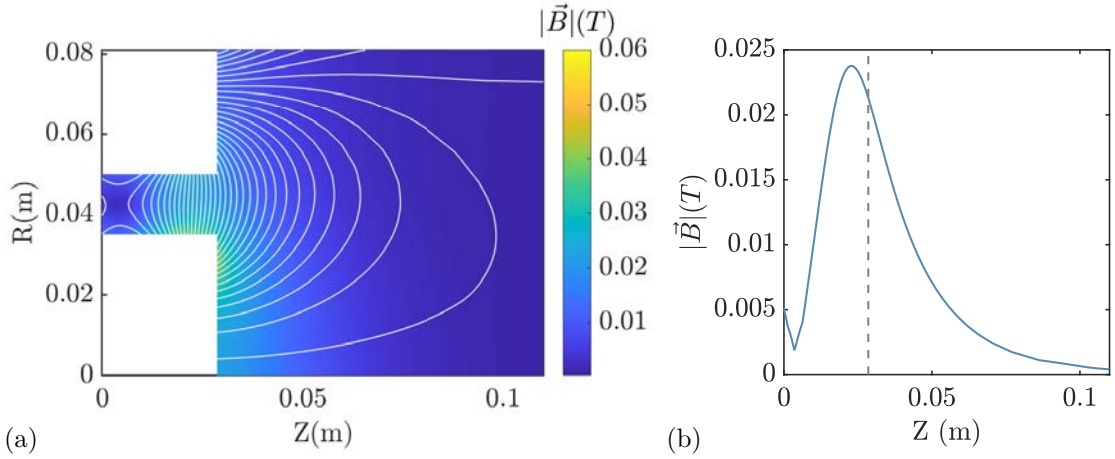

Figure 7.6: (a) Magnetic field intensity and magnetic field lines in the simulation domain and (b) magnetic field intensity at the TCL for Case 1SP of HYPHEN results (Table 7.4); (- - -) marks the channel exit

Lastly, the PIC mesh and the boundary types implemented in the simulation are the same as the ones in Section 6.8, shown in Fig. 6.15.

As a final comment for to this chapter, it is worth mentioning that the simulations presented here have been carried out assuming an isotropic distribution of electron temperature, solving only for the total electron temperature, through Eq. (4.44), and using the simplified heat-flow equation, Eq. (4.62). Although the anisotropic model has been developed, it has not been fully implemented at the time of writing this thesis and, therefore, results on temperature anisotropicity could not be included.

7.2 In-depth analysis

This section focuses on the results for simulation Cases 1, 2 and 1SP from Table 7.4, providing insight into the non-stationary nature of the thruster operation, 2D fluid profiles, sheath characterization, etc. A full comparison for all cases is given in Section 7.3; the analysis of performances, power balances and currents is reserved for that section.

7.2.1 Case 1

Commencing our analysis, we are interested in the NOMADS results from the numerical perspective. First, Fig. 7.7 shows the residuals at the last step of the NOMADS segment, for the data output time-steps in the simulation; both temperature and plasma potential residuals are below 0.1% and, on average, present values of $\sim 0.002\%$ and $\sim 0.005\%$, respectively. The residuals shown in Fig. 7.7 are a representative scenario of the simulations presented in this chapter; while these values may be far from the ones shown in Chapter 6 we consider them sufficiently acceptable, although the criterion for residual acceptance is arbitrary and up to each user of the code. If needed, residuals may be easily reduced by lowering the time-step value in the simulation and by incrementing the number of steps in NOMADS, $N_{e_{steps}}$.

We can also provide insight into the power balances of the electron population. Table 7.5 shows the mean of the partial contributions over the simulated time interval, considering that the data is only outputted on certain time steps.

$\mathbf{P_{adv_e}}\vert_{\mathbf{FF}}$	-9.8
$\mathbf{P_{sh_e}}\vert_{\mathbf{AB}}$	-58.6
$\mathbf{P_{sh_e}}\vert_{\mathbf{D}}$	-215.3
$\mathbf{P_{exp_e}}\top$	-88.2
$\mathbf{P_{exp_e}}\parallel$	-10.6
$\mathbf{P_{heat_e}}$	446.9
$\mathbf{P_{inel_e}}\,(\mathbf{i01}, \mathbf{i02}, \mathbf{i12}, \mathbf{ex})$	$-46.9, -2.9, -2.3, -35.9$
$\langle\mathbf{Err}\rangle$	-23.5
$\mathbf{P_{cath_e}}$	13.7

Table 7.5: Global-mean partial contributions to electron energy balance and cathode energy (all values given in W) for Case 1 of HYPHEN results (Table 7.4)

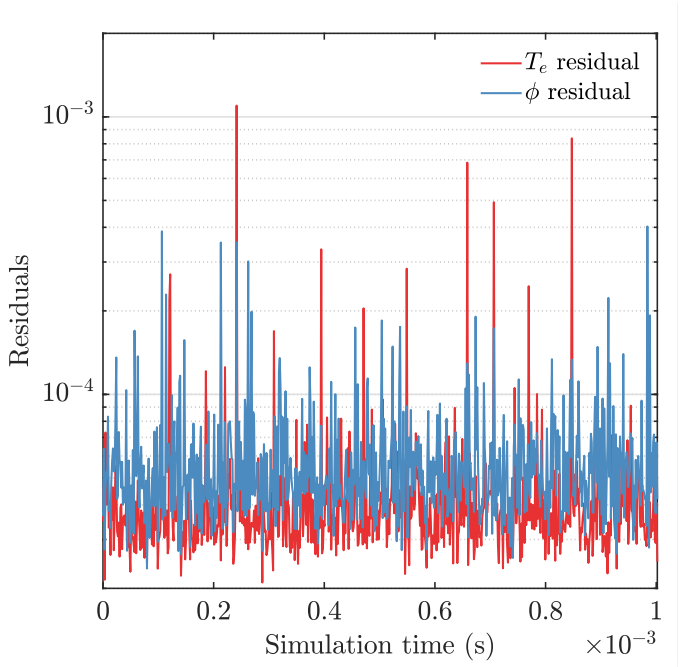

Figure 7.7: NOMADS exit-step residuals for Case 1 of HYPHEN results (Table 7.4)

Note that the cathode energy is, again, included as reference, since its contribution is included in the heating and gas expansion terms. The average balance error is now higher than what was shown in Chapter 6, which corresponds to higher exit residuals. Note that this summation is over all of the approximately 1300 elements in the MFAM and that the effective time-step for NOMADS is $10^{-10}s$. Considering a representative volume for the elements of $10^{-6}m^3$ and a plasma density in the domain of $10^{17}1/m^3$, the average change in electron temperature for each element due to the imbalance (at the NOMADS exit time-step) would be $\mathcal{O}\left(10^{-3}eV\right)$. We consider this value sufficiently low for our purposes. Additional comments on the electron energy balances for Case 1 are made next in comparison to other cases.

Delving further into the results from full simulations, Fig. 7.8 presents time-resolved values for the discharge current, I_d, and the ion beam current, I_i. The first $1ms$ of the plot shows time resolved results, averaged over the number of steps given by the steps-to-average value in Table 7.3. In addition, the data was outputted according to the steps-to-output value. In contrast, the last $0.3ms$ of the plot show instantaneous current values, where all steps of the simulation are plotted[4]. The differences in both current values are related to the current efficiency (Eq. (7.6) and Table 7.7), which denotes the need for an electron current that is larger than the exiting ion beam current to maintain the discharge. This is due to a combination of ion neutralization at the thruster walls, of a certain electron current required for ionization to take place and anomalous

[4]Writing data into the `PostData.hdf5` file is expensive in terms of computation time, which is why we use the steps-to-output value to reduce the number of writing operations; producing output data at every single step of the simulation is only done in Section 7.2.1.

electron transport.

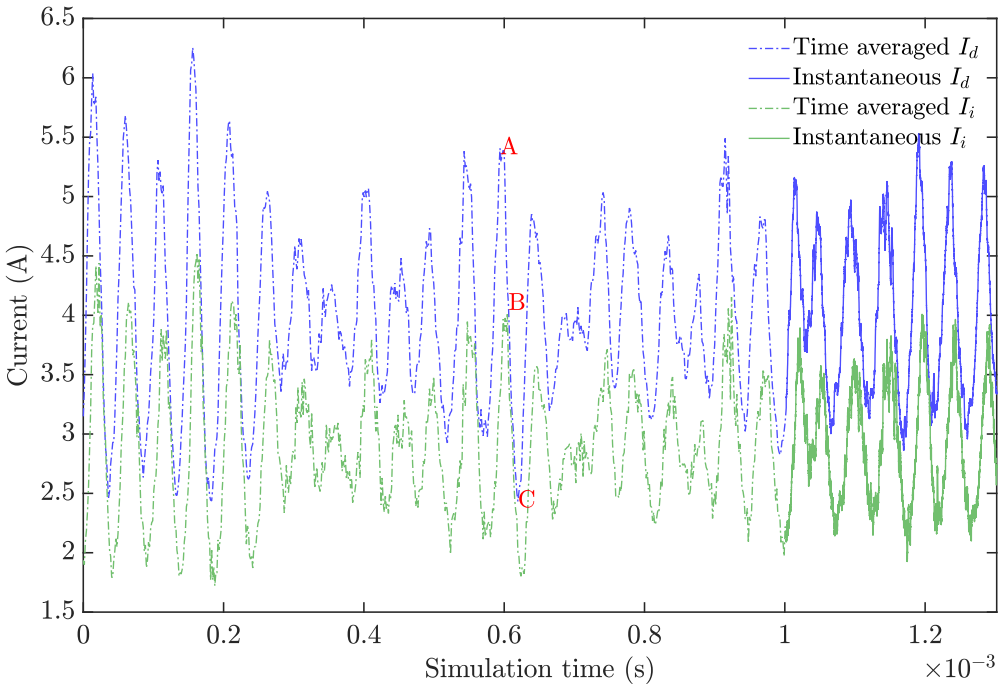

Figure 7.8: Time-averaged and Instantaneous Discharge Current, I_d, and Ion Beam Current, I_i, for Case 1 of HYPHEN results (Table 7.4); time-steps A (high I_d), B (medium I_d) and C (low I_d) are marked for further reference

The well known HET "breathing mode", or ionization oscillation, is instantly recognizable in Fig. 7.8. Other additional modes seem to also be present in the results and, in order to fully characterize them, we have conducted a frequency-amplitude analysis based on the Fast Fourier Transform (FFT); the results are shown in Fig. 7.9. The FFT has been applied to the instantaneous data to avoid spurious results that may appear due to time-averaging and the frequency of data-output; obviously, the frequency analysis will only be able to resolve down to the frequency associated to the time-step in the simulation.

The breathing mode oscillation is represented by the largest amplitude peak in Fig. 7.9, appearing at around $20kHz$. This ionization oscillation was observed experimentally and reported by various authors, including Bouchoule[301] and Darnon[302] to be between $10-20kHz$ or possibly up to $30kHz$[221, 223]. This oscillation occurs in the thruster due to the dynamics of neutral atom "depletion" in the ionization region and the acceleration of ions: the resistive heating mechanism in the plasma is tied mainly to the electron-neutral collisions, which depend on both the neutral and plasma densities, as well as on the electron temperature, forming a feedback loop. Ionization leads to increasing plasma density and temperature, but neutrals may be ionized faster than they are being replenished through injection, leading to a reduction in neutral density that lowers both the ionization rate and the electron temperature; once the electric field removes sufficient ions from the ionization region and the neutral density begins to rise again, the cycle repeats itself.

Fife[76] compared this mechanism to a predator-prey behavior between the neutral and electron populations and Boeuf[128], using a simple 1D code, demonstrating that, indeed, the neutral depletion mechanism was responsible for the ionization oscillation.

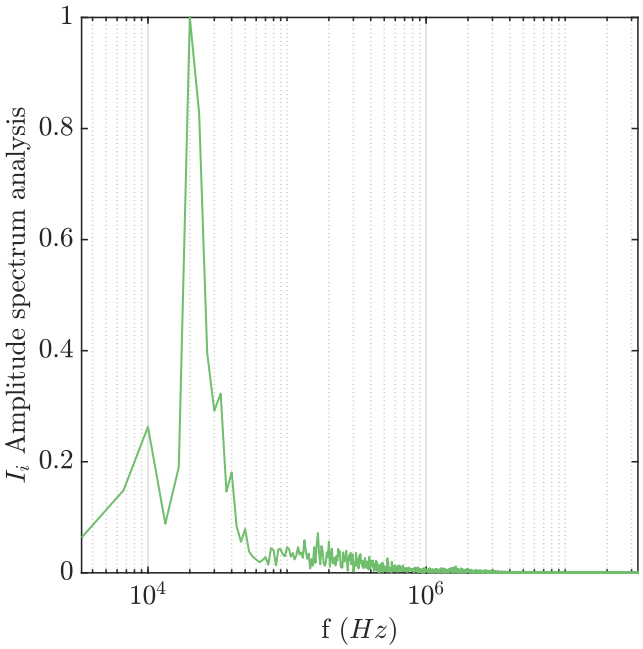

Figure 7.9: FFT normalized amplitude spectrum analysis of instantaneous Ion Beam Current (I_i) for Case 1 of HYPHEN results (Table 7.4)

Figure 7.9 presents other distinctive peaks: smaller amplitude oscillations appear both at higher (30, 40 and $50kHz$) and lower ($10kH$) frequencies than the main oscillation and their positions seem to imply that they are harmonics from the main breathing mode. The physical explanation for these is more elusive, though, as they could be related to double-ion production, to spatial shifting of the ionization region within the channel or to some other phenomena. Alternatively, recent contributions[303] have proposed that this mode is consistent with cnoidal type oscillations, where the harmonics appear naturally. More resolution in the FFT would be needed to fully characterize these "harmonics"; unfortunately, this can only be achieved by incrementing the simulated time and, due to lack of time, we have not been able to provide additional results. At higher frequencies, a range of peaks exists around $\sim 100kHz$ and even up to $\sim 1MHz$; these can only be associated to the ion transit or ''flight" oscillations[223], and the dispersion can be related to the fact that both double and single ions are simulated and also that the macro-particles in the PIC approach may present a large dispersion in particle weights (i.e., the number of elementary particles contained in the macro-particle) depending on where within the domain ionization occurred and the particular history of the macro-particle. Further efforts to reduce this weight dispersion would be useful, although this topic lays outside of the scope of this thesis.

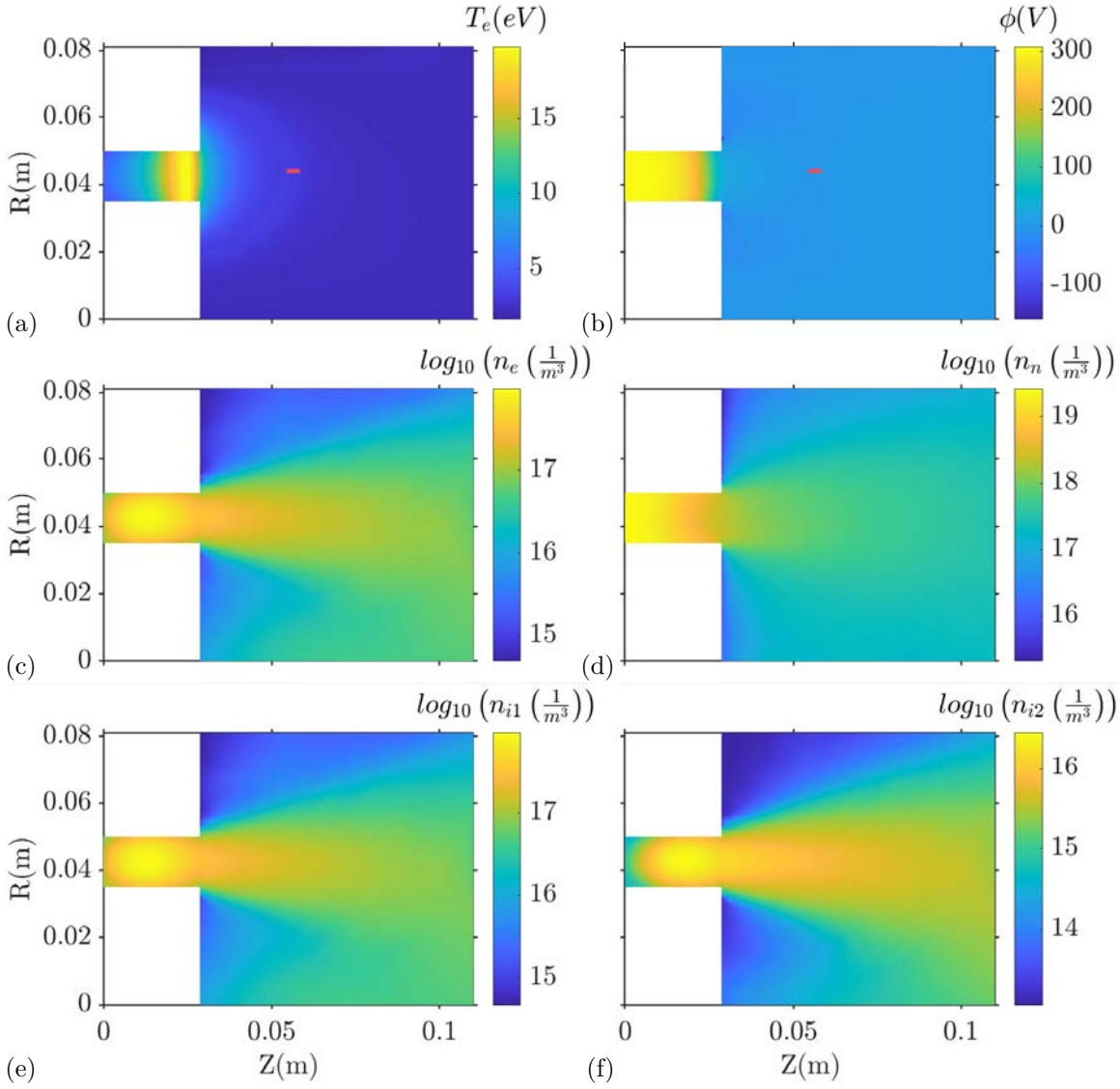

Figure 7.10: Global-mean 2D maps of (a) T_e, (b) ϕ, (c) n_e, (d) n_n, (e) n_{i1}, (f) n_{i2} for Case 1 of HYPHEN results (Table 7.4); volumetric cathode element (also, potential reference point) is shown in red in subfigures (a) and (b)

Figure 7.10 shows the 2D maps for the mean values of the electron fluid quantities, electron temperature and plasma potential, and the densities of the various populations simulated; in addition, Figure 7.12 presents the 1D profiles for those same mean quantities, and also the profiles for the time-steps associated with low, mid and high discharge currents shown in Fig. 7.8.

Both the highest electron temperature and axial electric field (given by the slope of the plasma potential curve) are located within the thruster channel and present little variability between the mean value and the instantaneous values. The locations of these "maximums" are related to the profile of α_{ano}: the electric field in the plasma ultimately exists because of the potential difference between anode and cathode, the plasma potential, however, self-adjusts mainly in relation to the

cross-field conductivity exhibited by the electron population (which depends solely on collisions, since electrons are trapped by the magnetic field) and partly due to the gradients of electron pressure. These two effects compete in order to determine an electric field that ensures that current continuity is satisfied[5]. In general, this means that the electric field is stronger in regions of lower cross-field transport, which is accounted for by the Hall parameter shown in Fig. 7.14(b). It is clear that the effective Hall parameter differs greatly from the "natural" one, and it is because of this that the plasma potential is mostly flat outside of the thruster channel, since very little electric field is required in this very conductive region.

The electric potential rises slightly from the cathode to the thruster channel exit; since the effective Hall parameter is small until just before the channel exit, this increase must be due to the gradient of electron pressure (dominated by changes in both electron density and temperature). Once within the thruster channel, the effective Hall parameter rises greatly, which is accompanied by a sharp jump in the electric potential. The electron temperature increases as well, mainly as a consequence of a large azimuthal Hall current being established there[6], which can be seen in Fig. 7.16(d), and directly influences the resistive heating term. Downstream from the channel exit the azimuthal current takes on very low values, since the effective Hall parameter there is also small. Continuing toward the anode, the temperature decreases as energy is deposited in the dielectric walls and consumed in the ionization and excitation processes. Outside the channel, the heat-flow term in the energy equation allows the electron temperature to diffuse downstream. Note that the cathode element location can be clearly seen in both the 2D and 1D results, particularly because of the local temperature rise due to the injected cathode energy.

The 2D maps and 1D profiles of electron temperature and plasma potential, which are ultimately the most characteristic results of the electron fluid model, are typical of HET discharges. Experimental results for Xenon presented by Kim[293], reproduced here in Fig. 7.11, are very similar to those for Case 1, allowing for the different propellant mass-flow, which is slightly smaller than in our simulation. The maximum values and location of the temperature peak and acceleration region (Fig. 7.12), as well as the ion current, seen in Fig. 7.30(a) for the TCL, are comparable in their likeness. On the other hand, the reported performances are better than the ones we obtain, even when accounting for the reduced mass-flow.

A later reference by Kim[288] provided lower values of electron temperature ($\sim 12eV$) than the ones obtained in the simulation, for a similar discharge[7], but most of the literature, both experimental[289, 290] and simulation-oriented[298, 173], presents peak temperatures closer to, or higher, than the ones for Case 1, ranging $30 - 50eV$, as well as higher values downstream from the channel exit, ranging $5 - 10eV$. From the perspective of simulations, this could be tied to the use of electron-neutral collision rates that offer higher values than the ones used here, such as the model provided by McEachran & Stauffer[267], and to different values and distributions of the anomalous frequency factor. In addition, the performances provided in Table 7.7 show that the discharge current is still below the nominal operation point for the SPT-100; a larger anomalous

[5]This explanation accounts for the physics of the momentum transport equation, Eq. (4.34)
[6]The Hall current is obtained in our model once Ohm's law has been resolved, by using Eq. (4.42).
[7]The discharge shown in Kim[288] imposed $V_d = 350V$ and $\dot{m} = 4.27^{mg}/_{s}$.

collisional frequency factor outside the thruster would increase the axial electron current and with it the value of the Hall current in the channel, which would imply higher electron temperatures.

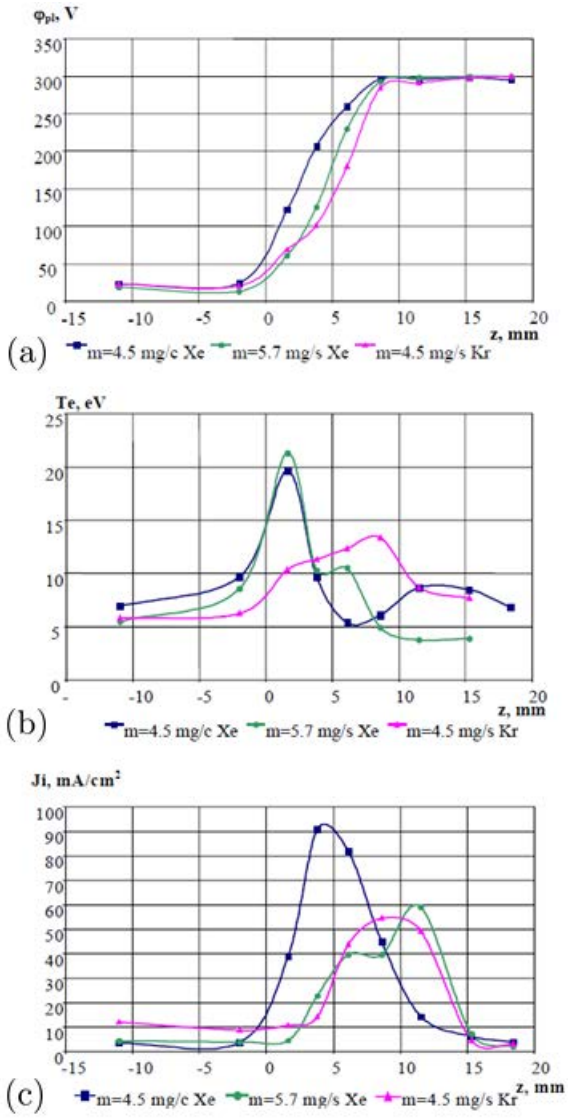

Figure 7.11: Experimental results for (a) ϕ, (b) T_e and (c) ion current density for the SPT-100, reproduced from Kim[293]; $z = 0$ represents the thruster exit, $z < 0$ represents the region downstream from the thruster

As a final comment, the reader may note that the temperature peak presented in Case 4 is larger than in Case 1, as demonstrated by Fig. 7.29(a). This was achieved by moving the location of the "step" for α_{ano} and, although greater in value, the electron temperature peak is too far removed from the thruster channel and the discharge current (and thus the axial electron current) is too low. An intermediate position for the step of α_{ano} coupled with a larger value of the anomalous transport factor before or after the step may yield results which are both closer to nominal performances and to experimentally measured profiles of the plasma quantities.

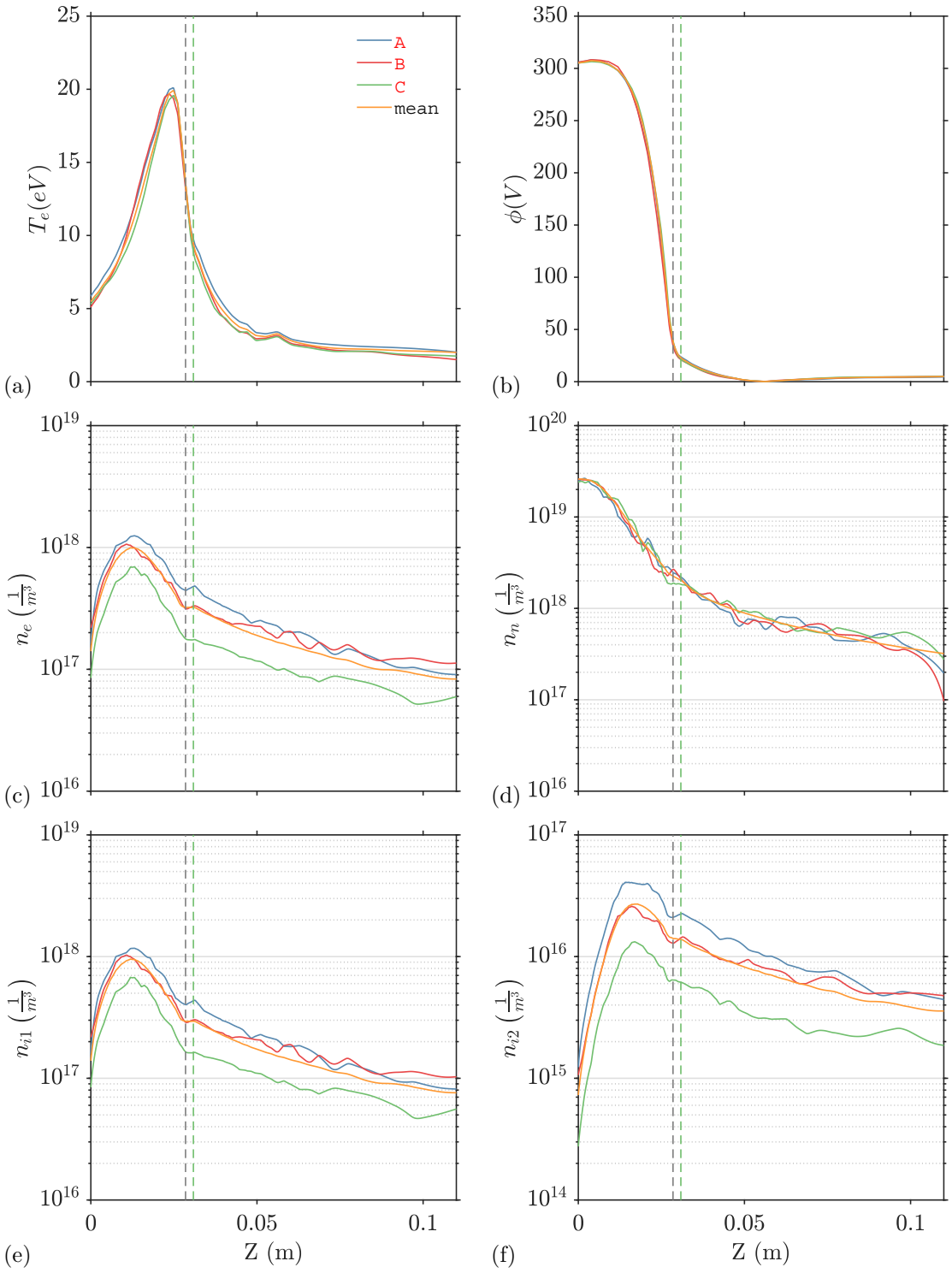

Figure 7.12: 1D profiles of (a) T_e, (b) ϕ, (c) n_e, (d) n_n, (e) n_{i1}, (f) n_{i2} at TCL, corresponding to time-steps A, B, C from Fig. 7.8 and global-mean profiles for Case 1 of HYPHEN results (Table 7.4); (- - -) marks the channel exit and (- - -) the step change in α_{ano}

Regarding the electron and ion populations, densities show a larger variability among the various time-steps (Fig. 7.12), which is expected and relate to the breathing mode oscillation discussed at the beginning of this section. Note that the oscillation process cannot be captured in a single time-step, which is why some overlapping exists between the curves (in addition to the typical noise from PIC methods), particularly, between time-steps A and B.

Generally, the density for both ion species rises quickly in the NAR, reaching a maximum and then dropping sharply in the acceleration region within the channel; ion neutralization in the dielectric walls also happens within the channel, lowering the overall density. Once out of the channel, the density drops at a lower rate, driven by the expansion of the plasma in vacuum; the divergence in the plume is caused by radial ambipolar electric fields (due to the residual electron temperature) and the ion population's own velocity distribution, and not due to diffusion processes, since the heavy species are non-collisional.

Considering the orders of magnitude in the electron and ion densities, it is clear that the single-ion population dominates in the plasma; the double-ion density is lower by more than one order of magnitude. The double-ion density peak occurs slightly further downstream from the single-ion peak, closer to the electron temperature peak, which is expected, considering that the ionization reactions that produce double-ions occur at a lower rate than the single-ion reaction, for the same electron temperature (see Section 5.2); in the case of the single-to-double process, they also require a certain ion density in order to present significant rates.

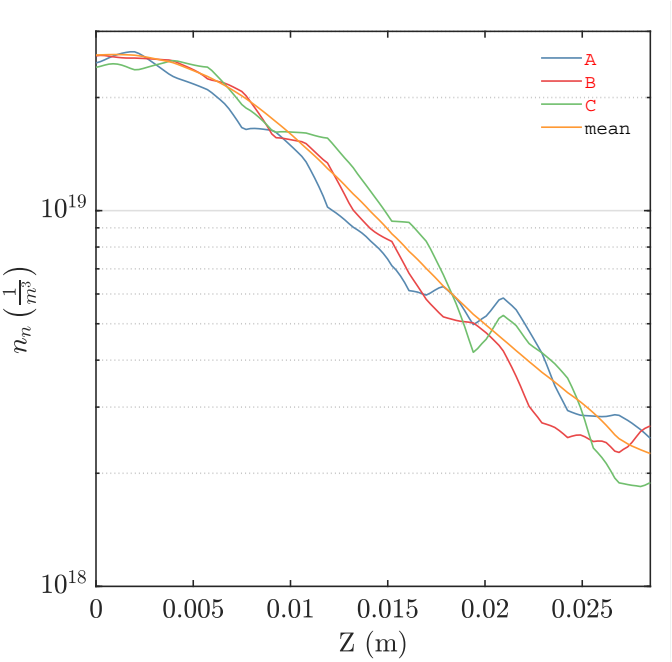

Figure 7.13: Detail of n_n 1D profiles at TCL within the thruster channel length, corresponding to time-steps A, B, C from Fig. 7.8 and global-mean profiles for Case 1 of HYPHEN results (Table 7.4)

Regarding the neutral species density, Figs. 7.10 and 7.12 show how the density decreases rapidly in the ionization region and then more slowly in the near plume. Figure 7.13 provides a

detail of the neutral density within the thruster channel; even though the variability among the different time-steps seems small, it is sufficient to represent the neutral depletion mechanism that is responsible for the breathing mode, if one considers the different orders of magnitude between neutrals and the ionic species.

Continuing with some of the main physical processes driving the results, Fig. 7.14 presents the 1D profiles for all of the relevant frequencies in the simulation, as well as the total and total effective Hall parameters, whose influence in the results has already been discussed. The frequency plot shows that electron-neutral elastic collisions are dominant, except perhaps in the downstream region of the simulation domain, where the electron-single-ion elastic collisions are of the same order. Nonetheless, the effective frequency is dictated almost solely by the anomalous collision frequency, once the α_{ano} takes a value different from 0. It is worth noting that the ionization frequencies all have a local peak around the cathode position, because of the local temperature increase in this region.

The values shown in Fig. 7.14 are comparable to others found in simulations[298, 231] and, in particular, the peak value for the effective total Hall parameter agrees well with experimental results[41].

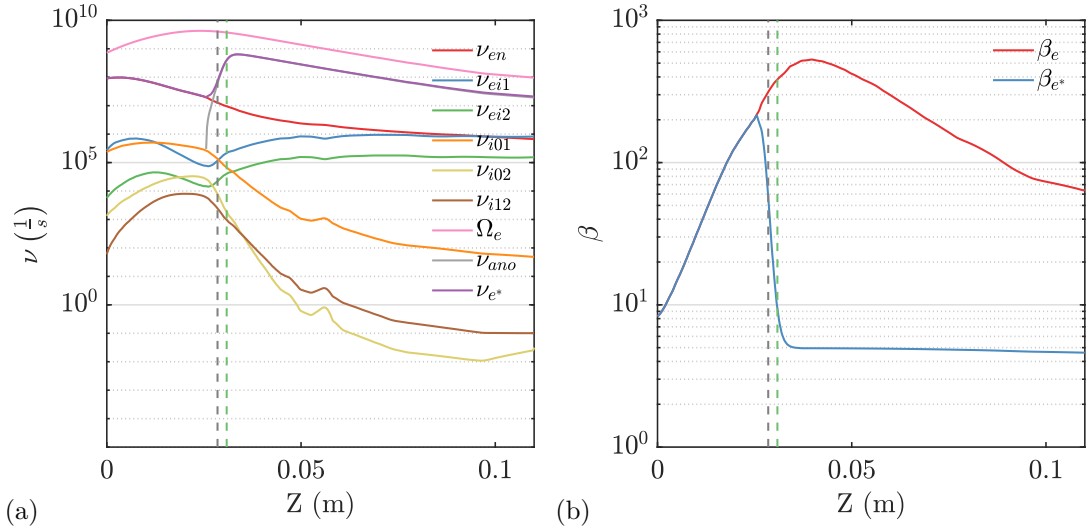

Figure 7.14: (a) Global-mean collisional, ionization, gyro, anomalous and total-effective frequencies and (b) total and total-effective Hall parameter, β_e and β_{e^*}, at TCL for Case 1 of HYPHEN results (Table 7.4); (- - -) marks the channel exit and (- - -) the step change in α_{ano}

Figure 7.15 shows the variability in the physical frequencies for the various time-steps specified in Fig. 7.8. Changes between the different time steps chosen are subtle, due to the logarithmic scale of the plot. The exception is the downstream region of the plume, where the breathing mode oscillations lead to more notable variation, specially among the elastic collision rates for electron-neutral and electron to single-ion and the ionization rates for double-ions. These changes may only be related to oscillations of the densities of the various populations, since the electron temperature has been shown to vary very slightly.

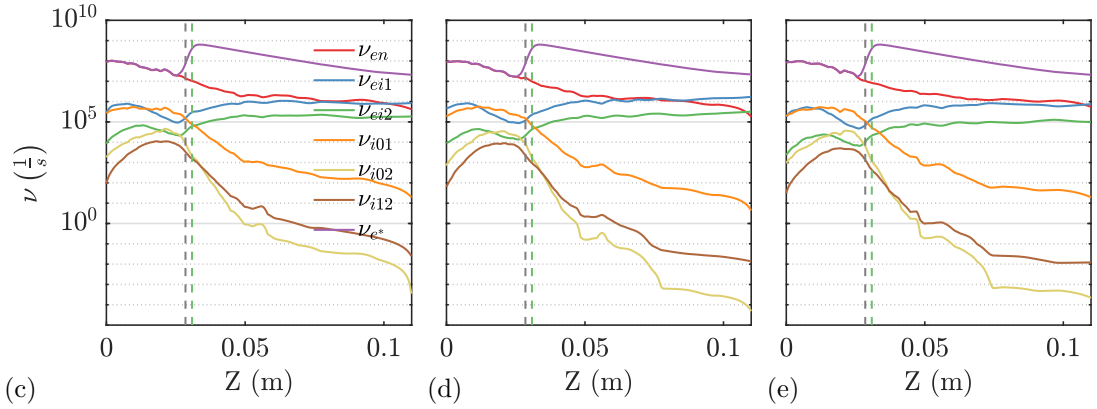

Figure 7.15: Collisional, ionization, gyro, anomalous and total-effective frequencies at TCL for time-steps (a) A, (b) B, (c) C from Fig. 7.8 for Case 1 of HYPHEN results (Table 7.4); (- - -) marks the channel exit and (- - -) the step change in α_{ano}

Figure 7.16 offers a global-mean reconstruction of the ion current and the z-r plane components of the electron current and total current stream-lines, as well as the azimuthal electron Hall current. As expected from previous results, ions present clear and smooth lines, with the largest current density developing in the acceleration region and immediately at the exit of the thruster channel. Some back-flow exists around the NAR as well as near the dielectric walls outside of the channel. The divergence of the plume as well as the currents parallel to the domain axis are also clearly visible

The electron currents present a rather less smooth appearance, mainly in the area between the neutralization region and the channel, as well as in the elements around the upper Far-Field boundary; this effect is somewhat downplayed in the thruster channel and in the stream-lines downstream from the cathode element and the domain boundary. It is clear that the discharge current injection in the cathode has a strong influence in the vicinity, where most of the current is distributed parallel to the magnetic field lines. In contrast, the way the electron current makes its way towards the channel is more chaotic. It was already alluded to in Section 6.3 that a number of effects may be at play here, including mesh quality and gradient reconstruction related issues. However, we theorized that this was most likely related to the way stream-lines are built, following local current density vectors and how these behave in regions of low current density, due to localized effects.

Figure 7.16(c) shows the total currents in the simulation domain, $\vec{j} = \vec{j}_i + \vec{j}_e$. We have attempted to show how electron and ion currents neutralize in the near-plume by having the color-scheme in the figure reflect the very low currents. As expected, the part of the discharge current that is used to sustain the discharge (plus the one due to anomalous transport) seamlessly flows from cathode to anode; note that, in this case, the total current at the channel walls is parallel to them, since the normal components of both the electron and ion currents cancel out there. This last trend continues in the dielectric walls outside of the channel, although the currents reaching these walls have neutralized closer to the cathode element.

Finally, the plume downstream from the neutralization zone presents a characteristic “looping”;

we theorize that these shapes appear because the electron and ion currents neutralize in the direction of the plume expansion, but that some of the local effects in the electron currents (mainly in the parallel direction to the magnetic field) remain, and are responsible for the commented shape.

To instill further confidence in the reader that the solutions we have presented here are valid from the point of view of plasma currents, it is worth mentioning that the errors committed in current-continuity in the simulation, when solving the Iterative Matching algorithm (Section 4.2.4) and the global current continuity equation, Eq. (4.69), are extremely low: of the order of 10^{-11} for all time-steps.

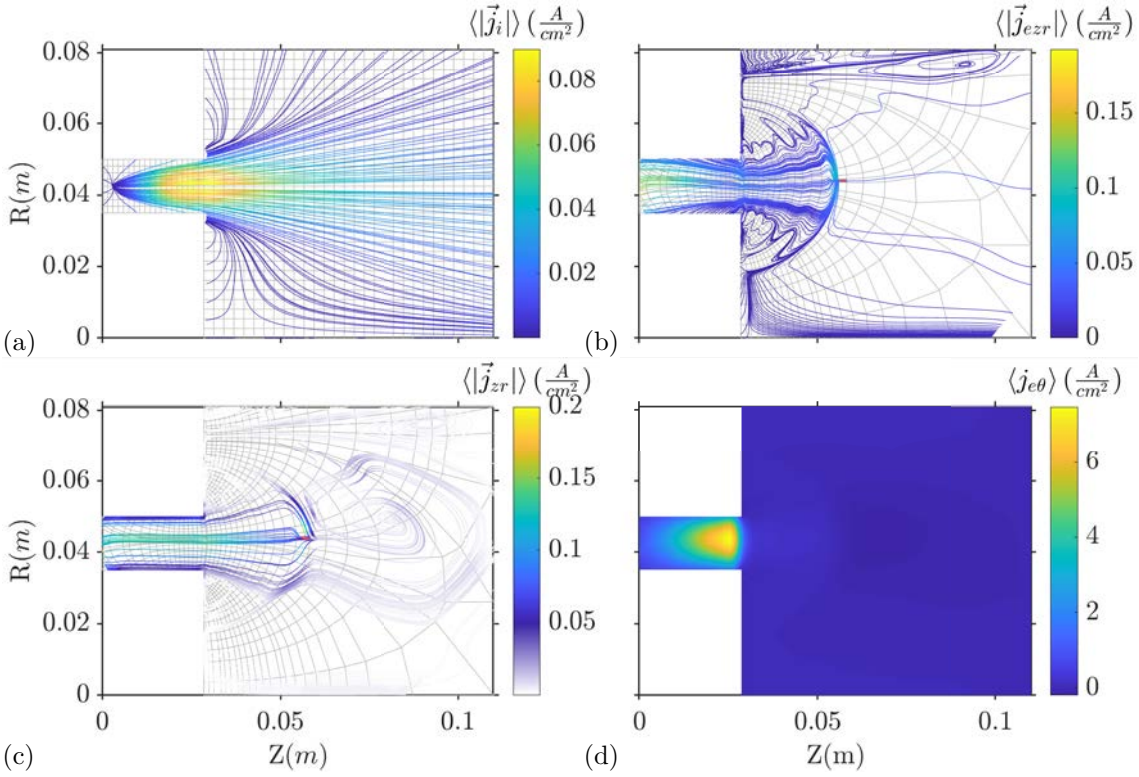

Figure 7.16: Global-mean streamlines of (a) $\vec{j}_i$, z-r plane components of (b) $\vec{j}_e$ and (c) $\vec{j}$, and (d) azimuthal electron current for Case 1 of HYPHEN results (Table 7.4); volumetric cathode element (also, potential reference point) is shown in red in (b)

As a last comment, Fig. 7.16(d) shows that the azimuthal current reverses in direction once past the cathode element, since the perpendicular electron current following the ion current changes in sign. This presents a sort of shearing of the electron current which could also be involved in some of the physical mechanisms proposed for the anomalous transport. This effect is more apparent in the results for Case 2, shown in Fig. 7.22.

Closing this section, we provide results on the response of the dielectric and conducting (anode) sheaths: Fig. 7.17 provides insight into the value of the sheath potential drop, SEE current density and energy deposited both in the sheath and in the material wall. All depend on the plasma

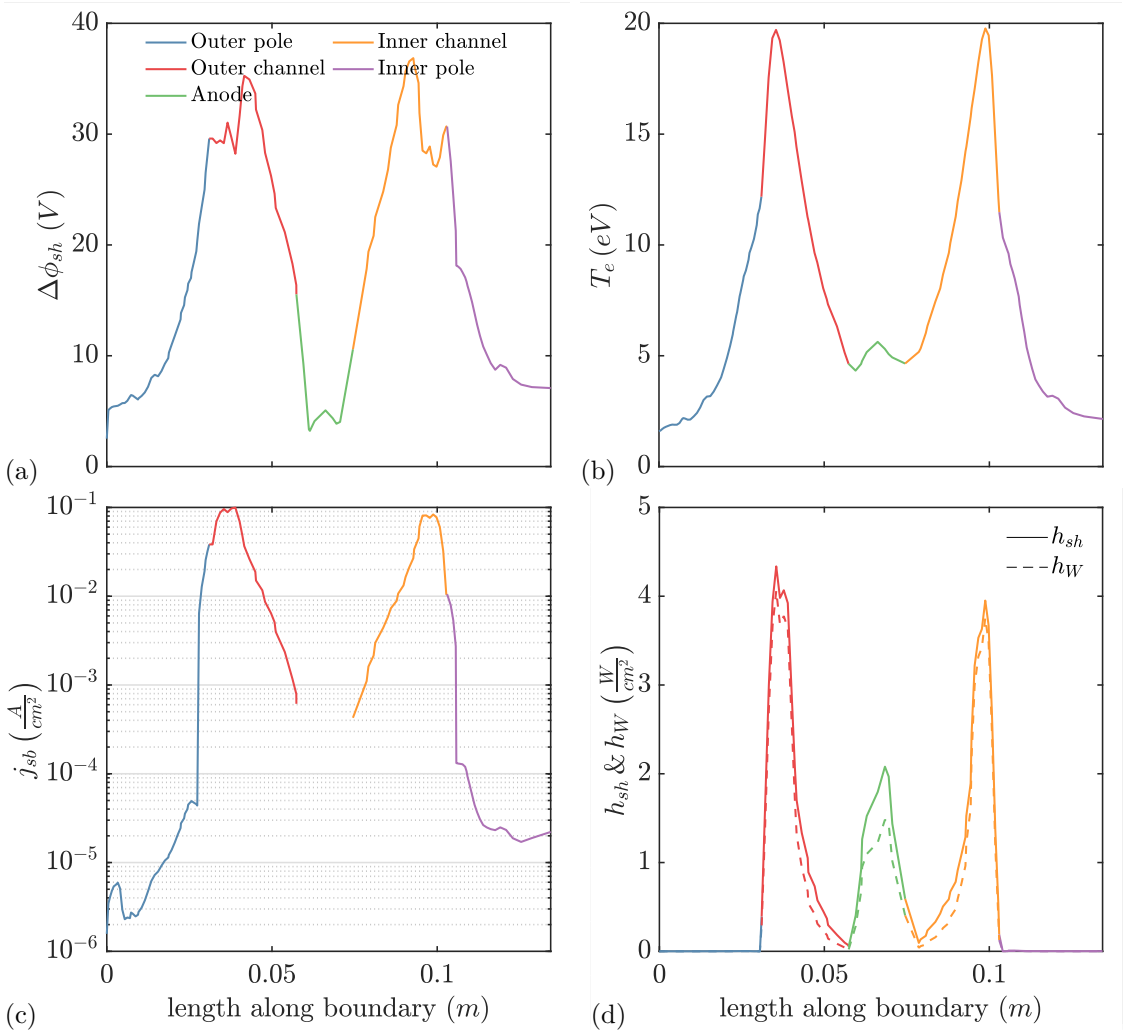

Figure 7.17: Global-mean profiles of (a) $\Delta\phi_{sh}$, (b) T_e, (c) g_{sb} and (d) h_{sh} & h_W along physical walls for Case 1 of HYPHEN results (Table 7.4); the specific wall sections to which each of the curves refer are shown in Fig 6.15. Note that the anode boundary has no SEE

density, ion or electron currents and electron temperature at a particular position in the wall. The values of the sheath potential drop are similar to the ones provided for SPT-100 simulations by Hofer[298] and Barral[124], if somewhat smaller. In both cases a thermalization fraction parameter of $\sigma_{th} = 1$ was retained, which is the most probable explanation for this effect, although a lower electron temperature and density could also play an important role. The energy deposition is found to be of the same order as the one shown by Ahedo[277], although the sheath quantities obtained from the simulation detailed in this reference were obtained for a different thruster than the SPT-100. The effect of the sheath potential drop is larger in the anode sheath than it is in the dielectric, even for widely different values of electric potential drop, which is in line with the fact that the electron current extracted at the anode is much larger than at the dielectric walls.

Finally, the SEE current peaks are located at the channel exit, with values that are comparable to the largest ion current in the simulation domain, immediately downstream from the acceleration region. This can only occur due to the dielectric sheath operating in the CSR, which coincides with the largest energy deposition values (see Section 5.1.4). Once within the channel, the SEE drops with the wall temperature, reaching a minimum at the anode; presumably, the sheath will not operate past the CSL in the first-half of the channel, which explains the large drop in energy deposition. In the walls facing the plume, the SEE drops drastically, as is expected for both lower temperature and ion-currents.

7.2.2 Case 2

Case 2 and Case 3 were simulated to characterize the effects of neglecting the anomalous electron transport in the HET plasma discharge; the two cases only differ in the anomalous collision frequency factor for the heat-flow equation, α_Q. The results presented in this section constitute a "non-physical" solution in the sense that it cannot be correlated to any experimental evidence in HETs. However it can be understood from the perspective of the implemented models and the physics they resolve. If anything, this section serves to demonstrate, from a mechanistic point of view, why and where we need anomalous transport to occur.

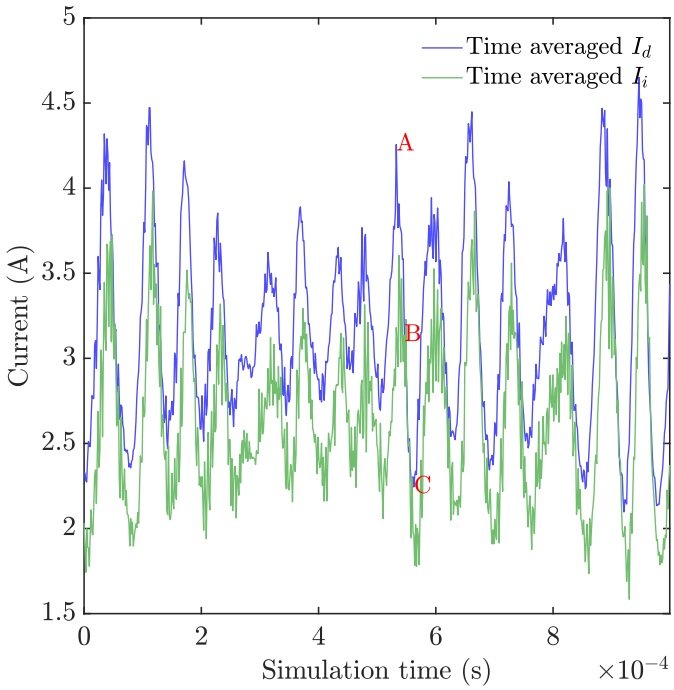

Figure 7.18: Time-averaged discharge Current, I_d, and Ion Beam Current, I_i, for Case 2 of HYPHEN results (Table 7.4; time-steps A (high I_d), B (medium I_d) and C (low I_d) are marked for further reference

Figure 7.18 shows the ion beam and discharge currents for Case 2. In comparison to Case 1, the discharge current is much closer to the ion beam current and thus, smaller in value; this appears to be reasonable, since no anomalous transport implies that I_d becomes the sum of the

neutralization current (equal to the ion beam current) and the electron current needed to mantain the discharge, through ionization of the neutral species. These results are in-line to the ones provided by Boeuf[128] for the SPT-100 with no anomalous transport, accounting for the larger noise shown in our result. Clearly, the breathing mode is still present, although the frequency analysis has not been carried out for these results.

Table 7.6 shows the global-means of the partial contributions to the electron energy equation. We will start by comparing the energy lost due to ionization and excitation, which is larger than in Case 1. The first can be tied to Figs. 7.19 and 7.20 which show a second, larger, maximum of plasma density downstream from the thruster channel exit, higher electron temperature and a steeper descent of the neutral species density, meaning that inelastic collision processes outside of the thruster play an important role, hence the increased energy loss.

$\mathbf{P_{adv_e}}\vert_{\mathbf{FF}}$	-56.6
$\mathbf{P_{sh_e}}\vert_{\mathbf{AB}}$	-21.1
$\mathbf{P_{sh_e}}\vert_{\mathbf{D}}$	-213.3
$\mathbf{P_{exp_e}}\top$	-224.1
$\mathbf{P_{exp_e}}\parallel$	-24.6
$\mathbf{P_{heat_e}}$	633.0
$\mathbf{P_{inel_e}}$ $(\mathbf{i01}, \mathbf{i02}, \mathbf{i12}, \mathbf{ex})$	$-54.6, -2.6, -12.5, -43.6$
$\langle \mathbf{Err} \rangle$	-20.0
$\mathbf{P_{cath_e}}$	10.7

Table 7.6: Global-mean partial contributions to electron energy balance and cathode energy (all values given in W) for Case 2 of HYPHEN results (Table 7.4)

Nonetheless, ionization cannot solely account for the large increase in plasma density outside of the channel. This phenomenon is mainly tied to the electric potential profile, which rises downstream from the neutralization zone, presenting an electric potential barrier for the ion population, which must either slow-down or repel ionic macro-particles, depending on their mass and the effective potential drop experienced in the acceleration zone. The peculiar shape of the electric potential can be explained simply through the Hall parameter shown in Fig. 7.21: since anomalous transport has not been simulated in this case, the Hall parameter maintains a very high value of $200 - 400$ outside the channel. This implies that the magnetic confinement of the electrons in that region actually dominates that of the thruster channel. From the perspective of the electron population, when the neutralization current attempts to "follow" the ions, the plasma self-establishes an electric field to allow sufficient cross-field transport. Incidentally, this electric field also hinders the movement of the ions, and the response of both populations ensures that current continuity is satisfied. The plasma potential will also react to the gradient of electron pressure, which can play a significant role considering the values of density and temperature there.

The Hall parameter also explains the large temperatures seen outside the thruster, which can be directly tied to the azimuthal electron current, shown in Fig. 7.22(d). The smaller temperature peak in the channel, when compared to Case 1, is related to the fact that the axial (or

perpendicular) electron current is ultimately lower due to the lack of anomalous transport, which is reflected in a lower peak value of the azimuthal current in the channel (where neither Case 1 nor Case 2 present any anomalous transport) and less resistive heating in that region. Nonetheless, the overall heating power is much larger in Case 2 than in Case 1, as seen in Table 7.6.

The gas expansion terms in the electron energy balances also present much larger values in Case 2 than in Case 1. This can be linked with the rise in electron temperature outside the thruster, coinciding with the region where energy is expended to expand the gas.

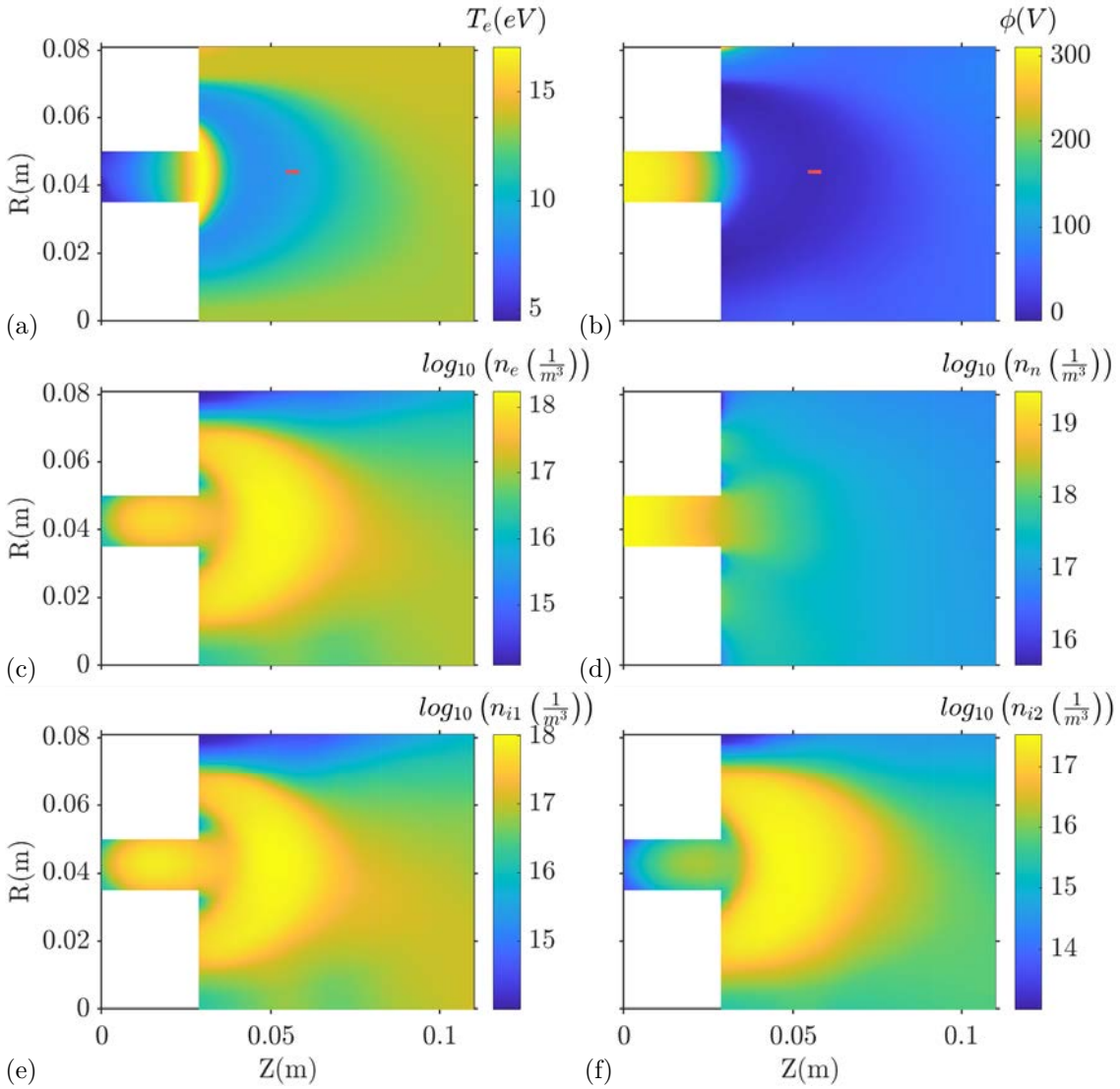

Figure 7.19: Global-mean 2D maps of (a) T_e, (b) ϕ, (c) n_e, (d) n_n, (e) n_{i1}, (f) n_{i2} for Case 2 of HYPHEN results (Table 7.4); volumetric cathode element (also, potential reference point) is shown in red in subfigures (a) and (b)

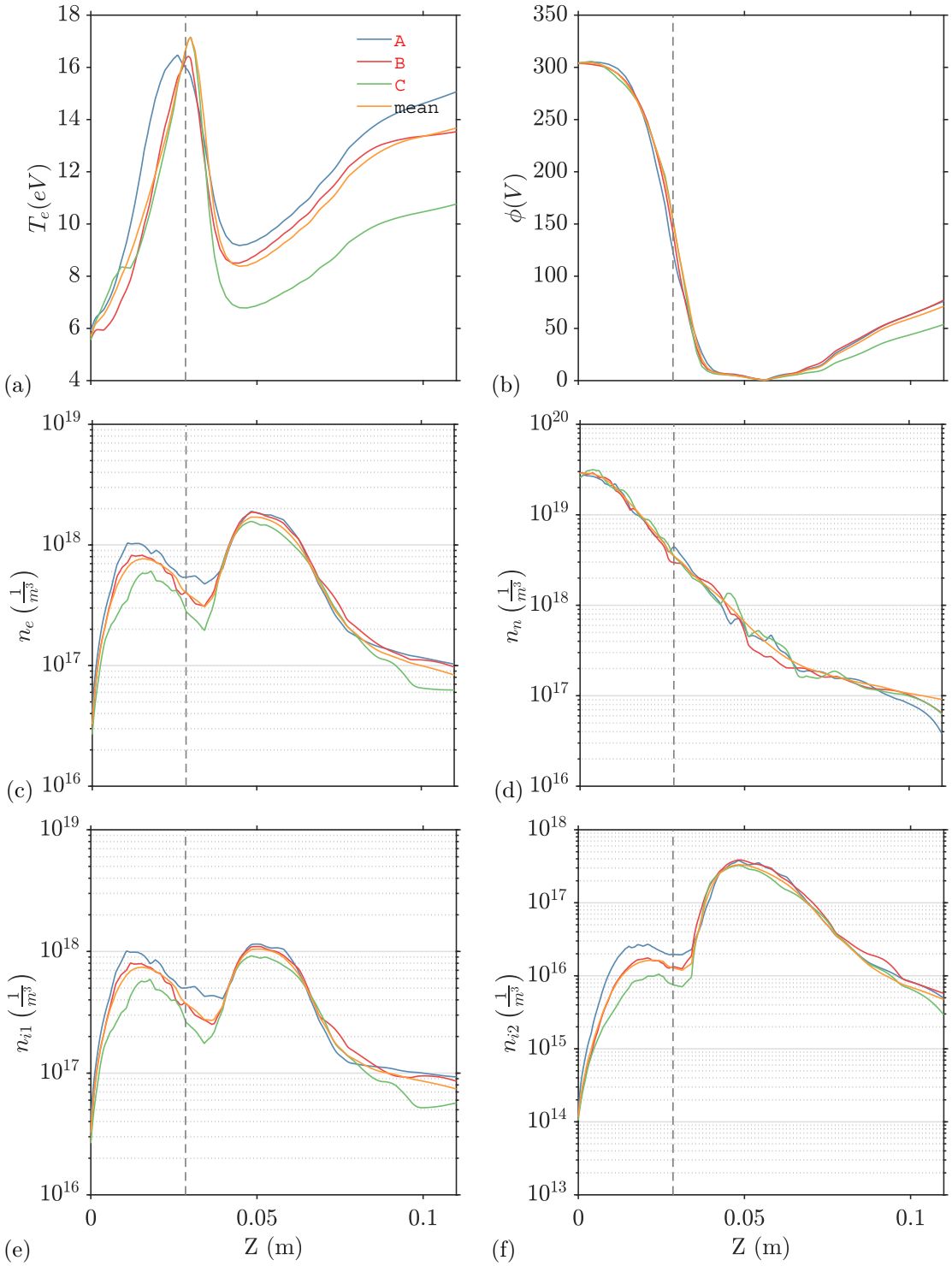

Figure 7.20: 1D profiles of (a) T_e, (b) ϕ, (c) n_e, (d) n_n, (e) n_{i1}, (f) n_{i2} at TCL, corresponding to time-steps A, B, C from Fig. 7.18 and global-mean profiles for Case 2 of HYPHEN results (Table 7.4); (- - -) marks the channel exit

Some final comments on the 2D maps presented in Fig. 7.19: the peculiar shape of the densities of the various populations is a direct result of the ion streamlines turning back toward the thruster walls (also seen in Fig. 7.22) due to the electric potential field; this also explains the lower density in the domain axis. The back-flow of ions is seconded by the two local peaks of neutral density that may be appreciated in the outer an inner pole covers, which can only appear due to ion recombination. Note that the double-ion density is now larger than in Case 1 and comparable in value to the single ion density. This also explains the larger energy sink due to the single-to-double ionization reaction, seen in Table 7.6. Lastly, the upper left corner of the domain shows a large electric potential which appears because said region presents a local increase in magnetic field intensity (seen in Fig. 7.4 as the larger density of magnetic field lines in that region). Since the density of all species is low in that corner, a localized rise in the Hall parameter must be present, and thus the plasma self-establishes the electric potential in order to maintain current continuity. The phenomenon in the upper left corner is accompanied by a local increase in electron temperature.

The 1D profiles in Fig. 7.20 add little to what has already been mentioned, with the exception of the fact that a much larger variability exists among the low, mid and high I_d time-steps, particularly in the electron temperature profile. It is possible that the anomalous transport dampens out some of the modes in the discharge oscillations although it is difficult to say without further analysis of the existing frequencies; since this solution is not considered physical, further insight into this matter has not been deemed valuable.

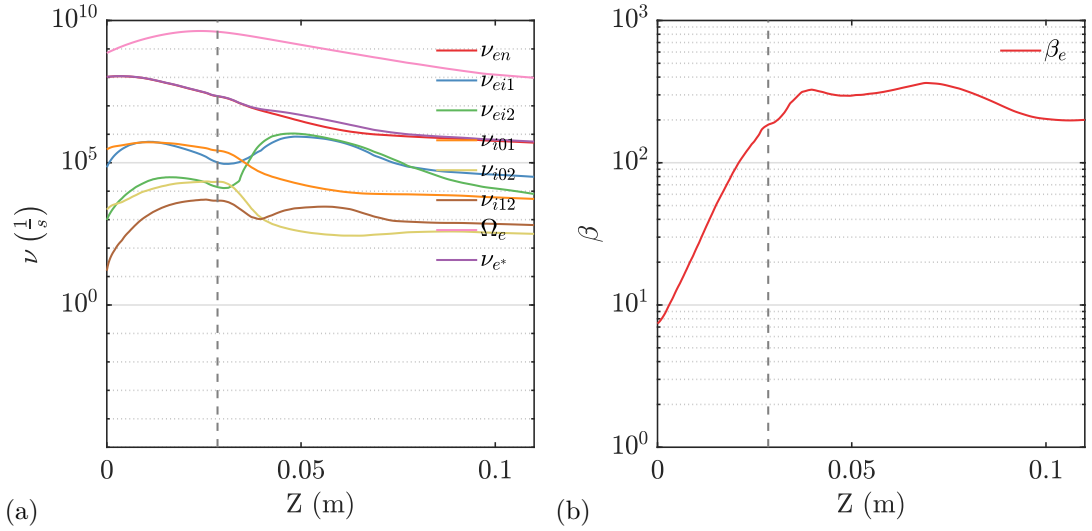

Figure 7.21: (a) Global-mean collisional, ionization, gyro, anomalous and total-effective frequencies and (b) total and total-effective Hall parameter at TCL for Case 2 of HYPHEN results (Table 7.4); (- - -) marks the channel exit

The frequencies of the physical processes in the discharge for Case 2, shown in Fig. 7.21, are not unusual considering the densities of the various populations and the electron temperatures. It is worth noting that the frequencies are dominated by the electron-neutral elastic collisions

throughout the simulation domain, in comparison to Case 1 in which the electron-ion collisions became comparable to the previous ones close to the Far-Field boundaries.

Figure 7.22 presents the global-mean of the current streamlines for Case 2. The ion current back-flow toward the outer and inner pole covers has already been discussed. In this case, the electron currents present a much smoother appearance than in other cases, particularly, in the region between the cathode and the channel exit. These currents possibly align better with expectations of how the electron population should behave. It is possible that the solution of the continuity equation is affected by the addition of anomalous transport or that the larger plasma density and ion currents in the region have a stabilizing effect over the current density vectors; further trials with other configurations will be sought out in the future to fully characterize this phenomenon.

Lastly, the total currents present a similar look to the ones for Case 1. Some coherent structures still exist in the region downstream from the cathode, although the current continuity is satisfied in the domain with the same error value detailed in Case 1; the comments made there are also applicable here.

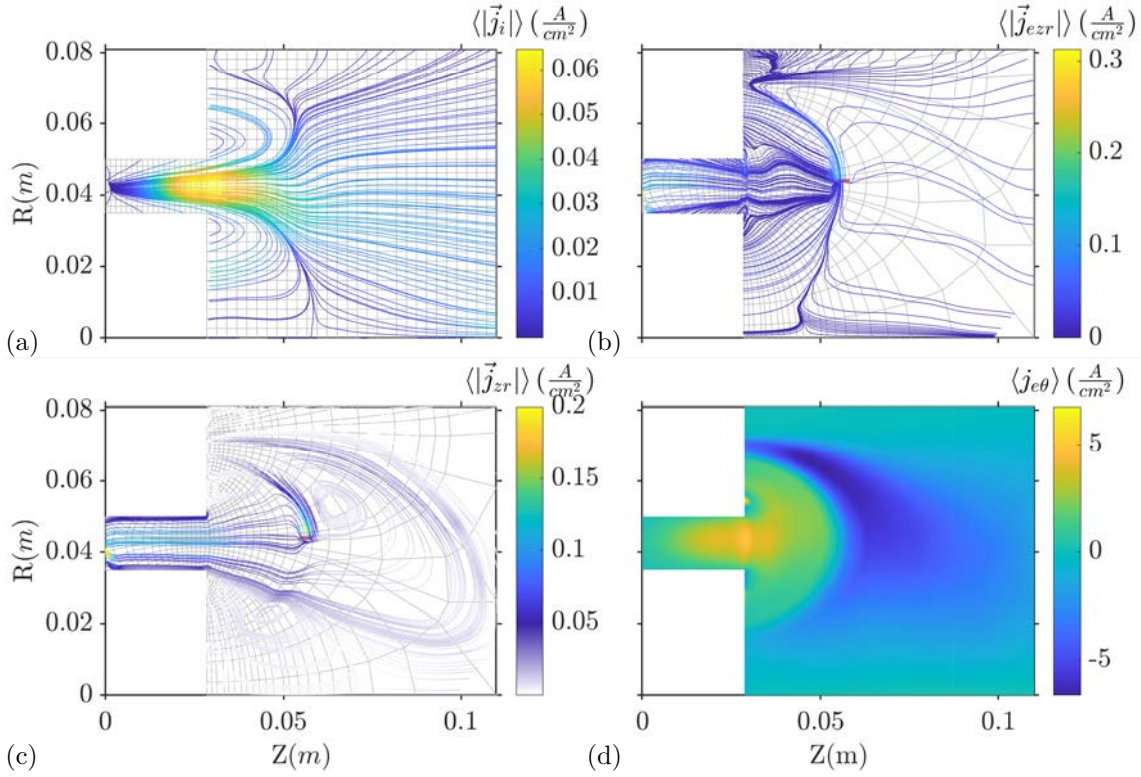

Figure 7.22: Global-mean streamlines of (a) $\vec{j}_i$, z-r plane components of (b) $\vec{j}_e$ and (c) $\vec{j}$, and (d) azimuthal electron current for Case 2 of HYPHEN results (Table 7.4); volumetric cathode element (also, potential reference point) is shown in red in (b)

Closing this section, we provide results to characterize the anode and dielectric sheaths in Case 2. The profiles along the wall are decidedly different, although this is undoubtedly a consequence of the different temperature, density and ion-current maps presented by the plasma, all of which have larger values in the region outside of the thruster. The sheath potential drop does not rapidly decay outside of the thruster as happened in Case 1, but remains constant and even increases due to the temperature peak in the upper left corner. Both the energy deposited and the SEE current density respond clearly to the increase in ion current past the channel exit, which appear as two secondary peaks of these quantities in the outer and inner pole covers. It is worth noting that the anode energy deposition in the sheath is smaller due to the lower incident electron current, which is also reflected by a lower sheath potential drop (compared in Table 7.8).

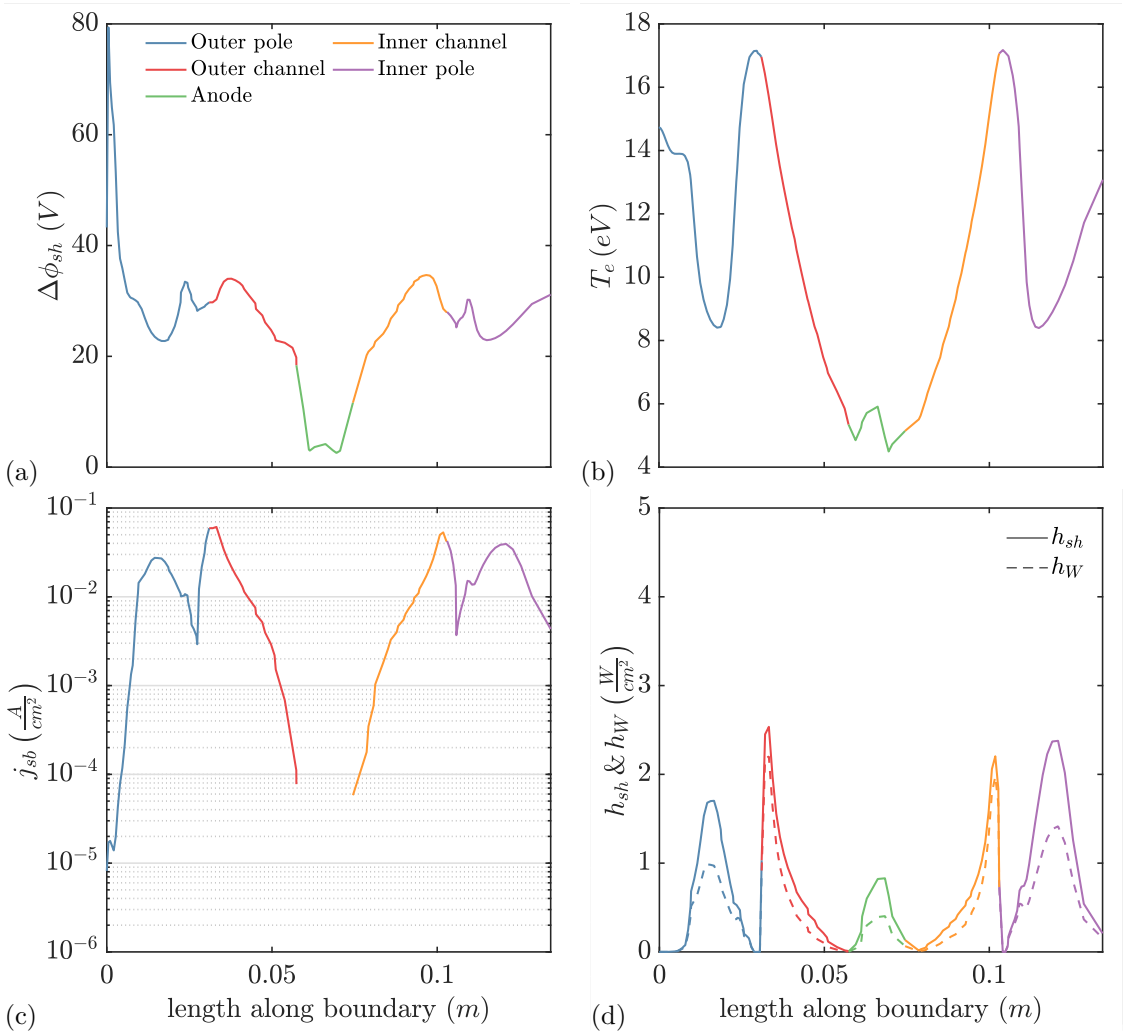

Figure 7.23: Global-mean profiles of (a) $\Delta\phi_{sh}$, (b) T_e, (c) g_{sb} and (d) h_{sh} & h_W along physical walls for Case 2 of HYPHEN results (Table 7.4); note that the anode boundary has no SEE

7.2.3 Case 1SP

Case 1SP will only be commented briefly and only from the perspective of the changes introduced as a result of the existence of the magnetic field singular point in the NAR; many of the arguments presented in this section are done in reference to the data provided in Section 7.3. Note that the anomalous collision frequency factor and the position of the cathode element have been kept as similar as possible to Case 1, to allow for a direct comparison.

Figure 7.24 presents the time-averaged discharge current and the total ion current as well as the FFT analysis performed for the latter; by comparison, the breathing mode presents a higher frequency, of $\mathcal{O}(30kHz)$, than Case 1 and possibly a larger amplitude. The NAR undoubtedly plays a large role in this mode, since it also coincides with the ionization region. The dynamics leading to the appearance of the mode are complex and the rationale for the increased mode frequency is not ultimately clear. Nonetheless, this result is contrary to the results presented by Ref. [202], in which a SPT-100 thruster configuration with a trim coil was simulated, which appear to show that the breathing mode amplitude is reduced due to the appearance of the singular point. The results were likened to the ones for the ATON-class HET reported by Touzeau[304] and Morozov[36], although the low-amplitude oscillations seemed to be driven by the operation of the thruster at lower discharge voltage instead of the singular magnetic topology. Regardless, the influence of the singular point on the anomalous transport is also not clear, so the discussion is purposeless without additional experimental results for comparison.

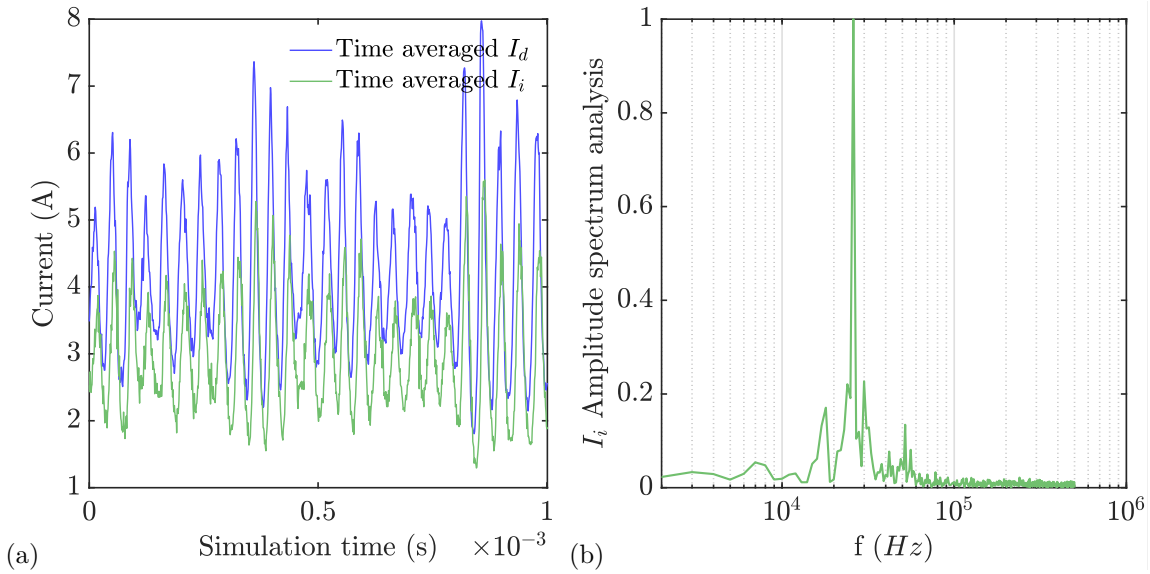

Figure 7.24: (a) Time-averaged discharge Current, I_d, and Ion Beam Current, I_i, and (b) FFT normalized amplitude spectrum analysis for time-averaged I_i for Case 1SP of HYPHEN results (Table 7.4)

Focusing on the NAR, Fig. 7.25 shows that, while the various frequencies associated to physical processes take values similar to the reference case (with the exception of the ionization frequencies close to the domain exit, which exhibit larger values, due to a larger electron temperature), the

Hall parameter is decidedly different, due to the drop in magnetic field intensity caused by the singular point. This has two effects: first, the discharge current is larger than for Case 1, as seen in Table 7.8, and, particularly, the overall axial electron current is also larger, as seen in Fig. 7.30(c); this is a consequence of the lower magnetic confinement in the NAR, whose effects are felt throughout the whole discharge, due to the continuity equation. Second, the lower Hall parameter in the NAR reduces the azimuthal current value and, with it, the resistive heating term and the electron temperature; this effect is presented in Figs. 7.19, 7.30(d) and 7.29(a). Incidentally, the larger overall axial (or perpendicular) current and hall parameter at the channel exit (which takes the same value as in Case 1) implies that the peak temperature is larger in Case 1SP, which leads to a slightly larger ion density and ion beam current (Table 7.8).

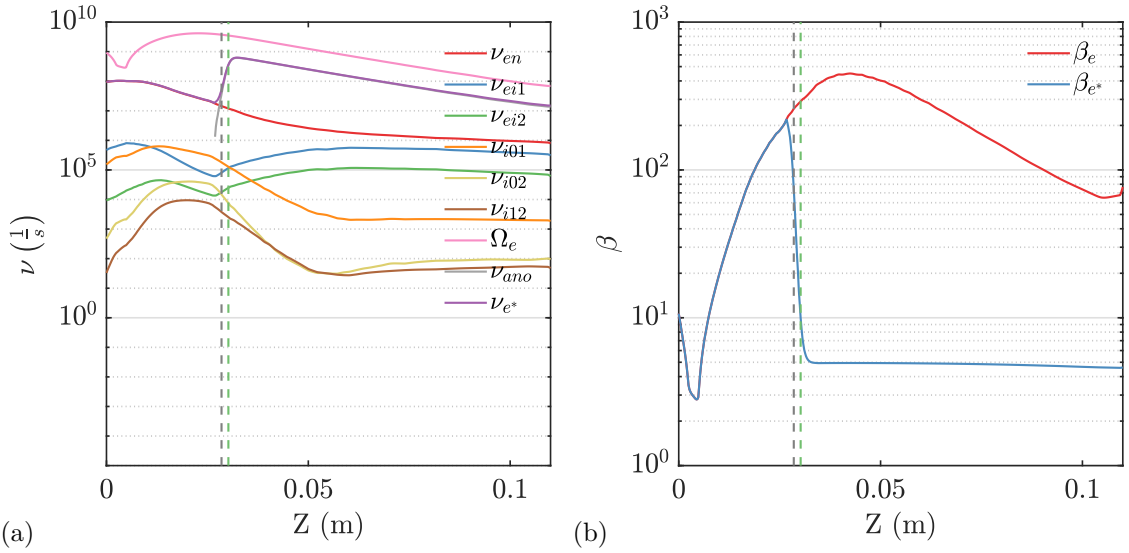

Figure 7.25: (a) Global-mean collisional, ionization, gyro, anomalous and total-effective frequencies and (b) total and total-effective Hall parameter at TCL for Case 1SP of HYPHEN results (Table 7.4); (- - -) marks the channel exit

The electric potential is very similar to the reference case although Fig. 7.29(b) shows that there is a larger potential drop between the maximum established and the anode potential, which increases the ion-backflow and the value of ion current reaching the anode, presented in Table 7.8. This is related to the effect of the positive axial gradient of magnetic field intensity on the plasma potential, which is steeper and occurs further downstream from the anode as seen when comparing Figs. 7.4(b) and 7.6(b). The ion stream-lines show that this ion back-flow now represents a larger portion of the channel than in Case 1.

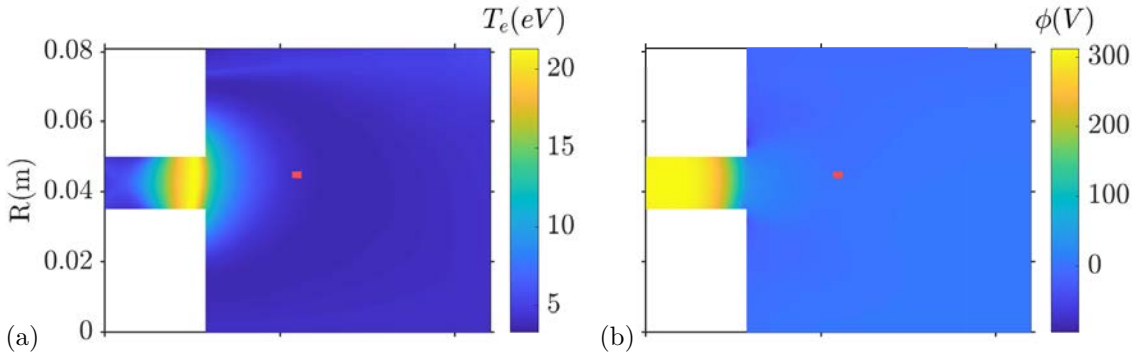

Figure 7.26: Global-mean 2D maps of (a) T_e, (b) ϕ for Case 1SP of HYPHEN results (Table 7.4); volumetric cathode element (also, potential reference point) is shown in red

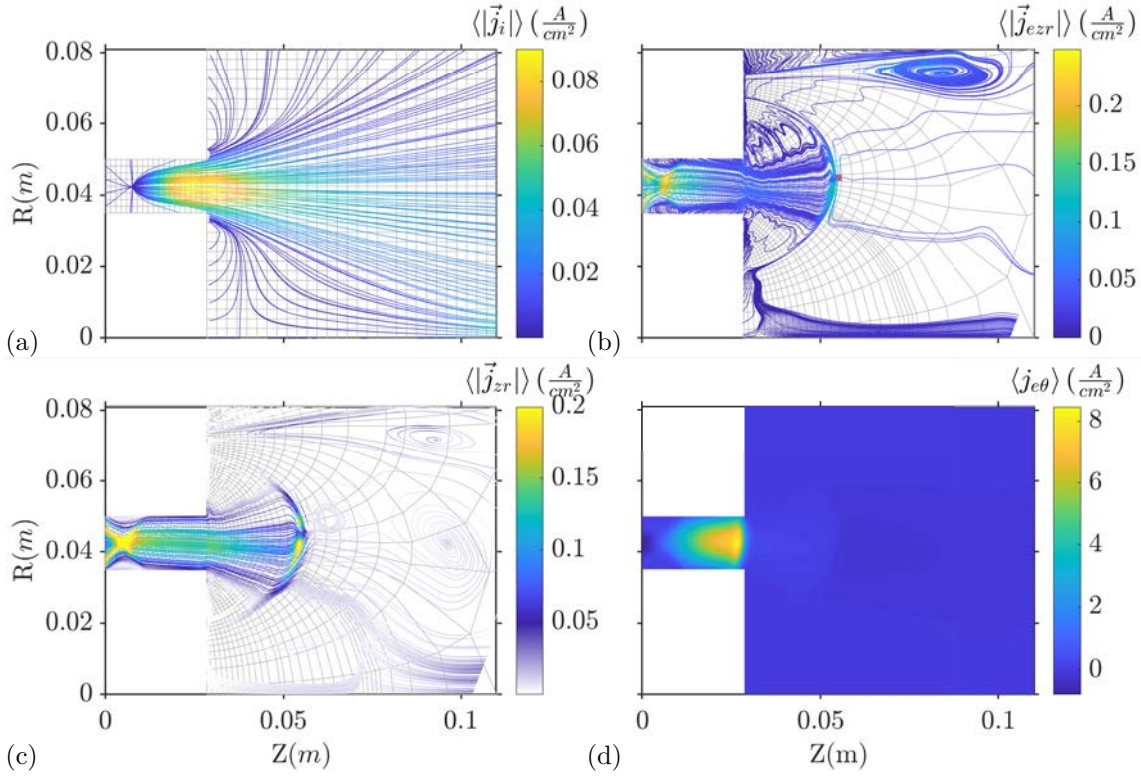

Figure 7.27: Global-mean streamlines of (a) $\vec{j}_i$, z-r plane components of (b) $\vec{j}_e$ and (c) $\vec{j}$, and (d) azimuthal electron current for Case 1sp of HYPHEN results (Table 7.4); volumetric cathode element (also, potential reference point) is shown in red in (b)

Finally, the electron and total current streamlines are also shown in lieu of the discussion around the singular point: Fig. 7.27 shows how the magnetic field lines adopt a sort of "nozzle throat" configuration in the dielectric walls of the NAR and a magnetic shielding configuration on the anode itself; even though the magnetic field intensity is small in this region ($\sim 0.005T$, or

$\sim 50G$), the model responds by curving the electron streamlines in order to preferentially follow the magnetic field lines; note that the sudden drop in axial electron current shown for the TCL in Fig. 7.30(c), near the anode region, responds precisely to the current being diverted because of the shielding there. However, this effect is not reproduced in the ion streamlines since the electric field is not affected, as the singular point coincides with a region of low Hall parameter; the total plasma current, on the other hand, clearly reproduces the "choking" shape. Note that, as in Case 1, the electron current streamlines present a largely oscillating profile in the region between the cathode and the channel exit.

The results shown here provide confidence that HYPHEN is capable of correctly resolving a magnetic field configuration with singular points within the simulation domain and, incidentally, add a condition for future trials on magnetic shielding configurations: these will only be effective as long as the Hall parameter, representing magnetic confinement, is large enough for the plasma potential to be perturbed.

7.3 Case comparison

This final section provides a comparison for all of the cases simulated based on the overall engine performances, Table 7.7, and total current distributions and sheath potentials, Table 7.8. The energy balances for the electron population, Table 7.9, provide additional insight into how the physical response of the electron population (electron temperature, plasma potential, ionization rates, etc.) impact the simulated thruster performances. Finally, the electric energy balance, Table 7.10, and the global energy balance, Tables 7.11, 7.12 and 7.13, offer further confidence that HYPHEN operates in an energy conserving way and offer a global view of the energy flows among the various species.

In relation to thruster performances, engine Thrust, I_{sp} and anode efficiency have been calculated using the expressions for both the "heavy-species" and "electromagnetic" thrust, Eq. (7.2). A certain bias is exhibited in Table 7.7 showing that, with the exception of Case 2, performances calculated from the electron population data are always better than the ones using the PIC data, and in some cases differ greatly between them. The source of this bias is not easily identifiable; it may be related to interpolation errors between the meshes or, possibly, to discretization errors in the FVM for NOMADS, which lead to assuming that the current at the center of a volume element is representative of the whole element. Trials for coherent mesh refinement on both meshes can be carried out in the future to attempt bias reduction.

Another comment worth mentioning is that the divergence efficiency, η_{div}, is unusually high (with the exception of Case 4) considering experimental results for HETs[305, 306]. This could be tied to the particular plasma potential profile obtained for these simulations, since, in most cases, the acceleration zone occurs completely within the thruster channel; possibly, a solution such as the one presented in Cases 2, 3 and 4 is more realistic from this particular perspective, although other issues appeared there. It is also possible that the size of the simulation domain is slightly constricting in the development of the full divergence angle of the plume; larger simulation domains will be trialled in future tests.

In relation to the power balances, a few general comments can be made: the electron population energy imbalances in the simulated cases are of the same order (and lower, in general) than the imbalance in Case 1, which, as was already discussed in Section 7.2.1, would be responsible for very small changes in the electron temperature for each element volume in the MFAM. The electric energy imbalances are very small, lower than 1% (as a percentage of discharge power, P_d) in all cases, which is an exceptional result. Lastly, the global energy balances peak at a 5% error (as a percentage of P_d), which can be attributed in part to the electron population imbalance, but are also tied to the fact that these balances account for the heavy-species populations, modeled in the PIC segment. Typically, this method is prone to certain inaccuracies in energy conservation due to numerical noise and errors committed in the particle weighting process, which are also exacerbated by potential interpolation issues between the MFAM and the PIC mesh (which were discussed in Section 6.8). Overall, we consider that this result is valid. Future efforts will be focused on further reducing this imbalance, solving some of the controversies that have already been identified.

If Section 7.2 was devoted to an in-depth study of the physics of the simulated plasma for various conditions, this section provides a "by-case" analysis of the results. Although the physical response will not be commented in great detail, a compilation of the most relevant 1D profiles for the plasma quantities is provided: Fig. 7.28 shows the mean total effective Hall parameter for all cases, Fig. 7.29 presents the mean electron temperature, plasma potential and plasma and neutral species densities and Fig. 7.30 offers the mean profiles for the ion current, the electron current modulus and electron axial and azimuthal currents.

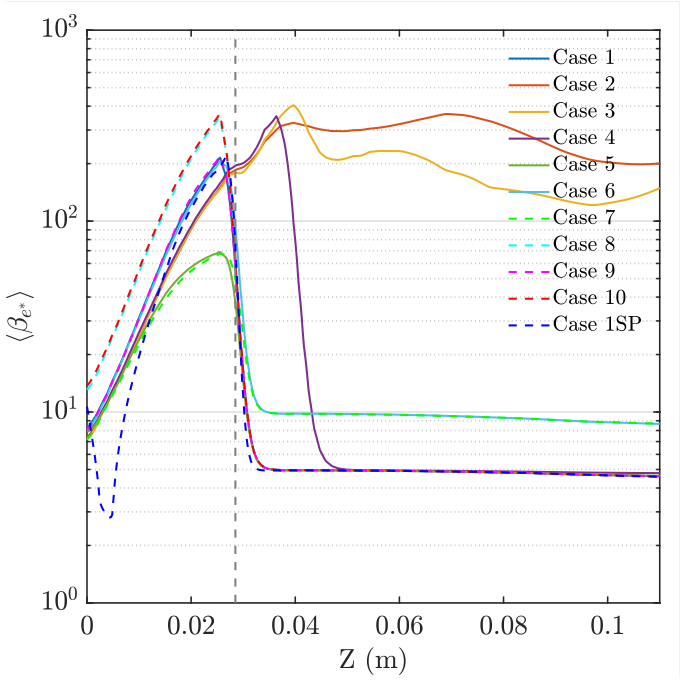

Figure 7.28: 1D profile comparisons for Cases referenced in Table 7.4 of total effective Hall parameter, β_{e^*}; (- - -) marks the channel exit

The following comments are made for each of the individual cases; explicit references to each of the figures and tables in this chapter are avoided for the sake of brevity and we recommend the readers to familiarize themselves with them prior to diving into this analysis.

- **Case 1** was chosen as a reference since its performance values fall within 10% discrepancy (the largest disparity is in the discharge current and power) with the nominal operating values of the SPT-100[38], which was deemed acceptable for this parametric analysis.

- **Case 2 and 3** represent a non-physical solution, due to the lack of anomalous transport. Case 2 was analyzed in detail in Section 7.2.2. Both the temperature and plasma potential profiles increase downstream from the neutralization region, which is not coherent with experimental results; this leads to a large energy lost to advection on the Far-Field boundary and to the plasma density peaking around the plasma potential minimum. The Hall current plays a large role in the near-plume region in these cases: since the azimuthal current reverses downstream from the neutralization region and is large, its contribution to the Lorentz force over the magnetic circuit will be to reduce the thrust; in reality, the anomalous transport must contribute largely to hindering the development of a significant azimuthal drift current in this region. Cases 2 and 3 differ only in the use of a non-zero α_Q or not, which in Case 3 leads to a less smooth electron temperature solution, which has an effect over the remaining plasma quantities.

  From the perspective of performances, they are both clearly non-representative of a normal operation of the device, with low thrust and I_{sp} and meager efficiencies. This is true for all of the partial efficiencies and, in particular, for the production efficiency, which is lower due to a larger ion current reaching the material walls (versus the ion beam current), stemming from the particular plasma potential map. The sole exception is the current efficiency, which is larger than in the other cases since the lack of anomalous transport implies that ion and discharge currents will be more alike.

- **Case 4** was discussed briefly in Section 7.2.1. The position of the step in the function used for α_{ano} was moved downstream from the channel exit, while the values of the function remain equal to those in Case 1. Similarly to Cases 2 and 3, the plasma potential profile within the channel is less steep and continues to fall past its exit. The temperature within the channel is also similar to those two cases and smaller than the other cases, although the temperature peak is the largest in the parametric investigation due to the relatively large Hall current immediately downstream from the channel exit (which is a consequence of the Hall parameter). The density profile "shifts" downstream in the acceleration channel, compared to the reference case, which is a combination of the lower channel temperature and the plasma potential profile. Nonetheless, the plasma density is higher at the channel exit than in Case 1, which, coupled with a lower neutral density downstream from the thruster (but larger in the channel) signals a large ionziation rate near the exit. While the overall energy spent in ionization is similar in Cases 4 and 1, the ion beam current (and the partial single and double ion currents) is larger than in the reference, which reflects into a larger production and utilization efficiencies.

The fact that the acceleration region is partly outside of the thruster is responsible for the lower divergence efficiency (in comparison to others); when coupled to the lower peak density in the channel, this leads to reducing the ion current density in the TCL. However, this is positively reflected in the ion current deposited in the dielectric wall, which is smaller than in Case 1 and leads to less power deposited in the sheath by the electron population. The sheath potential drop in the dielectric, however, remains high due to the large electron temperature.

Lastly, the current efficiency is unrealistically high, due to the discharge current being only slightly above the ion beam current.

- **Cases 5 and 7** add a 1% for the anomalous transport factor in the thruster channel. Case 5 maintains the value of 20% outside the thruster while Case 7 reduces it to 10%. This is translated to a lower peak value of the Hall parameter near the thruster exit, in comparison to other cases; on the other hand, the Hall parameter converges to the values of the remaining simulations in the NAR, where the magnetic field intensity is small (together with the electron gyrofrequency) and thus becomes dominated by the collisional processes. A lower peak Hall parameter leads to a lower azimuthal Hall current, although, in this case, it is offset by the fact that the thruster draws a larger axial electron current (responsible for the much larger discharge current in these cases). Again, this occurs because, even though the change in α_{ano} was only made for the thruster channel, current continuity ensures that it becomes a global effect. The plasma potential profile reacts to reflect said effect, in this case by changing the slope in the region between the cathode and the channel exit. Outside the thruster, the β_{e^*} in Case 5 coincides with that of other cases, although Case 7 presents a value similar to the one of Case 6, due to the anomalous transport factor past the channel exit.

  The overall effect is that the electron temperature peak in Cases 5 and 7 is smaller than in the reference case and smaller that what is reported experimentally and by other simulations, although the temperature past the channel exit is slightly larger in Case 7. The channel temperature, on the other hand, coincides with the other cases. In view of the results, the overall ionization rate must be similar to Case 1, which is corroborated by the single and double ion beam currents exiting the device, as well as the thrust and I_{sp}, when compared to the reference.

  In general, the thruster performances in both cases are comparable to Case 1, with the exception of the discharge current (and thus, current efficiency), which are not in line with operational values. It is worth noting that the values for I_d are much more affected by the change in α_{ano} than the remainder of the performance parameters, which implies that there is a sort of "saturation" effect for the discharge current in the simulation, with regards to the production of net thrust. Focusing on the electrical power balance, the work of the electric field over the ions is similar to other cases (as is the power lost to ionization), but not so the work of the electric field over the electrons, meaning that the thruster is devoting extra power to simply moving the electron current along, without a positive net effect on the performances.

- **Case 6** Explores the effect of a lower α_{ano} downstream from the channel exit, by lowering it to 10%, in comparison to the 20% of Case 1. Te main consequence of lowering α_{ano} downstream from the channel exit is lowering the axial electron current, which reduces the Hall current and the electron temperature. As in cases 5 and 7, the performances differ very slightly from the reference case, although in Case 6 the discharge current only varies slightly; this implies that the sensibility of the solution to the value of α_{ano} *outside* of the thruster is smaller than within the channel.

- **Case 8** retains the α_{ano} profile from the reference but uses the experimental data by Hayashi[259] for the electron-neutral elastic collision frequency. This model affects both the resistive heating term in the electron population (since the electron-neutral resistivity is the dominant term) as well as the electron cross-field transport. This reflects both in the lower discharge current (which implies a larger current efficiency), compared to the reference case, and the lower ion beam current and ion production (characterized by a smaller value of the energy spent in ionization and excitation). In a positive contrast, this leads to less ions being neutralized at the dielectric walls of the channel, and a higher production efficiency, although the fact that the acceleration zone is shifted upstream in the channel will undoubtedly play a role in this.

  Although the Hall parameter takes a larger value within the thruster channel, it is not compensated by the lower axial electron current, leading to a smaller Hall current than in Case 1, and an expected smaller peak electron temperature. Since the data by Hayashi for the electron-neutral collisions is obtained from experimental results, the Mitchner & Krueger model represents an over-estimation in comparison. The reader may doubt the capacity for the code to correctly reproduce the discharge without the added "collisionality" of the latter model; however, it would be possible to increase the anomalous transport collision frequency in the thruster exit to achieve a larger axial electron current that compensates for the use of the Hayashi model, therefore yielding results that are more in line with what is expected. Since α_{ano} is a "free" parameter in the simulation (within certain reasonable values) this should be seen as a means to ultimately adapt the results, if more realistic values for the ancillary models become available.

- **Cases 9 and 10** explore the effects of a lower thermalization fraction, σ_{th}, in the sheath model for the dielectric walls. Case 10 also uses the Hayashi data for the electron-neutral collision frequency, which makes it comparable to Case 8. The consequences of lowering σ_{th} are subtle: the power lost to the dielectric walls is slightly smaller, which allows more of the resistive heating power to be spent in ionization and excitation, which explains the larger ion beam and discharge currents, as well as the larger thrust.

  The major apparent change is in the average sheath potential drop in the dielectric wall. The change in the thermalization fraction implies that a smaller portion of the energetic tails of the EVDF is replenished. The sheath model reacts by lowering the potential drop, so that sufficient electrons reach the wall without being electro-statically reflected, in order to ensure null net current. The overall energy deposition, however, remains similar in both

cases. This response of the sheath model is coherent with the sheath model characterization presented in Section 5.1.4.

The value for the thermalization fraction could be further tuned through experimental results for the wall potential. A correct modeling of this quantity is important for certain types of simulations, specially those in which the energy deposited by the ions to the wall is relevant, such as those looking to obtain the sputtering behavior of the material walls in the thruster.

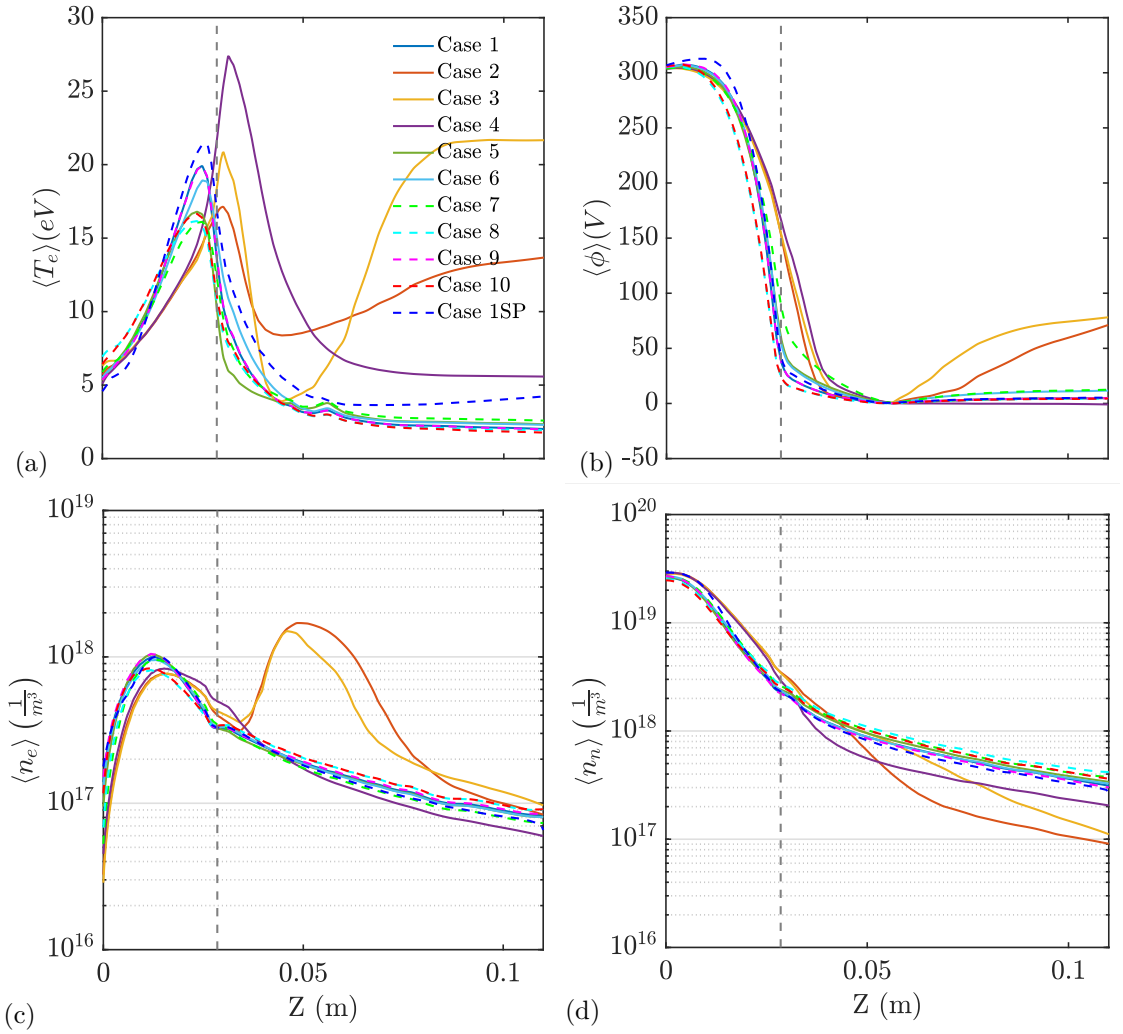

Figure 7.29: 1D profile comparisons for Cases referenced in Table 7.4 of (a) electron temperature, (b) plasma potential, (c) electron density (d) neutral species density; (- - -) marks the channel exit

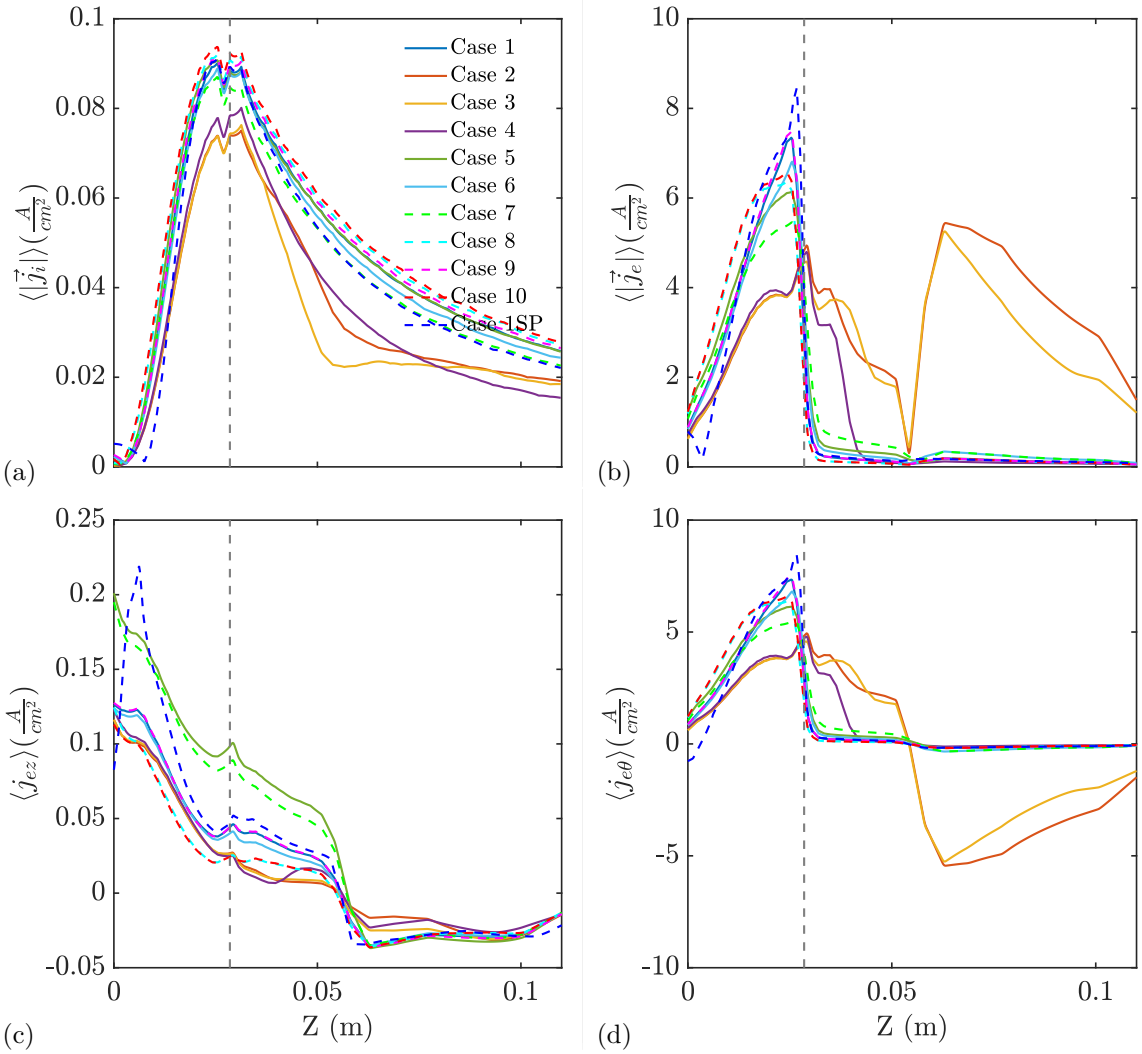

Figure 7.30: 1D profile comparisons for Cases referenced in Table 7.4 of (a) total ion current, (b) total electron current, (c) axial electron current and (d) azimuthal electron current; (- - -) marks the channel exit

Case	$\mathbf{P_d}$	$\mathbf{T_e}, \mathbf{T_{hs}}$	$\mathbf{I_{sp_e}}, \mathbf{I_{sp_i}}$	$\eta_{\mathbf{a_e}}, \eta_{\mathbf{a_{hs}}}$	$\eta_{\mathbf{utiliz}}$	$\eta_{\mathbf{curr}}$	$\eta_{\mathbf{prod}}$	$\eta_{\mathbf{div}}$
1	$1213.8W$	$76.2, 72.1mN$	$1556, 1472s$	$0.48, 0.44$	0.74	0.73	0.70	0.97
2	$950.4W$	$51.3, 56.8mN$	$1047, 1160s$	$0.28, 0.34$	0.67	0.83	0.50	0.96
3	$953.4W$	$55.6, 54.3mN$	$1135, 1103s$	$0.33, 0.32$	0.72	0.90	0.63	0.94
4	$993.6W$	$74.3, 67.9mN$	$1515, 1384s$	$0.56, 0.49$	0.80	0.97	0.74	0.87
5	$1695.4W$	$77.0, 72.5mN$	$1571, 1480s$	$0.35, 0.32$	0.73	0.51	0.71	0.97
6	$1167.3W$	$74.3, 70.8mN$	$1516, 1444s$	$0.47, 0.46$	0.75	0.76	0.70	0.94
7	$1584.1W$	$73.6, 69.6mN$	$1503, 1421s$	$0.34, 0.31$	0.72	0.53	0.72	0.96
8	$988.6W$	$71.2, 68.3mN$	$1455, 1393s$	$0.51, 0.51$	0.72	0.87	0.78	0.97
9	$1216.4W$	$77.7, 73.5mN$	$1585, 1499s$	$0.49, 0.45$	0.75	0.73	0.69	0.97
10	$1003.3W$	$73.8, 70.0mN$	$1499, 1428s$	$0.54, 0.50$	0.74	0.86	0.76	0.97
1SP	$1246.0W$	$75.0, 72.2mN$	$1530, 1473s$	$0.45, 0.45$	0.75	0.74	0.67	0.95

Table 7.7: Global-mean thruster performances for Cases referenced in Table 7.4

Case	$\mathbf{I_d}$	$\mathbf{I_i}$	$\mathbf{I_{i1}}$	$\mathbf{I_{i2}}$	$\mathbf{I_{e_{anode}}}$	$\mathbf{I_{i_{anode}}}$	$\mathbf{\Delta\phi_{sh_{anode}}}$	$\mathbf{I_{i_{dielec}}}$	$\mathbf{\Delta\phi_{sh_{dielec}}}$
1	$4.05A$	$2.89A$	$2.56A$	$0.32A$	$-4.13A$	$0.08A$	$3.96V$	$1.0A$	$26.36V$
2	$3.17A$	$2.62A$	$2.33A$	$0.29A$	$-3.18A$	$0.01A$	$3.2V$	$1.48A$	$40.8V$
3	$3.18A$	$2.86A$	$2.47A$	$0.39A$	$-3.19A$	$0.01A$	$3.4V$	$1.49A$	$38.3V$
4	$3.31A$	$3.16A$	$2.73A$	$0.39A$	$-3.32A$	$0.02A$	$2.8V$	$0.88A$	$38.7V$
5	$5.65A$	$2.84A$	$2.53A$	$0.31A$	$5.70A$	$0.05A$	$2.79V$	$0.97A$	$24.8V$
6	$3.89A$	$2.9A$	$2.57A$	$0.33A$	$-3.96A$	$0.07A$	$3.58V$	$0.96A$	$28.4V$
7	$5.28A$	$2.8A$	$2.51A$	$0.29A$	$5.3A$	$0.02A$	$3.17V$	$0.87A$	$27.1V$
8	$3.29A$	$2.8A$	$2.52A$	$0.28A$	$-3.32A$	$0.03A$	$4.2V$	$0.63A$	$25.6V$
9	$4.06A$	$2.94A$	$2.60A$	$0.33A$	$-4.1A$	$0.09A$	$4.1V$	$1.0A$	$17.9V$
10	$3.34A$	$2.85A$	$2.57A$	$0.28A$	$-3.40A$	$0.05A$	$4.6V$	$0.7A$	$17.8V$
1SP	$4.15A$	$2.97A$	$2.59A$	$0.38A$	$-4.34A$	$0.19A$	$5.64V$	$1.1A$	$25.5V$

Table 7.8: Global-mean discharge current, total and partial Ion Beam currents, electron and ion currents toward material walls and sheath potential drop for Cases referenced in Table 7.4

A few conclusions may be drawn from the parametric investigation, in way of a short summary: the analysis presented in this chapter was intended to provide sufficient insight into the physical response of a HET and how the various models we have implemented interact and are ultimately responsible for the overall simulated performance and response of the thruster. On this occasion, we have simulated an SPT-100 configuration in order to perform the analysis, and also to demonstrate that performance values and plasma quantities can be reasonably approximated with HYPHEN. However, it is clear that there is a high degree of coupling between all of the variables that govern the plasma discharge and that simulations are a, decidedly, inverse problem, where the final response of the thruster to the various simulation conditions and parameters is difficult to quantify a priori.

Case	$\mathbf{P_{adv_e}}\vert_{\mathbf{FF}}$	$\mathbf{P_{sh_e}}\vert_{\mathbf{AB}}$	$\mathbf{P_{sh_e}}\vert_{\mathbf{D}}$	$\mathbf{P_{exp_e\top}}$	$\mathbf{P_{exp_e\parallel}}$	$\mathbf{P_{heat_e}}$	$\mathbf{P_{inel_e}}$	$\langle\mathbf{Err}\rangle$	$\mathbf{P_{cath}}$
1	−9.8	−58.6	−215.3	−88.2	−10.6	446.9	−88.0	−23.5	13.7
2	−56.6	−21.1	−213.3	−224.1	−24.6	633.0	−113.3	−20.0	10.7
3	−95.2	−23.1	−193.5	−208.7	−14.4	624.1	−95.3	−6.9	10.7
4	−26.8	−21.6	−180.9	−132.1	−13.1	455.1	−89.2	−8.6	11.2
5	−11.3	−50.1	−165.1	−107.2	8.8	422.5	−86.2	11.4	19.11
6	−10.8	−59.1	−197.7	−90.7	−7.6	433.1	−87.6	−21.6	13.3
7	−11.7	−35.5	−134.2	−134.0	5.7	397.5	−82.4	5.4	17.7
8	−9.0	−41.5	−101.8	−115.3	0.5	348.0	−75.6	5.3	11.2
9	−9.8	−59.0	−211.5	−89.7	−11.6	442.3	−90.5	−29.8	11.2
10	−8.6	−57.3	−102.5	−93.4	−6.5	329.5	−79.7	−18.5	11.4
1SP	−19.3	−67.4	−250.6	−58.9	−15.2	489.0	−92.0	−32.9	12.5

Table 7.9: Global-mean partial contributions to electron energy balance and cathode energy (all values given in W) for Cases referenced in Table 7.4

Case	$\mathbf{P_d}$	$\mathbf{P_{elec_i}}$	$\mathbf{P_{elec_e}}$	$\mathbf{P_{elec_a}}$	$\langle\vert\mathbf{Err}\vert\rangle$ (%$\mathbf{Pd}$)
1	1213.8	756.9	462.4	−16.9	3.3 (0.3%)
2	950.4	501.2	461.4	−10.8	1.5 (0.2%)
3	953.4	465.9	494.4	−11.6	4.7 (0.5%)
4	993.6	712.1	294.5	−10.3	2.7 (0.3%)
5	1695.4	762.2	949.5	−17.3	1.1 (0.1%)
6	1167.3	724.9	459.4	−15	2.1 (0.2%)
7	1584.1	711.0	888.7	−17.9	2.3 (0.1%)
8	988.6	696.2	312.6	−15.1	5.6 (0.6%)
9	1216.4	773.8	462.0	−17.5	2.9 (0.2%)
10	1003.3	722.9	301.7	−16.7	4.6 (0.5%)
1SP	1246.0	768.1	491.4	−22.3	8.8 (0.7%)

Table 7.10: Global-mean partial contributions to electric energy balance (all values given in W) for Cases referenced in Table 7.4

The summary provided next hopefully establishes some generalities, such as:

- Many of the particularities of the plasma response can be fundamentally linked back to the effective Hall parameter profile: while the values of the different physical frequencies vary only slightly from one simulation to the other, the effective Hall parameter varies greatly with the distribution of α_{ano}, and, thus, it would be possible to have some prior qualitative knowledge of the thruster response based solely on an approximation to the resulting Hall parameter.

- The quantitative response of the thruster can only be obtained through the simulation, due to the large variability of the physical quantities resolved by our model with α_{ano}, which is far greater than that of any other variable in the parametric search.

- In general, the response of the thruster is more sensible to changes in α_{ano} within the channel than downstream from the thruster exit and can be penalized in terms of performances for imposing anomalous transport in the channel, due to the asymmetric transfer of momentum between azimuthal and axial drifts, and its effect over the resistive heating term. Additionally, it is clear that the region between the exit and the cathode is relevant: since both the ionization and acceleration regions occur mostly within the channel, the downstream region may be "primed" through a given value of α_{ano} in order to obtain responses in the channel that are in line with experimental considerations, by drawing more or less axial current from the cathode. This is a mechanistic approach to how we choose to implement different regions of anomalous transport, but informs a qualitative understanding of where and how said transport needs to develop in order to recover the experimentally measured responses of HETs. Additionally, from Cases 2 and 3, it is clear that a lack of anomalous transport downstream from the cathode leads to an increase in the plasma potential, which has not been observed experimentally. This implies that the phenomena driving anomalous transport is also present far downstream from the thruster.

- Some distributions of α_{ano} can lead to nonsensical or non-physical solutions. The search space for α_{ano} thus lends itself to being "curated" by a trial-and-error process that will typically require experimental knowledge beforehand for fine-tuning, as was the case with legacy codes.

- The plasma quantities in the NAR, electron temperature and plasma potential are more or less consistent throughout the trialed cases, although not necessarily the plasma density (due to the high sensibility of ionization rates to temperature). Potentially, this is due to a combination of the collisional regime of electrons in the region (due to high electron-neutral collision rate) and the Iterative Matching algorithm, which self-consistently adjusts the sheath response to the plasma discharge.

- The average performances of the thruster, with the exception of discharge current and power and the non-physical cases (Cases 5 and 7) are also consistent throughout the different cases. This implies that the mechanisms for generating thrust, when considering a *correct* distribution of the α_{ano} free parameter, are working close to a "plateau" region, or saturation.

- The parametric search has been done around a case which we consider to represent the thruster response adequately. A larger and more diverse parametric search would thus benefit from the general conclusions extracted here.

Case	1	2	3	4	5
$\mathbf{P_{elec_i}}$	756.9	501.2	465.9	712.1	762.2
$\mathbf{P_{inj_n}}$	1.9	1.3	1.3	1.43	1.9
$\mathbf{P_{heat_e}}$	446.9	633.0	624.1	455.1	422.5
$\mathbf{P_{inel_e}}$	−88.0	−113.3	−95.3	−89.2	−86.2
$\mathbf{P_{jet_i}}$	−723.8	−459.4	−432.9	−690.1	−731.8
$\mathbf{P_{w_i}}$	−105.9	−149.2	−108.3	−86.0	−100.9
$\mathbf{P_{b_n}}$	−16.4	−19.6	−16.0	−13.6	−15.8
$\mathbf{P_{adv_e}}\vert_{\mathbf{FF}}$	−9.8	−56.6	−95.2	−26.8	−11.3
$\mathbf{P_{w_e}}$	−223.6	−154.4	−165.2	−163.0	−164.5
$\mathbf{P_{exp_e}}$	−98.8	−248.7	−223.1	−145.2	−98.4
$\langle\vert\mathbf{Err}\vert\rangle$ (%**Pd**)	60.6 (5.0%)	44.4 (4.6%)	33.2 (3.4%)	45.3 (4.5%)	22.3 (1.3%)

Table 7.11: Global-mean partial contributions to global energy balance (all values given in W) for Cases 1-5 referenced in Table 7.4

Case	6	7	8	9	10
$\mathbf{P_{elec_i}}$	724.9	711.0	696.2	773.8	722.9
$\mathbf{P_{inj_n}}$	1.8	1.7	1.6	1.6	1.4
$\mathbf{P_{heat_e}}$	433.1	397.5	348.0	442.3	329.5
$\mathbf{P_{inel_e}}$	−87.6	−82.4	−75.6	−90.5	−79.7
$\mathbf{P_{jet_i}}$	−700.8	−686.9	−666.1	−741.1	−689.2
$\mathbf{P_{w_i}}$	−101.0	−93.2	−83.9	−91.96	−78.6
$\mathbf{P_{b_n}}$	−16.4	−14.9	−13.7	−14.4	−12.7
$\mathbf{P_{adv_e}}\vert_{\mathbf{FF}}$	−10.8	−11.7	−9.0	−9.8	−8.6
$\mathbf{P_{w_e}}$	−200.7	−120.1	−105.3	−224.1	−127.5
$\mathbf{P_{exp_e}}$	−98.3	−128.3	−114.8	−101.3	−99.9
$\langle\vert\mathbf{Err}\vert\rangle$ (%**Pd**)	55.8 (4.8%)	27.8 (1.8%)	22.6 (2.3%)	55.8 (4.6%)	42.4 (4.2%)

Table 7.12: Global-mean partial contributions to global energy balance (all values given in W) for Cases 6-10 referenced in Table 7.4

Case	1SP
$\mathbf{P_{elec_i}}$	768.1
$\mathbf{P_{inj_n}}$	1.8
$\mathbf{P_{heat_e}}$	489.0
$\mathbf{P_{inel_e}}$	−92.0
$\mathbf{P_{jet_i}}$	−741.7
$\mathbf{P_{w_i}}$	−106.2
$\mathbf{P_{b_n}}$	−16.3
$\mathbf{P_{adv_e}}\vert_{\mathbf{FF}}$	−19.3
$\mathbf{P_{w_e}}$	−266.4
$\mathbf{P_{exp_e}}$	−74.7
$\langle\vert\mathbf{Err}\vert\rangle$ (%**Pd**)	57.7 (4.6%)

Table 7.13: Global-mean partial contributions to global energy balance (all values given in W) for Case 1SP referenced in Table 7.4

CHAPTER
EIGHT

Conclusions and future work

This thesis has been oriented toward the development of the electron population module in a new Hybrid PIC-Fluid code for the simulation of weakly collisional plasma discharges under applied magnetic fields in Hall Effect Thrusters. A number of milestones and conclusions are summarized next:

- A 2D(r-z)-axisymmetric fluid model for the electron population has been implemented in HYPHEN, based on a two-temperature bi-Maxwellian closure for the mass, momentum and energy equations, and a collisional closure for the heat transport equations. The main assumptions are related to quasi-neutrality, neglecting spatial scales in the order of the Debye length, neglecting the viscous stress tensor, assuming that the thermal energy is much larger than the kinetic energy of the bulk electron motion and the use of a "free" parameter to describe the effects over electron transport associated to the azimuthal direction, wave-like phenomena and near-wall scattering: the anomalous collision frequency.

  The main difference to previous models is the anisotropic two-temperature approach, which permits taking into account the effects of magnetic field non-uniformity in electron transport and preferential heating. While the latter effect may not be of such importance in HETs, it is paramount in the simulation of other types of devices, which we hope to tackle in the near future. The model can also be solved for the isotropic case, which has been the sole focus of the results obtained in this work.

- The electron fluid model has been resolved in a 2D-MFAM. The rationale for the use of this mesh was based on an analysis on numerical diffusion in Cartesian meshes for anisotropic transport problems, which showed that, in order to avoid excessive numerical diffusion, the resolution of the transport equations should be done in a numerical mesh aligned with the preferential directions of the problem. A script was developed offering various strategies for mesh generation and correction; the quality of the mesh was assessed both from the perspective of geometric quality indicators as well as in a representative numerical problem. An ad-hoc gradient reconstruction script was also delivered, based on the well known WLSQR method. The Order-of-Accuracy of the method was checked for a representative mesh with various refinement levels and different analytical trial functions, and was found to be between first and second order, which is in line with results from the literature and is acceptable for the problem presented here.

- The electron fluid model was discretized on the numerical mesh and solved using the well

known FVM, which poses the transport equations in the strong integral form and is recommended for unstructured meshes in conservation-law type problems. Two temporal schemes were implemented: a forward Euler method and a semi-implicit scheme based both on the forward and backward Euler methods. The stability and convergence of both methods were investigated, concluding that only the semi-implicit scheme is capable of delivering coherent solutions with a reasonable computational toll.

- A new ancillary 1D-fluid model for plasma boundary layers (plasma sheaths) in material walls has been developed based on a first principles approach to the sheath's physical mechanisms. The model was expanded from previous results obtained in the EP^2 group to include anisotropicity in the primary electron population and generalized for arbitrary magnetic angles at the wall, under the assumption that the Larmor radius is much larger than the Debye length. The combined influence of the anisotropicty and the magnetic angle was found to be non-negligible, which is an important result toward reducing the number of assumptions in the simulations, in the search for more realistic results.

- The plasma sheath model for conducting (metallic) walls has been utilized to obtain a self-consistent solution of anode boundaries and the NAR in HETs, which is also a consequence of using a generalized 2D-MFAM. The solution is based on a Newton-Raphson type algorithm which iteratively matches the currents in the discharge and the currents accepted by the boundary.

- A number of different collision frequency models and experimental data from well known data repositories were compared for various types of collisions, for Xenon and Argon propellants. The frequencies were averaged over the two-temperature EPDF in order to obtain collision rates and collision energy yields. It was found that a large variability exists among the different data surveyed, which can lead to very different simulation results being recovered; the justification for the use of one or other model can presently only be done in view of said results.

- The electron fluid module was tested against a previous solution for a HET discharge obtained from legacy codes. The sensitivity of the numerical scheme was evaluated for initial conditions, time-step values and various simulation conditions, including different control schemes for the PPU, current injection modes, etc. The analysis was done from the perspective of energy balances and residuals of the plasma quantities represented by the electron population. The tests performed were oriented toward providing sufficient confidence in the electron population segment, before trialing it alongside the PIC module.

- A parametric investigation was carried out for various parameters in the simulation, mainly, the anomalous collision frequency factor, the thermalization fraction for the plasma sheath boundary condition model and the electron-neutral collision models. The analysis was done for a complete hybrid simulation, allowing the fluid and particle modules to interact and advance in time, although the kinetic Bohm condition and CEX type collisions were not included in the analysis. The backdrop chosen for this investigation was the SPT-100 HET;

this allowed the results to be compared to the experimental performance of the thruster and the reported plasma quantities of the discharge. The reference simulation performance values fall within 10% of the nominal operation performances of the thruster; the recovered plasma profiles are also comparable to the ones measured and found in the literature. Known oscillations in the discharge, associated to the breathing mode and ion transit times were also recovered in the results. The current continuity and the energy balances for the discharge, the electron population and the plasma, show that the simulation conserves the main transport quantities, providing further confidence in the results.

- As was already shown by many authors preceding our work, the approach implemented in regard to the anomalous collision frequency factor, which has been the main focus of the parametric investigation, possesses the largest influence over the plasma profiles and thruster performances; neglecting the existence of anomalous transport in the simulation leads to decidedly non-physical results. The electron-neutral collision model also has a large influence in the simulation, although secondary to the anomalous collision frequency factor. It was also found that an anomalous collision frequency factor particular to the heat-flow equations (different to the one used for the generalized Ohm's law) could be implemented to obtain solutions that are consistent with reported plasma diagnostics. A larger parametric study is required to understand the implications of this two-parameter approach, or if the use of a single parameter (where both factors are equal) can lead to acceptable solutions.
- A version of the magnetic circuit of the SPT-100 which adds a trim magnet, inducing a singular point in the thruster channel, was also simulated, to demonstrate the capabilities of the code for obtaining solutions in complex magnetic topologies. The simulation results show the effects over the electron population of having magnetic field lines that run mostly parallel to the thruster's material walls, as well as the influence of the singular point.
- Other dedicated scripts have also delivered for this project; in particular, a script for magnetic circuit simulation based on FEMM was developed and trialed for various magnetic configuration flavors, including magnetic lensing and magnetic shielding topologies, following recent trends in HETs. The script is prepared to produce batches of magnetic circuit designs which, in combination with HYPHEN, allow us to easily extend parametric investigations to the magnetic circuit design.
- A new development methodology for plasma discharge simulation codes in the EP^2 group, which is shared with other codes such as EP2-PLUS, has been cemented, based on TDD, modularity, flexibility and a focus on industry and developer community standards and well known libraries. Commonality in different program modules has been encouraged in order to reduce development times and spur reusability. Sufficient documentation for developers/users has been produced in an effort to ensure continued development of simulation codes in the future; this includes a clear understanding of algorithmic flow and interaction among the different modules.

Furthermore, the work developed in this thesis will be used as a base for future developments, some of which are now ongoing. The most important aspects of future work are summarized next:

- The MFAM quality may be improved through local refinement and/or clustering of elements through the use of hanging-nodes[204, 205]. Low-quality boundary elements may also be reduced by altering the meshing procedure so that it starts from a single family of contour lines (constant λ or constant σ), and then obtains the opposite family from the intersection points of the first family with the domain boundary; this method, however, will not fully eliminate the existence of low-quality boundary elements.
- The OOA of the WLSQR method should be further investigated for additional levels of mesh refinement as well as for different weights and recommended number of stencils. The possibility of using hybrid methods, such as the GG/WLSQR method[207] should also be explored.
- The accuracy of GR using cylindrical coordinates instead of magnetic coordinates was proven to be substantially better by Zhou[164]. The implementation of this flavor of GR, which could be done by projecting said gradients into the preferential directions of the problem, and its influence over simulation results is an important contribution to be performed in the future.
- The implementation of floating conducting wall boundaries, as well as active electrode surfaces, which are used in "multi-stage" HETs, remains a venue for future efforts. We have proposed in this work that they may be resolved by adapting the BC for dielectric or anode walls implemented in HYPHEN. Furthermore, the self-consistent solution for the anode boundary which was obtained through the use of the 2D-MFAM and the iterative matching algorithm could be exploited for the simulation of TAL type HETs.
- As an overarching comment on future updates for the electron fluid model, a self-consistent description of the anomalous electron transport (whether it is due to near-wall conductivity effects or azimuthal plasma oscillations, or a combination of both) remains an open question in the EP community as a whole and, in particular, in the EP^2 group. HYPHEN is prepared to be coupled with future self-consistent models proposed for anomalous transport.
- Partial accommodation of the reflected primary electrons in the sheath model could be implemented in the future, leading to a diffusive type reflection in the wall.
- The experimentally reported influence of the impact angle of impinging-primary-electrons over both the primary reflected, and secondary electron populations[153, 244, 248] could be taken into account even under the assumption that the sheath spatial thickness is much smaller than the Larmor radius; nonetheless, both the gyrophase and the sheath potential drop would have to be considered for the calculation of the impact angle. Even considering the average effects of the gyrophase, in addition to the magnetic angle, the varying yields will also affect the electric potential drop in the sheath, leading to an increasingly coupled problem.
- The sheath model only approximates the influence of multiply charged ions over the response of the boundary layer. The model could be easily expanded to include the influence of various distinct population of ions, at the expense of increasing the dimensionality of the problem.

- The collision frequency models have been averaged over the DF in order to obtain collision rates and yields. This average assumes that the drift velocity of the electron population is negligible versus the thermal velocity. Since this may not be the case for some regions in the thruster, an additional parameter could be included to account for a dominant term in the bulk motion of electrons. This may suppose a non-negligible departure in the response of the collisional processes in the aforementioned regions.

- Since the excitation of neutrals to a non-ionized state occurs at a similar rate as the first-ionization process, we propose that the separate tracking of excited neutrals needs to be performed in order to facilitate the simulation of excited-to-single-charged ionization. This is supported by the fact that this process is as statistically relevant as the single-to-double-charged ionization, which we simulate; additionally, the excitation energy is close to the energy for first ionization, meaning that the excited-to-singly-charged reaction does not require a large energy expenditure.

- Additional models and experimental results can be added to our collision frequency database in the future, specially for Argon, Krypton, or other, more rare, propellants, such as Iodine. The data repositories referenced in this thesis[260, 263] contain this information in easily accessible formats.

- Regarding mesh interpolation, we have proposed the implementation of an algorithm that takes into account the possibility of having PIC and MFAM meshes with regions of largely disparate sizes. The algorithm would forgo the point-to-point interpolation in favor of taking into account the possibility of various cells overlapping with a single element, or viceversa. For example, this could be done through the WLSQR method by using weights based on the area of the sections of elements or cells that overlap, and would help to ensure that less information is potentially "lost" in the interpolation process.

- A larger parametric investigation of the anomalous collision frequency factor (both for the momentum and heat-flow equations separately) would help to chart the possible solution space resolved by the code and may offer clues or constraints into the values that this factor can present in order to obtain realistic solutions, which, in turn, could inform the different physical mechanisms that have been proposed as responsible for this phenomenon. In particular, the use of quenching type functions for the anomalous transport factor[231, 278] should be studied. Note that, since it was found that a secondary, but large, influence on the simulation response is determined by the electron-neutral collisional model, the investigation into the anomalous collision frequency factor should consider this aspect.

- One of the aspects of the code that requires further attention is the volumetric cathode, since present studies have been limited in position and number of elements. This is an important aspect to analyze, since the sensitivity of the simulation to this aspect has been found by other authors to be non-negligible[307]. Although it was not part of the results shown, we have found that if very low density elements are selected for the volumetric cathode, a non-physical temperature solution is recovered. We propose that the volumetric cathode should

be accompanied by neutral and ion injection on the PIC segment, as occurs in real hollow cathodes, and has been shown to be critical[307].

- Regarding the simulation domain, future trials should be performed to determine the effects of the domain size over the response of the plasma, as was done in Hall2De[307], and also in order to characterize the behavior of electron fluid model in very low magnetization regions. The Far-Field boundary conditions will also play a role in this study.

- The effects of concurrent mesh refinement both in the PIC and MFAM meshes should be characterized from the perspective of the simulation response and the scaling of computational requirements.

- While some tests have been performed for the electron population, mostly from the numerical perspective, it is paramount that some simple, physics-oriented, *benchmarks* are developed and tested to gain further confidence in this segment. These benchmarks could be based on experimentally identifiable or known theoretical mechanisms and should opened to the EP community in order to set simulation standards for different codes; these could also be expanded to encompass the full simulation of the plasma.

- Lastly, new magnetic topologies should be simulated in order to characterize the extent to which HYPHEN is able to resolve the influence of different magnetic fields. We propose the magnetic shielding HET configuration, as well as the cusped field topology in HEMPTs as candidates for future studies.

Conclusiones y trabajo futuro

Esta tesis se ha centrado en el desarrollo del módulo asociado a la población de electrones en un nuevo código híbrido PIC-fluido. El código está orientado a la simulación de descargas de plasma poco colisionales inmersas en campos magnéticos aplicados, en motores de efecto Hall. Varias conclusiones e hitos se resumen a continuación:

- *Un modelo fluido, axisimétrico 2D(r-z) se ha implementado en HYPHEN, basado en un cierre bi-Maxwelliano de dos temperaturas para las ecuaciones de transporte de masa, cantidad de movimiento y energía. Los principales supuestos se resumen en: asumir cuasi-neutralidad, despreciar escalas espaciales comparables a la longitud de Debye, omitir el tensor de esfuerzo viscoso y asumir que la energía térmica es mucho mayor que la energía cinética del movimiento de deriva de los electrones. A su vez, se utiliza un parámetro "libre", la frecuencia colisional anómala, para describir los efectos sobre el transporte de electrones asociados a la dirección azimutal, a fenómenos de tipo onda y a dispersión cercana a la pared.*

  La mayor diferencia respecto a anteriores modelos es el enfoque de dos temperaturas, el cual permite tener en cuenta los efectos de la no uniformidad del campo magnético sobre el transporte de electrones, así como el calentamiento preferencial respecto de una de las direcciones del problema. A pesar de que este último efecto puede que no sea de gran importancia en motores Hall, es decisivo en otros tipos de motores, los cuales esperamos poder simular en un futuro cercano. El modelo puede resolverse únicamente para el caso isótropo, en el cual se han centrado los resultados obtenidos.

- *El modelo de electrones se ha resuelto en una malla 2D alineada con el campo magnético. La lógica tras el uso de este tipo de mallas se ha basado en un análisis sobre la difusión numérica en mallas Cartesianas para problemas de transporte anisotrópicos. Dicho estudio demostró que las ecuaciones de transporte deben ser resueltas en mallas alineadas con las direcciones preferentes del problema, si se desea evitar un exceso de difusión numérica. Se ha desarrollado un código que ofrece varias estrategias para la generación y corrección de mallas alineadas. La calidad de estas mallas se ha evaluado desde la perspectiva de indicadores geométricos y también en un problema numérico representativo. Un código ad-hoc de reconstrucción de gradientes también se ha desarrollado, basado en el conocido método de mínimos cuadrados pesados. El orden de precisión del método se ha estudiado para una malla relevante en el contexto del problema en cuestión, para varios niveles de refinado y diferentes funciones analíticas. El método resultó estar entre primer y segundo orden de precisión, lo cual es coherente con los resultados provenientes de la literatura y se considera aceptable para nuestros propositos.*

- *El modelo fluido de electrones se ha discretizado en la malla numérica y ha sido resuelto utilizando el conocido método de volúmenes finitos. Dicho método formula las ecuaciones de*

transporte en su forma integral conservativa y se recomienda para mallas no estructuradas. Dos esquemas temporales han sido implementados: un Euler explícito y un método semi-implícito basado en los Euler explícito e implícito. La estabilidad y convergencia de ambos métodos se ha estudiado, concluyendo que únicamente el método semi-implícito es capaz de proporcionar soluciones coherentes bajo esfuerzos computacionales razonables.

- *Un nuevo modelo auxiliar fluido-1D se ha desarrollado para el tratamiento de la capa límite del plasma (la vaina del plasma) entorno a paredes materiales. El modelo está basado en los principios fundamentales de los mecanismos físicos de la vaina. Este modelo expande los resultados de modelos anteriores obtenidos en el grupo EP^2 al incluir la anisotropicidad de la población primaria de electrones y generalizar el modelo para cualquier inclinación del campo magnético en la pared, bajo el supuesto de que el radio de Larmor es mucho mayor que la longitud de Debye. Se ha realizado un estudio paramétrico que demuestra que el efecto combinado de la anisotropicidad y el ángulo magnético no es despreciable, lo cual supone un paso hacia delante para reducir el número de supuestos en las simulaciones, con el objetivo de obtener resultados más realistas.*

- *El modelo de vaina se ha utilizado en paredes conductoras (metálicas) para obtener una solución autoconsistente para las paredes de ánodo y la región cercana a este, en motores de efecto Hall. Esta solución responde también al uso de una malla alineada 2D. La solución se basa en un algoritmo tipo Newton-Raphson, el cual busca la convergencia de la corriente extraída en la pared y las corrientes presentes en la descarga, de forma iterativa.*

- *Se han comparado diferentes modelos para las frecuencias de colisión de diferentes procesos colisionales en el Xenon y el Argón, así como datos experimentales de conocidos repositorios de datos. Las frecuencias colisionales se han promediado utilizando la función de distribución de probabilidad de los electrones, basada en dos temperaturas. Dicho promedio ha permitido obtener los ritmos de colisión y de cesión de energía en dichos procesos. Se ha encontrado que existe una gran variabilidad en los datos encuestados, la cual puede dar lugar a resultados dispares en las simulaciones; por tanto, la justificación del uso de un modelo en concreto únicamente puede hacerse desde la perspectiva de dichos resultados.*

- *El módulo fluido de electrones se ha puesto a prueba en el contexto de una solución existente para la descarga de plasma de un motor Hall, obtenida utilizando anteriores herramientas de simulación. La sensibilidad del esquema numérico se ha evaluado respecto a las condiciones iniciales, los valores del paso temporal, y distintas condiciones de simulación: el sistema de control de la planta de potencia del motor, diversos modos de inyección de corriente, etc. El análisis se ha llevado a cabo teniendo en cuenta los balances de energía y los residuales de aquellas propiedades físicas del plasma asociadas a la población de electrones. Las pruebas realizadas se han encaminado a obtener un grado suficiente de confianza en el segmento de la población de electrones, antes de probarlo junto con el módulo de partículas.*

- *Se ha llevado a cabo un estudio paramétrico de las simulaciones para ciertas variables: principalmente, el factor asociado a la frecuencia colisional anómala y la fracción de termalización para el modelo de capa límite del plasma, y para varios modelos de colisión entre*

electrones y neutros. El análisis se ha llevado a cabo para una simulación híbrida completa, permitiendo que los módulos fluido y de partículas interaccionen y avancen en el tiempo. La condición cinética de Bohm y las colisiones de tipo CEX no se han incluido en este análisis. El contexto para este estudio ha sido el conocido motor SPT-100, lo que ha permitido que los resultados se comparasen a actuaciones obtenidas experimentalmente, así como a valores físicos de la descarga. La simulación de "referencia" obtuvo valores en las actuaciones que únicamente se diferencian en un 10% *con respecto a los valores nominales del propulsor. Los perfiles del plasma también son comparables con perfiles que han sido medidos y que pueden encontrarse en la literatura. Conocidas oscilaciones en la descarga de motores Hall, asociadas al modo de "respiración" del motor y al tránsito de los iones, también han sido identificadas en las simulaciones. Finalmente, la continuidad de corrientes y los balances de energía en la descarga, la población de electrones y el plasma demuestran que la simulación conserva las cantidades transportadas, lo cual otorga un nivel de confianza adicional en los resultados.*

- *Como muchos autores han demostrado precediendo a nuestro trabajo, el factor asociado a la frecuencia colisional anómala, en el cual se ha centrado nuestra investigación paramétrica, posee la mayor influencia sobre los perfiles del plasma y las actuaciones del motor. Además, si se desprecia la existencia del transporte anómalo, la simulación produce resultados no físicos. Los modelos de colisión electrón-neutro también tienen una gran influencia sobre la simulación, aunque esta se encuentra en segundo lugar respecto al anterior factor. Adicionalmente, se implementó un factor adicional asociado a la frecuencia de colisión anómala únicamente en las ecuaciones de flujo de calor (diferente al factor usado en la ley de Ohm generalizada). Este factor adicional permite obtener soluciones que son más consistentes con los perfiles de plasma obtenidos experimentalmente. Un estudio paramétrico más extenso sería necesario para comprender las implicaciones de este enfoque de "dos parámetros", o si el uso de un único factor (cuando ambos toman el mismo valor) puede llevar a soluciones razonables.*

- *Adicionalmente, se ha simulado una versión del circuito magnético del SPT-100 que incluye un imán permanente de ajuste, el cual induce un punto singular en el canal del motor. Esta simulación se llevó a cabo para demostrar las capacidades del código para obtener soluciones en topologías magnéticas complejas. Los resultados de la simulación muestran los efectos sobre la población de electrones de líneas de campo magnético que corren paralelas a la pared. También pueden observarse las consecuencias de la existencia de un punto singular.*

- *Otras herramientas también han sido desarrolladas en el seno de este proyecto; en concreto, se ha trabajado en un código de simulación de circuitos magnéticos basado en FEMM[178]. Este código se ha utilizado para obtener diversas configuraciones magnéticas, incluyendo topologías de lente magnética y escudo magnético (siguiendo tendencias recientes en motores Hall). El código está preparado para producir múltiples diseños de circuito magnético, los cuales, en combinación con HYPHEN, permitirían expandir los estudios paramétricos al diseño de circuitos magnéticos.*

- *Se ha cimentado una nueva metodología de diseño para códigos de simulación de plasma en el grupo EP^2, la cual se comparte en otros códigos como EP2-PLUS. Dicha metodología está basada en diseño dirigido por testeo, modularidad, flexibilidad y el uso de estándares utilizados por la industria y la comunidad de desarrolladores, así como de librerías de código bien conocidas. También se ha fomentado el uso de módulos de programa compartidos con el objetivo de reducir los tiempos de desarrollo y estimular la reusabilidad. Se ha generado suficiente documentación para usuarios y desarrolladores de cara a asegurar el futuro desarrollo de códigos de simulación; esto incluye una perspectiva clara del flujo algorítmico en el código y de la interacción entre los distintos módulos.*

Adicionalmente, el trabajo desarrollado en esta tesis se utilizará como base para desarrollos futuros, algunos de los cuales ya han comenzado. Los aspectos más importantes de estos se resumen a continuación:

- *La calidad de la malla alineada con el campo magnético puede mejorarse a través de refinamiento o agrupamiento localizados de los elementos que la conforman, haciendo uso de "nodos colgantes"[204, 205]. La existencia de elementos de baja calidad cercanos a las fronteras del dominio puede reducirse alterando el procedimiento de mallado, de tal manera que se comience desde una única familia de líneas de contorno (λ constante o σ constante), y, a continuación, se obtenga la familia contraria a través de los puntos de intersección de la primera familia con el límite del dominio. No obstante, ningún método puede eliminar completamente la existencia de estos elementos de baja calidad en el contorno.*

- *El orden de precisión del método de mínimos cuadrados pesados puede estudiarse para niveles adicionales de refinado de malla. Dicho estudio puede ampliarse a diferentes pesos y al número recomendado de elementos utilizados. También podría explorarse la posibilidad de usar métodos híbridos, como el propuesto por Shima[207].*

- *Zhou[164] demostró que la precisión de la reconstrucción de gradientes utilizando coordenadas cilíndricas es considerablemente mejor que en el caso de utilizar coordenadas magnéticas. La implementación de este tipo de reconstrucción de gradientes implicaría proyectar el gradiente en las direcciones preferentes del problema. El estudio de su influencia sobre los resultados de la simulación supone un aspecto importante de contribuciones futuras.*

- *La implementación de condiciones de contorno para paredes de tipo conductoras flotantes y paredes de electrodos activos, los cuales se utilizan en motores Hall "multi etapa", es un área reservada para trabajo futuro. Se ha propuesto que estas condiciones de contorno pueden resolverse adaptando las condiciones para paredes dieléctricas o paredes de ánodo que se encuentran implementadas en HYPHEN. Adicionalmente, la solución autoconsistente de paredes de ánodo que se obtuvo gracias al uso de la malla 2D alineada con el campo magnético y al algoritmo iterativo de convergencia de corrientes podría explotarse para la simulación de motores Hall de tipo TAL.*

- *Como comentario genérico respecto a futuras mejoras del modelo fluido de electrones, podemos decir que la descripción autoconsistente del transporte anómalo de electrones (ya sea*

debido a efectos de conductividad cercana a la pared, oscilaciones del plasma en la dirección azimutal o una combinación de ambas) continua siendo un interrogante tanto en la comunidad de propulsión eléctrica en general como en el grupo EP². HYPHEN se ha preparado para ser acoplado con futuros modelos que se propongan para describir el transporte anómalo.

- *La acomodación parcial en la pared de la energía de electrones primarios reflejados en el modelo de vaina podría ser implementada en futuras versiones para incluir la opción de reflexiones de tipo difusivas.*

- *La influencia, demostrada experimentalmente, del ángulo de impacto de electrones primarios en paredes materiales sobre las poblaciones de electrones reflejados y secundarios[153, 244, 248] podría tenerse en cuenta aún suponiendo que el espesor de la vaina es mucho menor que el radio de Larmor. No obstante, tanto la giro-fase como el salto de potencial eléctrico en la vaina eberían considerarse en el cálculo del ángulo de impacto. Dicho potencial eléctrico se vería afectado por los cambios en la emisión de electrones secundarios y reflejados, aún si únicamente tenemos encuenta un efecto promedio de la giro-fase (junto con el ángulo de incidencia del campo magnético); como puede verse, esto da lugar a un problema con un mayor grado de acoplamiento que el modelo estudiado en esta tesis.*

- *El modelo de vaina utiliza una aproximación para incluir la influencia de iones de carga múltiple sobre la respuesta de la capa límite. El modelo podría expandirse para incluir los efectos de varias poblaciones de iones, lo cual conllevaría un coste adicional debido a la mayor complejidad del modelo, al aumentar el número de variables.*

- *Los modelos de frecuencia de colisiones se han promediado sobre la función de distribución con el objetivo de obtener los ritmos de colisión y de cesión de energía. Este promedio asume que la velocidad de deriva de la población de electrones es despreciable frente a su velocidad térmica. Sin embargo, es posible que este no sea el caso en ciertas regiones del motor, por lo que el modelo podría incluir un parámetro adicional que tuviese en cuenta el término dominante en el movimiento promedio de los electrones. Dicho cambio podría suponer una desviación apreciable en la respuesta de los procesos colisionales en las regiones mencionadas.*

- *Dado que la excitación de neutros a un estado no ionizado ocurre a un ritmo similar al proceso de primera ionización, proponemos un seguimiento por separado de estos neutros "excitados", de cara a permitir la simulación del proceso colisional que transforma neutros excitados en iones simples. Esta propuesta se nutre del hecho de que este proceso está igual de presente, desde el punto de vista estadístico, que el proceso de transformación de iones simples en iones dobles. Adicionalmente, dado que la energía de excitación se parece a la de primera ionización, la reacción que lleva a la partícula de un estado a otro no requiere un gasto energético importante.*

- *Una mayor cantidad de modelos y resultados experimentales podrían ser añadidos en el futuro a nuestra base de datos de frecuencias de colisión; concretamente, para el Argón, el Kriptón u otros propelentes más atípicos, como el Yodo. Los repositorios de datos que se*

han referenciado en esta tesis[260, 263] disponen de esta información en formatos facilmente accesibles.

- *En relación a la interpolación entre las mallas, se ha propuesto la implementación de un algoritmo que tenga en cuenta la posibilidad de que existan mallas para el segmento de partículas y para el segmento fluido con regiones que contengan elementos o celdas de tamaños muy dispares. El algoritmo descartaría la interpolación de tipo "punto a punto" a favor de tener en cuenta aquellas celdas que se solapen con más de un elemento, o viceversa. Como ejemplo, este algoritmo podría implementarse a través del método de mínimos cuadrados pesados basándose en el área de las secciones de los elementos o celdas que solapan; este enfoque ayudaría a evitar que se pierda información en el proceso de interpolación.*

- *Un estudio paramétrico más extenso, centrado en el factor asociado a la frecuencia de colisión anómala (tanto para las ecuaciones de cantidad de movimiento como de flujo de calor) ayudaría a determinar el espacio de soluciones resuelto por el código, ofreciendo pistas o restricciones sobre los valores que dicho factor puede tomar, si se buscan soluciones realistas. Dichos valores podrían informar a los mecanismos físicos que se han propuesto para describir este fenómeno. Concretamente, el uso de funciones de transporte anómalo de tipo "tres regiones"[231, 278] debería ser estudiado. Téngase en cuenta que, dado que la influencia sobre la respuesta de la simulación ante el modelo de colisiones electrón-neutro es secundaria, pero relevante, el estudio del factor de frecuencia de colisión anómala debe tener dicha influencia en cuenta.*

- *Uno de los aspectos del código que requieren una mayor atención es el cátodo volumétrico, dado que los estudios realizados han estado limitados a un número de elementos y posición de los mismos fijos. Esta es un área de estudio importante, ya que varios autores han demostrado que la sensibilidad de las simulaciones a este aspecto del código no es decpreciable[307]. A pesar de que no se ha mostrado en esta tesis, se ha determinado, a lo largo de las pruebas realizadas, que si el cátodo volumétrico se asigna a elementos que presentan bajas densidades de plasma en tiempo de simulación, la solución de la temperatura de electrones deja de ser física. Proponemos que el cátodo volumétrico se acompañe de la inyección de neutros e iones en el segmento de partículas, tal y como ocurre en los cátodos huecos en la realidad, y que ha demostrado ser un aspecto crítico en simulaciones[307].*

- *En relación al dominio de simulación, se deberían dedicar esfuerzos futuros a entender los efectos del tamaño del dominio sobre la respuesta del plasma, como se hizo en Hall2De[307]. Estos esfuerzos deberían estar enfocados también a caracterizar el comportamiento del modelo fluido de electrones en regiones de muy baja magnetización. Las condiciones de contorno de campo lejano también deben tenerse en cuenta en este estudio.*

- *Los efectos del refinamiento de la malla, tanto en el las mallas asociadas a partículas y al fluido, deberían caracterizarse desde la perspectiva de los resultados de simulación y respecto al escalado de los requisitos computacionales.*

- *A pesar de que se han realizado algunas pruebas en la población de electrones, principalmente desde el punto de vista numérico, es importante que se lleven a cabo ciertas simulaciones de referencia que representen fenómenos físicos simples, de tal manera que se tenga una mayor confianza en este segmento. Estas referencias deberán basarse en mecanismos físicos teóricos conocidos o identificables experimentalmente que puedan ser contrastados con las simulaciones. Estas referencias podrían ser presentadas ante la comunidad de propulsión eléctrica con el objetivo de establecer estándares de simulación para los diferentes códigos. Dichas referencias también podrían expandirse para incluir la simulación completa del plasma.*

- *Finalmente, se deben simular nuevas topologías magnéticas para caracterizar las capacidades de HYPHEN a la hora de resolver la influencia de distintos campos magnéticos. Proponemos como próximos candidatos la configuración de escudo magnético en motores Hall y la topología de cúspides que aparece en motores HEMPT.*

Annex

Within the framework of this thesis, the author has participated in the following journal publications:

- Daniel Perez-Grande, Oscar Gonzalez-Martinez, Pablo Fajardo, and Eduardo Ahedo. Analysis of the numerical diffusion in anisotropic mediums: Benchmarks for magnetic field aligned meshes in space propulsion simulations. *Applied Sciences*, 6(11):354, 2016
- Christopher A. Dodson, Daniel Perez-Grande, Benjamin A. Jorns, Dan M. Goebel, and Richard E. Wirz. Ion heating measurements on the centerline of a high-current hollow cathode plume. *Journal of Propulsion and Power*, Accepted for publication
- M Wijnen, N Aguera-Lopez, S Correyero-Plaza, and D Perez-Grande. Cubesat lunar positioning system enabled by novel on-board electric propulsion. *IEEE TRANSACTIONS ON PLASMA SCIENCE PSI*, 46(2):319–329, 2018

In addition, a number of contributions have been made to conference proceedings:

- D Perez-Grande, P Fajardo, and E Ahedo. Evaluation of erosion reduction mechanisms in hall effect thrusters. In *34th International Electric Propulsion Conference, paper IEPC-2017-201*, 2015
- D Perez-Grande, O Gonzalez-Martinez, P Fajardo, and E Ahedo. Benchmarks for magnetic field aligned meshes in electromagnetic plasma thruster simulations. In *34th International Electric Propulsion Conference, paper IEPC-2015-203*, 2015
- Christopher Dodson, Daniel Perez-Grande, Benjamin Jorns, Dan M Goebel, and Richard E Wirz. Laser-induced fluorescence measurements of energetic ions in a 100-a lab6 hollow cathode plume. In *52nd AIAA/SAE/ASEE Joint Propulsion Conference*, page 4838, 2016
- A. Domínguez, D. Perez-Grande, P. Fajardo, and E. Ahedo. NOMADS: development of a versatile plasma discharge simulation plarform for electric propulsion. In *Space Propulsion Conference*, number 3124869, Rome, Italy, 2016
- Daniel Perez-Grande, Jiewei Zhou, Adrián Domınguez, Mario Merino, Pablo Fajardo, and Eduardo Ahedo. Development updates for a two-dimensional axisymmetric hybrid code for plasma thruster discharges. In *35th International Electric Propulsion Conference, paper IEPC-2017-201*, 2017
- M Wijnen, S Correyero-Plaza, N Agüera-López, and D Perez-Grande. Innovative electric propulsion trends, concurrent mission design and enabling technologies for a bold cubesat lunar positioning system. In *35th International Electric Propulsion Conference, Atlanta, GA, paper IEPC-2017-603*, 2017

The paper *"Innovative Electric Propulsion trends, concurrent mission design and enabling technologies for a bold CubeSat Lunar Positioning System"* became the winning entry for the *Young Visionary Paper Competition* organized by the Electric Propulsion Rocket Society (ERPS) and the 2017 International Electric Propulsion Conference (IEPC) Organizing Committee, in an effort to promote novel ideas using a unique combination of technical knowledge, foresight, and articulation.

Finally, two international placements have also been completed throughout this thesis:

- NASA Jet Propulsion Laboratory (JPL) in Pasadena, California (2015), supported through UC3M's *Ayudas para la movilidad de investigadores en formación predoctoral* and the JPL Visiting Student Researcher program.
- Ad Astra Rocket Company in Liberia, Costa Rica (2018), supported through Santander Bank's *Beca Iberoamerica Santander Jovenes Investigadores.*

Bibliography

[1] Luis Espinoza Anil Natha. Voyager mission status. https://voyager.jpl.nasa.gov/mission/status/, 2018.

[2] S Alan Stern. The new horizons pluto kuiper belt mission: an overview with historical context. In *New Horizons*, pages 3–21. Springer, 2009.

[3] Fran Rodriguez. Kids (image reproduced here with the author's permission). http://cargocollective.com/lacabezaenlasnubes, 2015.

[4] Space Foundation. The space report 2015: The authoritative guide to global space activity. https://www.spacefoundation.org/news/space-foundation-report-reveals-global-space-economy-climb-330-billion, 2015.

[5] NASA. Earth from space (image not subjected to copyright). https://explorer1.jpl.nasa.gov/galleries/earth-from-space/, 1958.

[6] NASA/Johns Hopkins University Applied Physics Laboratory/Southwest Research Center/Chandra X-Ray Center. X-rays from pluto (permission for reuse under pd-usgov-nasa). https://explorer1.jpl.nasa.gov/galleries/earth-from-space/, 2016.

[7] M Wijnen, N Aguera-Lopez, S Correyero-Plaza, and D Perez-Grande. Cubesat lunar positioning system enabled by novel on-board electric propulsion. *IEEE TRANSACTIONS ON PLASMA SCIENCE PSI*, 46(2):319–329, 2018.

[8] W Gerstenmaier. Progress in defining the deep space gateway and transport plan. In *NASA Advisory Council Human Exploration and Operations Committee Meeting*, 2017.

[9] Kathryn Hambleton. Deep space gateway to open opportunities for distant destinations. *NASA,(March 28, 2017) https://www. nasa. gov/feature/deep-space-gateway-to-open-opportunities-for-distant-destinations (17 August 2017) Google Scholar*, 2017.

[10] Johannes Benkhoff, Jan van Casteren, Hajime Hayakawa, Masaki Fujimoto, Harri Laakso, Mauro Novara, Paolo Ferri, Helen R Middleton, and Ruth Ziethe. Bepicolombo-comprehensive exploration of mercury: Mission overview and science goals. *Planetary and Space Science*, 58(1-2):2–20, 2010.

[11] Christophe Koppel, Frederic Marchandise, Mathieu Prioul, Denis Estublier, and Franck Darnon. The smart-1 electric propulsion subsystem around the moon: In flight experience. In *41st AIAA/ASME/SAE/ASEE Joint Propulsion Conference & Exhibit*, page 3671, 2005.

[12] GD Racca, A Marini, L Stagnaro, J Van Dooren, L Di Napoli, BH Foing, R Lumb, J Volp, J Brinkmann, R Grünagel, et al. Smart-1 mission description and development status. *Planetary and space science*, 50(14-15):1323–1337, 2002.

[13] CT Russell and CA Raymond. The dawn mission to vesta and ceres. *Space Science Reviews*, 163(1-4):3–23, 2011.

[14] John Brophy, Charles Garner, Barry Nakazono, Mike Marcucci, Mike Henry, and Don Noon. The ion propulsion system for dawn. In *39th AIAA/ASME/SAE/ASEE Joint Propulsion Conference and Exhibit*, page 4542, 2003.

[15] Ulysse Carion. Delta-v budgets (courtesy of imgur). https://i.imgur.com/AAGJvD1.png.

[16] George P Sutton and Oscar Biblarz. *Rocket propulsion elements*. John Wiley & Sons, 2016.

[17] W Robbins. An historical perspective of the nerva nuclear rocket engine technology program. In *Conference on Advanced SEI Technologies*, page 3451, 1991.

[18] Enrico Lorenzini and Juan Sanmartín. Electrodynamic tethers in space. *Scientific American*, 291(2):50–57, 2004.

[19] Hermann Oberth. *Ways to spaceflight*. Number 622. National Aeronautics and Space Administration, 1972.

[20] James S Sovey, Vincent K Rawlin, and Michael J Patterson. Ion propulsion development projects in us: Space electric rocket test i to deep space 1. *Journal of Propulsion and Power*, 17(3):517–526, 2001.

[21] Steven A Feuerborn, Julie Perkins, and David A Neary. Finding a way: Boeing's all electric propulsion satellite. In *49th AIAA/ASME/SAE/ASEE Joint PropulsionConference*, page 4126. 2013.

[22] Andrew Klesh and Joel Krajewski. Marco: Cubesats to mars in 2016. 2015.

[23] Franklin Chang Diaz, Jared Squire, Edgar Bering, III, Jeffrey George, Andrew Ilin, Andrew Petro, and Leonard Casady. The vasimr engine approach to solar system exploration. In *39th Aerospace Sciences Meeting and Exhibit*, page 960, 2001.

[24] Roland Florenz, Thomas Liu, Alec Gallimore, Hani Kamhawi, Daniel Brown, Richard Hofer, and James Polk. Electric propulsion of a different class: The challenges of testing for megawatt missions. In *48th AIAA/ASME/SAE/ASEE Joint Propulsion Conference & Exhibit*, page 3942, 2012.

[25] Robert G Jahn and Edgar Y Choueiri. Electric propulsion. 2001.

[26] M Martinez-Sanchez and James E Pollard. Spacecraft electric propulsion-an overview. *Journal of Propulsion and Power*, 14(5):688–699, 1998.

[27] Dan M Goebel and Ira Katz. *Fundamentals of electric propulsion: ion and Hall thrusters*, volume 1. John Wiley & Sons, 2008.

[28] Scott Benson, Lynn Arrington, W Hoskins, and Nicole Meckel. Development of a ppt for the eo-1 spacecraft. In *35th Joint Propulsion Conference and Exhibit*, page 2276, 2000.

[29] F Cannat, T Lafleur, J Jarrige, P Chabert, P-Q Elias, and D Packan. Optimization of a coaxial electron cyclotron resonance plasma thruster with an analytical model. *Physics of Plasmas*, 22(5):053503, 2015.

[30] David Krejci, Fernando Mier-Hicks, Corey Fucetola, Paulo Lozano, Andrea Hsu Schouten, and Francois Martel. Design and characterization of a scalable ion electrospray propulsion system. 2015.

[31] Jaume Navarro-Cavallé, Eduardo Ahedo, Mario Merino, Vıctor Gómez, Mercedes Ruiz, and José Antonio Gonzalez del Amo. Helicon plasma thrusters: prototypes and advances on modeling. In *33rd Int. Electric Propulsion Conf.(Washington, DC)*, 2013.

[32] Benjamin W Longmier, Jared P Squire, Leonard D Cassady, Maxwell G Ballenger, Mark D Carter, Chris Olsen, Andrew V Ilin, Tim W Glover, Greg E McCaskill, FR Chang Dıaz, et al. Vasimr vx-200 performance measurements and helicon throttle tables using argon and krypton. In *32nd International Electric Propulsion Conference*, 2011.

[33] NASA/JPL-Caltech. The engine burns blue (permission for reuse under pd-usgov-nasa). https://www.nasa.gov/multimedia/imagegallery/image_feature_2516.html, 2013.

[34] Jet Propulsion Laboratory. Nexis dm1a ion engine (permission for reuse under pd-usgov-nasa). https://upload.wikimedia.org/wikipedia/commons/8/8e/NEXIS_thruster_working.jpg, 2013.

[35] Ryan W Conversano, Dan M Goebel, Richard R Hofer, and Nitin Arora. Performance enhancement of a long-life, low-power hall thruster for deep-space smallsats. In *Aerospace Conference, 2017 IEEE*, pages 1–12. IEEE, 2017.

[36] AI Morozov and VV Savelyev. Fundamentals of stationary plasma thruster theory. In *Reviews of plasma physics*, pages 203–391. Springer, 2000.

[37] Harold R Kaufman. Technology of closed-drift thrusters. *AIAA journal*, 23(1):78–87, 1985.

[38] John R Brophy. Stationary plasma thruster evaluation in russia. 1992.

[39] Edgar Choueiri. Fundamental difference between the two variants of hall thrusters-spt and tal. In *37th Joint Propulsion Conference and Exhibit*, page 3504, 2001.

[40] Richard R Hofer and David Jacobson. Development and characterization of high-efficiency, high-specific impulse xenon hall thrusters. 2004.

[41] Richard Hofer and Alec Gallimore. Efficiency analysis of a high-specific impulse hall thruster. In *40th AIAA/ASME/SAE/ASEE Joint Propulsion Conference and Exhibit*, page 3602, 2004.

[42] Richard R Hofer, Peter Y Peterson, Alec D Gallimore, and Robert S Jankovsky. A high specific impulse two-stage hall thruster with plasma lens focusing. IEPC-01-036, 27th International Electric Propulsion Conference, Pasadena, CA, 2001.

[43] A Fruchtman and A Cohen-Zur. Plasma lens and plume divergence in the hall thruster. *Applied physics letters*, 89(11):111501, 2006.

[44] Michael Keidar and Isak I Beilis. Sheath and boundary conditions for plasma simulations of a hall thruster discharge with magnetic lenses. *Applied Physics Letters*, 94(19):191501, 2009.

[45] Kristi de Grys, Alex Mathers, Ben Welander, and Vadim Khayms. Demonstration of 10,400 hours of operation on 4.5 kw qualification model hall thruster. In *46th AIAA/ASME/SAE/ASEE Joint Propulsion Conference & Exhibit*, page 6698, 2010.

[46] Ioannis G Mikellides, Ira Katz, Richard R Hofer, Dan M Goebel, Kristi De Grys, and Alex Mathers. Magnetic shielding of the channel walls in a hall plasma accelerator. *Physics of Plasmas*, 18(3):033501, 2011.

[47] Ioannis G Mikellides, Ira Katz, Richard R Hofer, and Dan M Goebel. Magnetic shielding of a laboratory hall thruster. i. theory and validation. *Journal of Applied Physics*, 115(4):043303, 2014.

[48] N Koch, M Schirra, S Weis, A Lazurenko, B van Reijen, J Haderspeck, A Genovese, P Holtmann, R Schneider, K Matyash, et al. The hempt concept-a survey on theoretical considerations and experimental evidences. In *32nd International Electric Propulsion Conference, Wiesbaden, Germany September*, volume 11, page 15, 2011.

[49] Yevgeny Raitses, Artem Smirnov, and Nathaniel Fisch. Cylindrical hall thrusters. In *37th AIAA Plasmadynamics and Lasers Conference*, page 3245, 2006.

[50] W Hargus, Jr and M Cappelli. Development of a linear hall thruster. In *34th AIAA/ASME/SAE/ASEE Joint Propulsion Conference and Exhibit*, page 3336, 1998.

[51] Roland Florenz, Alec D Gallimore, and Peter Y Peterson. Developmental status of a 100-kw class laboratory nested channel hall thruster. In *32nd International Electric Propulsion Conference, Wiesbaden, Germany, paper IEPC-2011-9*, 2011.

[52] John Raymond Brophy. Ion thruster performance model. 1984.

[53] Dan M Goebel, Richard E Wirz, and Ira Katz. Analytical ion thruster discharge performance model. *Journal of Propulsion and Power*, 23(5):1055–1067, 2007.

[54] Mantas Dobkevicius. *Modelling and design of inductively coupled radio frequency gridded ion thrusters with an application to Ion Beam Shepherd type space missions.* PhD thesis, University of Southampton, 2017.

[55] F. Cichocki, M. Merino, E. Ahedo, M. Smirnova, A. Mingo, and M. Dobkevicius. Electric propulsion subsystem optimization for ion beam shepherd missions. *Journal of Propulsion and Power*, 33(2):370–378, 2017.

[56] Vladimir Kim. Main physical features and processes determining the performance of stationary plasma thrusters. *Journal of Propulsion and Power*, 14(5):736–743, 1998.

[57] AI Bugrova, N Maslennikov, and AI Morozov. Similarity laws for the global properties of a hall accelerator. *Sov. Phys. Tech. Phys*, 36(6):612–615, 1991.

[58] E Ahedo and JM Gallardo. Scaling down hall thrusters. In *28th Int. Electric Propulsion Conf., Toulouse, France, paper IEPC-2003-104*, 2003.

[59] Yu Daren, Ding Yongjie, and Zeng Zhi. Improvement on the scaling theory of the stationary plasma thruster. *Journal of Propulsion and Power*, 21(1):139–143, 2005.

[60] Tommaso Misuri, Francesco Battista, and Mariano Andrenucci. Het scaling methodology: Improvement and assessment. In *Proc. 44th AIAA/ASME/SAE/ASEE Joint Propulsion Conference*, 2008.

[61] Käthe Dannenmayer and Stéphane Mazouffre. Elementary scaling relations for hall effect thrusters. *Journal of Propulsion and Power*, 27(1):236, 2011.

[62] Richard Geller. *Electron cyclotron resonance ion sources and ECR plasmas.* CRC Press, 1996.

[63] Justin M Little. *Performance scaling of magnetic nozzles for electric propulsion.* PhD thesis, 2015.

[64] Lou Grimaud and C Boniface. Performance comparison between standard and magnetically shielded 200 w hall thrusters with bn-sio2 and graphite channel walls. In *35th International Electric Propulsion Conference, paper IEPC-2017-172*, 2017.

[65] RJ Cedolin, WA Hargus Jr, PV Storm, RK Hanson, and MA Cappelli. Laser-induced fluorescence study of a xenon hall thruster. *Applied Physics B: Lasers and Optics*, 65(4):459–469, 1997.

[66] JP Sheehan, Yevgeny Raitses, Noah Hershkowitz, and Michael McDonald. Recommended practice for use of emissive probes in electric propulsion testing. *Journal of Propulsion and Power*, 2016.

[67] S Mazouffre, G Largeau, L Garrigues, C Boniface, and K Dannenmayer. Evaluation of various probe designs for measuring the ion current density in a hall thruster plume. In *35th International Electric Propulsion Conference, paper IEPC-2017-336*, 2017.

[68] James E Polk, Anthony Pancotti, Thomas Haag, Scott King, Mitchell Walker, Joseph Blakely, and John Ziemer. Recommended practice for thrust measurement in electric propulsion testing. *Journal of Propulsion and Power*, 2017.

[69] James E Polk, Anthony Pancotti, Thomas Haag, Scott King, Mitchell Walker, Joseph Blakely, and John Ziemer. Recommended practices in thrust measurements. Technical report, CALIFORNIA INST OF TECHNOLOGY PASADENA JET PROPULSION LAB, 2013.

[70] JAMESS SOVEY and MARISA MANTENIEKS. Performance and lifetime assessment of magnetoplasmadynamic arc thruster technology. *Journal of Propulsion and Power*, 7(1):71–83, 1991.

[71] Eric J Pencil, Thomas Randolph, and David H Manzella. End-of-life stationary plasma thruster far-field plume characterization. *AIAA Paper*, 2709:1996, 1996.

[72] Wensheng Huang. *Study of Hall thruster discharge channel wall erosion via optical diagnostics*. PhD thesis, University of Michigan, 2011.

[73] J.R. Brophy. Legacy of the asteroid redirect robotic mission (arrm). In *35th International Electric Propulsion Conference, paper IEPC-2017-31*, 2017.

[74] John Michael Fife. *Two-dimensional hybrid particle-in-cell modeling of Hall thrusters*. PhD thesis, Massachusetts Institute of Technology, 1995.

[75] John Michael Fife, Manuel Martinez-Sanchez, and James Szabo. A numerical study of low-frequency discharge oscillations in hall thrusters. *AIAA paper*, 3052:1997, 1997.

[76] J.M. Fife. *Hybrid-PIC Modeling and Electrostatic Probe Survey of Hall Thrusters*. PhD thesis, 1998.

[77] Charles K Birdsall. Particle-in-cell charged-particle simulations, plus monte carlo collisions with neutral atoms, pic-mcc. *IEEE Transactions on Plasma Science*, 19(2):65–85, 1991.

[78] D Perez-Grande, P Fajardo, and E Ahedo. Evaluation of erosion reduction mechanisms in hall effect thrusters. In *34th International Electric Propulsion Conference, paper IEPC-2017-201*, 2015.

[79] Shannon Cheng and Manuel Martinez-Sanchez. Hybrid particle-in-cell erosion modeling of two hall thrusters. *Journal of Propulsion and Power*, 24(5):987–998, 2008.

[80] E Ahedo, A Antón, I Garmendia, I Caro, and J González del Amo. Simulation of wall erosion in hall thrusters. In *30th Int. Electric Propulsion Conf., Florence, Italy, paper IEPC-2007-067*, 2007.

[81] Michael Patterson, Vincent Rawlin, James Sovey, Michael Kussmaul, and James Parkes. 3 kw ion thruster wear test. In *31st Joint Propulsion Conference and Exhibit*, page 2516, 1995.

[82] JE Polk, JR Anderson, JR Brophy, VK Rawlin, MJ Patterson, J Sovey, and J Hamley. An overview of the results from an 8200 hour wear test of the nstar ion thruster. *AIAA paper*, 2446:1999, 1999.

[83] Anita Sengupta, John R Brophy, and Keith D Goodfellow. *Status of the extended life test of the Deep Space 1 flight spare ion engine after 30,352 hours of operation*. Pasadena, CA: Jet Propulsion Laboratory, National Aeronautics and Space Administration, 2003.

[84] F. Cichocki. *Analysis of the expansion of a plasma thruster plume into vacuum*. PhD thesis, Universidad Carlos III de Madrid (UC3M), Leganés, Spain, 2017.

[85] ID Boyd and A Ketsdever. Interactions between spacecraft and thruster plumes. *Journal of Spacecraft and Rockets*, 38(3):380, 2001.

[86] Jean-FranÇois Roussel, FranÇois Rogier, Guillaume Dufour, Jean-Charles Mateo-Velez, Julien Forest, Alain Hilgers, David Rodgers, Laurence Girard, and Denis Payan. Spis open-source code: Methods, capabilities, achievements, and prospects. *IEEE Transactions on Plasma Science*, 36(5):2360–2368, 2008.

[87] Roger W Hockney and James W Eastwood. *Computer simulation using particles*. crc Press, 1988.

[88] George Keith Batchelor. *An introduction to fluid dynamics*. Cambridge university press, 2000.

[89] Graeme Austin Bird. Molecular gas dynamics. *NASA STI/Recon Technical Report A*, 76, 1976.

[90] D. Tskhakaya, K. Matyash, R. Schneider, and F. Taccogna. The particle-in-cell method. *Contributions to Plasma Physics*, 47(8-9):563–594, 2007.

[91] Hong-yu Wang, Wei Jiang, and You-nian Wang. Implicit and electrostatic particle-in-cell/monte carlo model in two-dimensional and axisymmetric geometry: I. analysis of numerical techniques. *Plasma Sources Science and Technology*, 19(4):045023, 2010.

[92] JC Adam, A Héron, and G Laval. Study of stationary plasma thrusters using two-dimensional fully kinetic simulations. *Physics of Plasmas*, 11(1):295–305, 2004.

[93] A Ducrocq, JC Adam, A Héron, and G Laval. High-frequency electron drift instability in the cross-field configuration of hall thrusters. *Physics of Plasmas*, 13(10):102111, 2006.

[94] A Héron and JC Adam. Anomalous conductivity in hall thrusters: effects of the non-linear coupling of the electron-cyclotron drift instability with secondary electron emission of the walls. *Physics of Plasmas*, 20(8):082313, 2013.

[95] Francesco Taccogna, Savino Longo, Mario Capitelli, and Ralf Schneider. Plasma flow in a hall thruster. *Physics of plasmas*, 12(4):043502, 2005.

[96] F Taccogna, R Schneider, S Longo, and M Capitelli. Kinetic simulations of a plasma thruster. *Plasma Sources Science and Technology*, 17(2):024003, 2008.

[97] Konstantin Matyash, Ralf Schneider, Andreas Mutzke, Oleksandr Kalentev, Francesco Taccogna, Norbert Koch, and Martin Schirra. Kinetic simulations of spt and hemp thrusters including the near-field plume region. *IEEE Transactions on Plasma Science*, 38(9):2274–2280, 2010.

[98] F Taccogna, D Pagano, F Scortecci, and A Garulli. Three-dimensional plume simulation of multi-channel thruster configuration. *Plasma Sources Science and Technology*, 23(6):065034, 2014.

[99] D Sydorenko, A Smolyakov, I Kaganovich, and Y Raitses. Kinetic simulation of effects of secondary electron emission on electron temperature in hall thrusters. In *The 29th Annual International Electric Propulsion Conference, paper IEPC-2005-078*, 2005.

[100] D. Sydorenko, A. Smolyakov, I. Kaganovich, and Y. Raitses. Modification of electron velocity distribution in bounded plasmas by secondary electron emission. *Plasma Science, IEEE Transactions on*, 34(3):815–824, 2006.

[101] ID Kaganovich, Yevgeny Raitses, Dmytro Sydorenko, and Andrei Smolyakov. Kinetic effects in a hall thruster discharge a. *Physics of Plasmas*, 14(5):057104, 2007.

[102] P Coche and L Garrigues. Study of stochastic effects in a hall effect thruster using a test particles monte-carlo model. In *Proceedings of the 32nd International Electric Propulsion Conference, paper IEPC-2011-255*, 2011.

[103] P Coche and L Garrigues. A two-dimensional (azimuthal-axial) particle-in-cell model of a hall thruster. *Physics of Plasmas*, 21(2):023503, 2014.

[104] Vivien Croes, Trevor Lafleur, Zdeněk Bonaventura, Anne Bourdon, and Pascal Chabert. 2d particle-in-cell simulations of the electron drift instability and associated anomalous electron transport in hall-effect thrusters. *Plasma Sources Science and Technology*, 26(3):034001, 2017.

[105] Vivien Croes, Antoine Tavant, Romain Lucken, Trevor Lafleur, Anne Bourdon, and Pascal Chabert. Study of electron transport in a hall effect thruster with 2d ?- θ particle-in-cell simulations. 2017.

[106] Romain Lucken, Vivien Croes, Trevor Lafleur, Jean-Luc Raimbault, Anne Bourdon, and Pascal Chabert. Global models of plasma thrusters: Insights from pic simulation and fluid theory. 2017.

[107] Miharu Hirakawa and Yoshihiro Arakawa. Numerical simulation of plasma particle behavior in a hall thruster. *AIAA.ÂŮ1996.ÂŮ?*, 3195, 1996.

[108] K Sullivan, M Martinez-Sanchez, and O Batishchev. Pic-dsmc hybrid simulation of the high-voltage hall discharge with wall effect. In *Proceedings of the 18th International Conference on the Numerical Simulation of Plasmas*, 2003.

[109] Hui Liu, Boying Wu, Daren Yu, Yong Cao, and Ping Duan. Particle-in-cell simulation of a hall thruster. *Journal of Physics D: Applied Physics*, 43(16):165202, 2010.

[110] John R Brophy, Ira Katz, James E Polk, and John R Anderson. Numerical simulations of ion thruster accelerator grid erosion. *AIAA Paper*, 4261:7–10, 2002.

[111] Joseph Wang, James Polk, John Brophy, and Ira Katz. Three-dimensional particle simulations of ion-optics plasma flow and grid erosion. *Journal of Propulsion and Power*, 19(6):1192–1199, 2003.

[112] Harald JW Müller-Kirsten. *Basics of statistical physics*. World Scientific, 2013.

[113] Carlo Cercignani. The boltzmann equation. In *The Boltzmann Equation and Its Applications*, pages 40–103. Springer, 1988.

[114] Iain D Boyd. Numerical modeling of spacecraft electric propulsion thrusters. *Progress in Aerospace Sciences*, 41(8):669–687, 2005.

[115] M Martinez-Sanchez, J Navarro-Cavallé, and E Ahedo. Electron cooling and finite potential drop in a magnetized plasma expansion. *Physics of Plasmas*, 22(5):053501, 2015.

[116] Jaume Navarro, Manuel Martinez-Sanchez, and Eduardo Ahedo. Collisionless electron cooling in a magnetic nozzle. In *50th AIAA/ASME/SAE/ASEE Joint Propulsion Conference*, page 4028, 2014.

[117] G Sanchez-Arriaga, J Zhou, E Ahedo, M Martınez-Sánchez, and JJ Ramos. One-dimensional direct vlasov simulations of non-stationary plasma expansion in magnetic nozzle. 2017.

[118] Donald Rapp and William E Francis. Charge exchange between gaseous ions and atoms. *The Journal of Chemical Physics*, 37(11):2631–2645, 1962.

[119] Ioannis G Mikellides and Alejandro Lopez Ortega. Numerical simulations of a 100-kw class nested hall thruster with the 2-d axisymmetric code hall2de. 2017.

[120] Michael Keidar and Iain D Boyd. Progress in hydrodynamic modeling of hall thrusters. 2005.

[121] M Keidar, ID Boyd, and II Beilis. Plasma flow and plasma–wall transition in hall thruster channel. *Physics of Plasmas*, 8(12):5315–5322, 2001.

[122] Subrata Roy and BP Pandey. Numerical investigation of a hall thruster plasma. *Physics of Plasmas*, 9(9):4052–4060, 2002.

[123] Leonid Dorf, V Semenov, and Y Raitses. Anode sheath in hall thrusters. *Applied physics letters*, 83(13):2551–2553, 2003.

[124] S. Barral, K. Makowski, Z. Peradzynski, N. Gascon, and M. Dudeck. Wall material effects in stationary plasma thrusters. II. near-wall and in-wall conductivity. *Phys. Plasmas*, 10(10):4137–4152, 2003.

[125] Ioannis G Mikellides and Ira Katz. Numerical simulations of hall-effect plasma accelerators on a magnetic-field-aligned mesh. *Physical Review E*, 86(4):046703, 2012.

[126] Ioannis G Mikellides, Benjamin Jorns, Ira Katz, and Alejandro Lopez Ortega. Hall2de simulations with a first-principles electron transport model based on the electron cyclotron drift instability. In *52nd AIAA/SAE/ASEE Joint Propulsion Conference*, page 4618, 2016.

[127] Ioannis G Mikellides, Ira Katz, Kristina K Jameson, and Dan M Goebel. Numerical simulations of a hall thruster hollow cathode plasma. In *International Electric Propulsion Conference 2007 paper IEPC-2007-018*, 2007.

[128] JP Boeuf and L Garrigues. Low frequency oscillations in a stationary plasma thruster. *Journal of Applied Physics*, 84(7):3541–3554, 1998.

[129] Kimiya Komurasaki and Yoshihiro Arakawa. Two-dimensional numerical model of plasma flow in a hall thruster. *Journal of Propulsion and Power*, 11(6):1317–1323, 1995.

[130] John Fife and Manuel Martinez-Sanchez. Comparison of results from a two-dimensional numerical spt model with experiment. In *32nd Joint Propulsion Conference and Exhibit*, page 3197, 1996.

[131] FI Parra, E Ahedo, JM Fife, and M Martinez-Sanchez. A two-dimensional hybrid model of the hall thruster discharge. *Journal of Applied Physics*, 100(2):023304, 2006.

[132] Diego Escobar and Eduardo Ahedo. Two-dimensional electron model for a hybrid code of a two-stage hall thruster. *IEEE Transactions on Plasma Science*, 36(5):2043–2057, 2008.

[133] E. Ahedo, R. Santos, and F. I. Parra. Fulfillment of the kinetic Bohm criterion in a quasineutral particle-in-cell model. *Physics of Plasmas*, 17(7):073507, 2010.

[134] GJM Hagelaar, J Bareilles, L Garrigues, and J-P Boeuf. Modelling of stationary plasma thrusters. *Contributions to Plasma Physics*, 44(5-6):529–535, 2004.

[135] J Bareilles, GJM Hagelaar, L Garrigues, C Boniface, JP Boeuf, and N Gascon. Critical assessment of a two-dimensional hybrid hall thruster model: Comparisons with experiments. *Physics of Plasmas*, 11(6):3035–3046, 2004.

[136] GJM Hagelaar, J Bareilles, LBJP Garrigues, and J-P Boeuf. Two-dimensional model of a stationary plasma thruster. *Journal of Applied Physics*, 91(9):5592–5598, 2002.

[137] Justin W Koo and Iain D Boyd. Modeling of anomalous electron mobility in hall thrusters. *Physics of Plasmas*, 13(3):033501, 2006.

[138] Justin W Koo and Iain D Boyd. Computational model of a hall thruster. *Computer physics communications*, 164(1-3):442–447, 2004.

[139] Emmanuelle Sommier, Michelle K Scharfe, Nicolas Gascon, Mark A Cappelli, and Eduardo Fernandez. Simulating plasma-induced hall thruster wall erosion with a two-dimensional hybrid model. *IEEE Transactions on Plasma Science*, 35(5):1379–1387, 2007.

[140] C Boniface, L Garrigues, GJM Hagelaar, JP Boeuf, D Gawron, and S Mazouffre. Anomalous cross field electron transport in a hall effect thruster. *Applied Physics Letters*, 89(16):161503, 2006.

[141] Justin Fox, Alla Batishcheva, Oleg Batishchev, and Manuel Martinez-Sanchez. Adaptively meshed fully-kinetic pic-vlasov model for near vacuum hall thrusters. In *42nd AIAA/ASME/SAE/ASEE Joint Propulsion Conference & Exhibit*, page 4324, 2006.

[142] R. Santos GutiÃĺrrez. *Código Híbrido Avanzado de Motores de Plasma de Efecto Hall*. PhD thesis, 2012.

[143] Yasunori Yamamura and Hiro Tawara. Energy dependence of ion-induced sputtering yields from monatomic solids at normal incidence. *Atomic data and nuclear data tables*, 62(2):149–253, 1996.

[144] Y Yamamura and Shigeru Shindo. An empirical formula for angular dependence of sputtering yields. *Radiation effects*, 80(1-2):57–72, 1984.

[145] Azer Yalin, Vijaya Surla, Casey Farnell, Mark Butweiller, Christina Shadburn, and John Williams. Sputtering studies of multi-component materials by weight loss and cavity ring-down spectroscopy. In *42nd AIAA/ASME/SAE/ASEE Joint Propulsion Conference & Exhibit*, page 4338, 2006.

[146] AJ Dekker. Secondary electron emission. In *Solid State Physics*, volume 6, pages 251–311. Elsevier, 1958.

[147] A.I. Morozov and V.V. Savel'Ev. Theory of the near-wall conductivity. *Plasma Physics Reports*, 27(7):570–575, 2001.

[148] A.I. Morozov. Conditions for efficient current transport by near-wall conduction. *Soviet Physics-Tech. Physics*, 32(8):901–904, 1987.

[149] K.U. Riemann. The Bohm criterion and sheath formation. *J. Phys. D: Appl. Phys.*, 24:492–518, 1991.

[150] K.U. Riemann. The Bohm criterion and boundary conditions for a multicomponent system. *IEEE Transactions On Plasma Science*, 23:709–716, 1995.

[151] E Ahedo. Presheath/sheath model with secondary electron emission from two parallel walls. *Physics of plasmas*, 9(10):4340–4347, 2002.

[152] Nathan B Meezan and Mark A Cappelli. Kinetic study of wall collisions in a coaxial hall discharge. *Physical Review E*, 66(3):036401, 2002.

[153] F. Taccogna, S. Longo, and M. Capitelli. Plasma sheaths in Hall discharge. *Physics of Plasmas*, 12:093506, 2005.

[154] N Gascon, M Dudeck, and S Barral. Wall material effects in stationary plasma thrusters. i. parametric studies of an spt-100. *Physics of Plasmas*, 10(10):4123–4136, 2003.

[155] Joel Sercel. Simple model of plasma acceleration in a magnetic nozzle. In *21st International Electric Propulsion Conference*, page 2597, 1990.

[156] Joel Sercel. Electron-cyclotron-resonance (ecr) plasma acceleration. In *19th AIAA, Fluid Dynamics, Plasma Dynamics, and Lasers Conference*, page 1407, 1987.

[157] HG Kosmahl, DB Miller, and GW Bethke. Plasma acceleration with microwaves near cyclotron resonance. *Journal of Applied Physics*, 38(12):4576–4582, 1967.

[158] GW Bethke and DB Miller. Cyclotron resonance thruster design techniques. *AIAA Journal*, 4(5):835–840, 1966.

[159] Francis F Chen. Permanent magnet helicon source for ion propulsion. *IEEE Transactions on plasma science*, 36(5):2095–2110, 2008.

[160] Francis F Chen. Plasma ionization by helicon waves. *Plasma Physics and Controlled Fusion*, 33(4):339, 1991.

[161] The consortium for hall effect orbital propulsion system (cheops) project received funding from the european union's horizon 2020 research and innovation programme, under grant agreement no.730135.

[162] Adrián Domınguez, Filippo Cichocki, Mario Merino, Pablo Fajardo, and Eduardo Ahedo. 2d and 3d hybrid pic-fluid modeling of electric thruster plumes. In *35th International Electric Propulsion Conference, paper IEPC-2017-209*, 2017.

[163] Bryan O'Sullivan. *Mercurial: The Definitive Guide: The Definitive Guide.* " O'Reilly Media, Inc.", 2009.

[164] Daniel Perez-Grande, Jiewei Zhou, Adrián Domınguez, Mario Merino, Pablo Fajardo, and Eduardo Ahedo. Development updates for a two-dimensional axisymmetric hybrid code for plasma thruster discharges. In *35th International Electric Propulsion Conference, paper IEPC-2017-201*, 2017.

[165] Filippo Cichocki, Adrián Dominguez, Mario Merino, and Eduardo Ahedo. A 3d hybrid code to study electric thruster plumes. In *Space Propulsion Conference 2016*, number 3124968, 2016.

[166] The HDF Group. Hierarchical data format version 5. http://www.hdfgroup.org/HDF5, 2000-2010.

[167] Leonardo Dagum and Ramesh Menon. Openmp: an industry standard api for shared-memory programming. *IEEE computational science and engineering*, 5(1):46–55, 1998.

[168] Mario Merino, Filippo Cichocki, and Eduardo Ahedo. A collisionless plasma thruster plume expansion model. *Plasma Sources Science and Technology*, 24(3):035006, 2015.

[169] James E Polk, RY Kakuda, JR Anderson, John R Brophy, VK Rawlin, MJ Patterson, J Sovey, and J Hamley. Validation of the nstar ion propulsion system on the deep space one mission: overview and initial results. *AIAA paper*, 99:2274, 1999.

[170] A. Domínguez, D. Perez-Grande, P. Fajardo, and E. Ahedo. NOMADS: development of a versatile plasma discharge simulation plarform for electric propulsion. In *Space Propulsion Conference*, number 3124869, Rome, Italy, 2016.

[171] Christian P Robert. *Monte carlo methods*. Wiley Online Library, 2004.

[172] Vahid Vahedi and Maheswaran Surendra. A monte carlo collision model for the particle-in-cell method: applications to argon and oxygen discharges. *Computer Physics Communications*, 87(1-2):179–198, 1995.

[173] F.I. Parra, E. Ahedo, M. Fife, and M. Martínez-Sánchez. A two-dimensional hybrid model of the Hall thruster discharge. *Journal of Applied Physics*, 100:023304, 2006.

[174] Francis J Alexander and Alejandro L Garcia. The direct simulation monte carlo method. *Computers in Physics*, 11(6):588–593, 1997.

[175] Charles K Birdsall and Dieter Fuss. Clouds-in-clouds, clouds-in-cells physics for many-body plasma simulation. *Journal of Computational Physics*, 3(4):494–511, 1969.

[176] Charles K Birdsall and Dieter Fuss. Clouds-in-clouds, clouds-in-cells physics for many-body plasma simulation. *Journal of Computational Physics*, 135(2):141–148, 1997.

[177] R. Santos and E. Ahedo. Implementation of the kinetic Bohm condition in a Hall thruster hybrid code. In *45th Joint Propulsion Conference, Denver, CO*, AIAA 2009-4913, 2009.

[178] David Meeker. Finite element method magnetics. *FEMM*, 4:32, 2010.

[179] F.B. De Saavedra García Del Rio. Modelling and optimisation of magnetic circuits for next generation hall-effect thrusters. Master's thesis, Escuela Politécnica Superior, Universidad Carlos III de Madrid, 2017.

[180] Hrvoje Jasak, Aleksandar Jemcov, Zeljko Tukovic, et al. Openfoam: A c++ library for complex physics simulations. In *International workshop on coupled methods in numerical dynamics*, volume 1000, pages 1–20. IUC Dubrovnik, Croatia, 2007.

[181] Hrvoje Jasak. Openfoam: open source cfd in research and industry. *International Journal of Naval Architecture and Ocean Engineering*, 1(2):89–94, 2009.

[182] Boris Delaunay. Sur la sphere vide. *Izv. Akad. Nauk SSSR, Otdelenie Matematicheskii i Estestvennyka Nauk*, 7(793-800):1–2, 1934.

[183] SA Voloshin. Anisotropic flow. *Nuclear Physics A*, 715:379c–388c, 2003.

[184] Arthur M Poskanzer and Sergei A Voloshin. Methods for analyzing anisotropic flow in relativistic nuclear collisions. *Physical Review C*, 58(3):1671, 1998.

[185] Charles Gale, Sangyong Jeon, Björn Schenke, Prithwish Tribedy, and Raju Venugopalan. Event-by-event anisotropic flow in heavy-ion collisions from combined yang-mills and viscous fluid dynamics. *Physical review letters*, 110(1):012302, 2013.

[186] Alex Groisman and Stephen R Quake. A microfluidic rectifier: anisotropic flow resistance at low reynolds numbers. *Physical review letters*, 92(9):094501, 2004.

[187] Henry K Moffatt. *Field Generation in Electrically Conducting Fluids*. Cambridge University Press, Cambridge, London, New York, Melbourne, 1978.

[188] Franklin Chang-Diaz, Jared Squire, Roger Bengtson, Boris Breizman, Mark Carter, and F Baity. The physics and engineering of the vasimr engine. In *36th AIAA/ASME/SAE/ASEE Joint Propulsion Conference and Exhibit*, page 3756, 2000.

[189] AV Ilin, FR Chang-Diaz, JP Squire, AG Tarditi, BN Breizman, and MD Carter. Simulations of plasma detachment in vasimr. *AIAA paper*, 346, 2002.

[190] José A Bittencourt. *Fundamentals of plasma physics*. Springer Science & Business Media, 2013.

[191] Albert Simon. Diffusion of arc plasmas across a magnetic field. *Journal of Nuclear Energy (1954)*, 7(3-4):278–278, 1958.

[192] Richard E Wirz. *Discharge plasma processes of ring-cusp ion thrusters*. PhD thesis, California Institute of Technology, 2005.

[193] ET Meier, VS Lukin, and Uri Shumlak. Spectral element spatial discretization error in solving highly anisotropic heat conduction equation. *Computer Physics Communications*, 181(5):837–841, 2010.

[194] AH Glasser and XZ Tang. The sel macroscopic modeling code. *Computer physics communications*, 164(1):237–243, 2004.

[195] David V Anderson. Axisymmetric multifluid simulation of high beta plasmas with anisotropic transport using a moving flux coordinate grid. *Journal of Computational Physics*, 17(3):246–275, 1975.

[196] Robert E Peterkin Jr and Michael H Frese. Mach: A reference manual–. *Air Force Research Laboratory, Phillips Research Site*, 10, 1998.

[197] Yiangos George Mikellides. *Theoretical modeling and optimization of ablation-fed pulsed plasma thrusters*. PhD thesis, The Ohio State University, 1999.

[198] Pavlos G Mikellides, Peter J Turchi, and Norman F Roderick. Applied-field magnetoplasmadynamic thrusters, part 1: Numerical simulations using the mach2 code. *Journal of Propulsion and Power*, 16(5):887–893, 2000.

[199] Daniel Perez-Grande, Oscar Gonzalez-Martinez, Pablo Fajardo, and Eduardo Ahedo. Analysis of the numerical diffusion in anisotropic mediums: Benchmarks for magnetic field aligned meshes in space propulsion simulations. *Applied Sciences*, 6(11):354, 2016.

[200] O. González Martínez. Study on numerical diffusion in aligned and non-aligned meshes for magnetically confined plasma transport equations. Master's thesis, Escuela Politécnica Superior, Universidad Carlos III de Madrid, 2015.

[201] Samuel Araki and Richard E Wirz. Magnetic field aligned mesh for ring-cusp discharge chambers. In *50th AIAA/ASME/SAE/ASEE Joint Propulsion Conference*, page 3830, 2014.

[202] L Garrigues, GJM Hagelaar, J Bareilles, C Boniface, and JP Boeuf. Model study of the influence of the magnetic field configuration on the performance and lifetime of a hall thruster. *Physics of Plasmas*, 10(12):4886–4892, 2003.

[203] Boris Diskin and James L Thomas. Effects of mesh regularity on accuracy of finite-volume schemes. In *50th AIAA Aerospace Sciences Meeting*, pages 2012–0609, 2012.

[204] SR Mathur and JY Murthy. A pressure-based method for unstructured meshes. *Numerical Heat Transfer*, 31(2):195–215, 1997.

[205] Douglas N Arnold, Arup Mukherjee, and Luc Pouly. Locally adapted tetrahedral meshes using bisection. *SIAM Journal on Scientific Computing*, 22(2):431–448, 2000.

[206] Emre Sozer, Christoph Brehm, and Cetin C Kiris. Gradient calculation methods on arbitrary polyhedral unstructured meshes for cell-centered cfd solvers. In *Proceedings of the 52nd Aerospace Sciences Meeting, National Harbor, MD, USA*, volume 1317, 2014.

[207] Eiji Shima, Keiichi Kitamura, and Takanori Haga. Green–gauss/weighted-least-squares hybrid gradient reconstruction for arbitrary polyhedra unstructured grids. *AIAA journal*, 51(11):2740–2747, 2013.

[208] Dimitri Mavriplis. Revisiting the least-squares procedure for gradient reconstruction on unstructured meshes. In *16th AIAA Computational Fluid Dynamics Conference*, page 3986, 2003.

[209] Richard Franke. Scattered data interpolation: tests of some methods. *Mathematics of computation*, 38(157):181–200, 1982.

[210] Åke Björck. Least squares methods. *Handbook of numerical analysis*, 1:465–652, 1990.

[211] Donald Shepard. A two-dimensional interpolation function for irregularly-spaced data. In *Proceedings of the 1968 23rd ACM national conference*, pages 517–524. ACM, 1968.

[212] D. Escobar. Motores de efecto hall de alto impulso específico. Master's thesis, E.T.S.I. Aeronáuticos, Universidad Politécnica de Madrid, 2005.

[213] Igor Kaganovich, M Mišina, SV Berezhnoi, and Renaat Gijbels. Electron boltzmann kinetic equation averaged over fast electron bouncing and pitch-angle scattering for fast modeling of electron cyclotron resonance discharge. *Physical Review E*, 61(2):1875, 2000.

[214] AR Barakat and RW Schunk. Transport equations for multicomponent anisotropic space plasmas: A review. *Plasma Physics*, 24(4):389, 1982.

[215] J.A. Bittencourt. *Fundamentals of Plasma Physics*. Pergamon, Oxford, 1986.

[216] JJ Ramos. Fluid theory of magnetized plasma dynamics at low collisionality. *Physics of plasmas*, 14(5):052506, 2007.

[217] J. P. Boeuf. New insights from pic simulations on the exb electron drift instability in hall thrusters. In *35th International Electric Propulsion Conference, Atlanta, GA, paper IEPC-2017-216*, 2017.

[218] Jean-Pierre Boeuf. Rotating structures in low temperature magnetized plasmasâĂŤinsight from particle simulations. *Frontiers in Physics*, 2:74, 2014.

[219] E Ahedo, JM Gallardo, and M Martınez-Sánchez. Model of the plasma discharge in a hall thruster with heat conduction. *Physics of Plasmas*, 9(9):4061–4070, 2002.

[220] E. Ahedo, J.M. Gallardo, and M. Martínez-Sánchez. Effects of the radial-plasma wall interaction on the axial Hall thruster discharge. *Physics of Plasmas*, 10(8):3397–3409, 2003.

[221] E. Choueiri. Plasma oscillations in Hall thrusters. *Physics of Plasmas*, 8(4):1411–1426, 2001.

[222] E.Y. Choueiri. Anomalous resistivity and heating in current-driven plasma thrusters. *Physics of Plasmas*, 6:2290, 1999.

[223] E.Y. Choueiri. Characterization of oscillations in closed drift thrusters. In *30th AIAA Joint Propulsion Conference and Exhibit, 1994. AIAA-94*, volume 3013, 1994.

[224] S. Yoshikawa and D.J. Rose. Anomalous diffusion of a plasma across a magnetic field. *Physics of Fluids*, 5:334, 1962.

[225] G.S. Janes and R.S. Lowder. Anomalous electron diffusion and ion acceleration in a low-density plasma. *Physics of Fluids*, 9(6):1115–1123, 1966.

[226] Trevor Lafleur, SD Baalrud, and Pascal Chabert. Theory for the anomalous electron transport in hall effect thrusters. i. insights from particle-in-cell simulations. *Physics of Plasmas*, 23(5):053502, 2016.

[227] Trevor Lafleur, SD Baalrud, and Pascal Chabert. Theory for the anomalous electron transport in hall effect thrusters. ii. kinetic model. *Physics of Plasmas*, 23(5):053503, 2016.

[228] J Cavalier, N Lemoine, G Bonhomme, S Tsikata, C Honoré, and D Grésillon. Hall thruster plasma fluctuations identified as the e× b electron drift instability: Modeling and fitting on experimental data. *Physics of Plasmas*, 20(8):082107, 2013.

[229] Alejandro Lopez Ortega, Ira Katz, and Vernon H Chaplin. A first-principles model based on saturation of the electron cyclotron drift instability for electron transport in hydrodynamics simulations of hall thruster plasmas. In *35th International Electric Propulsion Conference, Atlanta, GA, paper IEPC-2017-178*, 2017.

[230] L. Garrigues, G.J.M. Hagelaar, C. Boniface, and J.P. Boeuf. Anomalous conductivity and secondary electron emission in Hall effect thrusters. *Journal of applied physics*, 100(12):123301, 2006.

[231] R.R. Hofer, I. Katz, I.G. Mikellides, D.M. Goebel, K.K. Jameson, R.M. Sullivan, and L.K. Johnson. Efficacy of electron mobility models in hybrid-pic Hall thruster simulations. *AIAA Paper*, 4924:2008, 2008.

[232] Sydney Chapman and Thomas George Cowling. *The mathematical theory of non-uniform gases: an account of the kinetic theory of viscosity, thermal conduction and diffusion in gases*. Cambridge university press, 1970.

[233] I. Maqueda, D. Escobar, and E. Ahedo. Advances on a Hall thruster hybrid code. In *30th International Electric Propulsion Conference, Florence, Italy*, IEPC 2007-066, 2007.

[234] Cosmin G. Petra, Olaf Schenk, Miles Lubin, and Klaus Gärtner. An augmented incomplete factorization approach for computing the schur complement in stochastic optimization. *SIAM Journal on Scientific Computing*, 36(2):C139–C162, 2014.

[235] Cosmin G. Petra, Olaf Schenk, and Mihai Anitescu. Real-time stochastic optimization of complex energy systems on high-performance computers. *IEEE Computing in Science & Engineering*, 16(5):32–42, 2014.

[236] Hisashi Kotakemori, Hidehiko Hasegawa, and Akira Nishida. Performance evaluation of a parallel iterative method library using openmp. In *High-Performance Computing in Asia-Pacific Region, 2005. Proceedings. Eighth International Conference on*, pages 5–pp. IEEE, 2005.

[237] Dan M Goebel, Richard R Hofer, Ioannis G Mikellides, Ira Katz, James E Polk, and Brandon N Dotson. Conducting wall hall thrusters. *IEEE Transactions on Plasma Science*, 43(1):118–126, 2015.

[238] E Ahedo. Plasma–wall interaction in an oblique magnetic field: Model of the space-charge sheath for large potentials and small debye lengths. *Physics of Plasmas*, 6(11):4200–4207, 1999.

[239] Eduardo Ahedo and Valentín De Pablo. Effects of electron secondary emission and partial thermalization on a hall thruster plasma. In *42nd AIAA/ASME/SAE/ASEE Joint Propulsion Conference & Exhibit*, page 4328, 2006.

[240] E. Ahedo and V. de Pablo. Combined effects of electron partial thermalization and secondary emission in Hall thruster discharges. *Physics of Plasmas*, 14:083501, 2007.

[241] G.D. Hobbs and J.A. Wesson. Heat flow through a langmuir sheath in the presence of electron emission. *Plasma Physics*, 9:85–87, 1967.

[242] E. Ahedo, J.M. Gallardo, and M. Martínez-Sánchez. Model of the plasma discharge in a Hall thruster with heat conduction. *Physics of Plasmas*, 9(9):4061–4070, 2002.

[243] D. Sydorenko, A. Smolyakov, I. Kaganovich, and Y. Raitses. Kinetic simulation of secondary electron emission effects in Hall thrusters. *Physics of Plasmas*, 13:014501, 2006.

[244] S.A. Schwarz. Application of a semi-empirical sputtering model to secondary electron emission. *Journal of Applied Physics*, 68(5):2382–2391, 1990.

[245] E. Ahedo and F.I. Parra. Model of radial plasma-wall interactions in a Hall thruster. In *Proc. 38th Joint Propulsion Conference, Indianapolis, IN*, AIAA 2002-4106, 2002.

[246] E. Ahedo and D. Escobar. Two-region model for positive and negative plasma sheaths and its application to Hall thruster metallic anodes. *Physics of Plasmas*, 15:033504, 2008.

[247] E. Ahedo and J.Rus. Vanishing of the negative anode sheath in a Hall thruster. *Journal of Applied Physics*, 98:043306, 2005.

[248] J Rodney M Vaughan. A new formula for secondary emission yield. *IEEE Transactions on Electron Devices*, 36(9):1963–1967, 1989.

[249] J Scott Miller, Steve H Pullins, Dale J Levandier, Yu-hui Chiu, and Rainer A Dressler. Xenon charge exchange cross sections for electrostatic thruster models. *Journal of Applied Physics*, 91(3):984–991, 2002.

[250] J.S. Miller, S.H. Pullins, D.J. Levandier, Y. Chiu, and R.A. Dressler. Xenon charge exchange cross sections for electrostatic thruster models. *Journal of Applied Physics*, 91(3):984–991, 2002.

[251] Morton Mitchner and Charles H Kruger Jr. Partially ionized gases. 1973.

[252] Michal Gryzinski. Classical theory of atomic collisions. i. theory of inelastic collisions. *Physical Review*, 138(2A):A336, 1965.

[253] Eric Henry Stoneley Burhop. *The Auger effect and other radiationless transitions*. Cambridge University Press, 2014.

[254] Wolfgang Lotz. Electron-impact ionization cross-sections and ionization rate coefficients for atoms and ions from hydrogen to calcium. *Zeitschrift für Physik*, 216(3):241–247, 1968.

[255] Hans-Werner Drawin. Collision and transport cross-sections. Technical report, European Atomic Energy Community. Commissariat a l'Energie Atomique, Fontenay-aux-Roses (France). Centre d'Etudes Nucleaires, 1967.

[256] D Mathur and C Badrinathan. Ionization of xenon by electrons: Partial cross sections for single, double, and triple ionization. *Physical Review A*, 35(3):1033, 1987.

[257] Alexander Borovik Jr, J Rausch, J Rudolph, M Gharaibeh, S Schippers, and A Müller. Electron impact ionization of xenon ions. In *Journal of Physics: Conference Series*, volume 194, page 062014. IOP Publishing, 2009.

[258] Makoto Hayashi. Determination of electron-xenon total excitation cross-sections, from threshold to 100 ev, from experimental values of townsend's α. *Journal of Physics D: Applied Physics*, 16(4):581, 1983.

[259] Makoto Hayashi. Bibliography of electron and photon cross sections with atoms and molecules published in the 20th century. Technical report, National Inst. for Fusion Science, 2003.

[260] LC Pitchford. Gec plasma data exchange project. *Journal of Physics D: Applied Physics*, 46(33):330301, 2013.

[261] V Puech and L Torchin. Collision cross sections and electron swarm parameters in argon. *Journal of Physics D: Applied Physics*, 19(12):2309, 1986.

[262] MC Bordage, GJM Hagelaar, LC Pitchford, SF Biagi, and V Puech. Comparisons of sets of electron-neutral scattering cross sections and calculated swarm parameters in kr and xe. In *APS Meeting Abstracts*, 2011.

[263] HP Summers and MG O'Mullane. Atomic data and modelling for fusion: the adas project. In *AIP Conference Proceedings*, volume 1344, pages 179–187. AIP, 2011.

[264] CJ Fontes, HL Zhang, J Abdallah Jr, REH Clark, DP Kilcrease, J Colgan, RT Cunningham, P Hakel, NH Magee, and ME Sherrill. The los alamos suite of relativistic atomic physics codes. *Journal of Physics B: Atomic, Molecular and Optical Physics*, 48(14):144014, 2015.

[265] SF Biagi. Monte carlo simulation of electron drift and diffusion in counting gases under the influence of electric and magnetic fields. *Nuclear Instruments and Methods in Physics Research Section A: Accelerators, Spectrometers, Detectors and Associated Equipment*, 421(1-2):234–240, 1999.

[266] S Pancheshnyi, S Biagi, MC Bordage, GJM Hagelaar, WL Morgan, AV Phelps, and LC Pitchford. The lxcat project: Electron scattering cross sections and swarm parameters for low temperature plasma modeling. *Chemical Physics*, 398:148–153, 2012.

[267] RP McEachran and AD Stauffer. Elastic scattering of electrons from krypton and xenon. *Journal of Physics B: Atomic and Molecular Physics*, 17(12):2507, 1984.

[268] Makoto Hayashi. Electron collision cross-sections for molecules determined from beam and swarm data. In *Swarm Studies and Inelastic Electron-Molecule Collisions*, pages 167–187. Springer, 1987.

[269] R.J. Goldston and P.H. Rutherford. *Introduction to Plasma Physics*. Institute of Physics Publishing, Bristol, 1995.

[270] Brandon D Smith, Iain D Boyd, and Hani Kamhawi. Influence of triply-charged ions and ionization cross-sections in a hybrid-pic model of a hall thruster discharge. 2014.

[271] E.W. Bell, N. Djurić, and G.H. Dunn. Electron-impact ionization of in^+ and xe^+. *Physical Review A*, 48(6):4286, 1993.

[272] CW Clenshaw. A note on the summation of chebyshev series. *Mathematics of Computation*, 9(51):118–120, 1955.

[273] GJM Hagelaar, J Bareilles, L Garrigues, and J-P Boeuf. Role of anomalous electron transport in a stationary plasma thruster simulation. *Journal of Applied Physics*, 93(1):67–75, 2003.

[274] M. Mitchner and C.H. Kruger Jr., editors. *Partially ionized gases*. Wiley, 1973.

[275] Timothy Barth, Raphaèle Herbin, and Mario Ohlberger. Finite volume methods: foundation and analysis. *Encyclopedia of Computational Mechanics Second Edition*, 2004.

[276] Ioannis G Mikellides, Ira Katz, Richard H Hofer, and Dan M Goebel. Hall-effect thruster simulations with 2-d electron transport and hydrodynamic ions. 2009.

[277] I Maqueda, D Escobar, and E Ahedo. Advances on a hall thruster hybrid code. *Simulation*, 40:50, 2007.

[278] Nathan Meezan and Mark Cappelli. Electron density measurements for determining the anomalous electron mobility in a coaxial hall discharge plasma. In *36th AIAA/ASME/SAE/ASEE Joint Propulsion Conference and Exhibit*, page 3420, 2000.

[279] E Ahedo and Diego Escobar. Two-region model for positive and negative plasma sheaths and its application to hall thruster metallic anodes. *Physics of plasmas*, 15(3):033504, 2008.

[280] E Ahedo and J Rus. Vanishing of the negative anode sheath in a hall thruster. *Journal of applied physics*, 98(4):043306, 2005.

[281] Sang-Wook Kim, John Foster, and Alec Gallimore. Very-near-field plume study of a 1.35 kw spt-100. In *32nd Joint Propulsion Conference and Exhibit*, page 2972, 1996.

[282] Michael R Nakles, WA Hargus, Jorge J Delgado, and Ronald L Corey. A performance comparison of xenon and krypton propellant on an spt-100 hall thruster. In *Proceedings of the 32nd International Electric Propulsion Conference*, volume 3, 2011.

[283] SK Absalamov, VB Andreev, T Colbert, M Day, VV Egorov, RU Gnizdor, H Kaufman, V Kim, AI Koriakin, and KN Kozubskii. Measurement of plasma parameters in the stationary plasma thruster (spt-100) plume and its effect on spacecraft components. In *Joint Propulsion Conference and Exhibit*, 1992.

[284] John M Sankovic, John A Hamley, and Thomas W Haag. Performance evaluation of the russian spt-100 thruster at nasa lerc. 1994.

[285] Charles E Garner, James C Polk, Keith M Goodfellow, Lewis C Pless, and John R Brophy. Performance evaluation and life testing of the spt-100. 1993.

[286] Charles Garner, John Brophy, James Polk, and Lewis Pless. Cyclic endurance test of a spt-100 stationary plasma thruster. In *30th Joint Propulsion Conference and Exhibit*, page 2856, 1994.

[287] Charles Garner, John Brophy, James Polk, and Lewis Pless. A 5,730-hr cyclic endurance test of the spt-100. In *31st Joint Propulsion Conference and Exhibit*, page 2667, 1995.

[288] Vladimir Kim, Vycheslav I Kozlov, Alexander I Skrylnikov, Lev N Umnitsin, Victoria V Svotina, Andre Bouchoule, and Mathieu Prioul. Investigation of the local plasma parameter distributions in the spt accelerating channel under increased discharge voltages. In *29th International Electric Propulsion Conference, Princeton, USA, IEPC-2005-004. Electric Rocket Propulsion Society, Fairview Park, OH*, 2005.

[289] Yevgeny Raitses, D Staack, M Keidar, and NJ Fisch. Electron-wall interaction in hall thrusters. *Physics of Plasmas*, 12(5):057104, 2005.

[290] Y Raitses, D Staack, A Smirnov, and NJ Fisch. Space charge saturated sheath regime and electron temperature saturation in hall thrusters. *Physics of Plasmas*, 12(7):073507, 2005.

[291] Nathan B Meezan, William A Hargus Jr, and Mark A Cappelli. Anomalous electron mobility in a coaxial hall discharge plasma. *Physical Review E*, 63(2):026410, 2001.

[292] N Dorval, J Bonnet, JP Marque, E Rosencher, S Chable, F Rogier, and P Lasgorceix. Determination of the ionization and acceleration zones in a stationary plasma thruster by optical spectroscopy study: Experiments and model. *Journal of Applied Physics*, 91(8):4811–4817, 2002.

[293] Vladimir Kim, Dmitry Grdlichko, Vyacheslav Kozlov, Alexei Lazourenko, Garry Popov, and Alexander Skrylnikov. Local plasma parameter measurements by nearwall probes inside the spt accelerating channel under thruster operation with kr. In *38th AIAA/ASME/SAE/ASEE Joint Propulsion Conference & Exhibit*, page 4108, 2002.

[294] Sang-Wook Kim. *Experimental investigations of plasma parameters and species-dependent ion energy distribution in the plasma exhaust plume of a Hall thruster*. PhD thesis, University of Michigan, 1999.

[295] Lyon B King and Alec D Gallimore. Ion-energy diagnostics in an spt-100 plume from thrust axis to backflow. *Journal of propulsion and power*, 20(2):228–242, 2004.

[296] Lyon B King and Alec D Gallimore. Mass spectral measurements in the plume of an spt-100 hall thruster. *Journal of Propulsion and Power*, 16(6):1086–1092, 2000.

[297] Lyon B King, Alec D Gallimore, and Colleen M Marrese. Transport-property measurements in the plume of an spt-100 hall thruster. *Journal of Propulsion and Power*, 14(3):327–335, 1998.

[298] Richard Hofer, Ioannis Mikellides, Ira Katz, and Dan Goebel. Wall sheath and electron mobility modeling in hybrid-pic hall thruster simulations. In *43rd AIAA/ASME/SAE/ASEE Joint Propulsion Conference & Exhibit*, page 5267, 2007.

[299] GS Janes and RS Lowder. Anomalous electron diffusion and ion acceleration in a low-density plasma. *The Physics of Fluids*, 9(6):1115–1123, 1966.

[300] L Garrigues, J Pérez-Luna, J Lo, GJM Hagelaar, JP Boeuf, and S Mazouffre. Empirical electron cross-field mobility in a hall effect thruster. *Applied Physics Letters*, 95(14):141501, 2009.

[301] A Bouchoule, Ch Philippe-Kadlec, M Prioul, F Darnon, M Lyszyk, L Magne, D Pagnon, S Roche, M Touzeau, S Béchu, et al. Transient phenomena in closed electron drift plasma thrusters: insights obtained in a french cooperative program. *Plasma Sources Science and Technology*, 10(2):364, 2001.

[302] F Darnon, L Garrigues, JP Boeuf, Andre Bouchoule, and M Lyszyk. Spontaneous oscillations in a hall thruster. *IEEE Transactions on Plasma science*, 27(1):98–99, 1999.

[303] A Smolyakov, O Koshkarov, I Romadanov, S Janhunen, O Chapurin, Y Raitses, I Kaganovich, and D Sydorenko. Fluid and kinetic modelling of instabilities and transport in exb plasma discharges. 2017.

[304] M Touzeau, M Prioul, S Roche, N Gascon, C Pérot, F Darnon, S Béchu, C Philippe-Kadlec, L Magne, P Lasgorceix, et al. Plasma diagnostic systems for hall-effect plasma thrusters. *Plasma Physics and Controlled Fusion*, 42(12B):B323, 2000.

[305] Jesse A Linnell and Alec D Gallimore. Efficiency analysis of a hall thruster operating with krypton and xenon. *Journal of Propulsion and Power*, 22(6):1402–1418, 2006.

[306] Richard R Hofer and Robert S Jankovsky. The influence of current density and magnetic field topography in optimizing the performance, divergence, and plasma oscillations of high specific impulse hall thrusters. 2003.

[307] Alejandro Lopez Ortega and Ioannis G Mikellides. The importance of the cathode plume and its interactions with the ion beam in numerical simulations of hall thrusters. *Physics of Plasmas*, 23(4):043515, 2016.

[308] Christopher A. Dodson, Daniel Perez-Grande, Benjamin A. Jorns, Dan M. Goebel, and Richard E. Wirz. Ion heating measurements on the centerline of a high-current hollow cathode plume. *Journal of Propulsion and Power*, Accepted for publication.

[309] D Perez-Grande, O Gonzalez-Martinez, P Fajardo, and E Ahedo. Benchmarks for magnetic field aligned meshes in electromagnetic plasma thruster simulations. In *34th International Electric Propulsion Conference, paper IEPC-2015-203*, 2015.

[310] Christopher Dodson, Daniel Perez-Grande, Benjamin Jorns, Dan M Goebel, and Richard E Wirz. Laser-induced fluorescence measurements of energetic ions in a 100-a lab6 hollow cathode plume. In *52nd AIAA/SAE/ASEE Joint Propulsion Conference*, page 4838, 2016.

[311] M Wijnen, S Correyero-Plaza, N Agüera-López, and D Perez-Grande. Innovative electric propulsion trends, concurrent mission design and enabling technologies for a bold cubesat lunar positioning system. In *35th International Electric Propulsion Conference, Atlanta, GA, paper IEPC-2017-603*, 2017.